Faculty of Chemistry
Department of Inorganic Chemistry, Analytical Chemistry and Electrochemistry

Кафедра прикладного матеріалознавства і технології конструкційних матеріалів

DOCTORAL THESIS

BIOACTIVE OXIDE COATINGS ENRICHED IN Ca, P, Si FORMED ON MAGNESIUM VIA HIGH-VOLTAGE ANODIZATION

BIOAKTYWNE POWŁOKI TLENKOWE WZBOGACONE W Ca, P, Si WYTWARZANE NA MAGNEZIE POPRZEZ ANODOWE UTLENIANIE WYSOKONAPIĘCIOWE

ФОРМУВАННЯ БІОАКТИВНИХ ПОКРИТТІВ ЗБАГАЧЕНИХ Ca, P, Si МЕТОДОМ ВИСОКОВОЛЬТНОЇ АНОДИЗАЦІЇ НА ПОВЕРХНІ МАГНІЄВИХ СПЛАВІВ

MSc Yevheniia HUSAK
Album number 5136

Scientific Discipline: Chemical Engineering

Doctoral School

Doctoral thesis supervisors:
prof. Wojciech SIMKA (SUT)
prof. Maksym POGORIELOV (SumDU)

Gliwice, 2025

"Coming together is a beginning; keeping together is progress; working together is success"

Henry Ford

I would like to express my deepest gratitude to Supervisors of the thesis prof. Wojciech Simka and prof. Maksym Pogorielov for their support, endless patience, motivating pushes, and the time they have devoted to me in my scientific journey.

I am deeply grateful to the wonderful colleagues of the Electrochemistry Group and the Biomaterial Research Centre for allowing me to be part of these scientific families and for the opportunity to achieve our goals together.

My deepest gratitude goes to my family, whose love, care, and support have been my greatest source of strength and inspiration in this scientific journey.

My heartfelt thanks go to my friends and companions, whose encouragement, understanding, and support have been of immeasurable value to me during this scientific journey.

I would like to express my sincere gratitude to the Silesian University of Technology and the University of Latvia for their invaluable support during the war in Ukraine. Their generosity and solidarity created the conditions that enabled the continuation of scientific work, provided a home for researchers, and offered me personally a safe place to pursue my studies. I am deeply thankful for their openness, encouragement, and for fostering an academic environment where resilience and hope prevailed despite the challenges.

LIST OF CONTENTS

ABSTRACT

In this thesis, the results of research on the development of multifunctional plasma electrolytic oxidation (PEO) coatings on magnesium for biomedical applications are presented. Owing to its biodegradable nature, magnesium is a promising candidate for temporary implants. However, its rapid corrosion, resulting in excessively high pH levels in the surrounding medium that can induce cell death, remains a major obstacle to its widespread clinical use.To overcome these limitations and provide controlled degradation with enhanced biological functionality, ceramic coatings were developed by PEO using electrolytes enriched with calcium, phosphorus, and silicon, supplemented with naturally derived feedstocks such as eggshell powder. Particular emphasis was placed on improving corrosion resistance, promoting bioactivity and osteoconductivity, and imparting antibacterial functionality to magnesium-based substrates. The effectiveness of the developed coatings was evaluated based on improved corrosion resistance, biological performance, and compatibility with host tissues, alongside the ecological sustainability of the processing routes.

The research was divided into four main stages. In the first stage, the influence of silicate concentration and applied voltage on coating morphology, uniformity, corrosion resistance, and bioactivity was investigated. The second stage focused on the incorporation of silver nanoparticles into silicate-based electrolytes to introduce antibacterial properties while maintaining anticorrosive performance. The third stage concerned the application of combined silicate–phosphate electrolytes to obtain oxide layers with enhanced corrosion resistance and improved cell adhesion. In the fourth stage, phosphate electrolytes containing calcium-based particles, including biowaste-derived components (eggshells), were employed to form coatings enriched with Ca and P, mimicking bone mineral composition and supporting osteointegration with enhanced corrosion resistance.

The obtained coatings were comprehensively characterized in terms of surface morphology, elemental composition, thickness, and wettability. Immersion tests and ion release studies confirmed the influence of processing parameters on the degradation behavior of both the coatings and the magnesium substrate. Biological assays included cell viability and bacterial adhesion tests.

This research demonstrated the feasibility of producing multifunctional PEO coatings on magnesium using both conventional electrolytes and sustainable additives, including silver nanoparticles and naturally derived materials. Silver-containing systems exhibited successful incorporation of Ag particles during the PEO process and demonstrated antibacterial effects.

Layers obtained from silicate–phosphate electrolytes displayed corrosion resistance and controlled ion release. Coatings fabricated in calcium–phosphate electrolytes, particularly alkaline hexametaphosphate systems enriched with eggshell powder, supported cell adhesion and metabolic activity through a favorable Ca/P ratio and adequate porosity.

STRESZCZENIE

W niniejszej rozprawie przedstawiono wyniki badań nad opracowaniem wielofunkcyjnych powłok wytwarzanych metodą plazmowego utleniania elektrolitycznego (PEO) na magnezie, przeznaczonych do zastosowań biomedycznych. Ze względu na biodegradowalny charakter magnez jest perspektywiczny do wytwarzania implantów tymczasowych. Jednak jego szybka korozja, prowadząca do nadmiernego wzrostu poziomu pH w otaczającym środowisku i mogąca indukować śmierć komórek, pozostaje główną przeszkodą w szerokim zastosowaniu klinicznym. Aby przezwyciężyć te ograniczenia i zapewnić kontrolowaną degradację przy jednoczesnym zwiększeniu funkcjonalności biologicznej, powłoki ceramiczne zostały wytworzone metodą PEO z wykorzystaniem elektrolitów wzbogaconych w wapń, fosfor i krzem, uzupełnionych naturalnymi składnikami, takimi jak proszek ze skorupek jaj kurzych. Szczególny nacisk położono na poprawę odporności korozyjnej, promowanie bioaktywności i osteokonduktywności oraz nadanie substratom magnezowym właściwości przeciwbakteryjnych. Skuteczność opracowanych powłok oceniano na podstawie poprawy odporności korozyjnej, odpowiedzi biologicznej i kompatybilności z tkankami.

Badania podzielono na cztery główne etapy. W pierwszym etapie zbadano wpływ stężenia krzemianów i przyłożonego napięcia na morfologię, jednorodność, odporność korozyjną i bioaktywność powłok. Drugi etap dotyczył wprowadzenia nanocząstek srebra do elektrolitów krzemianowych w celu nadania właściwości przeciwbakteryjnych przy jednoczesnym zachowaniu odporności korozyjnej. Trzeci etap obejmował zastosowanie elektrolitów krzemianowo–fosforanowych w celu uzyskania warstw tlenkowych o zwiększonej odporności korozyjnej i poprawionej adhezji komórek. W czwartym etapie wykorzystano elektrolity fosforanowe zawierające cząstki wapnia, w tym składniki pochodzenia odpadowego (skorupki jaj), w celu wytworzenia powłok wzbogaconych w Ca i P, imitujących skład mineralny kości i wspierających osteointegrację przy poprawionej odporności korozyjnej.

Uzyskane powłoki zostały kompleksowo scharakteryzowane pod względem morfologii powierzchni, składu pierwiastkowego, grubości oraz zwilżalności. Testy zanurzeniowe i badania uwalniania jonów potwierdziły wpływ parametrów procesu na charakter degradacji zarówno powłok, jak i podłoża magnezowego. Badania biologiczne obejmowały testy żywotności komórek oraz adhezji bakterii.

Przeprowadzone badania wykazały możliwość wytwarzania wielofunkcyjnych powłok PEO na magnezie przy użyciu zarówno konwencjonalnych elektrolitów, jak i zrównoważonych dodatków, w tym nanocząstek srebra oraz materiałów naturalnych. Systemy zawierające srebro

wykazały skuteczną inkorporację cząstek Ag w trakcie procesu PEO oraz działanie przeciwbakteryjne. Warstwy uzyskane z elektrolitów krzemianowo–fosforanowych charakteryzowały się odpornością korozyjną i kontrolowanym uwalnianiem jonów. Powłoki wytworzone w elektrolitach wapniowo–fosforanowych, zwłaszcza w zasadowych układach heksametafosforanowych wzbogaconych proszkiem ze skorupek jaj, wspierały adhezję komórek i aktywność metaboliczną dzięki korzystnemu stosunkowi Ca/P oraz odpowiedniej porowatości.

LIST OF IMPORTANT ABBREVIATIONS AND SYMBOLS

at.% – atomic percent

AXP – alkaline–hexametaphosphate

CA – contact angle, º

CFU – colony forming units

DAPI – 4′,6-diamidino-2-phenylindole (fluorescent nuclear stain)

EDX – Energy-Dispersive X-ray analysis

HA – hydroxyapatite

HEX – sodium hexametaphosphate

ICP–MS – Inductively Coupled Plasma – Mass Spectrometry

j – current density, $A \cdot m^2$

MG63 cells – human osteosarcoma cell line MG-63

MHB - Mueller Hinton Broth

Np – number of the pores

OCP – octacalcium phosphate

p – level of statistical significance (p-value)

PEO – Plasma Electrolytic Oxidation

P.s. – pore size, μm^2

Ra – arithmetic mean surface roughness, μm

SBF — simulated body fluid

SEM – Scanning Electron Microscope

Si – silicate-alkaline

Si-Ag – silicate-alkaline with silver nanoparticles (AgNPs)

SP – silicate-phosphate

T – temperature, °C

t – time, seconds

TCP – tricalcium phosphate

TSB – Tryptic Soy Broth

U – voltage, V

U2OS cells – human osteosarcoma cell line U-2 OS

UCMSC – umbilical cord-derived mesenchymal stem cells

XPS – X-ray Photoelectron Spectroscopy

σ – standard deviation

CHAPTER I – INTRODUCTION

1.1 Applications

Currently, among metallic materials, magnesium stands out in the biomedical field due to its biodegradable nature, which makes it a promising candidate for temporary implants. However, its rapid degradation and limited bioactivity pose significant challenges that hinder its widespread medical application.

The results of this research present a new concept for multifunctional coatings that address two critical challenges in the field of temporary biodegradable implants the rapid corrosion of magnesium-based materials and insufficient osseointegration leading to implant failure. Figure 1.1 represents the scheme of the scientific goal of the research. The developed plasma electrolytic oxidation (PEO) coatings—enhanced with bioactive and antimicrobial agents—offer promising potential for use in orthopedic implants that are designed to degrade after fulfilling their clinical function. These coatings support controlled degradation, facilitate bone tissue replacement, and reduce post-operative infection risks.

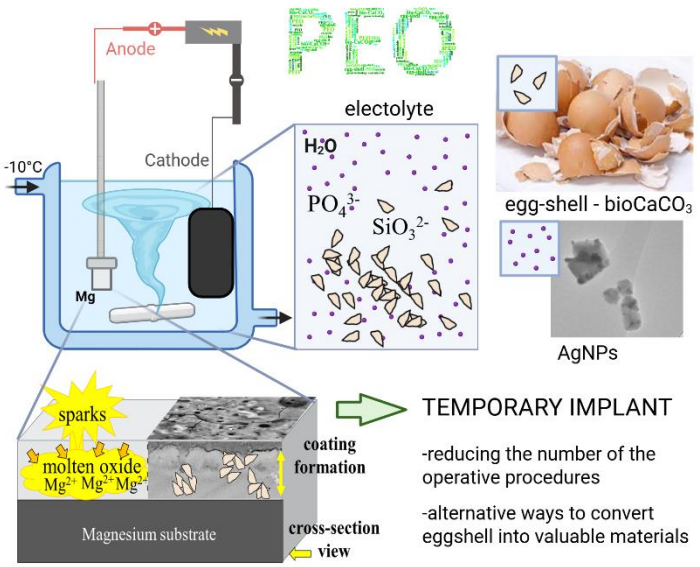

Figure 1.1 Scheme of the scientific goal of the research

By integrating expertise across electrochemistry, material science, cell biology, bacteriology, and medicine, this work contributes to the broader societal goal of improving patient outcomes, preserving organ and skeletal function, and enhancing the quality of life across age groups. Furthermore, the use of naturally derived and non-toxic materials aligns with ecological priorities, promoting the development of sustainable, environmentally friendly biomaterials suitable for future biomedical technologies.

1.2 Research aims

Nowadays, development of temporary biomaterials for bone repair goes by several ways: 1) as bone fixation material, 2) biodegradable polymer-based materials and 3) prototypes of biocompatible magnesium bone implants. These approaches are a revolutionary development in the clinical treatment of orthopaedic diseases.

However, the clinical application of the magnesium-based materials is hindered by rapid corrosion, limited bioactivity, and insufficient osseointegration. Plasma electrolytic oxidation (PEO) offers a promising surface modification strategy to address these limitations by forming multifunctional, oxide-based ceramic coatings. The key challenge lies in developing multifunctional PEO coatings on magnesium that provide long-term corrosion protection, support cell attachment and proliferation, and ensure compatibility with host tissues.

We hypothesize that an electrolyte composition based on naturally derived chemicals (egg-shell) with an appropriate combination of phosphates and silicates, governs the chemical structure and morphological features of the PEO coating, resulting in enhanced functional properties. Therefore, we focused on the incorporation of Ca, P, Si elements into the substrate surface. PEO process in the electrolyte with these elements can decrease the implant's degradation rate, improve surface morphology, and provide bioactive functional groups to increase the biological response. We also focused on naturally derived and non-toxic materials for enchancing the biocompatible function of the surface.

Therefore, the aim of this research was to develop biofunctional coatings enriched with calcium, phosphorus, and silicon on pure magnesium using the plasma electrolytic oxidation technique, and to investigate the influence of process parameters on the properties of the resulting materials in the context of their potential application as biodegradable implants.

The presented work was concentrated around the new electrolyte compositions: silicate-alkaline (Si), silicate-alkaline with AgNPs (Si-Ag), silicate-phosphate (SP) and alkaline–hexametaphosphate (AXP) with addition of Ca-based particles.

Taking into account previous experience in biomaterials development, and research aim the next task were realized:

1. To review the current state of knowledge on plasma electrolytic oxidation (PEO) coatings for magnesium, with a focus on improving corrosion resistance, bioactivity, and antibacterial properties, and identify knowledge gaps related to the use of natural and sustainable feedstocks.
2. To design electrolyte compositions enriched with calcium, phosphorus, and silicon, incorporating both conventional and naturally derived additives (e.g., biowaste-based compounds) to support sustainable processing and promote biofunctional performance.

3. To optimize PEO process parameters—particularly voltage and treatment duration—to obtain uniform, adherent, and hierarchically structured oxide coatings with controlled porosity and enhanced corrosion and biological properties.
4. To characterize the structural and surface properties of the fabricated coatings.
5. To evaluate the bioactivity and antibacterial performance of the developed coatings through in vitro biological assays and to identify the most promising formulations for further development as biodegradable implant surfaces.

CHAPTER II - LITERATURE REVIEW

2.1 Magnesium as biodegradable biomaterial

Magnesium (Mg), a metallic-based biomaterial, has gained significant attention in biomedical research due to its biodegradable and bioresorbable nature. These properties enable magnesium to safely dissolve within the human body over time, particularly during the process of tissue healing [1][2]. As a result, Mg-based implants eliminate the need for secondary surgical implant removal, offering a major advantage over permanent metallic devices.

One of the key factors that distinguishes magnesium from other metals is its mechanical compatibility with human bone. Magnesium and its alloys exhibit an elastic modulus and strength profile closely resembling that of natural bone, which helps to minimize the risk of stress shielding—a phenomenon where stiff implants interfere with normal bone remodeling and load transfer [3][4]. Furthermore, the density of Mg alloys is comparable to that of cortical bone, further enhancing their suitability for orthopedic applications [5]. Figure 2.1 shows most important advantages and disadvantages of magnesium.

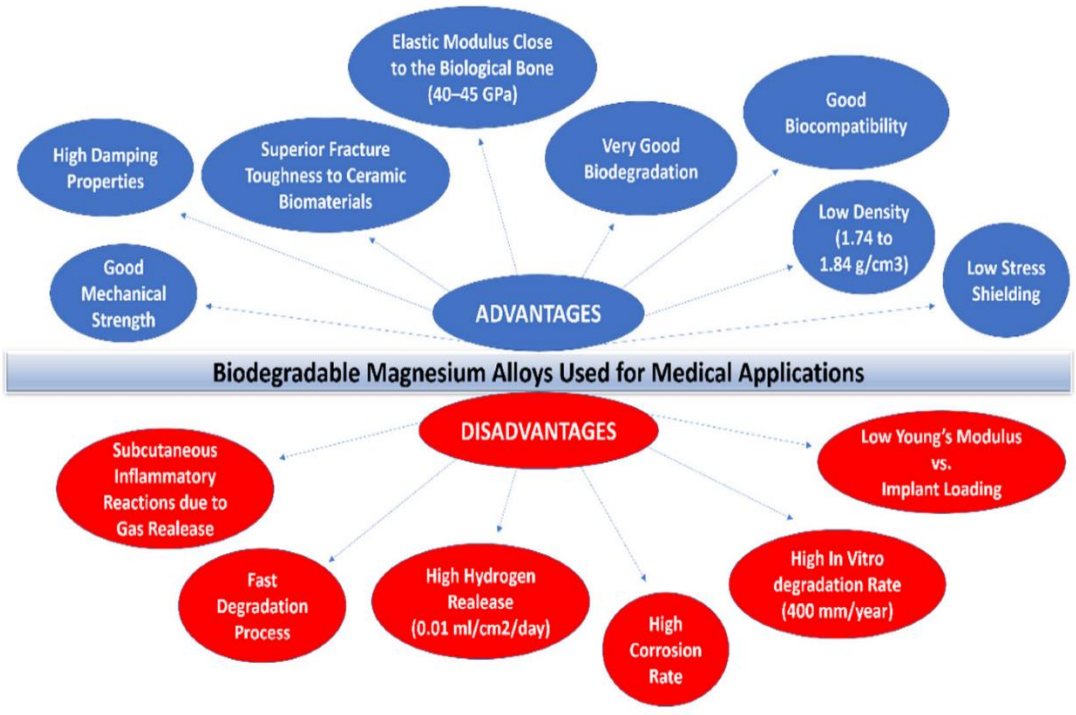

Figure 2.1 Main aspects of biodegradable magnesium alloys used in the medical domain [6]

The unique mechanical and biological characteristics of magnesium enable its use in a wide range of clinical scenarios [7]. Mg-based implants have been investigated for treating coronary artery blockages, vascular obstructions, and orthopedic deformities, such as angular malalignments of long bones, limb length discrepancies, and congenital anomalies including cleft

palate [1], [8]. These implants are particularly beneficial for younger patients with congenital heart defects, where permanent devices may lead to complications due to ongoing skeletal growth. In adults with restenosis, magnesium implants offer the additional benefit of gradual degradation, reducing the risks of chronic inflammation or late-stage thrombosis [9]. Collectively, these applications highlight the versatility and clinical adaptability of magnesium as a bioresorbable material.

A historical overview of magnesium in biomedical applications, as presented by Fatemeh Zahra Akbarzadeh, outlines the major milestones achieved in the development of Mg and Mg-based alloys over the past two centuries (Fig. 2.2) [1]. This timeline reflects not only the sustained scientific interest in magnesium, but also the ongoing evolution of its role in next-generation medical technologies.

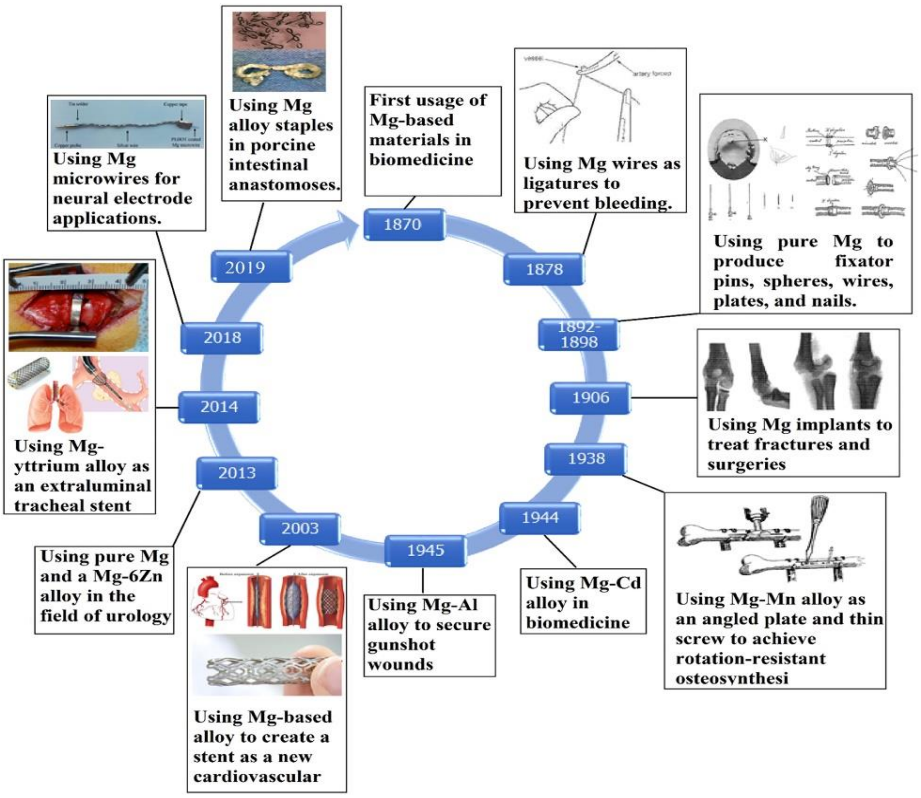

Figure 2.2 Historical milestones of Mg-based materials in biomedical applications [1]

Despite the many advantages of magnesium as a biomaterial, its high susceptibility to corrosion remains a major limitation, particularly in its pure form. Although Mg is capable of degrading within the body in a manner that aligns with tissue healing—ideally dissolving when the implant is no longer needed—its degradation rate often exceeds the desired timeframe for safe and effective healing [10]. In particular, unprotected Mg-based materials tend to corrode more rapidly than the typical tissue regeneration period, which is estimated to be at least 12 weeks.

This accelerated degradation leads to the release of hydrogen (H_2) and an increase in local pH, both of which can interfere with wound healing. Accumulation of gas and alkalisation at the surgical site may result in tissue necrosis and delay the integration of the implant [11]. Moreover, magnesium undergoes localized and pitting corrosion, a mechanism that is particularly dangerous when combined with mechanical loading, as it may compromise the structural integrity of the implant.

Although corrosion results in the formation of magnesium hydroxide ($Mg(OH)_2$), which can act as a passivating layer, the associated alkaline shift in pH is generally unfavorable for biological environments. Experimental data suggest that excessively high pH levels in the surrounding medium can induce cell death. However, dynamic physiological conditions, including the continuous flow of bodily fluids and mass transport of corrosion products, can significantly buffer these pH changes, mitigating their cytotoxic effects [12].

In light of these challenges, further improvement in Mg-based implant performance is necessary. Specifically, research is focused on: (i) reducing the initial healing period, (ii) enhancing osseointegration, particularly in patients with poor bone quality or systemic conditions such as osteoporosis and diabetes, and (iii) minimizing the risk of implant-associated infections, which is especially critical given the rising threat of multidrug-resistant pathogens [13].

2.2 Corrosion resistance, evaluation methods, and surface treatments of magnesium-based materials

Upon contact with the physiological environment, magnesium-based materials are highly susceptible to pitting and electrochemical corrosion (Fig. 2.3) [14]. This degradation process is primarily driven by the spontaneous formation of anodic and cathodic sites on the implant surface, which accelerates localized corrosion and leads to pit formation. As such, controlling the corrosion rate is critical for the clinical success of Mg-based implants.

To improve the corrosion resistance of magnesium, two major strategies are commonly employed: (i) intrinsic material improvement and (ii) surface modification [15]. Among these, surface development is widely recognized as one of the most effective approaches to delay or suppress degradation. A variety of surface coating techniques have been developed to protect magnesium, including chemical conversion coatings, electroplating, and anodizing [15].

Scientists mostly consider two strategies of corrosion resistance, namely intrinsic improvement and surface modification. The first one is improving of the composition or grain optimization via purification [16], [17], alloying [18], [19], [20], [21], and grain refinement [22], [22], [23]. These techniques aim to optimize the microstructure and composition of the material to

enhance its corrosion performance. However, a major drawback of these methods is that they often affect the mechanical integrity and overall structure of the base material, potentially compromising its function in load-bearing applications.

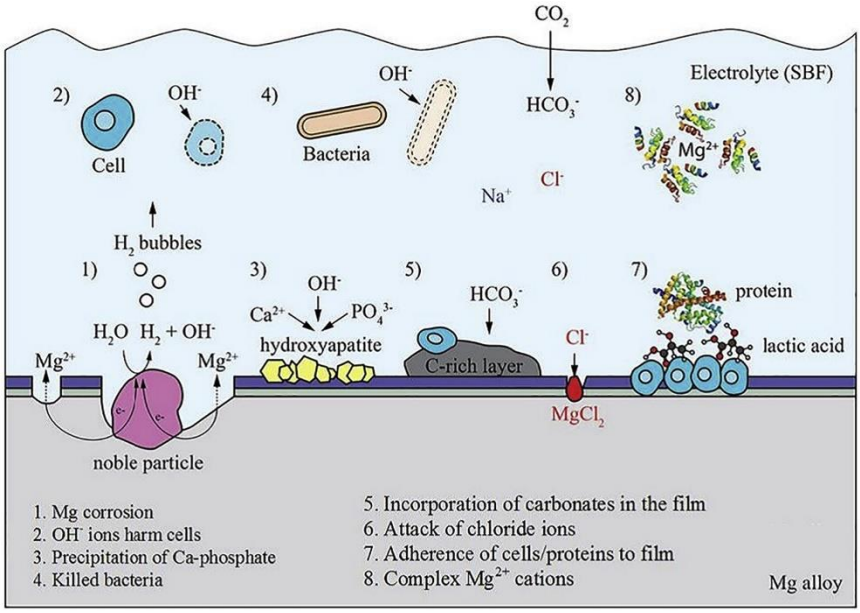

Figure 2.3 Schematic of the interactions between a corroding magnesium alloy and a biological environment [24]

On the other hand, surface modification techniques are considered more flexible and targeted for improving corrosion resistance without altering the bulk properties of magnesium [25]. Surface coatings can significantly reduce or delay localized degradation, preserving both the mechanical integrity and biocompatibility of the implant [26], [27], [28], [29]. A wide range of coating methods has been developed, including but not limited to:

- conversion coatings,
- plasma electrolytic oxidation (PEO),
- vapor-phase deposition,
- laser surface melting,
- electrochemical plating.

These techniques provide protective surface barriers that limit the exposure of the metal to corrosive biological fluids and can be tailored to offer additional functionalities, such as antibacterial properties or drug delivery [30].

To evaluate and compare the effectiveness of these protective coatings, a range of corrosion testing methods is employed. Common *in vitro* techniques include immersion tests, electrochemical polarization studies, and electrochemical impedance spectroscopy (EIS). These tests simulate body-like conditions to assess the degradation rate and corrosion resistance under

controlled laboratory settings. Additionally, *in vivo* studies are crucial to validate the performance of coatings under physiological conditions and real-time biological interactions [31].

However, comparing corrosion behavior across studies remains a challenge due to variability in testing conditions, materials, and evaluation criteria. This variability complicates the identification of optimal surface treatments for long-term clinical use. Therefore, the establishment of a comprehensive database that includes both short-term and long-term corrosion data - obtained from *in vitro* and *in vivo* environments - is essential to improve the understanding of degradation mechanisms and to guide the development of more reliable and durable coatings [32].

2.3 Protecting magnesium-based material using a plasma electrolytic oxidation process (PEO)

2.3.1 PEO processing

Recent studies indicate that the search for an ideal surface treatment for temporary biomaterials is still ongoing [33]. This ongoing effort reflects the global challenge of identifying suitable techniques and chemical approaches that can enhance the corrosion resistance of bioresorbable materials like magnesium. Among the various surface modification strategies, plasma electrolytic oxidation (PEO) has gained significant attention due to its ability to create protective ceramic-like coatings that effectively isolate the metal from the corrosive environment.

Other surface modification methods currently under investigation include anodic oxidation, chemical conversion coatings, sol-gel coatings, laser cladding, cold spray, electrophoretic deposition, layered double hydroxide coatings, and superhydrophobic coatings (Fig. 2.4)[34].

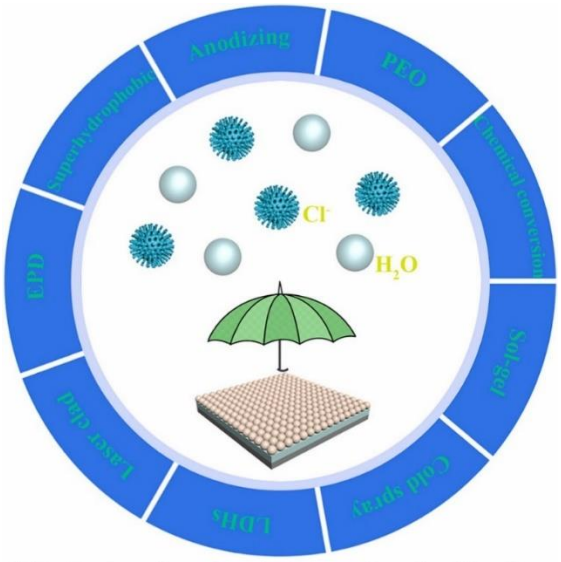

Figure 2.4 Effective isolation of protective coatings for Mg alloys [34]

PEO is a plasma-assisted anodic oxidation process that operates at high voltages, typically ranging from tens to hundreds of volts. The applied voltage causes a transition from conventional anodizing to the breakdown stage, where micro-discharges form due to localized dielectric breakdown (Fig. 2.5) [35]. These discharges generate high temperature and pressure within the oxide layer, leading to complex physicochemical transformations that enhance the coating.

The PEO process can be divided into three characteristic stages (Fig. 2.6):

(i) traditional anodizing,

(ii) discharge initiation or breakdown, and

(iii) steady-state arc discharge [36].

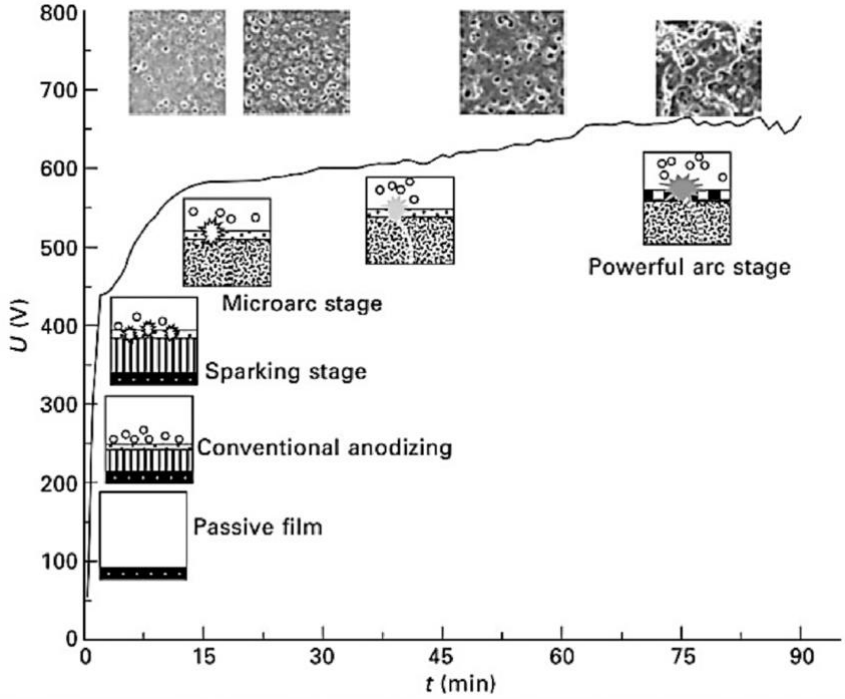

Figure 2.5 Schematic of different stages during PEO process [37]

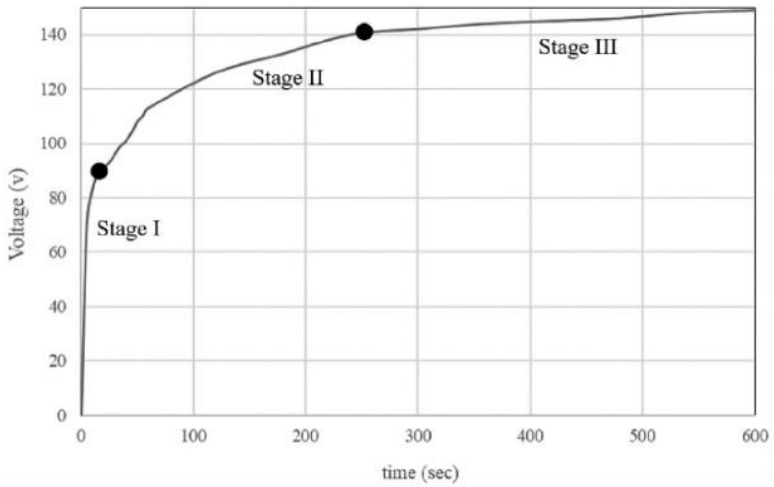

Figure 2.6 Voltage–time curves during PEO process

During the first stage, a thin initial oxide film is formed, accompanied by a linear voltage increase. Simultaneously, gas evolution occurs—oxygen bubbles at the anode and hydrogen bubbles at the cathode [38]. The key electrochemical reactions are as follows:

At the anode (oxidation of magnesium):

$$Mg \rightarrow Mg^{2+} + 2e^{-} \quad (1)$$

At the cathode (oxygen reduction):

$$O_2 + 4e^{-} + 2H_2O \rightarrow 4OH^{-} \quad (2)$$

At the cathode (hydrogen evolution):

$$2H_2O + 2e^{-} \rightarrow H_2 + 2OH^{-} \quad (3)$$

These reactions work together to drive the anodization process in PEO. Reactions result in the formation of magnesium oxide (MgO) and hydroxide ions, which together initiate the growth of the oxide layer. Simultaneously, at the cathode, oxygen reduction and hydrogen gas production ensure charge balance in the system [39].

In the second stage, voltage continues to rise more slowly. Surface discharges begin to appear, either due to exceeding the dielectric breakdown voltage or through discharge within pre-existing gas-filled pores [40], [41]. According to Zhang et al., these discharges progress through spark formation, micro-arc generation, and arc stabilization, governed by the relationship between breakdown voltage and gas envelope dynamics [42].

During the PEO coating process, three simultaneous mechanisms contribute to the growth and development of the oxide layer [43], [44], [45]:

1. electrochemical reactions,
2. plasma chemical reactions,
3. thermal diffusion.

The electrochemical reactions primarily occur at the substrate–electrolyte interface and initiate the formation of the initial oxide layer. As the process evolves, plasma chemical reactions - driven by micro-discharges - become dominant. These involve:

- charge transfer at the substrate/electrolyte interface, and
- intense ionization and charge exchange between the growing oxide layer and the electrolyte, facilitated by plasma discharges [46].

Thermal diffusion, induced by the localized high temperature of discharge events, also plays a significant role in phase formation, material transport, and structural rearrangement within the coating [47].

Figure 2.7 illustrates the stepwise development of a PEO coating on a magnesium alloy. In the initial stage (Fig. 2.7a), a thin magnesium oxide (MgO) layer forms under an applied potential.

As the oxide layer thickens, its insulating properties cause the voltage to rise sharply (Fig. 2.7b). Once the dielectric breakdown threshold is reached, localized plasma micro-discharges are triggered (Fig. 2.7c). These discharges generate extreme temperatures and pressures, which in turn:

- disrupt and reform the oxide layer,
- drive high-temperature plasma-assisted reactions, and
- promote growth via melting, re-solidification, diffusion, sintering, and densification [48].

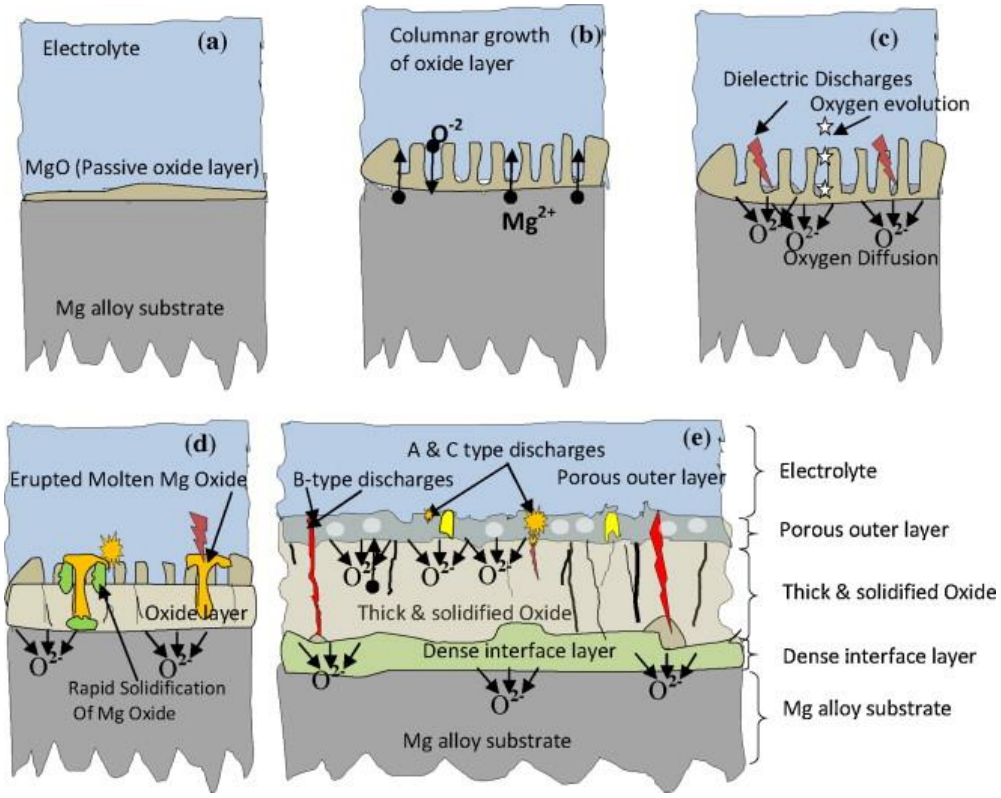

Figure 2.7 Schematic of the coating process during PEO treatment [48]

These micro-discharges are short-lived and highly localized, but they have a profound influence on the coating structure. As the coating continues to grow, discharges become less frequent, but more intense and prolonged, depending on the oxide layer thickness [43].

The thermal energy from the discharges initiates electron avalanches in the coating/substrate interface, leading to localized melting. Molten oxide is ejected toward the surface, where it cools rapidly upon contact with the surrounding electrolyte. This rapid solidification leads to re-crystallization of the oxide and decomposition of hydroxides, resulting in the formation of complex oxide phases (Fig 2.7 d–e) [43].

As shown in Figure 2.8, the PEO coating typically forms a three-layered structure:

- an outer porous layer rich in discharge features,
- a dense middle layer offering mechanical strength,
- an inner barrier layer that is compact and well-adhered to the substrate, contributing to corrosion protection.

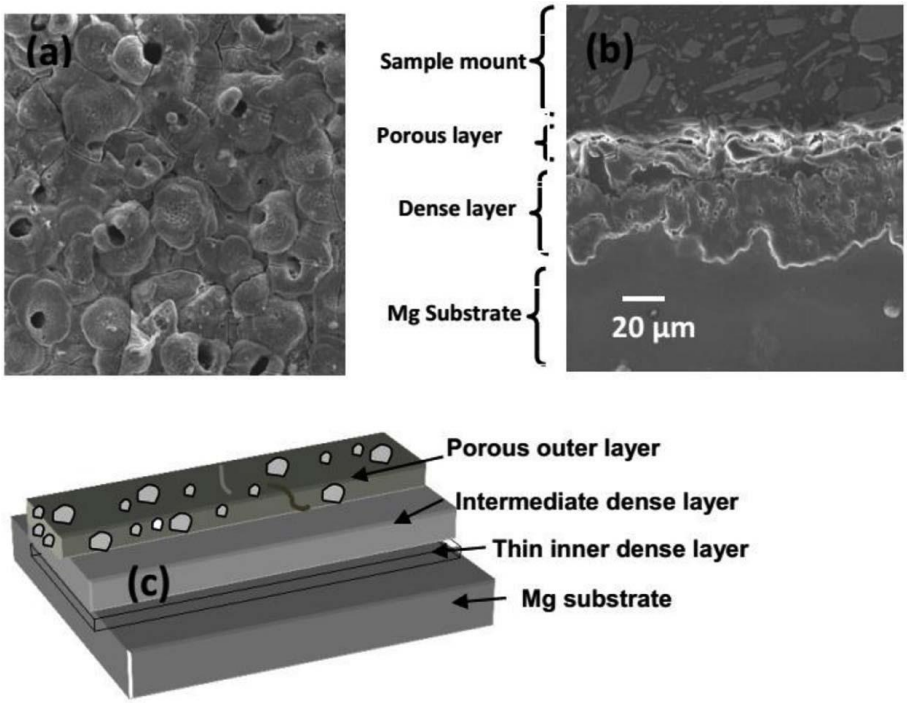

Figure 2.8 Schematic of a) PEO coating surface b) cross section and c) different layer of PEO coating [49]

The surface morphology is characterized by pancake-like structures, each centered around a former discharge channel [50]. During plasma discharge, molten oxide flows through these channels and rapidly solidifies, creating distinct boundaries between adjacent structures. The large voids observed at the center of these features are indicative of intense localized discharges, which may penetrate deeply into the coating.

Additionally, microcracks are frequently observed and are likely the result of thermal stress caused by the rapid cooling (quenching) of molten material upon exposure to the cold electrolyte. Although these features may compromise coating integrity, their formation is often inherent to high-energy discharge processes and can be mitigated by adjusting processing parameters [49].

2.3.2 The effect of electrolyte composition on coating structure and properties (phosphates and silicates)

The composition of the electrolyte plays a critical role in determining the microstructure, morphology, porosity, thickness, and corrosion resistance of coatings formed during PEO [51], [52]. Parameters such as electrical input, temperature, and the addition of secondary electrolyte additives also significantly influence the final properties of the coating [41], [53].

Electrolyte chemistry directly affects discharge behavior, coating growth mechanisms, and the nature of the phases formed within the oxide layer [54]. Alkaline electrolytes based on aluminate, silicate, and phosphate salts are among the most widely used for PEO treatment of magnesium alloys. These compounds facilitate voltage discharge and actively participate in the development of functional ceramic coatings [55]. For example, the addition of KOH enhances corrosion resistance by promoting the formation of $Mg_3(PO_4)_2$ and reducing coating porosity [56]. Similarly, silicate-based systems contribute to dense and uniform layers, while phosphate-based systems enhance biocompatibility. A summary of common electrolyte compositions and their effects is provided in Table 2.1.

Table 2.1 Role of common electrolyte compositions on PEO properties [57]

Composition	Main Composition	Effects
Phosphate-based electrolyte	Na_3PO_4–KOH–KF	Formation of a smooth surface without defects; high corrosion resistance
Silicate-based electrolyte	Na_2SiO_3–NaOH	Formation of severe sparking, increased PEO film thickness, and better tribocorrosion resistance
Ziconate-based electrolyte	$Zr(NO_3)_4$–KOH	Formation of a non-uniform layer with low thickness and poor corrosion resistance
Alluminate-based electrolyte	$NaAlO_2$–KOH	Formation of a compact, thick coating; high corrosion and wear resistance due to $MgAl_2O_4$ formation
NaOH	NaOH–$NaAlO_2$	Adjustment of solution pH and increase in conductivity
KOH	Na_2SiO_3–KOH	Decreased sparking voltage and increased solution conductivity

Phosphate electrolytes are often employed to improve the corrosion resistance [58], [59], [60]. Although phosphate-based coatings tend to be moderately thick and porous, the presence of

PO_4^{3-} ions contributes to rapid coating growth and supports cell attachment [61], [62]. Researchers have also suggested that coatings formed in phosphate electrolytes exhibit a higher growth rate, attributed to the greater reactivity between Mg^{2+} and PO_4^{3-} compared to other anions. An increase in phosphate concentration in the electrolyte enhances the corrosion resistance of the coatings proportionally to their thickness, primarily due to a notable reduction in porosity, despite an increase in the size of pores and micro-channels [60].

Studies have demonstrated that metasilicate ions (SiO_3^{2-}) are beneficial for producing coatings with improved hardness and corrosion stability [58]. Fukuda and Matsumoto [58] observed that combining potassium hydroxide with sodium silicate resulted in denser, thicker, and more uniform anodic films. As the concentration of silicates increases, the coatings generally become thicker, with a rougher structure and larger pores. Compared to phosphate-based electrolytes, silicate systems typically produce coatings with lower overall porosity [63], [64].

While silicate-based coatings typically exhibit higher hardness and compactness, phosphate-based coatings offer advantages in bioactivity [60]. For instance, Jun Liang et al. [65] found that coatings formed in silicate electrolytes were dense and uniform, while those formed in phosphate-based electrolytes were relatively porous.

In addition, the electrolyte composition also plays a decisive role in determining the chemical structure of the PEO coatings. The presence of specific anions (such as PO_4^{3-}, SiO_3^{2-}, AlO_2^-) directly influences the type and crystallinity of the ceramic phases that form during discharge events.

For example, MgO is typically the dominant crystalline phase in coatings formed in both silicate- and phosphate-based electrolytes. It results from direct oxidation of Mg^{2+} ions with O^{2-} within the micro-arc discharges and from the thermal dehydration of $Mg(OH)_2$ at the substrate-electrolyte interface under high temperature and pressure [58], [66], [67]. However, depending on the electrolyte composition, more complex phases can also form.

In silicate-based electrolytes, forsterite (Mg_2SiO_4) and enstatite ($MgSiO_3$) may develop via reactions between MgO and SiO_3^{2-}, especially under prolonged discharging conditions [57]. In phosphate-containing systems, phases such as magnesium pyrophosphate ($Mg_2P_2O_7$) and sodium magnesium phosphate ($NaMg(PO_3)_2$) are commonly observed, both of which contribute to improved corrosion protection and bioactivity [59], [52].

Thus, the chemical structure of the oxide layer - including the types of crystalline and amorphous phases present—is strongly influenced by the type, concentration, and reactivity of electrolyte components. This underlines the importance of tailoring electrolyte chemistry not only

to control surface morphology, but also to design coatings with specific chemical functionalities and targeted biomedical performance [68].

Therefore, electrolyte modifications not only influence corrosion behavior but can also significantly improve the bioactivity of the coating. Surface bioactivation aims to stimulate cellular responses such as adhesion, proliferation, collagen production, and mineralization [69].

Several strategies have been proposed:

- incorporation of calcium and phosphate ions to promote hydroxyapatite formation [70], [71];
- silicon-doping to enhance osteoconduction and cellular activity [72], [73];
- fluoride to reduce wettability and increase bioactivity [74], [75].

For instance, Gu et al. [76] investigated PEO coatings on Mg-Ca alloys and found that coatings formed in silicate + KOH electrolytes exhibited optimal corrosion resistance and enhanced cellular response. Similarly, Khiabani et al. [77] demonstrated that adding calcium fluoride (CaF_2) to phosphate-based electrolytes significantly increased bioactivity, reduced wettability, and improved the osteoconductive potential of AZ91 alloy coatings.

Valerio et al. [78] further showed that coatings containing silicon ions led to increased collagen secretion and cell survival compared to silicon-free coatings. The synergistic effect of combining Ca, P, and F ions has also been shown to promote the formation of a stable biocoating with superior corrosion resistance and osteointegration [77], [78], [79].

2.3.3 Influence of particle addition on composition, microstructure and morphology of PEO coatings

The properties of plasma electrolytic oxidation (PEO) coatings are governed by several interrelated factors, including treatment time [80], [81], electrical parameters [82], [83], electrolyte composition [84], [85], and the substrate material [86]. Among these, the electrolyte plays a particularly critical role, as it serves as the medium for both electrochemical reactions and material incorporation. In recent years, growing attention has been directed toward modifying PEO electrolytes with nanoparticles. This approach aims not only to trace the coating formation mechanisms but also to improve the physicochemical and biological performance of the resulting oxide layers [87], [88], [51].

The incorporation of nano- and micro-sized particles into PEO coatings has emerged as a key strategy to enhance functional properties and diversify the chemical composition of the coatings (Table 2.2) [89]. These particles are typically introduced into the electrolyte in the form of suspensions, powders, or colloidal sols. The influence of added particles depends on multiple factors, including their type, size, concentration, and electrical conductivity [90]. The presence of

particles can modify the characteristics of spark discharge, potentially influencing the energy distribution during the PEO process Additionally, the presence of particles can affect the formation, distribution, and characteristics of sparks, resulting in variations in the electrical behavior across the coating's surface [39].

In some cases, the incorporation mechanism occurs *in-situ* when the solubility of the added compounds in the electrolyte exceeds a certain threshold [34]. Regardless of the exact mechanism, introducing particles into the electrolyte has been shown to influence the electrical response of the system. For example, the addition of Al_2O_3 particles can delay the voltage ramp during PEO processing. Similarly, CeO_2 particles reduce the voltage required to initiate and sustain plasma discharge[39].

Table 2.2 Particles applied in PEO processing [39]

Particles	Substrate	Properties
Al_2O_3	AZ91 Mg alloy	Better performance of mechanical and anti-corrosion
CeO_2	AM50 Mg alloy	Corrosion properties
SiO_2	AM50 Mg alloy	Corrosion and wear resistance
Si_3N_4	AZ31 Mg alloy	Corrosion resistance, mechanical and tribological properties
ZrO_2	AZ91 Mg alloy	Corrosion properties
TiO_2	AM60B Mg alloy	Corrosion properties
HA (Hydroxyapatite)	Mg–Zn–Ca Mg alloy	Biodegradable
TiN	MA8 Mg alloy	Mechanical and corrosion characteristics
MoS_2	AZ31 Mg alloy	Corrosion, wear, and mechanical properties
Ag	Mg–Zn–Zr–RE alloy	Antimicrobial
SiC	AZ31 Mg alloy	Corrosion and wear resistance

According to the literature, particles can be incorporated into the coatings through several pathways: direct entrapment in the growing layer, electrophoretic deposition, and mechanical mixing [39]. Three main stages have been proposed for the successful integration of nanoparticles into PEO coatings: (1) delivery of particles to active discharge sites, (2) entrapment within the growing layer, and (3) preservation of the particles during subsequent coating growth [91]. The

particle transfer process is often divided into two key phases: uptake from the electrolyte and incorporation into the coating matrix [39]. Particle size plays a decisive role in this process — nanoparticles can penetrate deeper into the growing layer, whereas larger particles are often unable to pass through surface pores and may remain embedded only in the outer regions [92].

Because particles participate directly in the coating formation process, they influence both the microstructure and surface morphology of the resulting layer [93]. Under high-temperature discharge conditions, smaller particles may undergo partial melting or chemical interactions with electrolyte components. In contrast, some particles may remain inert and be physically embedded in the oxide matrix without chemical transformation [94].

The addition of particles affects several morphological parameters of the coatings, including porosity, compactness, and thickness. For instance, TiO_2 particles have been shown to reduce the number and size of surface pores, resulting in coatings with lower overall porosity [95]. Similarly, Arrabal et al. demonstrated that α-Al_2O_3 particles led to the formation of a denser and harder outer layer [96]. While particle-free coatings tend to exhibit a more uniform structure, the influence of particle addition on coating thickness remains controversial. Some studies report increases in thickness, others indicate reductions or no significant change, which may be attributed to variations in voltage and current behavior during the PEO process [39], [97], [98].

A wide variety of nanoparticles have been investigated to improve corrosion resistance, wear resistance, and biological performance of PEO coatings on magnesium alloys [99], [100]. For example, the addition of ZnO nanoparticles has demonstrated improvements in corrosion resistance [101]. Researchers are increasingly interested in incorporating particles that not only enhance mechanical and electrochemical performance but also improve biocompatibility and antibacterial properties. S. Esmaili et al. [102] reported that graphene oxide addition significantly increased corrosion resistance, while also enhancing cellular attachment and differentiation. Yang et al. [103], [104] explored a NaF-assisted PEO process with the addition of corrosion-resistant nanoparticles such as Al_2O_3, SiO_2, TiO_2, ZnO, and ZrO_2.

Ceramic particles like hydroxyapatite (HA) and tricalcium phosphate (TCP) are commonly used to enhance bioactivity and promote osseointegration by mimicking the mineral phase of bone, facilitating better integration between the implant and host tissue [105], [106]. Metallic nanoparticles such as silver (Ag) and copper (Cu) are incorporated to impart antimicrobial properties [107]. Among these, silver is especially valued for its broad-spectrum antibacterial effectiveness, which is particularly beneficial in preventing post-implantation infections [108]. Biocompatible oxides such as TiO_2 have also been extensively applied in PEO of magnesium to improve both corrosion resistance and cell compatibility [109].

2.3.4 “Green” and sustainable coating based on naturally sourced organic and inorganic origin material

In recent years, the utilization of renewable resources has become increasingly appealing in the context of environmental preservation and sustainable development [110]. Naturally derived materials, often underutilized or non-valorized, offer significant potential as raw materials for advanced biomaterial applications [111]. The incorporation of such materials into coating systems represents an emerging branch of „green” technologies, aimed at minimizing ecological impact while maintaining or even enhancing functional performance. These next-generation, sustainable biomaterials offer a promising platform for tailoring surface characteristics and opening new possibilities in the biomedical field [112].

A particularly attractive strategy involves introducing organic and inorganic additives of natural origin into the electrolyte during plasma electrolytic oxidation (PEO). This approach enables the development of coatings with enhanced protective, biological, and anticorrosive properties. The PEO process itself is well-suited for biomedical applications, as it modifies the surface structure and chemistry of materials without compromising their bulk properties [113]. The resulting micro-rough surface topographies are known to promote osteoblastic differentiation and improve integration with bone tissue [114].

Notably, the modification of plasma discharges through the careful design of electrolyte composition is receiving increasing attention. The use of naturally sourced compounds may influence plasma behavior by participating in complex chemical reactions during discharge events. However, despite growing interest, the specific roles and effects of organic-origin additives in PEO electrolytes—particularly regarding discharge behavior, phase formation, and coating functionality - remain unexplored [39].

In the pursuit of biomimetic implant coatings, calcium phosphate (CaP) compounds remain essential due to their chemical resemblance to the mineral phase of bone [115]. One widely studied inorganic additive is sodium hexametaphosphate (HEX), a versatile compound known for its applications as a sequestering agent, emulsifier, corrosion inhibitor, surface-active agent, and synergist [116]. HEX is also used in cosmetics and dental care products [117]. Bae et al [118]. demonstrated that HEX can stimulate the proliferation, differentiation, and angiogenic activity of human dental pulp cells. Additionally, HEX can serve as a phosphorus source in PEO electrolytes, contributing to improved corrosion resistance of the coated material.

As for calcium-based additives, early studies predominantly focused on hydroxyapatite (HA) - the principal inorganic component of bone [119]. While HA-based coatings have been used as analogs of calcified tissue, they often suffer from limited bioactivity [120]. Several studies have

reported poor formation of chemical bonds with bone, leading to insufficient osseointegration and premature implant failure [121]. These limitations have prompted researchers to investigate more soluble and bioavailable calcium sources.

Among alternative candidates, tricalcium phosphate (TCP) and octacalcium phosphate (OCP) have shown favorable properties when used as precursors for HA formation in implant coatings [122], [123]. In contrast, calcium carbonate ($CaCO_3$)—despite being widely available and biocompatible—has been largely overlooked. However, recent findings by Kambra et al. demonstrated the osteogenic potential of calcium carbonate in vitro. Importantly, $CaCO_3$ undergoes complete degradation without forming toxic by-products and is readily resorbed by the body [124]. Furthermore, in the presence of phosphate ions, $CaCO_3$ can be converted into hydroxyapatite or B-type carbonated HA, both of which are integral to the natural mineral phase of bone [125][126]. Zainab et al. further reported that calcium carbonate accelerates early-stage bone healing and supports mineralization processes, underscoring its potential in regenerative medicine [127]. These findings strongly support the rationale for incorporating calcium carbonate into the design of PEO coatings for biomedical implants.

-

CHAPTER III - EXPERIMENTAL PROCEDURE

3.1 Coating preparation

3.1.1 Substrate

The PhD thesis involves the investigation of the PEO process, including different electrolyte composition, to produce coatings on magnesium for biomedical applications. The first aspect of study relies the substrate and electrolite preparation. The pure Mg (99,99%) was obtained from Polmag (Kędzierzyn-Koźle, Poland). Sodium silicate - Na_2SiO_3, ammonium fluoride - NH_4F, sodium hydroxide – NaOH, Na_2HPO_4 – sodium hydro phosphate, NaH_2PO_4 – sodium dihydro phosphate were purchased from Chempur (Piekary Śląskie, Poland). Na_3PO_4 – sodium phosphate, $CaSiO_3$ – calcium silicate were obtained Avantor (Radnor, PA, USA). $(NaPO_3)_6$ – sodium hexametaphosphate, KOH – potassium hydroxide, $CaCO_3$ – calcium carbonate were purchased from Sigma–Aldrich (St. Louis, MO, USA Egg-shells were collected by colleagues from the department. Than egg-shells cleaned with distilled water, and air-dried to a constant mass. Next, egg-shells were grinded by Analytical Mill EGK (Dinkelsbuhl, Germany) to powder. Then egg-shell powder was grinded to more uniform particles size by Tube Mill 100 during 30 sec with 15 000 rpm. The use of the disposable grinding chambers eliminated the risk of cross-contamination. The grinding chamber and its cover are made of transparent material, which allows you to observe the course of grinding tests at any time. Then the powder was separated by a sieve with a cell of 5 μm (Fig. 3.1).

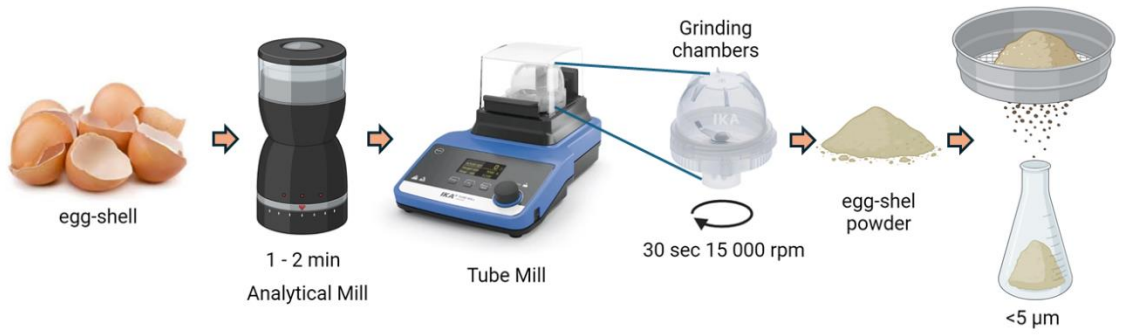

Figure 3.1 The scheme of the egg-shell powder preparation

The Mg samples in a form of cubes with 1x1x1 cm size were used in the experiments for Si-based solutions. For other experimental groups were used cubes with 1x1x0.5 cm size. The sample surfaces were grinded with a SiC paper up to #1000 grade. Then samples were rinsed with deionized water and propanol and dried in air to ensure good surface reproducibility after the cutting of the samples and prevent quick air corrosion. Silver nanoparticles suspension (AgNPs)

(3 mg·dm^{-3}) was provided by Nanowave Ltd (Warsaw, Poland). Their synthesis and characterisation were described in our paper [128].

3.1.2 Scheme of electrolyte composition

To fulfil the purpose of the research goal, it was proposed use different combinations of silicates and phosphates that were divided into three groups. All electrolyte solutions were prepared by dissolving the respective chemical compounds in 1 L of distilled water.

In the first group we used silicate-based solutions (Si group) with addition of AgNPs particles (Si-Ag group) to add antibacterial properties. I used different concentrations of Na_2SiO_3 (Si10, Si20, and Si30) to adjust the surface morphology and corrosion properties (Table 3.1).

Table 3.1 Chemical composition of the Si-based group PEO bath electrolytes per 1 dm^3 H_2O

Electrolyte	Na_2SiO_3· g·dm^{-3}	NH_4F g·dm^{-3}	NaOH g·dm^{-3}	H_2O dm^3	AgNPs suspension dm^3
Si10	10	5	10	1	-
Si20	20				
Si30	30				
Si10-Ag	10			0.95	0.05
Si20-Ag	20				
Si30-Ag	30				

The second group of electrolytes involved combinations of silicate and phosphate components with varying alkali sources (Table 3.2). The tested compositions differed in the type and concentration of phosphate salts, silicate sources, and alkaline agents. SP1–SP4 comprised solutions based on sodium silicate (Na_2SiO_3) and different sodium phosphate salts, including disodium phosphate (Na_2HPO_4) and monosodium phosphate (NaH_2PO_4). SP5 and SP6 represented trisodium phosphate (Na_3PO_4)-enriched systems, also incorporating Na_2SiO_3 at different concentrations. SP7–SP8 employed potassium hydroxide (KOH) as an alternative alkaline additive. Finally, SP9-SP10 combining KOH and Na_3PO_4 included calcium silicate ($CaSiO_3$) as a Ca-based and poorly soluble silicate source.

Table 3.2 Chemical composition of the silicates and phosphates PEO bath (P-Si-based electrolyte) per 1 dm^3 H_2O

Electrolyte	Na_2SiO_3· g·dm^{-3}	Na_2HPO_4 g·dm^{-3}	NaOH g·dm^{-3}	NaH_2PO_4 g·dm^{-3}	Na_3PO_4 g·dm^{-3}	KOH g·dm^{-3}	$CaSiO_3$ g·dm^{-3}
SP1	10	10	5	-	-	-	-
SP2		5		-	-	-	-
SP3		-		5	-	-	-
SP4	15	-		10	-	-	-
SP5	10	-	-	-	10	-	-
SP6	5	-	-	-	15	-	-
SP7	10	10	-	-	-	4.5	-
SP8			-	-	-	6.05	-
SP9	-	-	-	-	5	3	-
SP10	-	-	-	-			50

The third group represented hexametaphosphate-based electrolytes formulated using sodium hexametaphosphate ($(NaPO_3)_6$) as the primary phosphate source (Table 3.3).

Table 3.3 Chemical composition of the PEO bath electrolytes (P-Ca-based electrolyte) per 1 dm^3 H_2O

Electrolyte	$(NaPO_3)_6$, g·dm^{-3}	NaOH, g·dm^{-3}	Particles, g·dm^{-3}
AXP1	10	5	-
AXP2	10	10	-
AXP3	5	2	-
AXP4		10	-
AXP5		5	-
AXP6			Egg-shell, 31
AXP7			$CaSiO_3$,100
AXP8			$CaCO_3$, 5

To enhance the biocompatibility of the resulting PEO coatings, various calcium-based particles were incorporated, including egg-shell powder, calcium silicate ($CaSiO_3$), and calcium carbonate ($CaCO_3$). The particulate additives were uniformly dispersed within the solutions according to the compositions.

3.1.3 PEO processing

The PEO process was performed using the cell setup shown on the Figure 3.2.

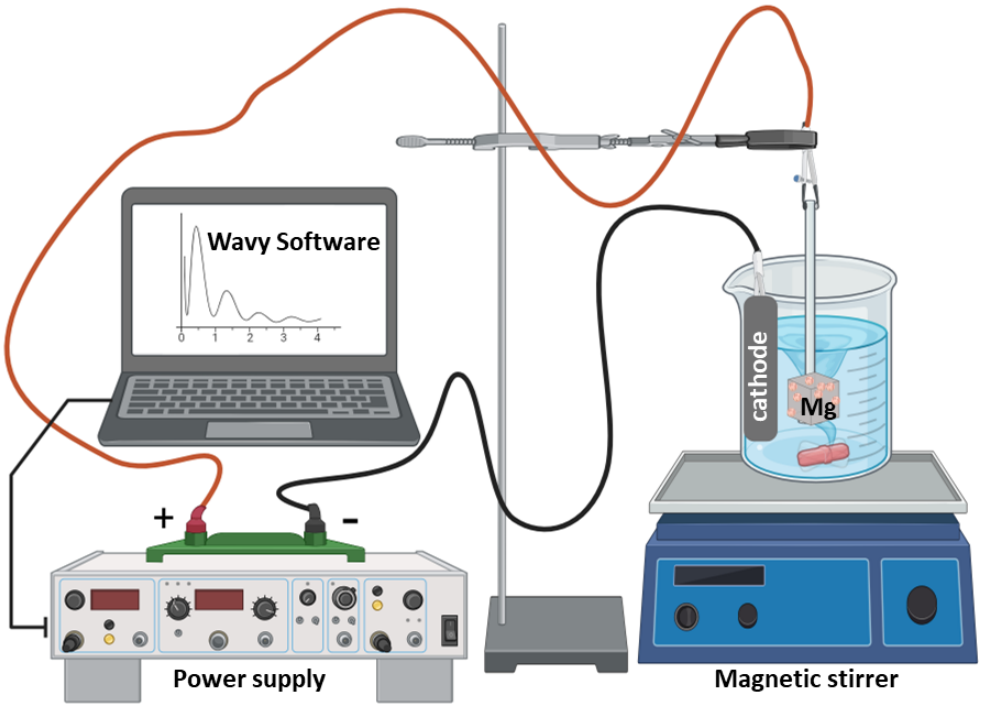

Figure 3.2. Schematic view of PEO set up

Magnesium cube was used as an anode electrode and a cathode was a stainless-steel plate. Prior to the PEO treatment the samples were immersed for 10 s in 20% HNO_3 to remove oxide layers and washed with distilled water. The PEO process was conducted under an impulse current up to a fixed voltage with use of a high-voltage power supply (PWR 800H, Kikusui, Japan) (Fig. 3.3). The PEO process was performed in a plastic, externally cooled electrolyzer (500 cm^3) fitted with a stainless-steel cathode ring and a magnetic stirrer. The process was realized in electrolytic baths presented in Tables 3.1-3.3. The electrolytes were kept at 10°C by an automated cooling system during the coating process. PEO process was accomplished under the limiting anodic current density of 100 $mA \cdot cm^{-2}$ and voltage (Tab. 3.4). The treatment time (t) was set to 180 s for Si-based electrolytes and to 300 s for other electrolytes. During the whole process the current flow and breakdown voltages were continuously recorded by Wavy Software (Wavy version 5.01). Finally, the samples were rinsed in distilled water and air dried at room temperature.

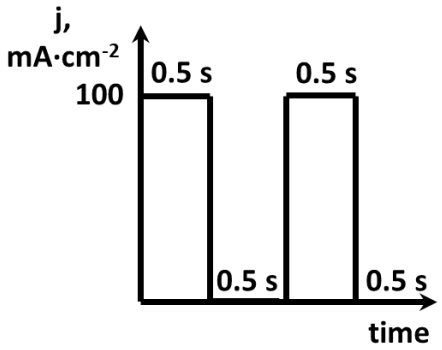

Figure 3.3 A schematic illustration of impulse current regime used

The processes parameters and samples labelling are presented in Tables 3.4 – 3.6.

Table 3.4 Description of samples and process parameters; j = 100 mA cm^{-2}, t = 180 s (Si-based electrolyte), t = 300 s (other electrolyte)

Sample no	Electrolyte	Voltage, V	Sample no	Electrolyte	Voltage, V
Si10-150	Si10	150	Si10-Ag-150	Si10-Ag	150
Si10-200		200	Si10-Ag-200		200
Si10-225		225	Si10-Ag-225		225
Si20-150	Si20	150	Si20-Ag-150	Si20-Ag	150
Si20-200		200	Si20-Ag-200		200
Si20-225		225	Si20-Ag-225		225
Si30-150	Si30	150	Si30-Ag-150	Si30-Ag	150
Si30-200		200	Si30-Ag-200		200

Table 3.5 Description of samples and process parameters; j = 100 mA cm^{-2}, t = 300 s (P-Si-based electrolyte)

Sample no	Electrolyte	V	Name	Electrolyte	V
SP1-200	SP1	200	SP2-150	SP2	150
SP1-225		225	SP2-200		200
SP3-150	SP3	150	SP4-200	SP4	200
SP3-200		200	SP4-250		250
SP3-250		250			
SP5-200	SP5	200	SP6-200	SP6	200
SP5-250		250	SP6-250		250
SP7-200	SP7	200	SP8-200	SP8	200
SP7-250		250	SP8-250		250
SP9-200	SP9	200	SP10-200	SP10	200
SP9-250		250	SP10-250		250
SP9-300		300	SP10-300		300
SP9-350		350	SP10-350		350

Table 3.6 Description of samples and process parameters; j = 100 mA cm^{-2}, t = 300 s (P-Ca-based electrolyte)

Sample no	Electrolyte	Voltage, V
AXP5-250	AXP5	250
AXP5-300		300
AXP5-350		350
AXP6-200	AXP6	250
AXP6-250		300
AXP6-350		350
AXP7-250	AXP7	250
AXP7-300		300
AXP7-350		350
AXP8-300	AXP8	300

3.2 Coating characterization

3.2.1 Scanning Electron Microscopy and Energy-Dispersive X-ray analysis

Scanning Electron Microscopy analysis and energy-dispersive X-ray analysis (EDX) were applied to observe the dimensional relief micro-structure and elementary composition of the modified magnesium samples (SEM, Phenom ProX, Phenom-World BV, Eindhoven, the Netherlands, accelerating voltage = 25 kV) [129].

Cross section was used to evaluate the inner structure of the PEO coating layer including the morphology, thickness and chemical composition (mapping). Obtained samples were embedded in epoxy resin (Eposir F 740 + Ipox EH 2260). Then, all samples were air-dried for 24 h and ground with a grinding machine (Einhell TH-US 400, 1440 rpm) using abrasive papers (Hermes BW114) with 400, 1000, 1200 and 1500 granulation [72]. Before SEM analysis, the samples were coated with gold sputter to make them electrically conductive.

A scanning electron microcop directs a focused beam of electrons over the surface of a sample, where the interaction between the electrons and the sample produces various signals that are collected by specialized detectors to generate high-resolution images and compositional information. The principle of operation of the device is based on utilization of a focused beam of high-energy electrons to create an assortment of signals outside of solid samples (Fig. 3.4). The electrons in the beam interact with the atoms within the sample, thereby producing various signals that can be used to obtain information about the surface's topography and composition. A detector collects the signals that are obtained from electron-sample interactions and exposes information about the sample including outer morphology (texture), elementary chemical composition, and crystalline structure and orientation of materials [103]. The SEM image is a 2D intensity map. Each image pixel relates to a point on the coating, which corresponds to the signal intensity [103].

The obtained SEM micrographs were used to evaluate surface porosity. The porose diameter and orientation and ' local porosity' were measured using Fiji software (ImageJ 1.51f; Java 1.8.0_102) [130]. The size of the pores was calculated using Image J software [131] . The calibration of pixel size was carried out according to the microscope scale bar to ensure measurement accuracy. The estimating of porose size distribution was conducted by the measuring the visible-from-surface voids are assumed to be pores (based on contrast) on the surface of the PEO coatings [132]. The pore distribution number was calculated as a number of pores per an observed surface. ImageJ software was also utilized to assess 'Porous area fraction'. 'Porous area fraction' was determined using computer binary image analysis. This involved segmenting images into black (porous) and white (substrate) regions via grey-level thresholding. The porous area fraction was calculated as the pore area ratio to the total investigated area. The average values of

porose diameters and 'porous area fraction' were reported along with their standard deviations. Fiji software was also applied to evaluate the thickness of the PEO coatings using cross-sectional SEM micrographs. For each specimen, multiple measurement lines were drawn perpendicular to the coating–substrate interface at randomly selected locations across the cross-section. The local thickness values obtained were averaged to calculate the mean coating thickness and the corresponding standard deviation.

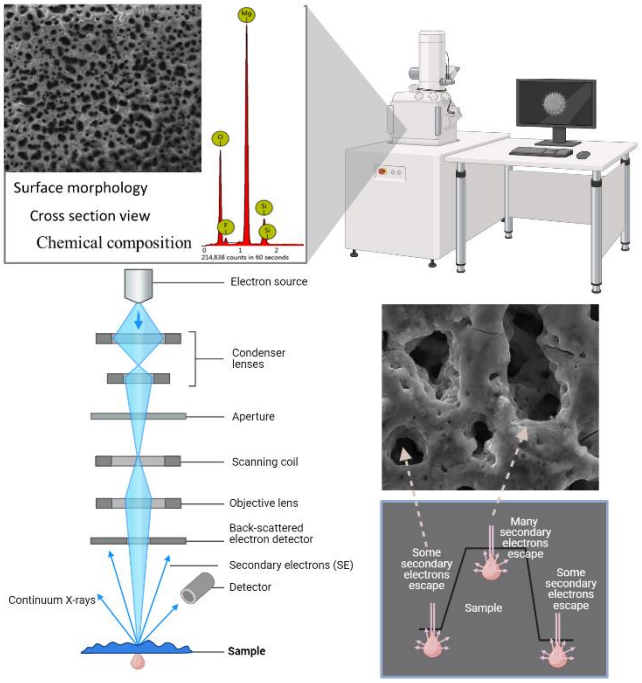

Figure 3.4 Schematic view of the operation of SEM

3.2.2 Eddy current method

Coating thickness was additionally determined by the eddy current method employing an ISOSCOPE MP10E device (Fischer, USA). Multiple measurements were performed on each specimen, and the average values were calculated to ensure reproducibility. The eddy current technique is a non-destructive method based on the interaction between an alternating electromagnetic field and the electrically conductive substrate. When the probe of the ISOSCOPE MP10E is brought close to the metallic surface, the alternating current in the measuring coil generates an electromagnetic field that induces circulating eddy currents in the conductive substrate. The magnitude of these eddy currents depends on the electrical conductivity of the substrate and the distance between the probe and the substrate surface. In the presence of a non-conductive coating, such as the plasma electrolytic oxidation (PEO) layer, the effective distance increases, causing a change in probe impedance. This impedance variation is converted by the instrument into coating thickness values. The method allows for rapid, contact-based, and non-

destructive determination of coating thickness on conductive materials.

3.2.3 Measurement of surface hydrophilicity

Contact angle (CA) measurement is method to determine the degree of hydrophilicity/hydrophobicity of the surface [133]. The schematic view of contact angel measurment set up and ranges of contact angle is visualized in Figure 3.5. Wettability of the PEO surfaces was studied using both the static and dynamic CA measurements. The experiments were conducted using a video-based optical contact angle measuring instrument (OCA 15 EC, Data Physics, USA). The CA value was recorded for 2 μL ultra-pure water for at least 3 parallel measurements and for the span of at least 330 s. Membrane surface wettability was measured with 2 μL droplets of deionized water using a video-based optical contact angle measuring equipment OCA 15 EC, Series GM-10-473 V-5.0 (Data Physics, Filderstadt, Germany). CA technique allows evaluate the hydrophobicity/hydrophilicity of a solid surface. The values of the static and dynamic contact angles point to different properties of the substrates [134]. Firstly, we evaluated the static contact angles values. The camera fixes the moment of the first interaction between water and the surface of the coating. We obtain the vizualisation when themdroplet was standing on the surface and it is expressed as the constant contact angle and, accordingly, the instant wetting characteristics of the substrate. In contrast, the dynamic investigation allows observing the wetting process of the PEO surface through the time. In this case, the camera recoder the data of the contact angle interaction between the coating and distilled water over a particular time. Thus, dynamic measurments characterize of the absorption of a water droplet by the surface and registered the dynamic changes in its shape. The wetting characteristics were measured on three different samples, and an average of three readings was reported for each sample. The contact angles less than 90° testified to hydrophilic properties of the surface, while the contact angles more than 90° testified to low wettability, namely hydrophobic surfaces [135].

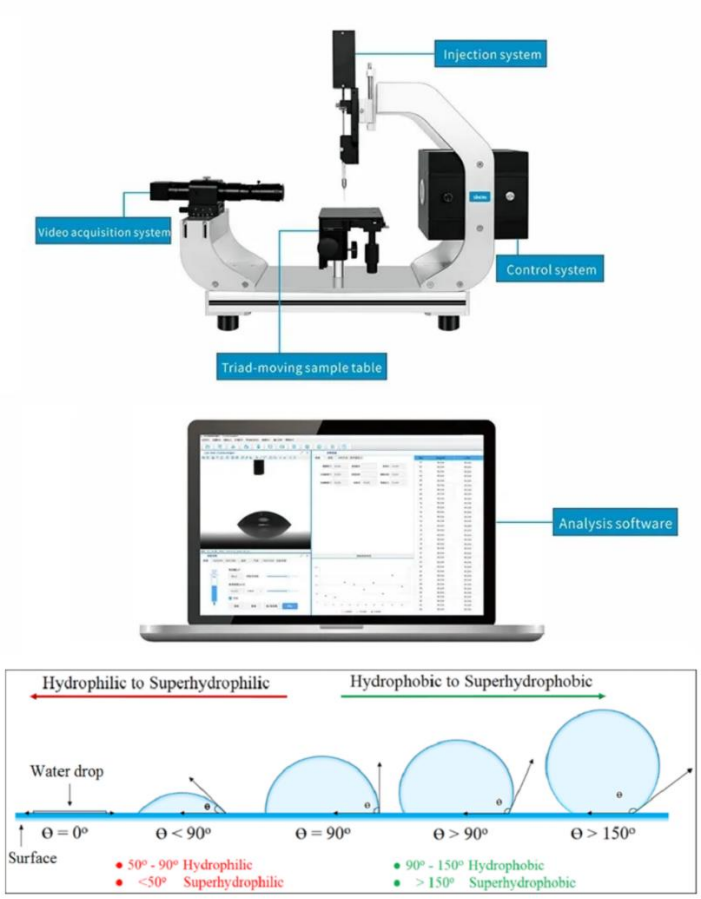

Figure 3.5 Schematic view of contact angel measurment set up and ranges of contact angle [136]

3.2.4 Measurement of surface roughness

Contact profilometer (Surftest SJ-301, Mitutoyo, Japan) was used to measure surface profile of the obtained coatings. The schematic view of contact profilometer measurement is visualized in Figure 3.6. The macroscopic roughness is illustrated by the ride of the stylus tip in a line across the surface, moving vertically over the peaks and valleys. The measured profile expresses the changes in the stylus' height are registered electrically. The 2-D roughness is described in the Ra values. 4 mm-long sections of the surface were measured at least 3 times for 3 samples.

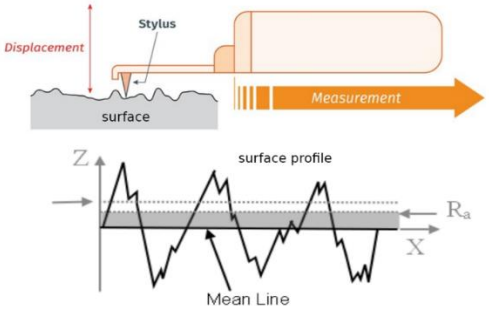

Figure 3.6 Schematic view of contact profilometer measurement

The Phenom ProX (Phenom-World BV, Eindhoven, the Netherlands, accelerating voltage = 25 kV) was used for surface topography analysis for SP and AXP series of samples. The Phenom's 3D roughness analysis tool was applied to calculate Ra roughness parameters. The Phenom microscope captures multiple high-resolution SEM images from different tilt angles. The system uses stereo pair imaging or tilted beam imaging to estimate height variations across the sample surface. By processing these images, the software reconstructs a 3D topographic model. Once the 3D surface model is generated, the software calculates roughness Ra metrics.

3.2.5 Ion release investigations

Ringer's investigation was applied for Si-based group solution allows describe the corrosion behaviour and ion release of the obtained coatings [137]. The Ringer solution was prepared by dissolution of the next salts 8.6 $g \cdot dm^{-3}$ NaCl, 0.3 $g \cdot dm^{-3}$ KCl and 0.48 $g \cdot dm^{-3}$ $CaCl_2$ x6H_2O. The obtained coatings were divided into two groups for Ringer investigation. The first one consisted of Si-based coatings. The samples were immersed in 0.025 dm^3 of the Ringer solution and performed this immersion for 15 days at 37°C. The samples were rinsed with distilled water and dried at room temperature after the first, 5th, 10th and 15th days. The surface was characterized after the first, 5th, 10th and 15th days. Then the surface morphology was characterized by scanning electron microscopy (Hitachi TM-3000, accelerating voltage – 15 kV). The Ringer solutions after immersion were examined by ICP Optical Emission Spectrometer (Varian 710-ES) for detection of the ion release characteristics of the coatings.

Another examined group contained the phosphate-based coatings were placed in 0.015 dm^3 of deionized water and performed this immersion for 42 hours at 37°C. The work solutions after immersion were examined by Agilent 8900 ICP-MS QQQ (Waltham, MA, USA).

3.2.6 *In-vitro* biological investigations

3.2.6.1 Biocompatibility in cell culture

The cytocompatibility of the prepared coatings Si10-Si30 and Si10-Ag-Si30-Ag was investigated by two approaches. Firstly, the Si-based group was assessed using human umbilical cord mesenchymal stem cells (HUMSCs). The specimens were placed into 24 well cell culture of Plate 1 (Fig. 3.7) and were covered with a complete cell culture medium with 40 000 cells per cm^2 of the well area. However, the upper area of the Mg cubes was smaller than the area of the wells, and therefore th e cells attached to both the plastic bottoms of the wells as well as to the upper surfaces of the cubes. The next day, the Mg specimens were carefully transferred with the sterile

forceps to the fresh wells of Plate 2 with medium, taking care to not let the upper edges of the specimens to turn around. The original plating wells (Plate 1) contained the cells, which precipitated past the specimens and adhered to the plastic bottoms in the medium which was in contact with the Mg specimens. Such cells I marked as the "Leftover cells".

The number of viable cells was evaluated with a resazurin reduction assay. For this, resazurin was added at 15 $\mu g \cdot cm^{-3}$ for 8 hours to overnight plates with Mg samples and "Leftover cells". The amount of reduced resazurin (resorufin formed) was evaluated by measuring optical density at 570 and 595 nm using a Multiskan FC plate reader (Thermo Fisher Scientific). The "Leftover cells" were examined by a light microscope Primo Star (Carl Zeiss Jena, Jena, Germany) with Plan Achromat bright-field lenses.

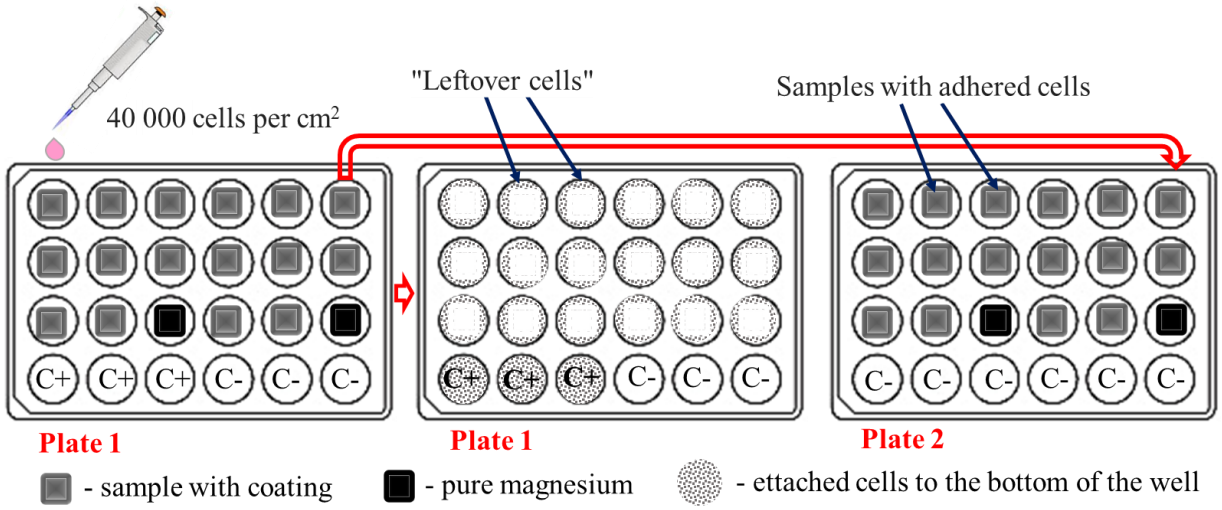

Figure 3.7 Scheme of the cytocompatibility test

To evaluate the possibility of a direct autocatalytic reduction of resazurin [138] by magnesium corrosion process Mg cubes were kept in complete cell culture medium without cells for 10 hr in 24-well plates in CO_2 incubator at 37 ºC (Fig. 3.8). The cubes were transferred from wells with Mg-conditioned medium to wells with fresh medium. Then resazurin was added to 15 $\mu g \cdot cm^{-3}$ final concentration and the plates were further incubated for 10 hours.

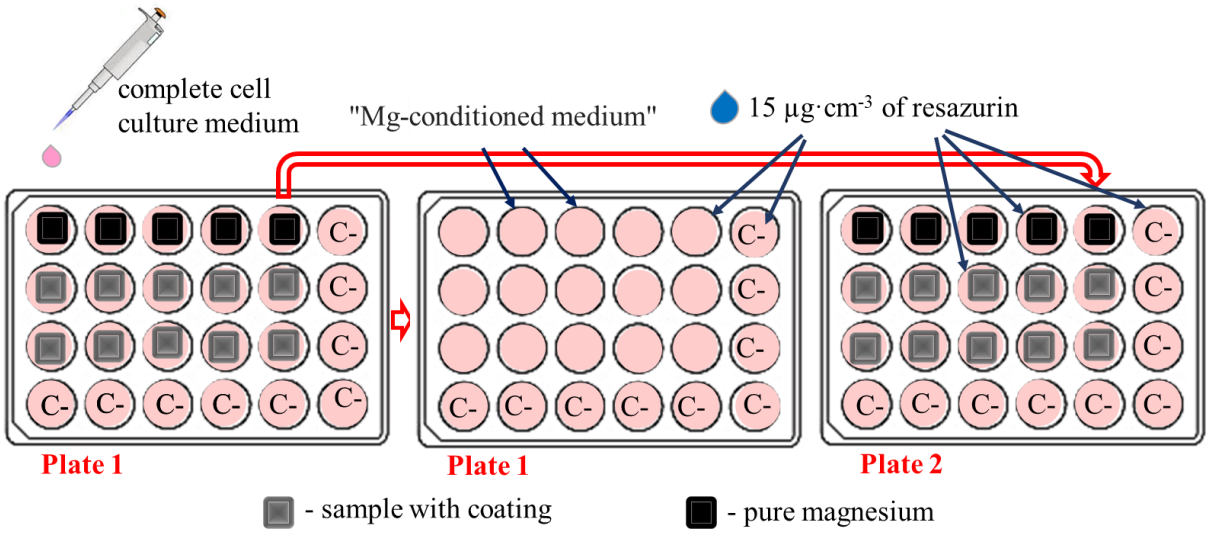

Figure 3.8 Scheme of detection of autocatalytic reduction of resazurin by magnesium implants

The percentage of resazurin reduction was calculated using Bio-Rad formula as described elsewhere [139]. Fluorescence microscopy was used for visualization analysis of adherent cells on surfaces of Mg samples after DAPI staining. DAPI acts through binding to DNA molecules and is used to stain and detect the nucleus [140].

The cytotoxicity of the coatings SP6-250, SP7-250, SP8-250, SP9(300, 350), SP10(300, 350), AXP5(300, 350), AXP6(300, 350), and AXP7(300, 350) was evaluated in comparison with pure magnesium using the U2OS and MG63 cell line, obtained from Umeå University (Sweden). The cells were cultured in a CO_2 incubator (Biosan, Latvia) using Dulbecco's Modified Eagle Medium (DMEM/F-12, Gibco, USA) supplemented with ampicillin sodium salt (100 U·mL^{-}), streptomycin (100 µg·mL^{-}), amphotericin B (2.5 µg·mL^{-}), and fetal bovine serum (10% of the medium volume) (Gibco, USA) at 37°C, 5% CO_2, and 98% humidity. The cells were seeded into 24-well plates with samples at a density of 2×10^4 cells·cm^{-2}. After 12 hours of incubation, samples were added to the cells in each well. After 24 hours, 100 µL (10% of the medium volume) of resazurin solution (15 mg·mL^{-}) was added to each well. Control wells contained only cells and medium without test samples. The plates were incubated for 4 hours at 37°C in the dark, and 100 µL of medium from each well was transferred to a 96-well plate for absorbance measurement using Multiskan FC (Thermo Fisher Scientific, Waltham, MA, USA) at 570 and 595 nm. The reduction of resazurin was determined on days 1, 3, and 6, with three replicates per condition.

After 6 days of incubation, the samples were washed twice with PBS and fixed with 3.5 % formaldehyde (Sigma-Aldrich) for 10 min. Permeabilization was achieved using a solution of 1 % BSA and 0.1 % Triton X-100, followed by staining with ActinRed 555 (Thermo Scientific, USA) to detect actin filaments, and Hoechst 33342 (Thermo Scientific, USA) to stain the nuclei. Samples

were examined using a Nikon Eclipse TI fluorescence microscope (Japan) with DAPI and TRITC channels.

3.2.6.2 Bacteria antiadhesive activity

The antiadhesive properties of the samples were investigated by two approaches. The time-dependent bacteria antiadhesive activity of the Si-based samples were evaluated using surface sampling methods by contact plating to assess the presence of bacterial cells on the tested samples. For the study of the silicate group of coatings with the addition of silver, an appropriate method was chosen, as such coatings possess potential antibacterial properties. *Staphylococcus aureus* B 918 was obtained from National Collection of Microorganisms (Institute of Microbiology and Virology NASU, Kyiv, Ukraine) and kept at the Bacterial Collection of Sumy State University. The Mg cubes were pre-wrapped with paraffin tape so that one face remained uncovered, placed into wells of sterile flat-bottom polystyrene 24-well plates, and left under ultraviolet bactericidal lamp for 12 hours. Subsequently, the samples were horizontally immersed in 2 cm^3 of bacterial suspension adjusted to a concentration of 10E5 colony forming units per cm^3 (CFU cm^{-3}) in Mueller Hinton Broth (MHB). Plates were incubated in a Microplate Incubator/Shaker (Stat-Fax-2200, Awareness Technology, inc.) at 37 °C under constant shaking at 625 rpm for 2, 4, 6, 8 and 24 hours. The surface sampling method allowed detection of bacteria from the surfaces of the samples by direct agar contact plating. After contact with the exposed face of the samples, detached bacteria were spread by the streak plate technique. Then, agar plates were incubated at 37 °C for 12 hours. The number of living cells (CFU cm^{-3}) was determined, followed by log 10 conversion. All the measurements were done in triplicates.

For the P-Si-based coatings, the antiadhesive test was not performed due to findings from previous studies and the absence of significant potential antibacterial properties. Instead, the P-Ca-based coatings were selected for the detection of antibacterial properties, as there is limited information in the literature regarding their electrochemical composition.

For the study of the P-Ca-based coatings were chosen to evaluate the antiadhesive properties (Fig. 3.9). For this purpose, the microorganism inoculum was initially cultured in 50 cm^3 of Bacto™ Tryptic Soy Broth (TSB) (Becton Dickinson) at 37 °C for 18 hours to ensure sufficient bacterial growth. To evaluate bacterial adhesion, triplicate samples were placed in 24-well tissue culture plates and treated with 2 mL of bacterial suspension (~1×10^6 CFU·cm^{-3}) prepared in TSB medium. These samples were incubated at 37 °C for 4 hours with gentle shaking at 60 rpm.

Following incubation, the samples were carefully rinsed three times with distilled water to remove non-adherent bacteria, leaving only those attached to the surface. The rinsed samples were

then transferred to new culture plates. Subsequently, 1 mL of distilled water was added to each well, and the samples were vigorously stirred to dislodge bacteria from their surfaces.

Finally, 10 µL of the resultant suspension containing the detached bacteria was collected, streaked onto agar plates using the streak plate technique, and incubated at 37 °C for 24 hours to allow for colony formation. This procedure facilitated the quantitative assessment of bacterial adhesion to the sample surfaces.

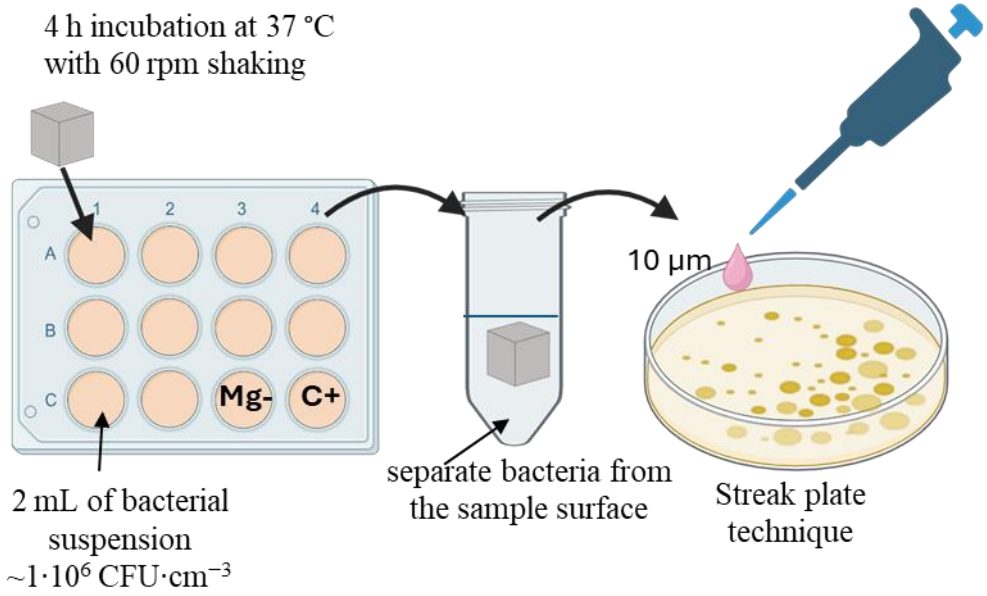

Figure 3.9 Scheme of the bacteria antiadhesive activity

CHAPTER IV - RESULTS AND DISCUSSION

The chapter is divided into four parts. The first part discusses the influences of the silicate concentration and applied voltages on the uniformity and morphology of coatings. The main aim was to achieve coatings with anti-corrosion properties. The second part focuses on the investigation of the morphological and antibacterial properties of coatings after the addition of AgNPs to the silicate electrolyte composition. The third part examines combinations of phosphates and silicates to enhance the anti-corrosion and biocompatible properties of the coatings. The fourth part explores the use of phosphate solutions in combination with calcium-containing particles. The goal of this section is to identify electrolyte systems that enhance the anti-corrosion and biocompatibility properties of magnesium. For comparison, all processes were conducted at the same current density, which was selected based on previous studies [72].

4.1 Plasma electrolytic oxidation coatings on Mg in silicate-based solution

4.1.1 Results

Through literature review, it was identified the gaps in the chemical compositions of silicate-based electrolytes for developing PEO coatings aligned with the objectives of this PhD research. The proposed compositions are outlined in Table 3.1. In the initial phase, the prepared solutions underwent testing. Figure 4.1 visualizes the voltage and current density evolution during PEO process. Based on the analysis of the curves, it was found that during the process the voltage reached the desired value, and its course was stable for a long time. However, after a short time, the current decreased to a minimum value, which is associated with the formation of an oxide layer, which is characterized by poor current conductivity. It should be noted that the oxide layer was built up until the minimum current strength was reached. For samples with higher voltage the time for the current decrease was longer.

The curve analysis for the Si30-225 sample indicates that during the process the voltage did not reach the desired value of 225 V and its course was unstable. The course of the current intensity over time was also chaotic, so it can be concluded that the process failed. This was caused by the formation of a dot oxide layer with an inappropriate structure at the corner of the cube-shaped sample. There was a phenomenon called "burning out" of the sample. Due to repeated adverse effects, the process was terminated at 225 V.

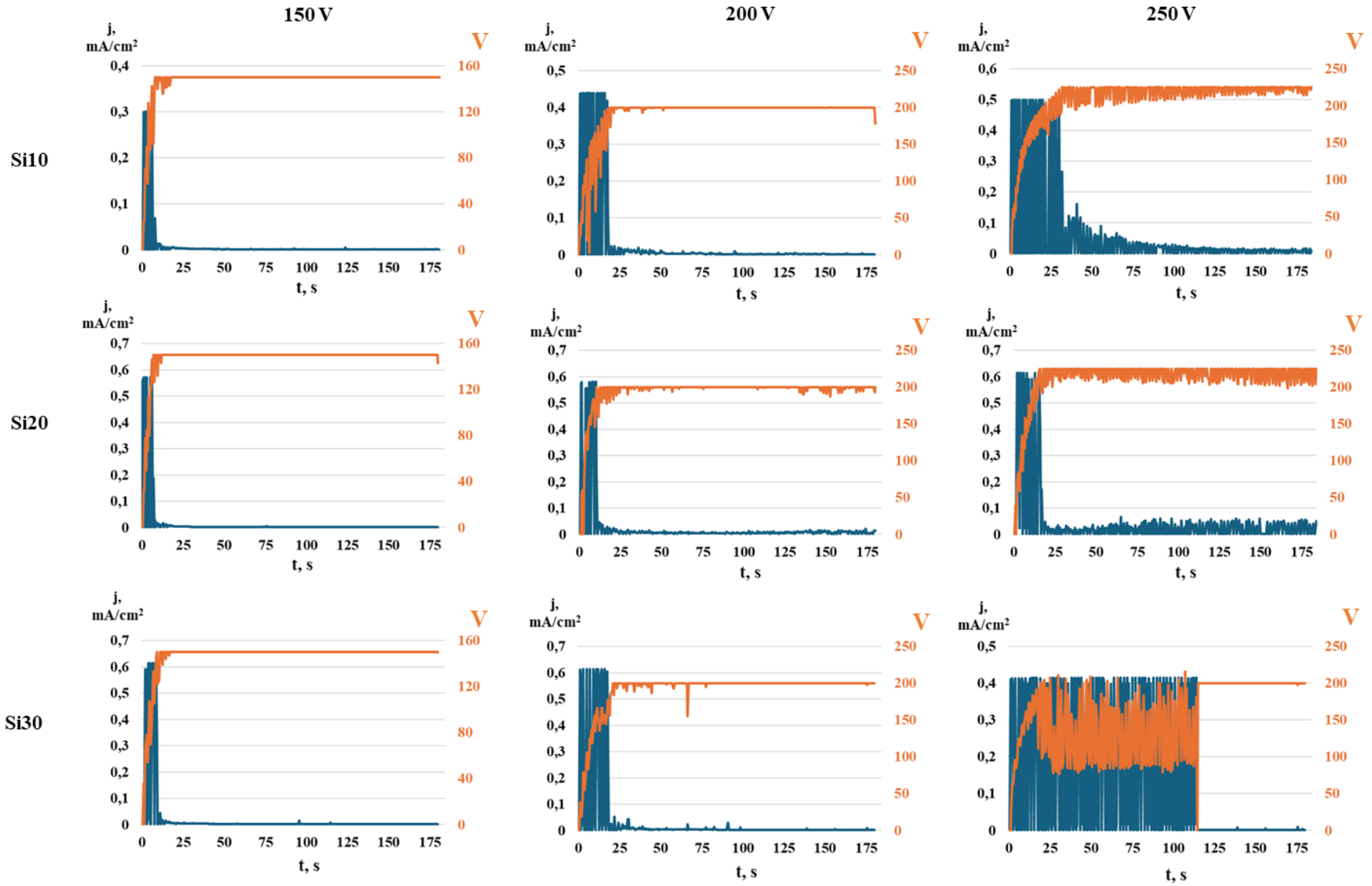

Figure 4.1. Voltage and current density evolution as a function of PEO processing time for Si10-Si30 electrolytes

The selected solutions with regimes allow obtain surfaces visualized on the Figure 4.2. The obtained surfaces are characterized by moderately uniform morphology. Si10-150 and Si20-150 surfaces exhibit a porous structure with numerous small holes. Other surfaces display a highly porous structure with small and medium-sized pores, organized into larger clusters, collectively forming the beginnings of larger pores. Their presence indicates that the PEO process is proceeding correctly. The appearance of large pores and the uneven surface structure indicates that subsequent layers of the oxide coating were deposited intensively and chaotically. However, Si20-225 coating seems rougher and fractured, with less uniformity in texture compared to the other samples. Moreover, on the surfaces of the coatings at 225V, crystalline structures were also observed. These structures may result from the deposition of salts or magnesium oxides.

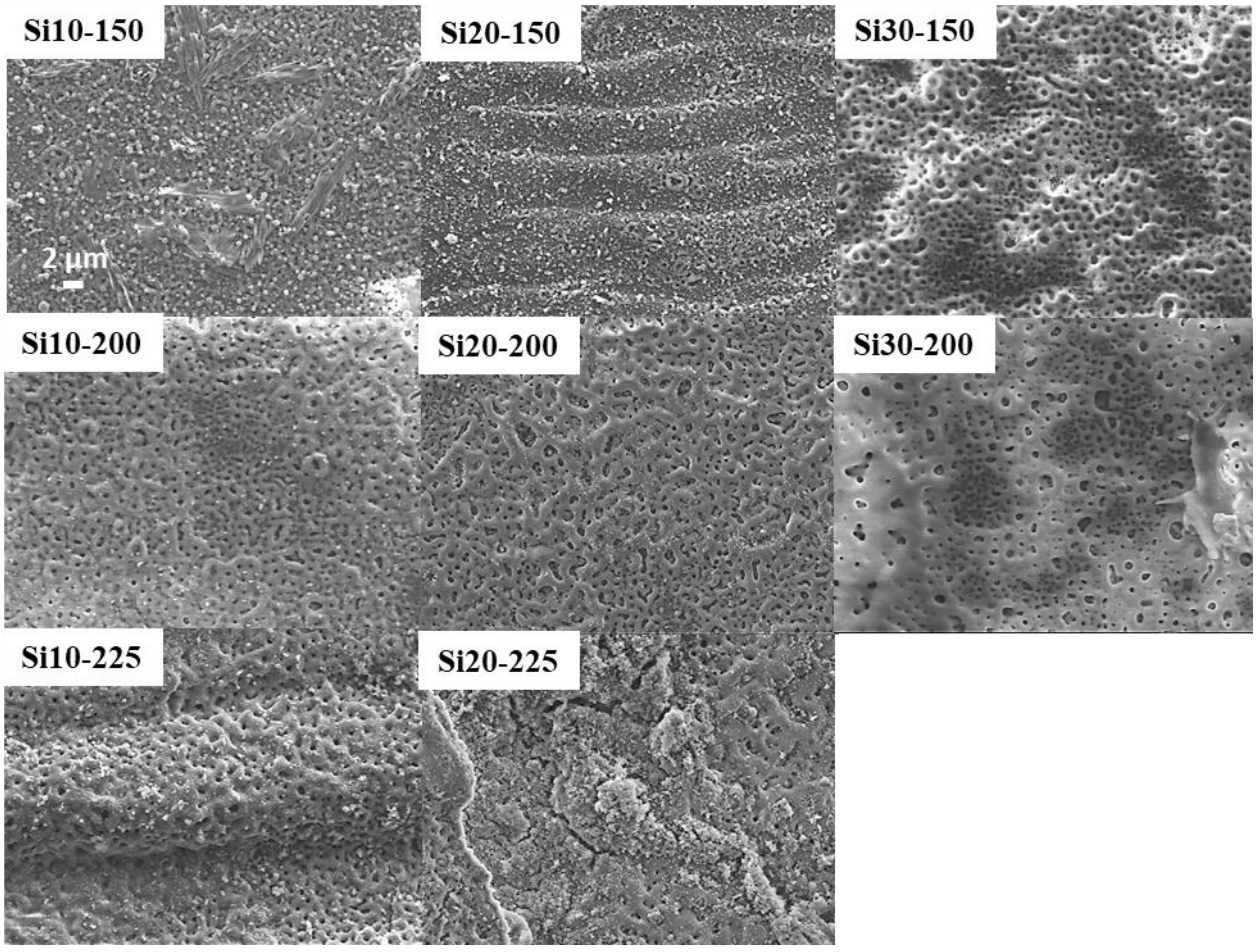

Figure 4.2 The SEM images of the magnesium PEO coatings formed in silicate-based bath electrolytes (Si10-Si30)

Table 4.1 summarized key parameters, including pore size and the number of pores. Si10-150 and Si10-200 coatings exhibit similar pore size. Si10-225 shows the largest pore size.

Si20- 150 has the smallest pore size among all samples. Si20-200 and Si20-225 features a significant increase in pore size. Si30-150 and Si30-200 shows a comparable pore size.

The Figure 4.3 presents a set of histograms showing the pore size distribution for PEO coatings obtained on samples with varying silicon concentrations (Si10, Si20, and Si30) and applied voltages (150V, 200V, and 225V). Each histogram provides the frequency (in percentage) of pores corresponding to specific pore size ranges (in μm^2). The highest bar corresponds the smallest pore size range (approximately 0.05 μm^2) for most samples. Larger pores are less frequent, with their occurrence reducing significantly as pore size increases.

Table 4.1 Data on pore analysis of the PEO coatings obtained in various bath electrolytes, P.s. – pore size, Np – number of the pores

Sample no	**P.s., μm^2**	**Np per μm^2**
Si10-150	0.021±0.02	2.5
Si10-200	0.022±0.02	1.7
Si10-225	0.033±0.03*	0.4
Si20-150	0.008±0.01	1.2
Si20-200	0.034±0.04*	2.6
Si20-225	0.034±0.03*	0.4
Si30-150	0.031±0.03	2.3
Si30-200	0.030±0.04	1.8

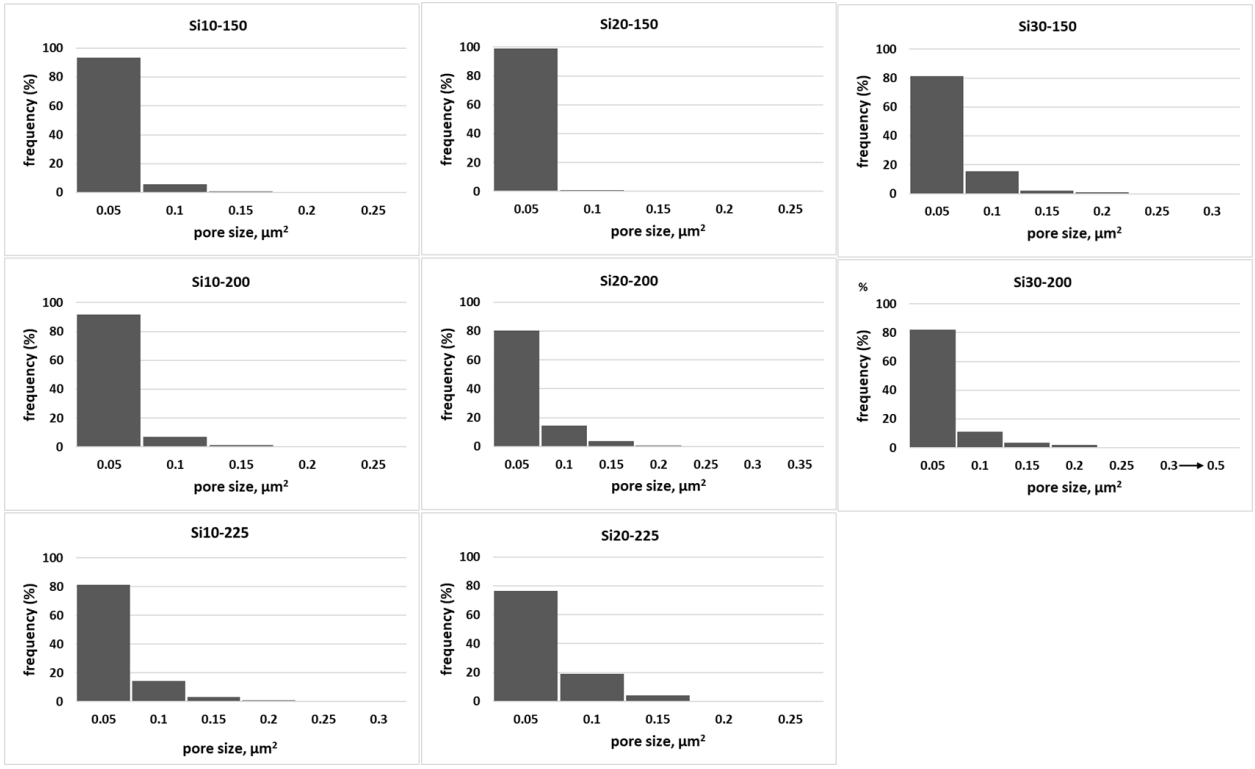

Figure 4.3 Pore size distribution on ceramic coatings formed after PEO in silicate-based bath electrolytes (Si10-Si30)

The provided Figure 4.4 contains a series of cross-sectional SEM images that represent microstructural characteristics of the coatings. Cross-sectional images revealed a relatively compact layer structure of the coatings, with pores discernible as remnants of microdischarge channels. The coatings formed at higher silicate concentration (Si-30) were thicker and exhibited a higher density of pores compared to the other coatings.

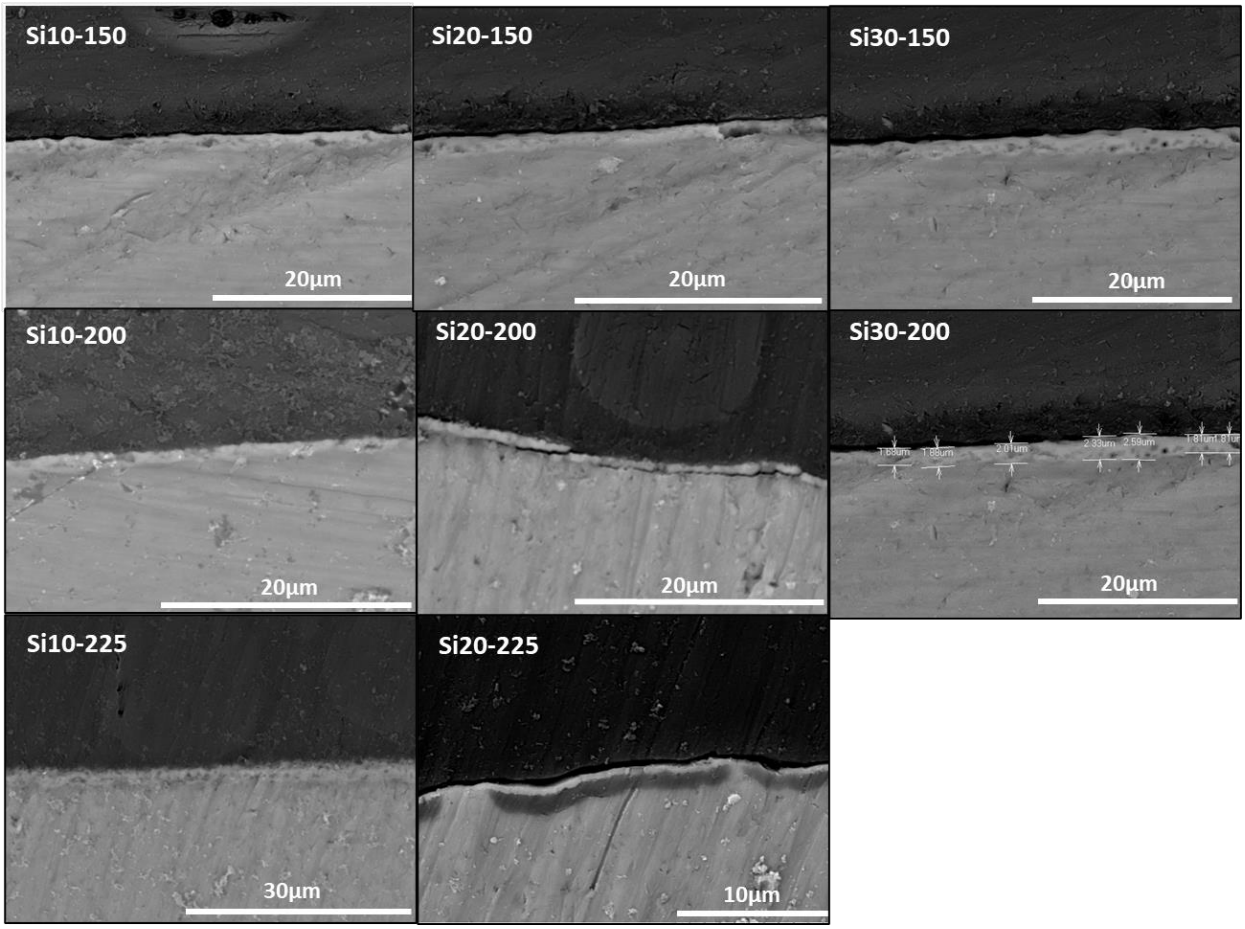

Figure 4.4 Scanning electron micrographs showing the cross-section of the PEO coatings formed in silicate-based bath electrolytes (Si10-Si30)

The Table 4.2 provided results of eddy current method. The obtained data showed the distance between the probe and the conductive layer. The device allowed accurately measure the thickness of oxide layers for PEO coatings formed in silicate-based bath electrolytes (Si10-Si30), with $p<0.05$. Values are presented as mean ± standard deviation, and * denotes statistically significant differences compared to the baseline (150 V). The thickness of the coating increases with increasing silicate concentration from Si10 to Si20, however decreased for Si30. The thickness also depended on the applied voltage, with higher voltage resulting in an increase in coating thickness for all type of the coating. Table 4.3 represented the parameter of the roughness for PEO coatings formed in silicate-based bath electrolytes (Si10-Si30), with $p<0.05$. Values are presented as mean ± standard deviation, and * denotes statistically significant differences compared to the baseline (150 V). Table observation detected the surface roughness generally increases with applied voltage across all electrolyte compositions, though the degree of increase varies by electrolyte. For Si-10, Ra increased significantly from 0.27 ± 0.02 at 150 V to 0.77 ±0.25

at 225 V. Si-20 displayed a modest increase, with values rising from 0.46 ± 0.07 to 0.38 ± 0.02. In the case of Si-30, roughness increased initially, from 0.22 ± 0.04 at 150 V to 0.30 ± 0.03 at 200 V.

Table 4.2 Thickness of the PEO coatings formed in silicate-based bath electrolytes (Si10-Si30) measured by eddy current method (μm), *p<0.05

V\Sample no	Si10	Si20	Si30
150	0.8 ± 0.3	2.0 ± 0.2	1.6 ± 0.2
200	3.9 ± 1.7*	5.0 ± 2.1*	3.4 ± 1.0*
225	6.6 ± 1.1*	7.4 ± 2.0*	—

Table 4.3 Parameter Ra (μm) of roughness of the PEO coatings formed in silicate-based bath electrolytes (Si10-Si30), p<0.05

V\Sample no	Si-10	Si-20	Si-30
150	0.27 ± 0.02	0.46 ± 0.07	0.22 ± 0.04
200	0.39 ± 0.1*	0.3 ± 0.01	0.3 ± 0.03
225	0.77 ± 0.25*	0.38 ± 0.02	—

Table 4.4 compiled the static water contact angle measurements for PEO coatings formed in silicate-based bath electrolytes (Si10-Si30) under different applied voltages (150 V, 200 V, and 225 V). The values are presented as mean ± standard deviation, and p<0.05. For Si-10 there is an increasing the angle value from 100 ± 2° at 150 V to 127 ± 11° at 200 V, followed by a sharp decrease to 76 ± 8° at 225 V, suggesting a voltage-dependent wettability trend. For Si-20 there is the contact angle decreasing from 122 ± 14° at 150 V to 92 ± 11° at 200 V and remained relatively stable at 93 ± 16° at 225 V. For Si-30 there is the minimal change of the contact angle, remaining around 99 ± 9° at 150 V and 96 ± 10° at 200 V.

Table 4.4 Static water contact angle for the PEO coatings formed in silicate-based bath electrolytes (Si10-Si30), p<0.05

V\Sample no	Si-10	Si-20	Si-30
150	100 ± 2	122 ± 14	99 ± 9
200	127 ± 11*	92 ± 11*	96 ± 10
225	76 ± 8	93 ± 16*	—

Figure 4.5 illustrates the dynamic water contact angle behavior of PEO coatings formed in silicate-based bath electrolytes (Si10-Si30) at different applied voltages (150 V, 200 V, and 225 V). The Si10 contact angle curves exhibit noticeable decline in the contact angle is observed with increasing voltage. The Si20 curves display a similar trend, with reduced contact angles at higher voltages. The contact angle increases significantly for 200 V compared with 150 V.

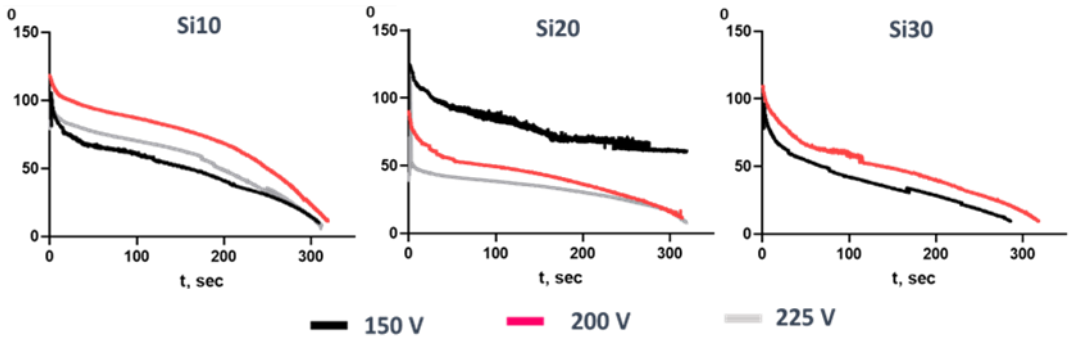

Figure 4.5 Dynamic water contact angle of the PEO coatings formed in silicate-based bath electrolytes (Si10-Si30)

The coating elementar composition was estimated by EDX measurements. The Table 4.5 summarizes data of magnesium (Mg), silicon (Si), sodium (Na), oxygen (O*), and fluorine (F*).

Table 4.5 Semi-quantitative EDX analysis of the PEO surface coatings on magnesium, at.%.

Sample no	Mg	Si	Na	O*	F*	Mg/Si
Si10-150	70	3	3	21	3	23.3
Si10-200	56	5	-	33	6	11.2
Si10-225	44	7	1	40	8	6.3
Si20-150	78	3	-	17	2	26
Si20-200	68	4	-	23	5	17
Si20-225	32	13	2	44	9	2.5
Si30-150	71	4	-	23	2	17.8
Si30-200	52	9	1	35	3	5.8

* the values are to be regarded as only informative

The Mg/Si ratio was also calculated to highlight the relative magnesium-to-silicon content. The results suggested elements incorporation to the coating from electrolite. There are several tendency effectively highlights the relationship between processing conditions (e.g., applied voltage) and the elemental composition of PEO coatings. Mg content decreases significantly with

applied voltages, while Si increases correspondingly. A similar pattern of reduced Mg and increased Si is observed for each group of the solutions. The increasing of Si concentraion in electrolyte causes to increasing the volume of silicates in the coating. Whereas the Si20 solution was optimal for higher amount of Si incorporation to the oxide layer.

Figure 4.6 visualize the surface morphology of the Si10-based samples after Ringer investigations. Considering the detailed analysis from the SEM images, it can be concluded that corrosion occurred on the magnesium samples during one day of immersion for all types of the surfaces. There are small pits of localized corrosion on the surface, which may have been caused by the chloride ions present in Ringer's solution. Five days of immersion causes a larger pits formation. Fine-crystalline corrosion products are observed on the 5th day of immersion for the Si20 and Si30 coatings, whereas for the Si10 coating, they appear on the 10th day. The numerous precipitations and crystals may have a positive effect in terms of corrosion protection, as these precipitations act as a barrier against further corrosion at their occurrence sites. For the Si20 and Si30 coatings cracks upper after approximately 10 days. After fifteen days of immersion, the coating shows signs of minor corrosion but remains intact and clearly visible.

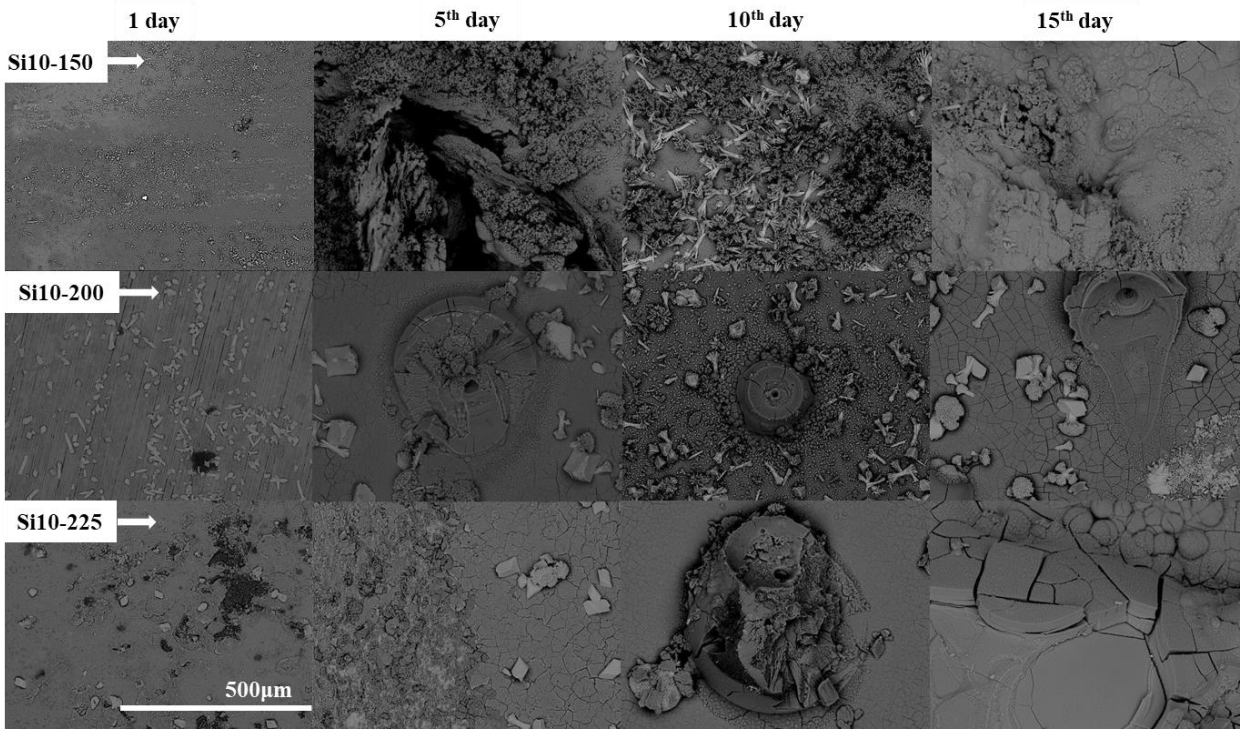

Figure 4.6 SEM images of the Si10-series samples surface after immersion in Ringer solution

The SEM images shown in Figure 4.7 reveal the corrosion process on the sample Si20-based surfaces. The corrosion is likely caused by chloride ions present in Ringer's solution. For Si20-150 samples noticeable changes are evident on the surface after just one day. The deep

perforations are dominated leading to delamination of the coating. The initial crystals agglomerates are visible after ten days. These deposits may have a positive effect in terms of corrosion protection, as they form a barrier against further corrosion at their location. However, the amount of these deposits is minimal, and only after approximately fifteen days can well-formed crystal salt structures be observed. Si20-200 samples surfaces characterized by small pitting corrosion sites. The fine-crystalline corrosion products can be observed after one day of immersion. The formation of these crystals at first stages may have a positive impact on corrosion protection, as the deposits act as a barrier to further corrosion at their location. The cracks in the coating begin to appear after approximately 10 days. The corrosion progresses by formation significantly increased number of surface cracks on the coating. This phenomenon is undesirable as it deteriorates the mechanical properties of both the coating and the underlying metal. Si20-225 coating showed the same corrosion effect. However, after five days, corrosion products become significantly larger than the deposits observed after one day.

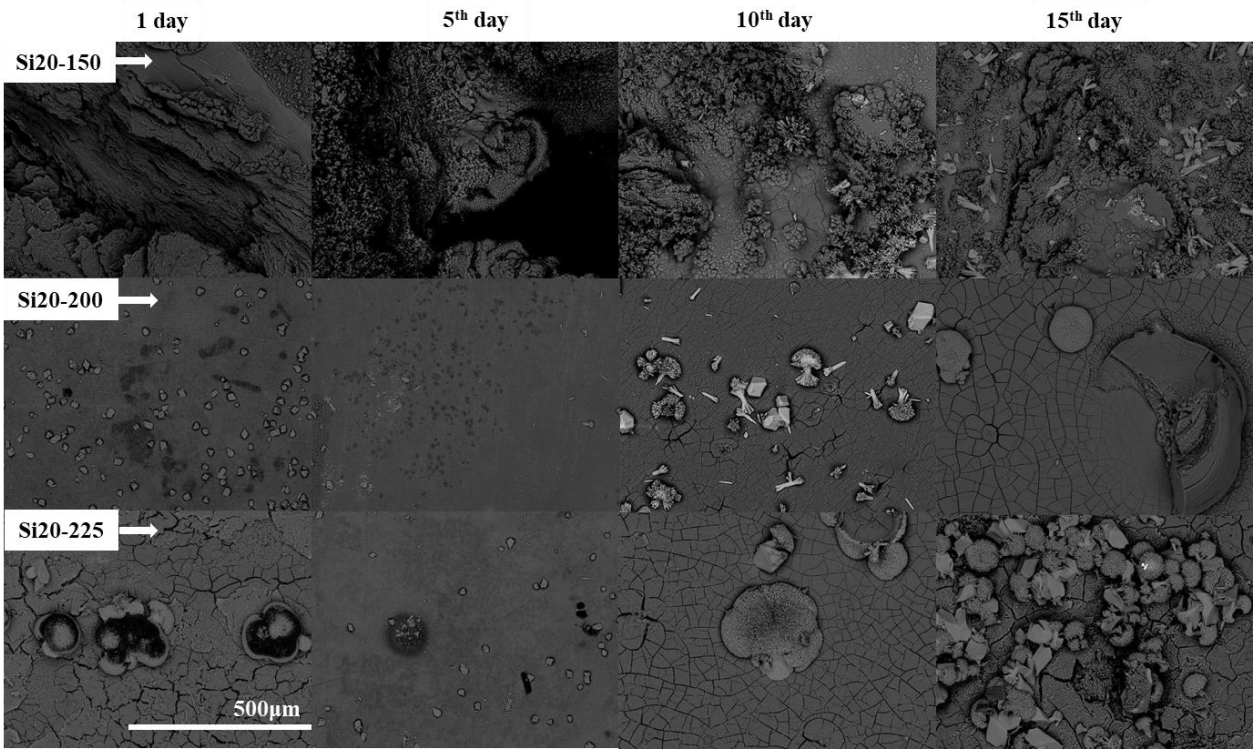

Figure 4.7 SEM images of the Si20-series samples surface after immersion in Ringer solution

The corrosion beginning of the Si30-150 coating is observed at the first days of the immersion (Fig. 4.8). There are a significant number of corrosion products on the surface on the first day of immersion. The crystals start to agglomerate after five days of immersion. These formations may have positive implications, as such salts create a natural anti-corrosion barrier.

The samples are marked by the appearance of the crack's throe whole surface on the 10th day of the immersion. After approximately 15 days, there is a noticeable increase in the amount of corrosion deposits and crystals. The surface Si30-200 appears intact with only a few visible crystalline corrosion products. However, there are dramatic changes after approximately five days. The significant corrosion pits can be observed on the coating. Numerous deep perforations and fractures indicate an active stage of corrosion. The images on ten and fifth day confirm the corrosion process visualized by cracks penetrating deeper into the coating. Based on the research data, it was found that the effects of corrosion intensify with the duration of sample immersion in Ringer's solution. However, the number of deposits increases, and the oxide layer remains visible, indicating a certain degree of corrosion protection. After 15 days of immersion, it can be concluded that the coating underwent significant corrosion but remained partially intact.

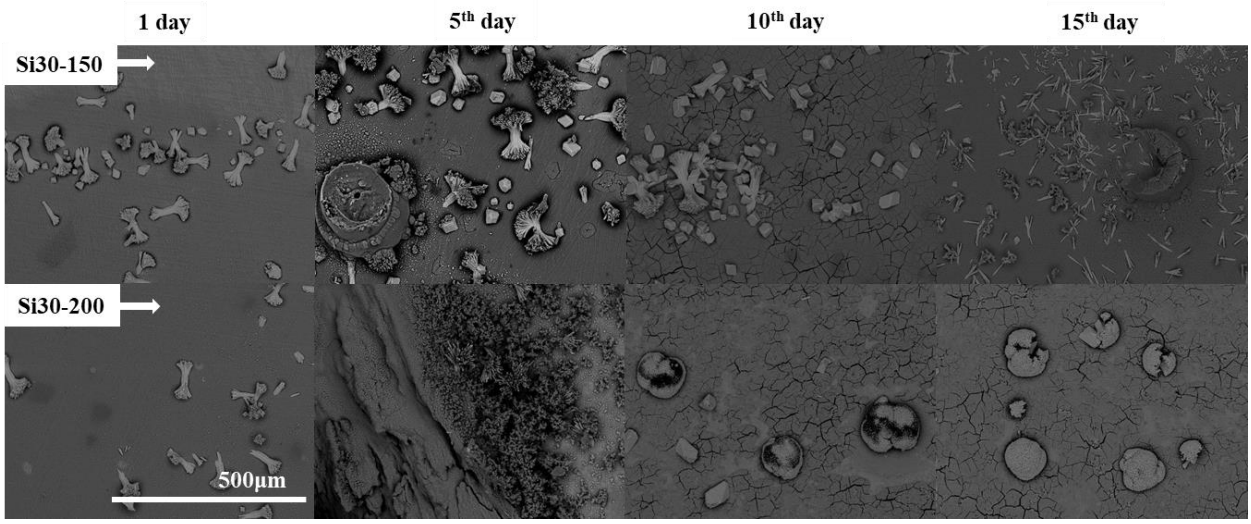

Figure 4.8 SEM images of the Si30-series samples surface after immersion in Ringer solution

Collected solutions after immersion test were evaluated by ICP analysis. The ion release characteristics of magnesium (Mg) and silicon (Si) from coatings were detected (Table 4.6). The data, expressed in milligrams per cubic decimeter ($mg \cdot dm^{-3}$), reflects the mean values and associated standard deviations (±SD) for each sample.

The Mg release varied significantly among the samples, with values ranging from 235 $mg \cdot dm^{-3}$ (Si20-200) to 420 $mg \cdot dm^{-3}$ (Si20-150). The highest Mg release was observed for the Si20-150 coating (420 ± 58 $mg \cdot dm^{-3}$). Silicon ion release was significantly lower compared to Mg, with values ranging from 0.270 $mg \cdot dm^{-3}$ (Si20-150) to 1.2 $mg \cdot dm^{-3}$ (Si10-225). Among the Si10 series, increasing trend in Si release dependent on the higher voltage value. The Si20 and Si30 series displayed relatively stable Si release across their respective samples, with Si20-200 and Si20-225 showing identical values (0.8 $mg \cdot dm^{-3}$) despite differing Mg release rates.

Table 4.6 The results of ICP analysis of the ion release characteristics ($mg \cdot dm^{-3}$) of the coatings after Ringer immersion test

Sample no	Mg	Si
Si10-150	258±18	0.280±0.010
Si10-200	270±91	0.5±0.2
Si10-225	270±26	1.2±0.3
Si20-150	420±58	0.270±0.001
Si20-200	235±32	0.8±0.2
Si20-225	293±57	0.8±0.3
Si30-150	244±50	0.36±0.12
Si30-200	278±48	0.37±0.06

The Mg specimens were placed into 24 well cell culture plates and were covered with complete cell culture medium with the amount of 40000 cells per square cm of the area of the bottom of the wells (Fig. 4.9a). However, the Mg specimens were smaller than the area of the wells and therefore the cells attached to both the plastic bottoms of the wells, as well as to the upper surfaces of the specimens. After 24 hours, there is visible gas formation and a change in the color of the medium in some wells. It was concluded to conduct the approximate pH measurement with litmus paper (Fig. 4.9b). The pH evaluation showed alkalization of the medium. Further resazurin reduction assay was used to evaluate the cellular metabolic activity in-vitro in presence of the obtained PEO coatings (Fig. 4.7c). Metabolically active cells reduced the blue-colored resazurin to bright-pink and highly fluorescent resorufin by aerobic respiration.

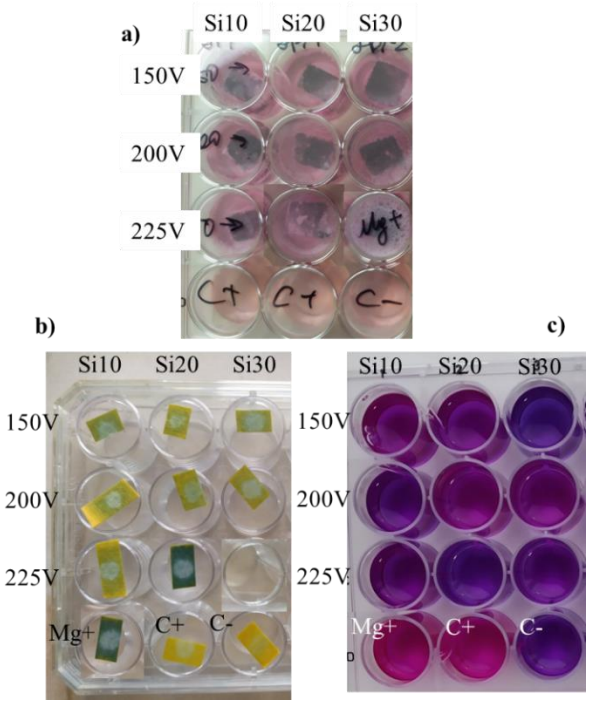

Figure 4.9 Scheme of cell culture investigation to Mg with the PEO coatings. a) UCMSC cells were incubated on PEO coatings with various concentrations of silicate under various voltage settings; b) pH measurements of the medium after 24 hours incubation; c) visualization of resazurin reduction assay

We detected that resazurin was substantially reduced in wells with Mg cubes but not in Mg-conditioned or control medium (Fig 4.10). Also obtained results showed that the level of resazurin reduction was dependent on the presence of a coating on Mg cubes. In the case of pure magnesium samples, the readings of the resazurin reduction assay were paradoxically going up without any cell plated. While a PEO coating protected Mg from quick corrosion and prevented a high rate of resazurin reduction.

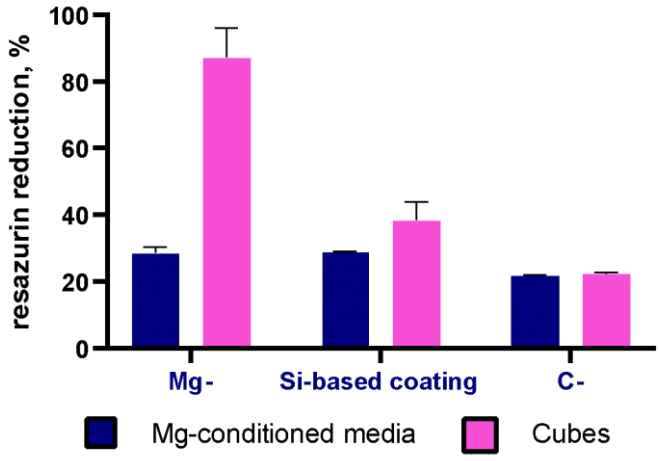

Figure 4.10 Autocatalytic reduction of resazurin with pure magnesium samples

Due to the reduction of resazurin connected with corrosion of Mg in the water environment without living cells, we interpreted results taking into account the possibility of unspecific (autocatalytic) reduction independently on metabolically active cells. Obtained results allows compare cell adhesion ability on coated Mg.

The provided panels depict DAPI staining for Si-based coatings. The presence of the blue fluorescence observed throughout the panels indicates adherence cell to the surface. The bright blue punctate structures indicate nuclear regions with their distinct morphology. Within a cultivation period of 24 h, the amount of adhered UCMSC cells was higher on PEO surfaces compared with pure magnesium. The DAPI staining images revealed cells with polygonal shape nuclei for surfaces with the coatings (Fig. 4.11). On pure Mg samples the nucleus had a round form.

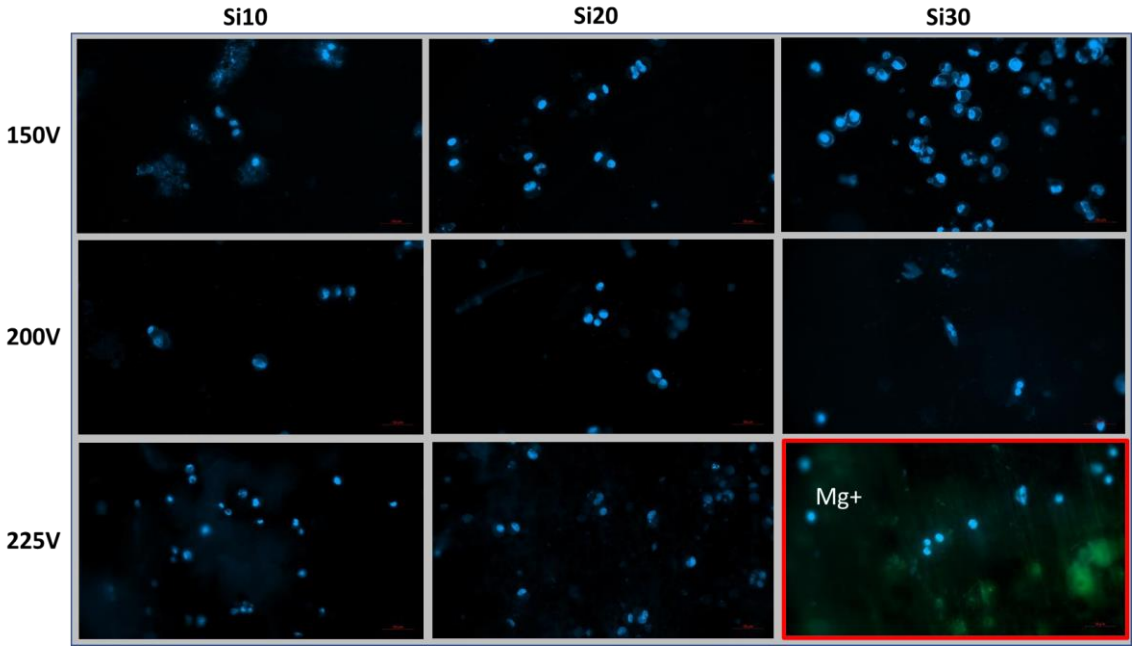

Figure 4.11 DAPI staining of cells attached to Mg with the PEO coatings. UCMSC cells were incubated on PEO coatings with various concentrations of silicate under various voltage settings as indicated; The controls with pure Mg are marked with red squares

The resazurin reduction assay on day 1 exhibited the highly cytotoxic effect of Mg (Fig. 4.12). Obtained results correlated with its rapidly increased initial corrosion rates. The high level of resazurin reduction with pure magnesium was connected to unspecific reaction due to autocatalytic effects. The low metabolic activity of the "leftover cells" in the pure Mg group confirmed this hypothesis. The initial period after plating indicated the higher cytotoxicity for all sets of Si20 and Si30 coatings. The cells on these samples were less metabolically active. The Si10-150 and S10-225 showed significant superiority over Si10-200 in cell attachment at the 1st day of incubation.

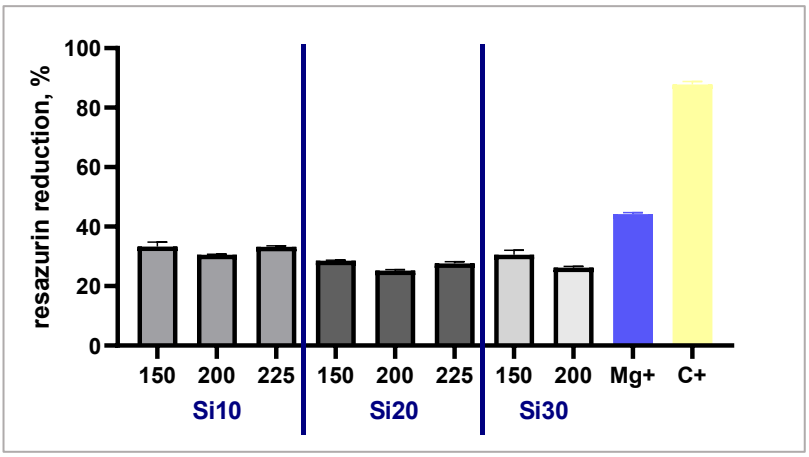

Figure 4.12 Cytotoxicity of PEO coatings examined by the resazurin reduction assay. UCMSC cells were incubated on PEO coatings obtained with various concentrations of silicate under various voltage settings as indicated

Examination of the wells with the “leftover cells” with an optical microscope allowed observe that the cells tolerated the presence of coated Mg cubes (Fig. 4.13.). The number of cells was lower compared with the control cells. The pure Mg group demonstrated the lowest number of cells with signs of apoptosis. Additionally, we detected the crystals of the corrosion products that were surrounding the dead cells.

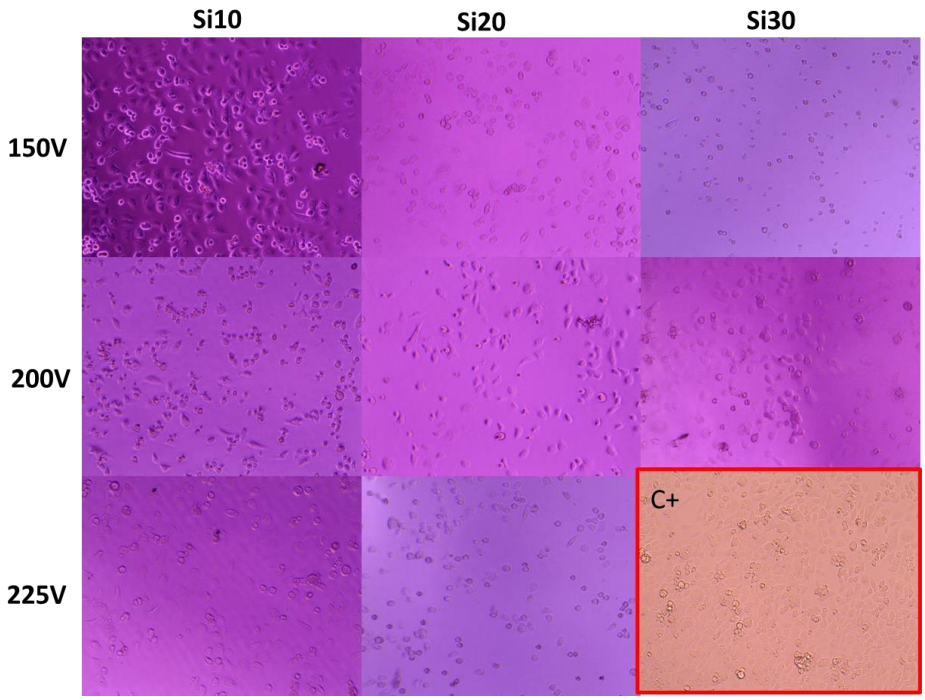

Figure 4.13 Observation of the effect various Mg samples on the “leftover cells” by light microscopy

The antibacterial activity of the magnesium oxide coatings was examined by *in vitro* bacteriological assay. The results obtained are illustrated in Figure 4.14. Untreated magnesium sample did not show the bacterial reduction. Although the antibacterial properties of the PEO coated Mg were not evident after the lower incubation time in the bacterial suspension (6 h). The antibacterial activities of the PEO coatings were increased presumably. The growth of bacteria was inhibited after pH exceeded values of 8.5~9. During the first 2 h, a very fast inhibitory effect was observed for samples Si10-150 and Si20-150. Also, the higher bactericidal effect was detected for samples Si30.

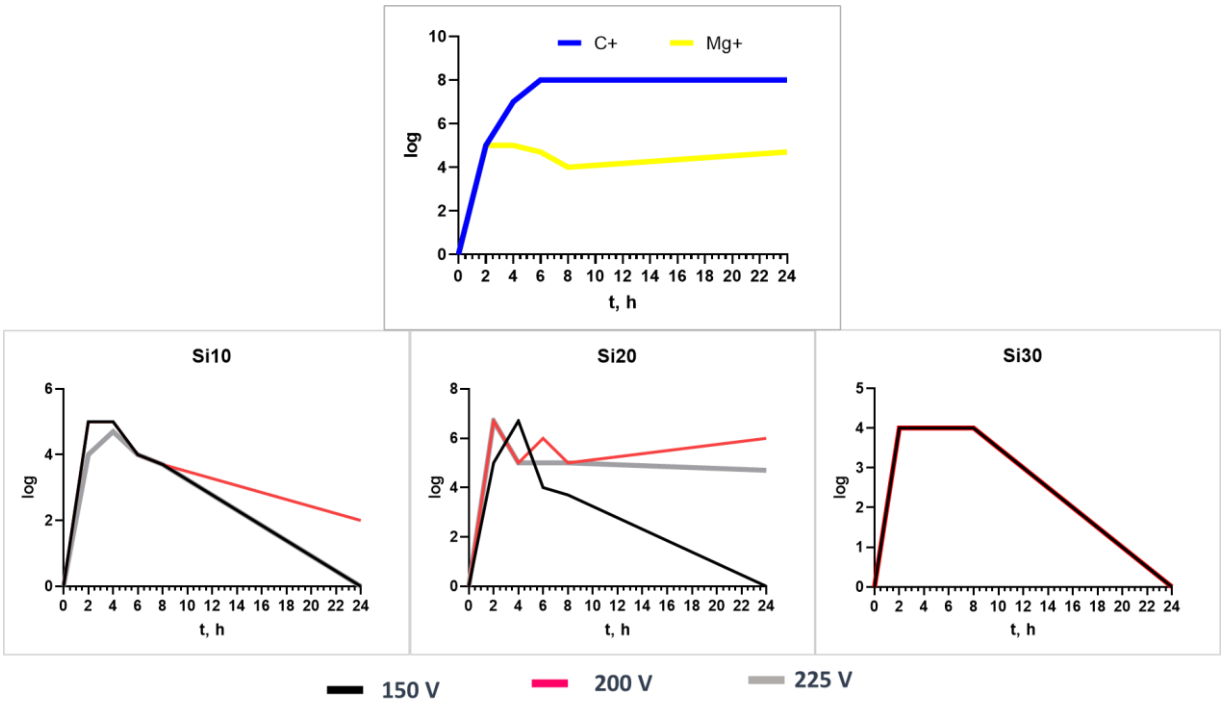

Figure 4.14 Time-dependent bacterial antiadhesive activity test

4.1.2. Discussion

All obtained surfaces have a highly porous structure. PEO oxide layers are characterized by presence of both micro- and nanopores, mostly up to 0.05 μm^2 in size. It is hypothesized that these pores originate from the discharge channels formed during the PEO process, which are associated with the release of gaseous by-products [128]. Also, there was observe surface morphology, resembling crater-like or volcano-like structures. The same structure was reported in other work [52]. It was detected that the higher voltage led to the develope of a more pronounced pore network. This net-like surface morphology resembled a foam or scaffold structure. Other works confirms that such surface features was typically observed on Mg alloys treated in silicate-based bath electrolytes [56]. It was found that most surfaces treated at 225 V exhibited micro-

cracks. According to the leterature these cracks were created by thermal stresses caused by the rapid solidification during formation of the PEO coating in the surrounding cold bath [141]. The more homogeneous PEO surfaces obtained at lower voltage confirmed the previous statment. The surfaces with crack may have lower corrosion resistance properties. However some authors shows, that these layers are favourable in orthopaedic applications by promoting cell attachment and osseointegration [142].

The size of the pores was dependent on the voltage and concentration of silicate. With the increase in silicate concentration in the bath electrolyte and the application of higher voltage, the pore size distribution was shift to larger. Also, higher voltage resulted in increasing average pore size. Especially it was visible for the Si10 bath electrolyte. Compared with the previous electrolyte, Si20 and Si30 surfaces exibited larger pores. Additionally, the density of surface pores decreased with increasing voltage. For example, the surface formed in the Si10 bath electrolyte exhibited a pore density of 2.5 pores•cm^{-2} at 150 V, which reduced to 0.4 pores•cm^{-2} at 225 V.

During the PEO process, plasma discharges induced partial, short-term surface melting, resulting in the formation of an oxide-ceramic layer. Additionally, the electrolyte components were incorporated into this hard ceramic layer [143]. The cross-section analysis allowed reveal that the PEO coatings consisted of open and interconnected pores and were firmly adhered to the underlying substrate. However, most of the coatings adjacent to the substrate showed an almost pore-free dense layer, which was in line with literature data [144]. It was detected that the higher voltage (225 V) remarkably enhanced the thickness of the coating. This was in line with other observations, which showed that voltage determined the coating thickness [145]. The measurements of coating thickness by Fischer ISOSCOPE- FMP10 portable eddy current meter and cross-sectional SEM micrographs coincided.

The surface roughness was determined by pores and pancake-like structures**.** During investigation there is no significant dependence the surface roughness of PEO-coated magnesium samples on the PEO process conditions. The highest roughness is observed in the coatings produced in Si-10 solution at 225V. Moreover, the higher voltage led to increase of not only the coating thickness, but the also the pore size, as well as their arrangement that also was repoted by other investigators [145]. Si20-200 coating demonstrated interconnected network of pores.

Semi-quantitative EDX analysis confirmed of the incorporation of Si, F. The Mg/Si ratio directly determines the types and proportions of phases formed within the PEO coating. In silicate-based electrolytes, common phases include magnesium oxide (MgO), forsterite (Mg_2SiO_4), and enstatite ($MgSiO_3$). The relative amounts of these phases are influenced by the availability of Mg^{2+} and SiO_3^{2-} ions during the oxidation process. For instance, a higher concentration of silicon can

lead to increased formation of silicate phases like Mg_2SiO_4 and $MgSiO_3$, which can enhance the coating's corrosion resistance and mechanical strength [70]. The Mg/Si ratio affects the microstructural features of the coating, such as porosity, thickness, and surface morphology. An optimal balance between magnesium and silicon can result in a denser and more uniform coating with reduced porosity, thereby improving its protective qualities. Conversely, an imbalanced ratio may lead to increased porosity and structural defects, compromising the coating's effectiveness [70]. The optimal Mg/Si ratio 99was 2.5.

Wettability and wetting are essential to coating characteristics. The wettability was evaluated by measuring the contact angle through tracing the contours of water droplets. A contact angle less than 90° indicates a hydrophilic surface, while a contact angle greater than 90° suggests a hydrophobic surface [146]. The results obtained showed that the wetting rate depends on the type of coating, pore size, porosity and degree of roughness. Smaller roughness on relatively smooth surfaces corresponded to increase in contact angle. Low contact angle value for samples Si10-225, Si20-200 and Si20-225 correlate to increasing the pore sizes of the coating. Thus, the contact angles ranged between 90° - 118°. The dynamic contact angle showed the kinetic characteristics of interection water with solid surface. The degree to which water spreads on the surface is a measurement of the polarity of the interface. For instance, a material with a water contact angle of 20° has a more polar surface than a material with a water contact angle of 95° [147].

Ringer immersion test was used for investigation for corrosion properties of the Mg. The results showed that the surface structure remained more corrosion resistant for samples obtained at higher voltage (Fig. 4.15). The PEO coatings with relatively large thickness provided the highest level of corrosion resistance at the corresponding voltage [148]. Figure 4.15 shows the selected surface morphologies of Si30-200 samples and the precipitations as a result of the interaction of the surfaces with the Ringer solution. The corrosion behaviour may be provided by the film compactness [149]. The coating retained its porous structure throughout the test. And the cracks that appeared signified beginning of the destruction inside the layers. The oxide film formed on Mg can get ruptured due to the significant difference in volume expansion between the metal and the oxide [150]. Gradual chemical dissolution led to the widening of cracks, which eventually developed into extensive pits by the fifth day of immersion. Furthermore, crystallized corrosion products, in combination with Ringer salts, formed irregular precipitates. This resulted in a surface featuring distinct regions, some covered with formed crystals and others with intact PEO coatings. Over the course of the immersion test, the corrosion products exhibited progressive growth, transforming from small, rod-like crystals into larger, cauliflower-like clusters. Analysis of the

chemical composition of the crystallized corrosion products revealed that they primarily contained O, Ca, Mg and Si, as shown in Fig. 4.15.

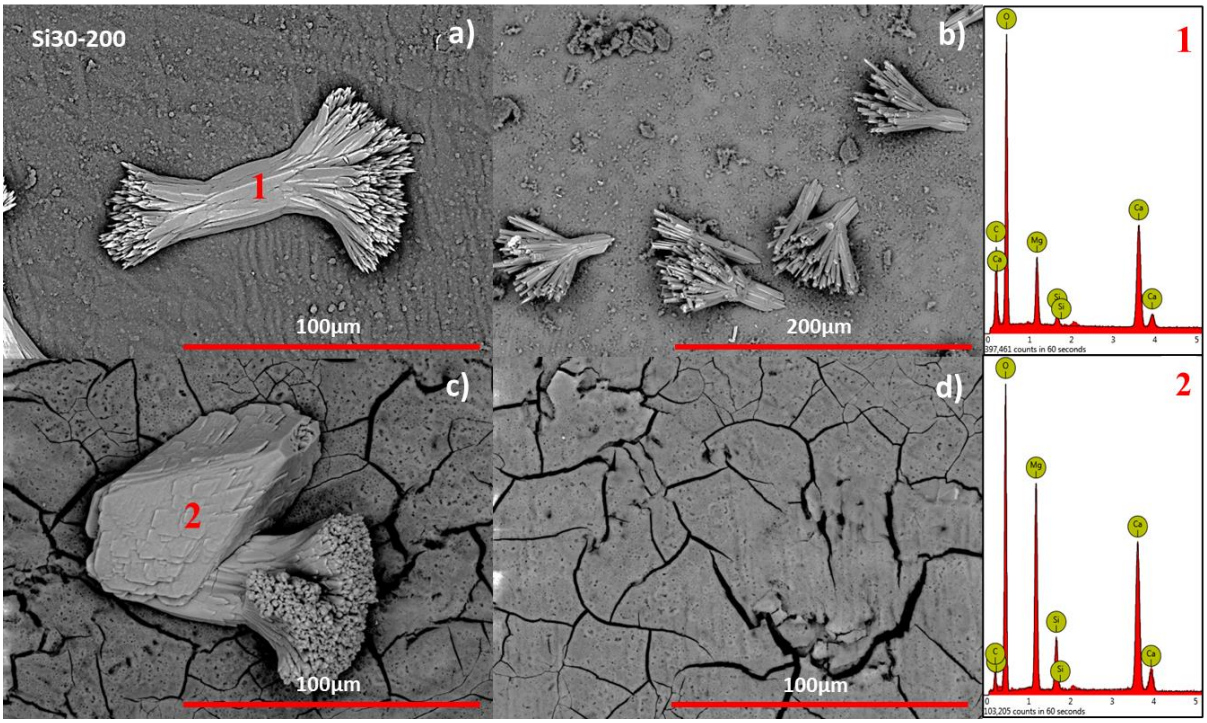

Figure 4.15 SEM images of the selected surface samples after immersion in Ringer solution (a) first, b) 5th, c) 10th and d) 15th day of the immersion) and EDS analysis of the precipitators (1 and 2 – places of the element analysis detection)

Mg and Si were identified as the primary elements released into the solution during the immersion test. Based on the calculated values, the average concentrations of Mg and Si in the solution were not influenced by the properties of the coating. However, crack formation significantly increased the dissolution rate of Mg in most samples. In contrast, the amount of Si released into the solution was consistently lower than that of Mg.

Cell culture investigation detected olso a possibility of reduction of resazurin via chemical reactions with Mg independent on alive cells leading to possible false positive results. Also, in our previous paper we observed that resazurin could be reduced in the presence of Ti_3C_2 MXene [138]. Moreover, a recent paper described the mechanism of the reduction of resazurin by redox reactions that occur by substrate corrosion [148].

Cell adhesion and spreading is an important event for adherent cells and precedes cell proliferation [150]. On PEO coatings the cells have polygonal shape nuclei. On pure Mg samples the nucleus had a round form that could be indicative of apoptosis [151]. Cell culture investigation

concluded that the PEO coatings susbstantially increased the corrosion resistance of the Mg and increased biocompatibility of the Mg samples.

The obtained coatings express the antibacterial properties, for some samples could be explained by increasing with pH level [152]. The presence of numerous pores and cracks in PEO coatings allowed for increased water and salt penetration into contact with reactive magnesium during extended incubation in bacterial suspension. Extending the incubation period from 6 to 24 hours intensified magnesium degradation and led to a rise in pH levels [153]. This prolonged exposure enhanced the antibacterial activity of the PEO coatings, likely due to the elevated pH. The higher alkalinity created an environment less conducive to bacterial growth, thereby reducing their proliferation.

4.2 Plasma electrolytic oxidation coatings on Mg in silicate-based solutions with addition of AgNPs

4.2.1 Results

To achieve the antibacterial properties of the PEO coatings the tasted chemical compositions were enriched with silver nanoparticles. The proposed compositions are shown in Table 3.1. The final concentration of AgNPs in the working solution for each set samples was 0.15 $mg \cdot dm^{-3}$. The electrolite was used for the PEO process immediately after preparation. Figure 4.16 visualizes the voltage and current density evolution during PEO process with the silver addition. Based on the analysis of the curves, it was found that during the process the voltage reached the desired value, and its course was stable for a long time. Nevertheless, after a short time, the current decreased to a minimum value, which is associated with the formation of an oxide layer, which is characterized by poor current conductivity. It is worth mentioning that the oxide layer was built up until the minimum current strength was reached. For samples with higher voltage the time for the current decrease was longer.

During PEO process coatings were obtained and visualized on the Figure 4.17. The surfaces are characterized by moderately uniform morphology. Si10-Ag-150 and Si20-Ag-150 surfaces exhibit a porous structure with numerous small holes. Whereas, other surfaces display a highly porous structure with small and medium-sized pores, organized into larger clusters, collectively forming the beginnings of larger pores. The presence of large pores indicates that the PEO process is proceeding correctly. The appearance of large pores and the uneven surface structure indicates that subsequent layers of the oxide coating were deposited intensively and chaotically. However, Si10-Ag-225 coating seems rougher and fractured, with less uniformity in texture compared to the other samples. Additionally, crystalline structures were observed on the surfaces of the coatings at 225V. These formations are likely attributed to the deposition of salts or magnesium oxides.

Table 4.7 expressed key parameters, including pore size and the number of pores. Si10-Ag-200 and Si10-Ag-250, Si30-Ag-200 coatings exhibit similar pore size. Si20-Ag-225 exhibits the largest pore size. Si10-150 has the smallest pore size among all samples. Si20-Ag-200 and Si30-Ag-150 features a significant increase in pore size.

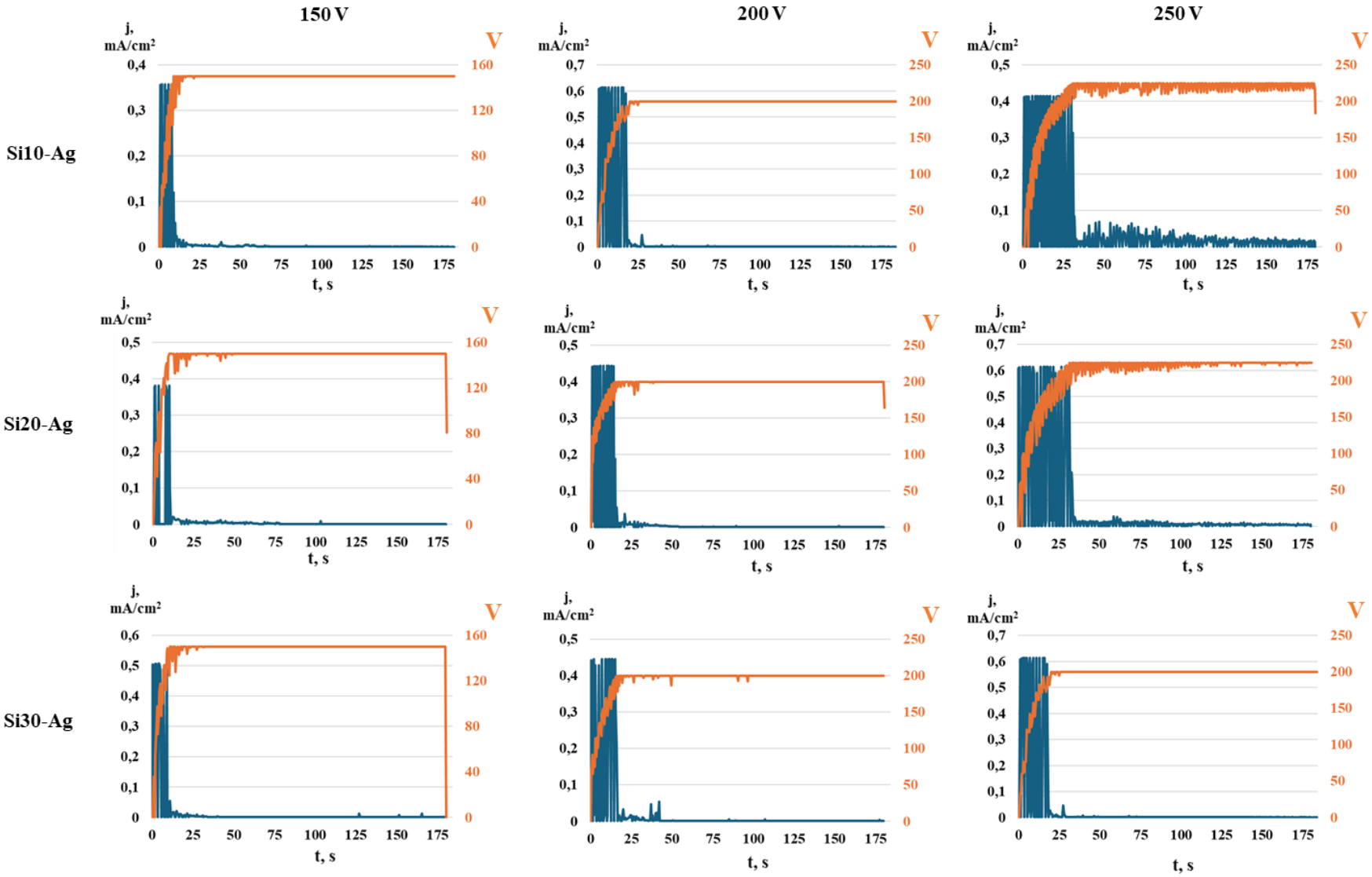

Figure 4.16 Voltage and current density evolution as a function of PEO processing time

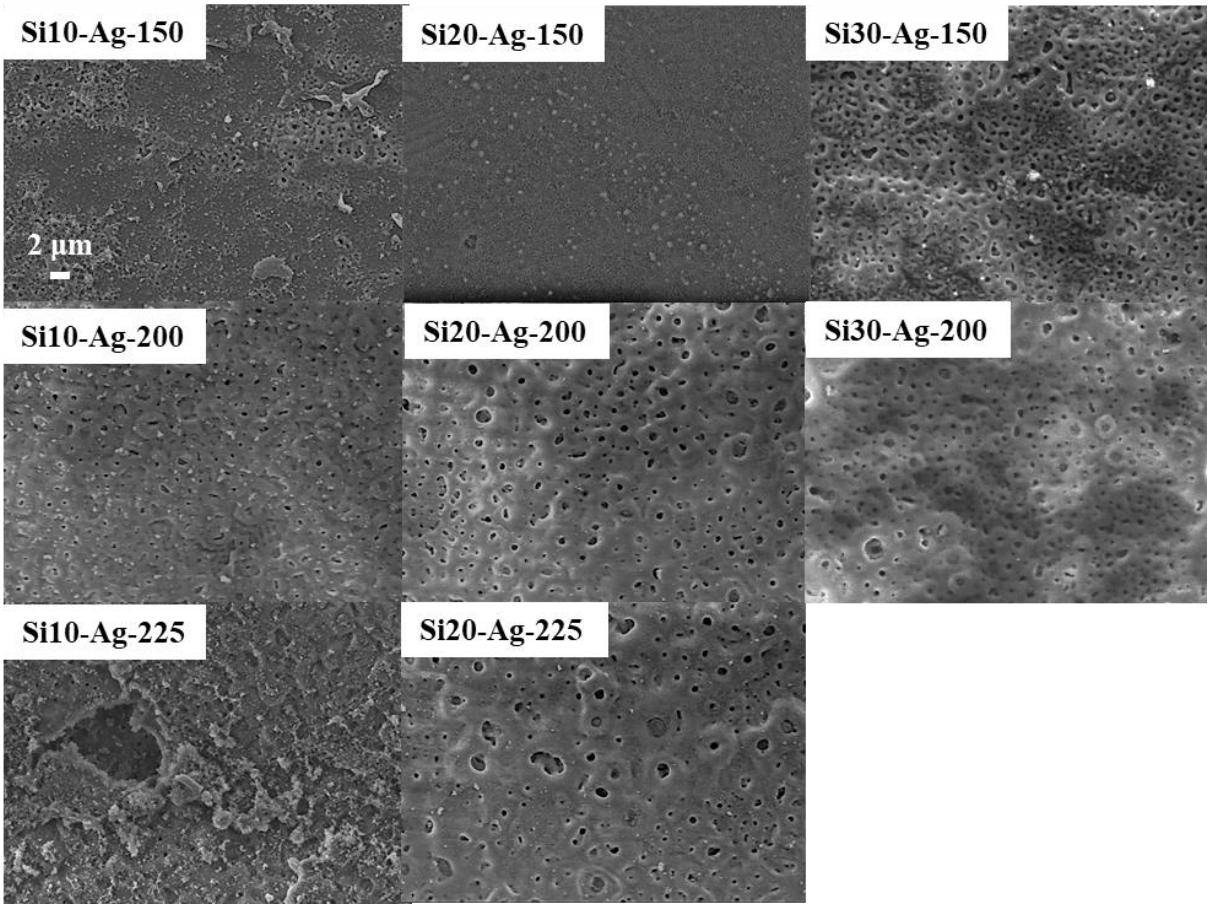

Figure.4.17 The SEM images of the magnesium PEO coatings formed in silicate-based bath electrolytes (Si10-Si30 with AgNPs addition)

Table 4.7 Data on pore analysis of the PEO coatings obtained in AgNPs-based bath electrolytes, P.s. – pore size, Np – number of the pores

Sample no	P.s., µm^2	Np per µm^2
Si10-Ag-150	0.015±0.01	2.8
Si10-Ag-200	0.036±0.03*	1.0
Si10-Ag-225	0.030±0.02*	0.2
Si20-Ag-150	0.023±0.13	0.6
Si20-Ag-200	0.072±0.07	0.6
Si20-Ag-225	0.098±0.14	0.4
Si30-Ag-150	0.054±0.87	2.5
Si30-Ag-200	0.032±0.04	0.9

The Figure 4.18 presents a set of histograms showing the pore size distribution for PEO AgNPs-based coatings obtained on samples with varying silicon concentrations (Si10, Si20, and

Si30) and applied voltages (150V, 200V, and 225V). Each histogram provides the frequency (in percentage) of pores corresponding to specific pore size ranges (in μm²). The highest bar corresponds the smallest pore size range (approximately 0.05 μm²) for most samples. Larger pores are less frequent, with their occurrence reducing significantly as pore size increases. Si20-Ag solution features a wider range of pore sizes, especially for Si20-Ag-150.

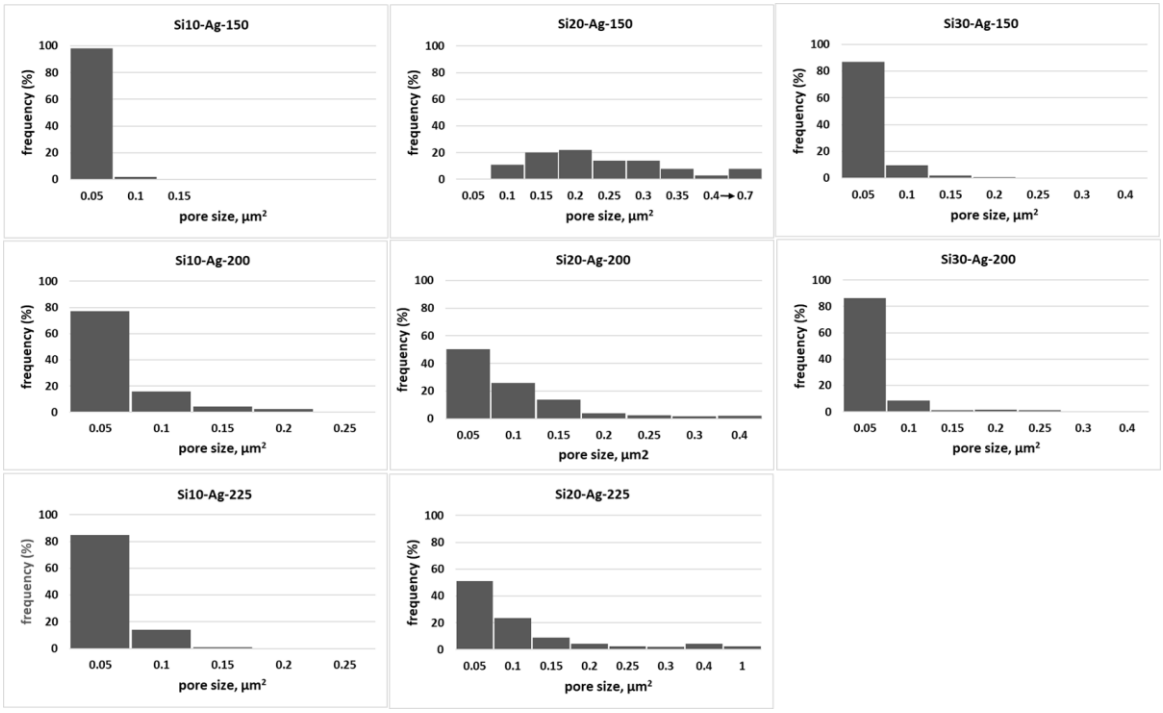

Figure 4.18 Pore size distribution on ceramic coatings formed after PEO in silicate-based bath electrolytes (Si10-Si30 with AgNPs addition)

The provided Figure 4.19 contains a series of cross-sectional SEM images that represent microstructural characteristics of the AgNPs-based coatings. Cross-sectional images revealed a relatively compact layer structure of the coatings, with pores discernible as remnants of microdischarge channels. The coatings formed at higher silicate concentration (Si-30) were thicker and exhibited a higher density of pores compared to the other coatings.

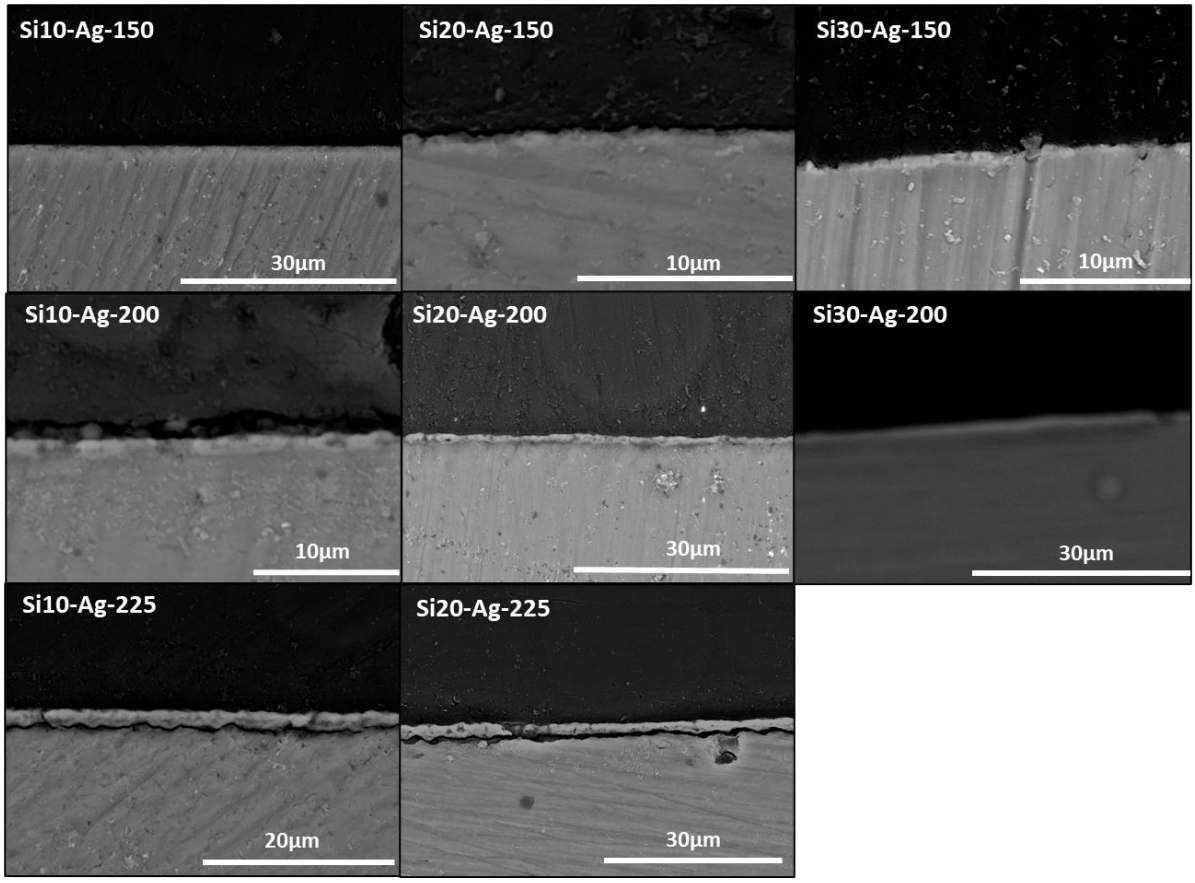

Figure 4.19 Scanning electron micrographs showing the cross-section of the PEO coatings formed in silicate-based bath electrolytes (Si10-Si30 with AgNPs addition)

Table 4.8 provided results of eddy current measurements for AgNPs enriched coatings. The obtained data showed the distance between the probe and the conductive layer. The device allowed accurately measure the thickness of oxide layers for PEO coatings formed in silicate-based bath electrolytes with silver nanoparticles, with $p<0.05$. Values are presented as mean ± standard deviation, and * denotes statistically significant differences compared to the baseline (150 V). The thickness of the coating increases with increasing of the voltage from 150 to 225V for all type of the coating. There are no significant differences connected with Si concentration.

Table 4.8 Thickness of the PEO coatings formed in silicate-based bath electrolytes (Si10-Si30) measured by eddy current method (µm), *p<0.05

V\Sample no	Si10-Ag	Si20-Ag	Si30-Ag
150	0.5 ± 0.2	0.4 ± 0.2	0.5 ± 0.1
200	3.0 ± 0.8*	3.5 ± 0.8*	4.0 ± 0.6*
225	6.4 ± 1.6*	6.0 ± 2.2*	—

Table 4.9 represented the parameter of the roughness for PEO coatings formed in silicate-based bath electrolytes loaded with AgNPs, with $p<0.05$. Values are presented as mean ± standard deviation, and * denotes statistically significant differences compared to the baseline (150 V). Table observation did not detect the general surface roughness changes connected with applied voltage. However, for Si10-Ag, Ra increased significantly from 0.26 ± 0.03 at 200 V to 1.46 ± 0.95 at 225 V. Si20-Ag exhibits the highest coating roughness. Si10-Ag and Si30-Ag samples have relatively similar roughness value for 150 and 200 V.

Table 4.9 Parameter Ra of the PEO coatings formed in silicate-based bath electrolytes (Si10-Si30), p<0.05

V\Sample no	Si10-Ag	Si20-Ag	Si30-Ag
150	0.28 ± 0.03	0.47 ± 0.07	0.23 ± 0.05
200	0.26 ± 0.03	0.3 ± 0.01	0.27 ± 0.03
225	1.46 ± 0.95*	0.45 ± 0.2	—

Table 4.10 compiled the static water contact angle measurements for PEO coatings formed in silicate-based bath electrolytes (Si10-Si30) enriched with AgNPs under different applied voltages (150 V, 200 V, and 225 V). The values are presented as mean ± standard deviation, and $p<0.05$. It was detected that Si10-Ag coatings tend to be the most hydrophobic, while Si20-Ag coatings show a strong trend toward hydrophilicity as the voltage increases. Si10-Ag exhibits the highest contact angle 107 ± 11°, indicating the most hydrophobic surface among the samples at this voltage. At 200 V the CA value remains high. A significant reduction in CA is observed for Si10-Ag 73 ± 7° and Si20-Ag 39 ± 11°, indicating these surfaces become more hydrophilic at higher voltages.

Table 4.10 Static water contact angle for the PEO coatings formed in silicate-based bath electrolytes (Si10-Si30), p<0.05

V\Sample no	Si10-Ag	Si20-Ag	Si30-Ag
150	107 ± 11	85 ± 1	66 ± 14
200	106 ± 23	72 ± 11	89 ± 15
225	73 ± 7	39 ± 11	—

Figure 4.20 illustrates the dynamic water contact angle behavior of PEO coatings formed in silicate-based bath electrolytes (Si10-Si30) enriched with AgNPs at different applied voltages

(150 V, 200 V, and 225 V). The curves reflect the behavior of water spreading over the surface in time. The curves demonstrate a gradual decrease in the contact angle values over time, indicating the dynamic wetting behavior of the surfaces. The time required for the droplet to spread is strongly influenced by the initial contact angle: surfaces with higher initial angles exhibit longer spreading times. This trend is particularly evident in the Si10-Ag samples, where the relationship between contact angle and spreading time is clearly pronounced.

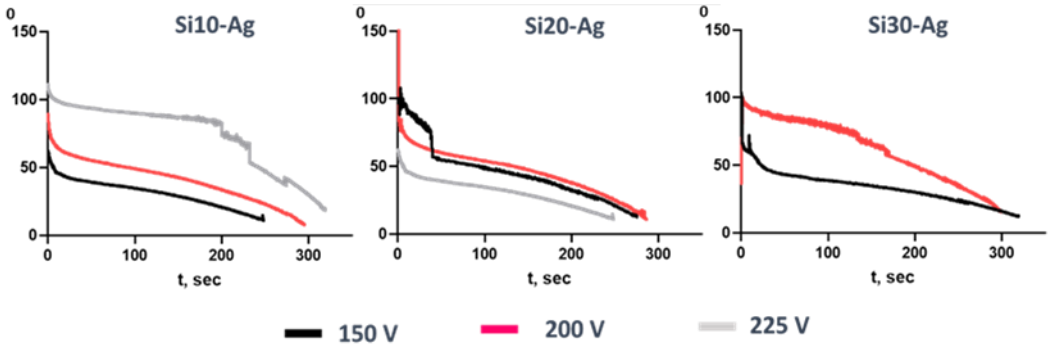

Figure 4.20 Dynamic water contact angle of the PEO coatings formed in silicate-based bath electrolytes (Si10-Si30 with AgNPs addition)

The coating composition was estimated by EDX measurements. The Table 4.11 summarizes data of magnesium (Mg), silicon (Si), sodium (Na), oxygen (O*), and fluorine (F*). The presence of Ag was not detected with the EDX analysis. The Mg/Si ratio was calculated to emphasize the relative magnesium-to-silicon content in the coatings. The results indicate the incorporation of elements from the electrolyte into the coating. Several observable trends effectively illustrate the relationship between processing conditions, such as applied voltage, and the elemental composition of the PEO coatings. There are significant Mg content decreasing with applied voltages, while Si increases correspondingly. A similar pattern of reduced Mg and increased Si is observed for each group of solutions. The increasing of Si concentraion in electrolyte causes to increasing the volume of silicates in the coating. This effect was more visible for Si20-Ag group. Whereas the Si20 solution was optimal for higher amount of Si incorporation to the oxide layer. Fluorine incorporation is influenced by both the applied voltage and the silicon concentration in the electrolyte. Higher voltages promote greater F integration into the PEO coatings.

Table 4.11 Semi-quantitative EDX analysis of the PEO surface coatings on magnesium, at.%

Sample no	Mg	Si	Na	O*	F*	Mg/Si
Si10-Ag-150	79	3	-	15	3	26.3
Si10-Ag-200	55	5	1	33	6	11
Si10-Ag-225	40	9	1	41	9	4.4
Si20-Ag-150	65	5	2	25	3	13
Si20-Ag-200	49	9	1	37	4	5.4
Si20-Ag-225	36	12	2	44	6	3
Si30-Ag-150	70	4	1	23	2	17.5
Si30-Ag-200	54	7	1	25	3	7.7

* the values are to be regarded as only informative

Figure 4.21 visualize the surface morphology of the Si10-AgNPs-based samples after Ringer investigations. Based on the analysis of SEM images presented in Figure, it can be concluded that corrosion occurred in magnesium samples subjected to the oxidation process. There are a few pits that can be observed, which might have been caused by chloride ions present in Ringer's solution. Numerous corrosion products are present on the first day of immersion for all samples. After about five-day crystals are organized into larger agglomerates, and their quantity increases. These structures may act to slow the progression of corrosion in specific areas. The surface for 200 and 225 V appears is uniform and free of cracks. Whereas the surface obtained at 150 V shows structural irregularities. After ten days, crystals exibit significantly better-developed structures. Their presence may have positive aspects, as such salts serve as a natural anti-corrosion barrier. The surface at 200 V shows symptoms of pitting corrosion can be observed in the form of cracks. The coating condition for sample 225 V can be considered moderately good, as shallow cracks are present. Approximately fifteen days later, the cracks appear at the coating 225 V. The collected research data, it was concluded that the effects of corrosion progress with the immersion time of the samples in Ringer's solution. However, the number of precipitates also increases, and the oxide layer remains visible, indicating a certain degree of corrosion protection.

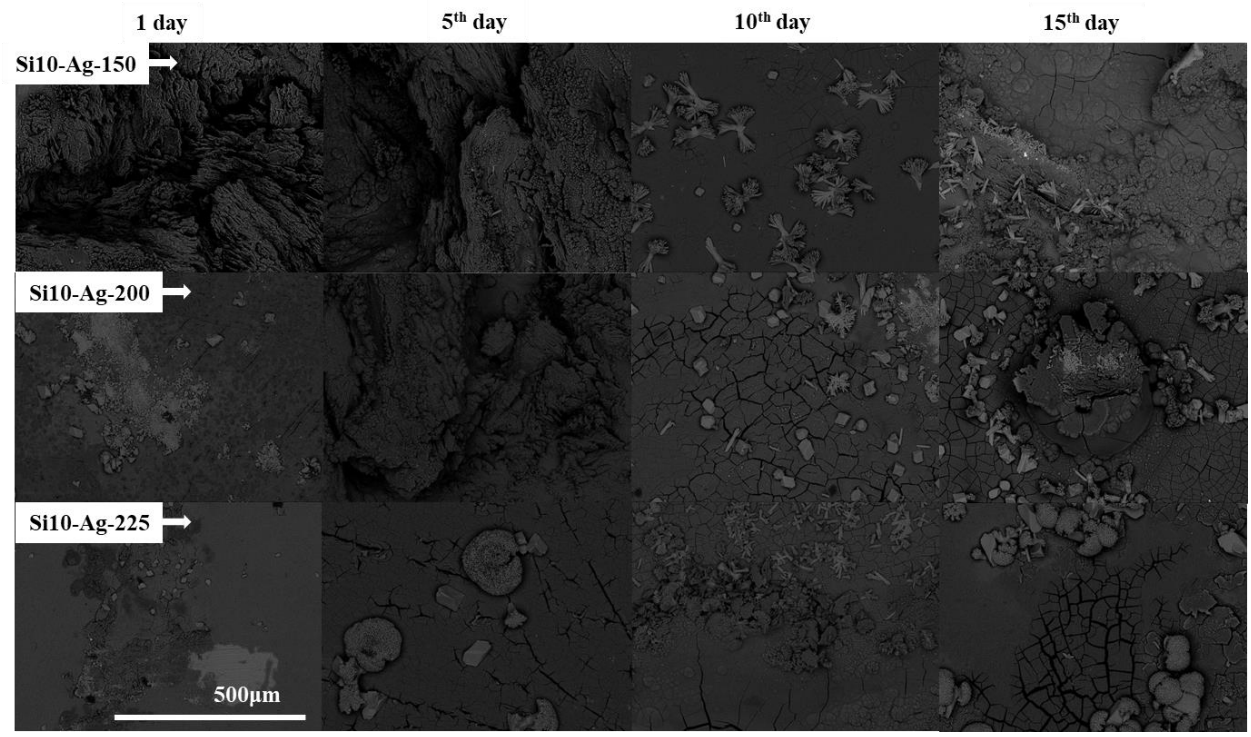

Figure 4.21 SEM images of the Si10-Ag-series samples surface after immersion in Ringer solution

The SEM images shown in Figure 4.22 reveal the corrosion process on the sample Si20-Ag-based surfaces. The corrosion is likely caused by chloride ions present in Ringer's solution. The initial crystals agglomerates are visible after one day of immersion. These deposits may have a positive effect in terms of corrosion protection, as they form a barrier against further corrosion at their location. However, the amount of these deposits is minimal, and only after approximately ten days can well-formed crystal salt structures be observed. For Si20-Ag-150 samples noticeable changes are evident on the surface after fifth day. The deep perforations are dominated leading to delamination of the coating. Si20-Ag-200 and Si20-Ag-225 samples surfaces characterized by small pitting corrosion sites on fifth and ten day of immersion. The cracks in the coating begin to appear after approximately 15 days and belong to the Si20-Ag-225 group. During the Ringer investigation the corrosion progresses by formation significantly increased number of surface cracks on the Si20-Ag-150 coating. This phenomenon is undesirable as it deteriorates the mechanical properties of both the coating and the underlying metal.

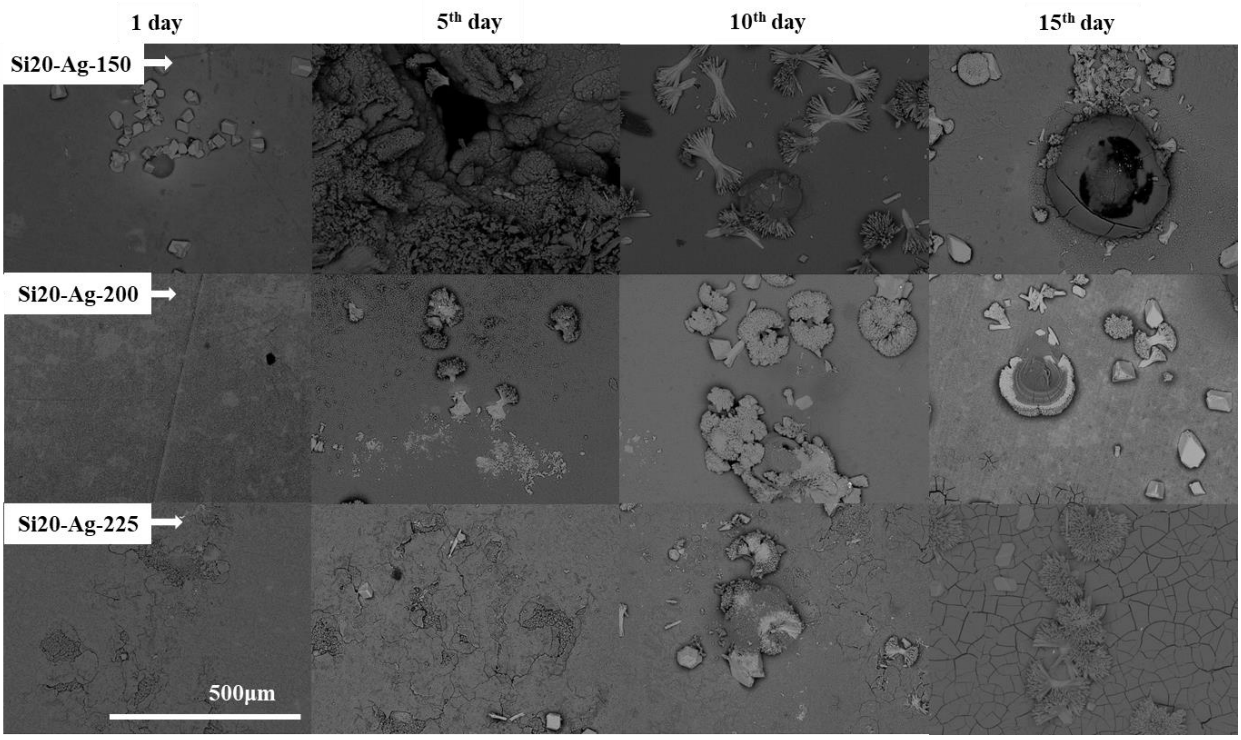

Figure 4.22 SEM images of the Si20-Ag-series samples surface after immersion in Ringer solution

The Figure 4.23 visualize the corrosion behavior of the coatings. There are a significant number of corrosion products on the surface on the first day of immersion. The crystals start to agglomerate after five days of immersion. These formations may have positive implications, as such salts create a natural anti-corrosion barrier. The samples are marked by the appearance of the crack's throe whole surface on the 10th day of the immersion. After approximately 15 days, there is a noticeable increase in the amount of corrosion deposits and crystals. The significant corrosion pits can be observed on the coating. Numerous perforations and fractures indicate an active stage of corrosion. The images on ten and fifth day confirm the corrosion process visualized by cracks penetrating deeper into the coating. Based on the research data, it was found that the effects of corrosion intensify with the duration of sample immersion in Ringer's solution. However, the number of deposits increases, and the oxide layer remains visible, indicating a certain degree of corrosion protection. After 15 days of immersion, it can be concluded that the coatings underwent significant corrosion but remained partially intact.

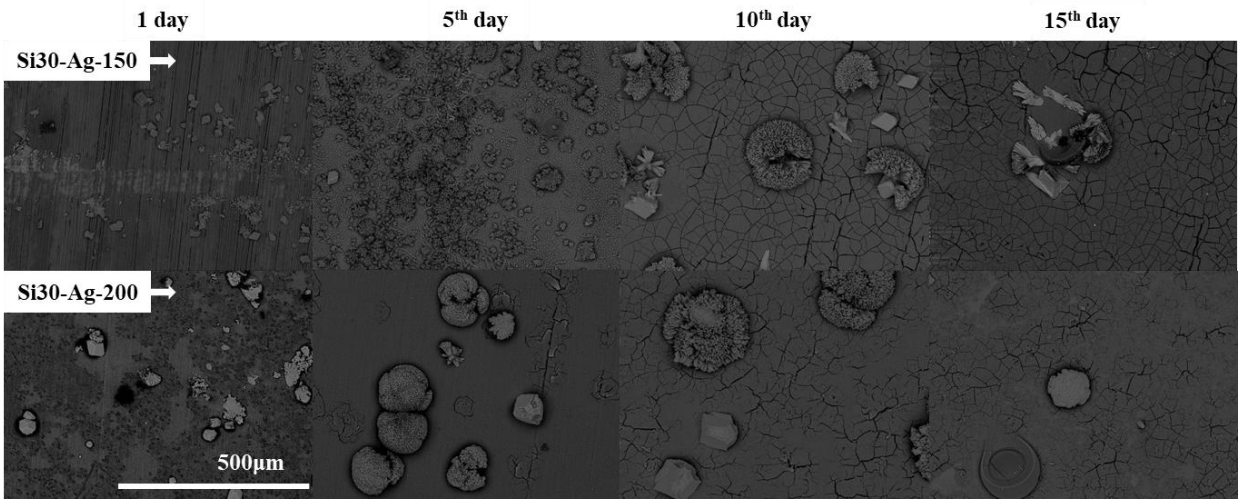

Figure 4.23 SEM images of the Si30-Ag-series samples surface after immersion in Ringer solution

Collected silver-based solutions after immersion test were evaluated by ICP analysis. The ions release characteristics of magnesium (Mg) and silicon (Si) and silver (Ag) from coatings were detected (Table 4.12). The data, expressed in milligrams per cubic decimeter ($mg \cdot dm^{-3}$), reflects the mean values and associated standard deviations (±SD) for each sample.

Obtained results showed that Mg release decrease with increasing voltage in most cases, but there are exceptions with Si10-Ag-200 sample. The Mg release varied significantly among the samples, with values ranging from 134 $mg \cdot dm^{-3}$ (Si20-Ag-225) to 404 $mg \cdot dm^{-3}$ (Si10-Ag-200). Silicon ion release was significantly lower compared to Mg, ranging from 0.19 ± 0.02 $mg \cdot dm^{-3}$ (Si30-Ag-150) to 2.1 ± 0.2 $mg \cdot dm^{-3}$ (Si20-Ag-225). In the Si10 series, Si release increases with higher voltages, reaching a peak of 0.91 ± 0.05 $mg \cdot dm^{-3}$ for Si10-Ag-225. For the Si20 series, the Si release rate peaks at 2.1 ± 0.2 $mg \cdot dm^{-3}$ for Si20-Ag-225, significantly higher compared to the other samples in this series. The Si30 series also shows relatively high Si release for Si30-Ag-200 (1.8 ± 0.4 $mg \cdot dm^{-3}$), suggesting a notable increase compared to the Si30-Ag-150 sample. The presence o f Ag confirmed silver incorporation to the coating during PEO. Ag release was generally low for most samples, with values below 1.0×10^{-3} $mg \cdot dm^{-3}$ for Si10-Ag-150, Si20-Ag-150, and Si30-Ag-150. The highest silver release was detected for Si20-Ag-225 coating. Ag release is highly dependent on the voltage, with the Si20 and Si30 series exhibiting the highest values at higher voltages.

Table 4.12 The results of ICP analysis of the ion release characteristics ($mg \cdot dm^{-3}$) of the coatings after Ringer immersion test

Sample no	Mg	Si	Ag, 10^{-3}
Si10-Ag-150	308±27	0.22±0.07	<1.0
Si10-Ag-200	404±20	0.31±0.07	4.3±0.5
Si10-Ag-225	293±88	0.91±0.05	3.7±1.0
Si20-Ag-150	311±47	0.21±0.02	<1.0
Si20-Ag-200	297±42	0.24±0.05	3.7±1.0
Si20-Ag-225	134±15	2.1±0.2	12.4±2.0
Si30-Ag-150	259±43	0.19±0.02	<1.0
Si30-Ag-200	331±9	1.8±0.4	12.0±4.0

Cell culture experiment was conducted to evaluate cytotoxic properties of the samples. The experiment was conducted into 24 well cell culture plates. The Mg specimens were placed into this plate and were covered with complete cell culture medium with the amount of 40000 cells per square cm of the area of the bottom of the wells (Fig. 4.24a). However, the Mg specimens were smaller than the area of the wells and therefore the cells attached to both the plastic bottoms of the wells, as well as to the upper surfaces of the specimens.

After 24 hours, gas formation and a change in the medium's color were observed in some wells. As a result, an approximate pH measurement was conducted using litmus paper (Fig. 4.24b), which indicated an alkalization of the medium. To further assess cellular metabolic activity in vitro in the presence of the PEO coatings, a resazurin reduction assay was performed (Fig. 4.24c). Metabolically active cells converted the blue resazurin into bright pink, highly fluorescent resorufin through aerobic respiration.

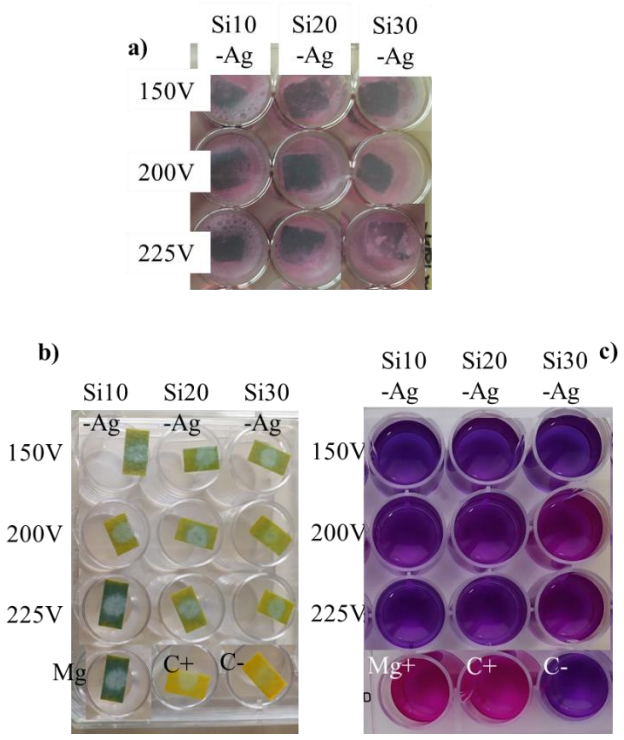

Figure 4.24 Scheme of cell culture investigation to Mg with the PEO coatings.enriched with AgNPs a) UCMSC cells were incubated on PEO coatings with various concentrations of silicate under various voltage settings; b) pH measurements of the medium after 24 hours incubation; c) visualization of resazurin reduction assay

Due to the reduction of resazurin, connected with corrosion of Mg in the water environment without living cells, that was confirmed by previous investigation, we interpreted results taking into account the possibility of unspecific (autocatalytic) reduction independently on metabolically active cells. Obtained results allows compare cell adhesion ability on coated Mg.

Figure 4.25 visualize the results of DAPI staining for Si-based coatings enriched with silver. The presence of the blue fluorescence observed throughout the panels indicates adherence cell to the surface. The bright blue punctate structures indicate nuclear regions with their distinct morphology. Within a cultivation period of 24 h, the amount of adhered UCMSC cells was higher on PEO surfaces compared with pure magnesium. The DAPI staining images revealed cells with polygonal shape nuclei for surfaces with the coatings. On pure Mg samples the nucleus had a round form.

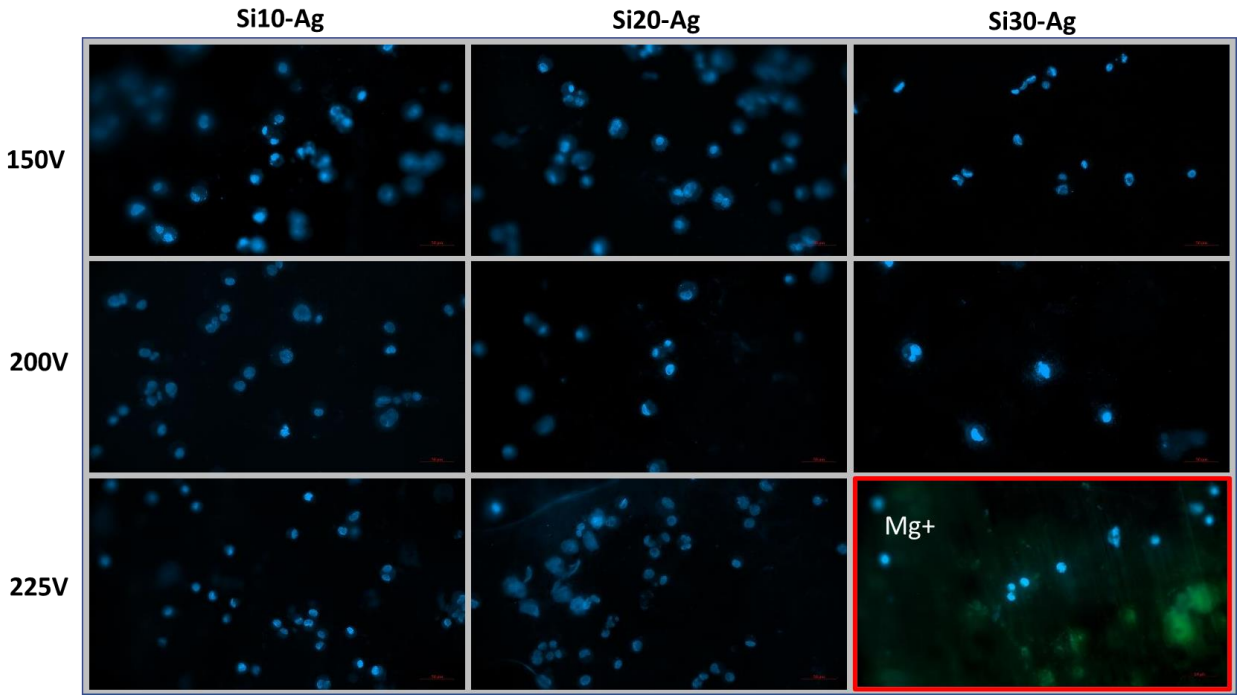

Figure 4.25 DAPI staining of cells attached to Mg with the PEO coatings. UCMSC cells were incubated on PEO coatings with various concentrations of silicate under various voltage settings as indicated; The controls with pure Mg are marked with red squares

The resazurin reduction assay on day 1 exhibited the highly cytotoxic effect of Mg (Fig. 4.26). Obtained results correlated with its rapidly increased initial corrosion rates. The high level of resazurin reduction with pure magnesium was connected to unspecific reaction due to autocatalytic effects. The low metabolic activity of the "leftover cells" in the pure Mg group confirmed this hypothesis. The initial period after plating indicated higher cytotoxicity for all sets of Si20-Ag and Si30-Ag coatings. The cells on these samples were less metabolically active. The Si10-Ag-150 and S10-Ag-225 showed significant superiority over Si10-200 in cell attachment at the 1st day of incubation.

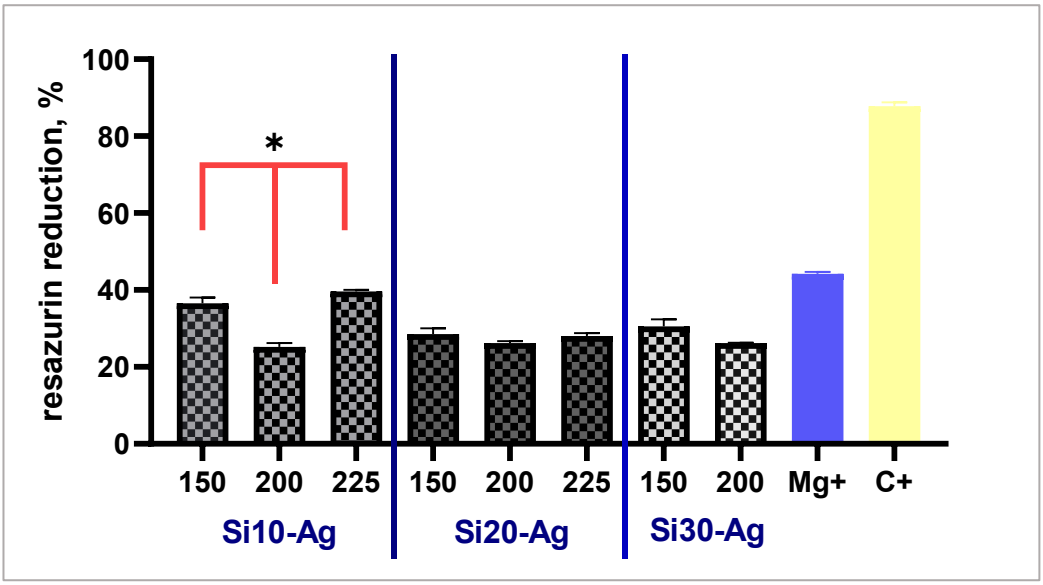

Figure 4.26 Cytotoxicity of PEO coatings examined by the resazurin reduction assay. UCMSC cells were incubated on PEO coatings obtained with various concentrations of silicate under various voltage settings as indicated

Observation of the wells containing "leftover cells" under an optical microscope revealed that the cells tolerated the presence of coated Mg cubes (Fig. 4.27). However, the number of cells was lower compared to the control group. The pure Mg group exhibited the lowest cell count, with signs of apoptosis observed. Additionally, crystals of corrosion products were detected surrounding the dead cells.

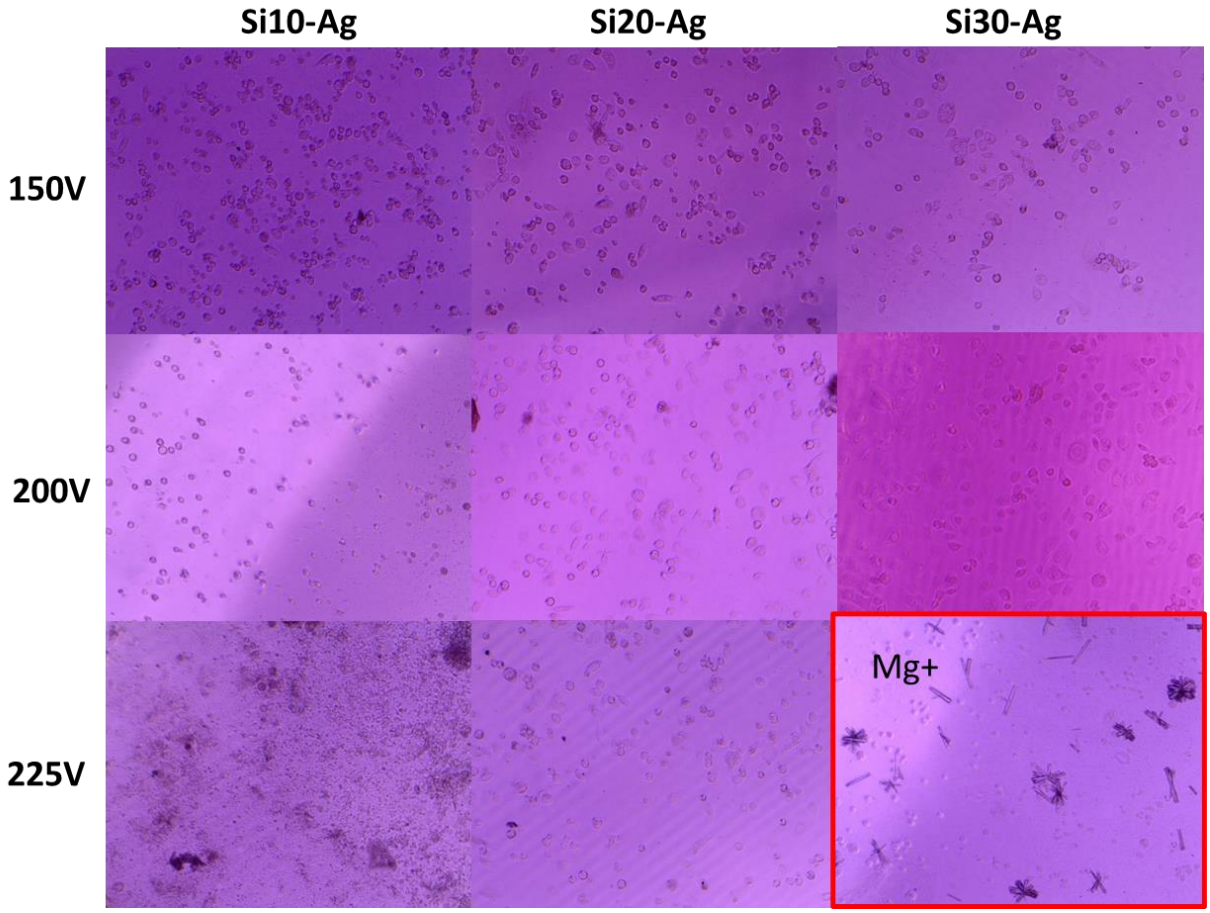

Figure 4.27 Observation of the effect various Mg samples on the "leftover cells" by light microscopy

The antibacterial activity of the magnesium oxide coatings was examined by in-vitro bacteriological assay. The results obtained are illustrated in Figure 4.28. Untreated magnesium sample did not show the bacterial reduction. Although the antibacterial properties of the PEO coated Mg were not evident after the lower incubation time in the bacterial suspension (6 h). The antibacterial activities of the PEO coatings were increased presumably. The growth of bacteria was inhibited after pH exceeded values of 8.5~9. During the first 2 h, a very fast inhibitory effect was observed for samples Si10-Ag groups. Also, the higher bactericidal effect was detected for samples Si20-200.

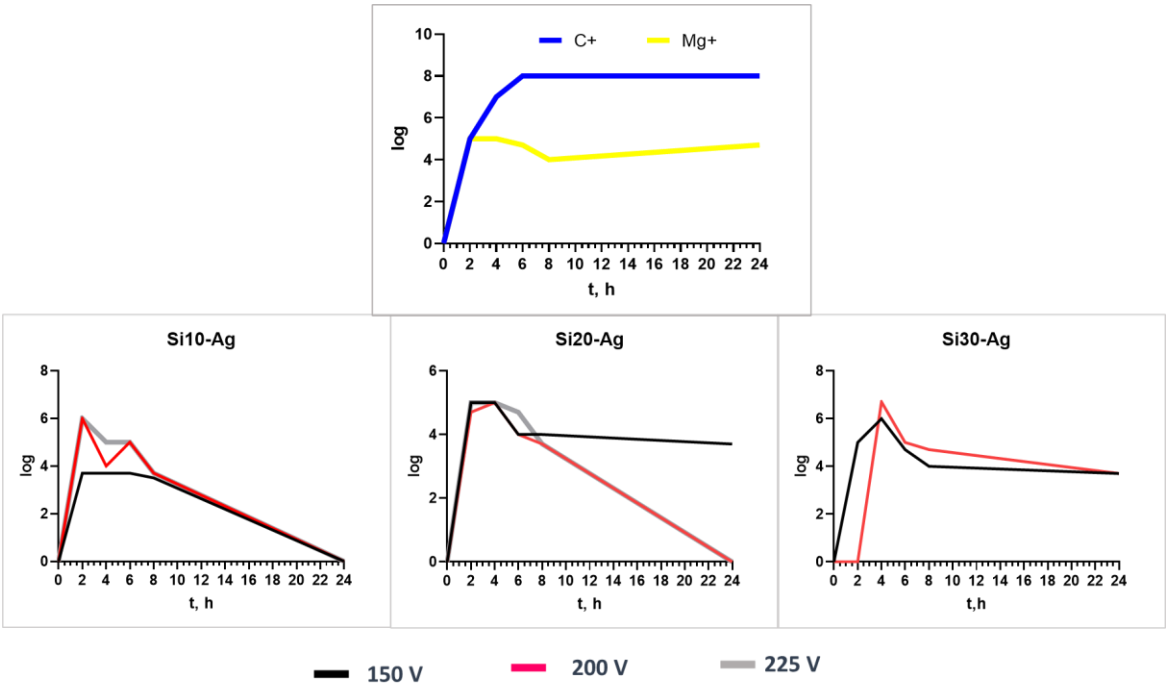

Figure 4.28 Time-dependent bacterial antiadhesive activity test

4.2.2. Discussion

During the PEO process, both the species in electrolyte and Ag incorporated into the PEO coating as proposed in scheme (Fig. 4.29).

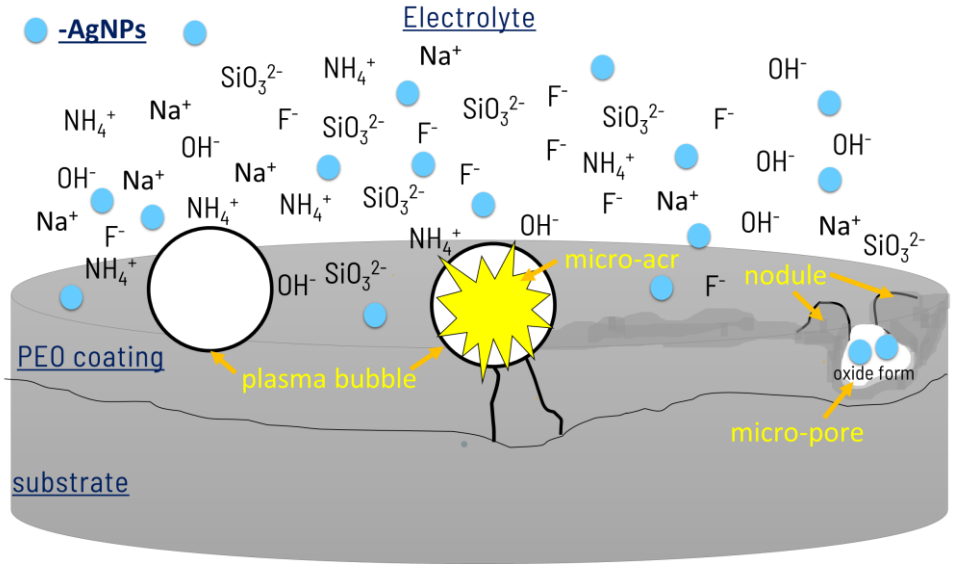

Figure 4.29 The scheme of PEO coating formation with AgNPs suspension

The PEO treatment with silver nanoparticles of magnesium samples led to the development of ceramic oxide coating, exhibiting also a characteristic morphology with open micro- and nanopores. The Si10-Ag and Si30-Ag surfaces haracteriazed with minimal variation in pore size

concentrated around 0.05 μm². In contrast, the Si20-Ag samples exhibited a broader distribution of pore sizes especially at higher voltages (225 V), including the presence of the significantly larger pores. Notably, the addition of silver nanoparticles significantly increased pore dimensions in the Si20 samples. This effect could be attributed to silver's ability to lower the melting point of the oxide substrate, thus increasing the melt volume. Consequently, the pool of melt surrounding the discharge expands, and the cooling rate decreases, extending the time available for the melt to flow back into the discharge channel before solidification occurs, as reported in the literature for particle addition [149]. This results in a larger pore diameter. However, the numerical values obtained for the average pore size of PEO surfaces treated in electrolytes containing AgNPs did not show a consistent relationship with the PEO parameters. Moreover, the addition of AgNPs did not affect the number of pores in the coatings. The obtained PEO coatings contained silver nanoparticles consisted also of open and interconnected pores. Addition silver nanoparticles changed the surface nature of the samples with decreased network connections and increased pore dimensions.

Measurement of the thickness showed that the addition of AgNPs led a general reduction of the thickness of the PEO layer, particulary at 150 V. The presence of silver nanoparticles likely reduced the oxide film thickness by decreasing the energy produced by micro-discharges, a phenomenon also observed by other researchers [149]. Nevertheless, the impact of the silver particles was weakened under the high voltage due to the faster growth rate that also was detected by others [145].

Surfaces with AgNPs addition characterized also by pores and pancake-like structures on the PEO surfaces determine roughness of the coatings. The roughness measurement did not show significant dependence the roughness parametress. Only solution Si-10 showed increased roughness at the higher voltage at 225 V.

Silver addition influenced on the wettability properties of the obtained coatings. The static contact angles decreased to 62° -111° after addition of AgNPs to the bath electrolyte. Obtained contact angle values indirectly evidence that AgNPs are distributed on the PEO surfaces. Variations in the contact angle vs. time showed decrease in kinetics of water sorption. The silver modification of the electrolyte could also influence electrical discharge mechanisms during PEO process [154]. The behaviour of electrical discharges during anodization could significantly affect the coating morphology and its properties.

The obtained EDX results proved that the chemical compositions of PEO coatings strongly depended on the composition of electrolytes The presence of Mg, F, Si, O and Na was detected in the PEO coatings. The amount of incorporated Si and F were depended on applied voltage. Its

increasing increase the atomic present of thes elements. Silicate and fluoride were incorporated into the layers from the bath electrolyte. From other site the concentration of Mg was lower with voltag icreasing. Lower content of magnesium could be related to the increasing thickness of the layers. However, EDX analysis did not detect the presens of silver into the coatings. The presence of the AgNPs in the solution did not significantly impact composition of the surface coatings.

Testing corrosion properties by Ringer immersion test showed that the decreasing of thickness in case samples with silver at higher voltage did not impact on corrosion properties. Figure 4.30 visualize the selected surface morphology of the Si10-Ag-225 samples. The surfaces exibit corrosion products continued to grow throughout the immersion test from the small rod-like crystals to large cauliflower like clusters. Determination to the chemical composition of crystallized corrosion products showed that they consisted mainly of O, Ca, Mg and Si.

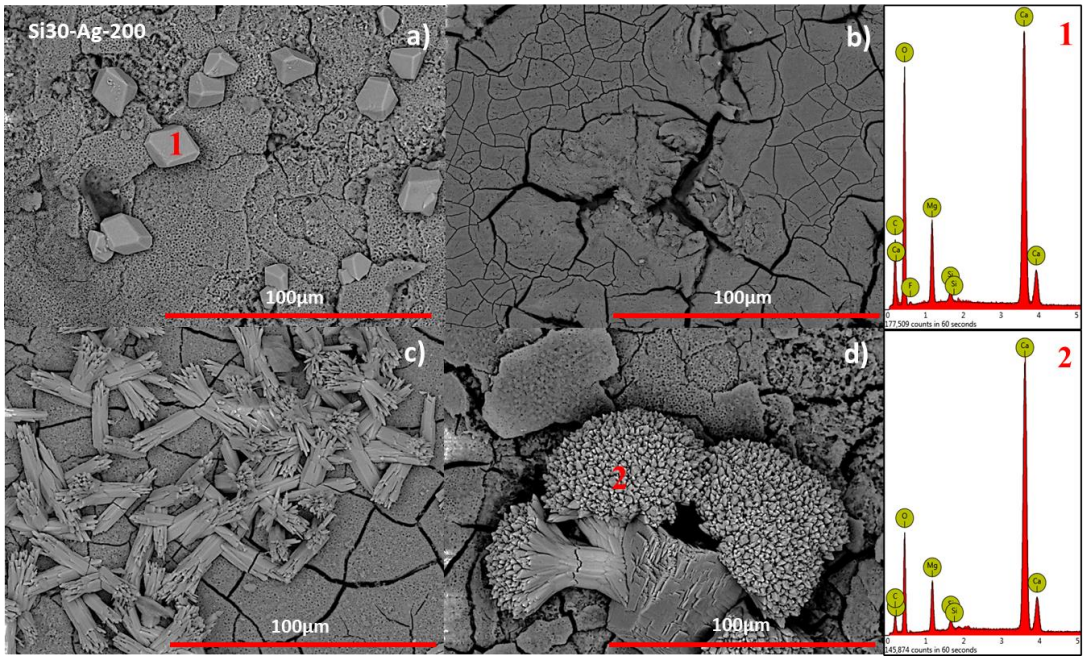

Figure 4.30 SEM images of the selected surface samples after immersion in Ringer solution (a) first, b) 5th, c) 10th and d) 15th day of the immersion) and EDS analysis of the precipitators (1 and 2 – places of the element analysis detection)

The cellular metabolic activity of the obtained coatings was evaluated by resazurin reduction assay. Silver addition did not show positive results on bioactive properties of the coatings. Also, DAPI staining expressed that AgNPs incorporation did not significantly influence cell adhesion and distribution over the samples. Only Si10-Ag-150 samples demonstrated low metabolic activity of cells compared to 200 and 225 V regimens.

The time-dependent antibacterial test demonstrated that AgNPs incorporated into the coatings enhance both bioinertness and anticorrosive behavior while providing sustained antibacterial activity. The mechanism underlying this antibacterial effect can be attributed to the chemical composition of the coatings and the pH changes in the microenvironment near the samples.

Firstly, elevated pH levels are known to contribute to stronger antibacterial activity, consistent with literature findings [152]. Due to the porous and cracked structure of PEO coatings, extending the incubation period in bacterial suspension from 6 to 24 hours allowed more intensive penetration of water and salts beneath the coating, leading to greater exposure of reactive magnesium. This, in turn, accelerated magnesium degradation and resulted in increased local pH values [153]. The observed enhancement in antibacterial activity over time is likely due to this elevated pH. Additionally, the release of magnesium ions may contribute further to antibacterial effects through alkalinization of the surrounding medium.

Cytotoxic effects were also confirmed by DAPI staining analysis. The presence of AgNPs enhanced the bioinertness of the surface toward bacterial strains, likely due to modifications in the chemical structure of the coating.

Secondly, XPS analysis presented in our study [155] revealed that silver is incorporated into the coating primarily in the form of silver oxide. Upon contact with inorganic salts present in Ringer's solution and bacterial culture media, Ag^+ ions are released from the PEO-coated surfaces, as confirmed by ICP analysis (Table 4.12).

PEO coatings containing AgNPs exhibited superior anticorrosive performance due to the compactness of the oxide layer. Their antibacterial efficacy was attributed to the continuous release of Ag^+ ions, which disrupt bacterial membranes, inhibit essential enzymatic activity, and interfere with DNA replication—ultimately suppressing bacterial growth and viability [156], [157].

4.3 Plasma electrolytic oxidation coatings on Mg in phosphate-based solutions

4.3.1 Results

Based on literature reviews, I found the gaps of chemical compositions of phosphates and silicates that can be used for creating coatings according to the goal of the PhD work. The proposed compositions are presented in Table 3.2. The obtained voltage–time curves of the PEO process were analyzed to determine the maximum applicable voltage for each electrolyte (Fig. 4.31).

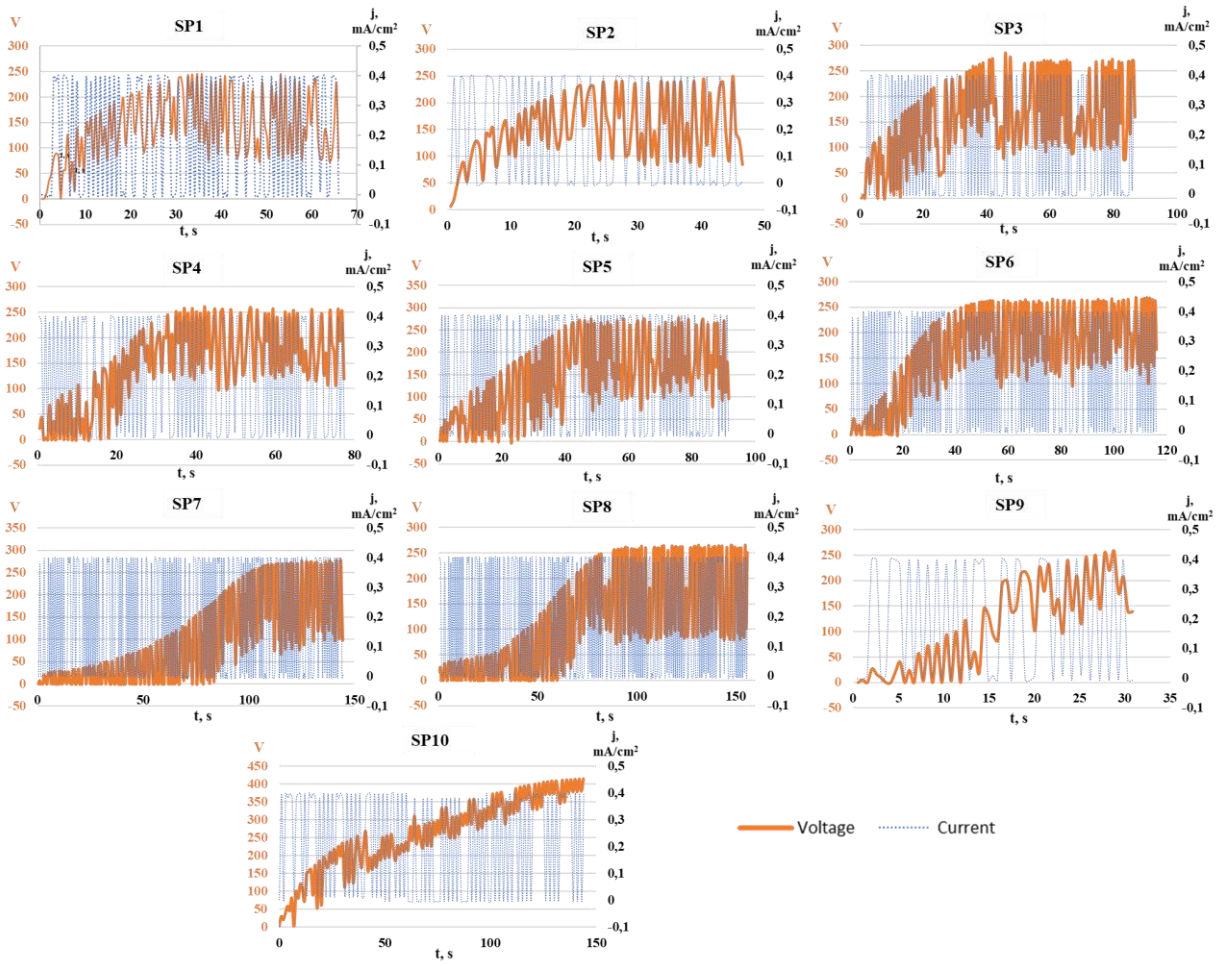

Figure 4.31 Graphs of voltage and current versus time for a PEO process pertaining to tasted solutions

Each electrolyte was subjected to preliminary test runs to establish its breakdown behavior and to define the range of stable working voltages. The working voltage range was defined as the interval where uniform microdischarges occurred without evidence of coating delamination, substrate overheating, or electrolyte instability. The graphs show the characteristic voltage and current flows of the plasma electrolytic oxidation process for each electrolytic system. Obtained

graphs show resultant voltage value for each solution. The voltage could increase up to 400V and the current remained rather stable. The chosen voltages were noted in Table 3.5.

Figure 4.32 illustrates the evolution of voltage and current density during the PEO process for P-Si-based electrolytes.

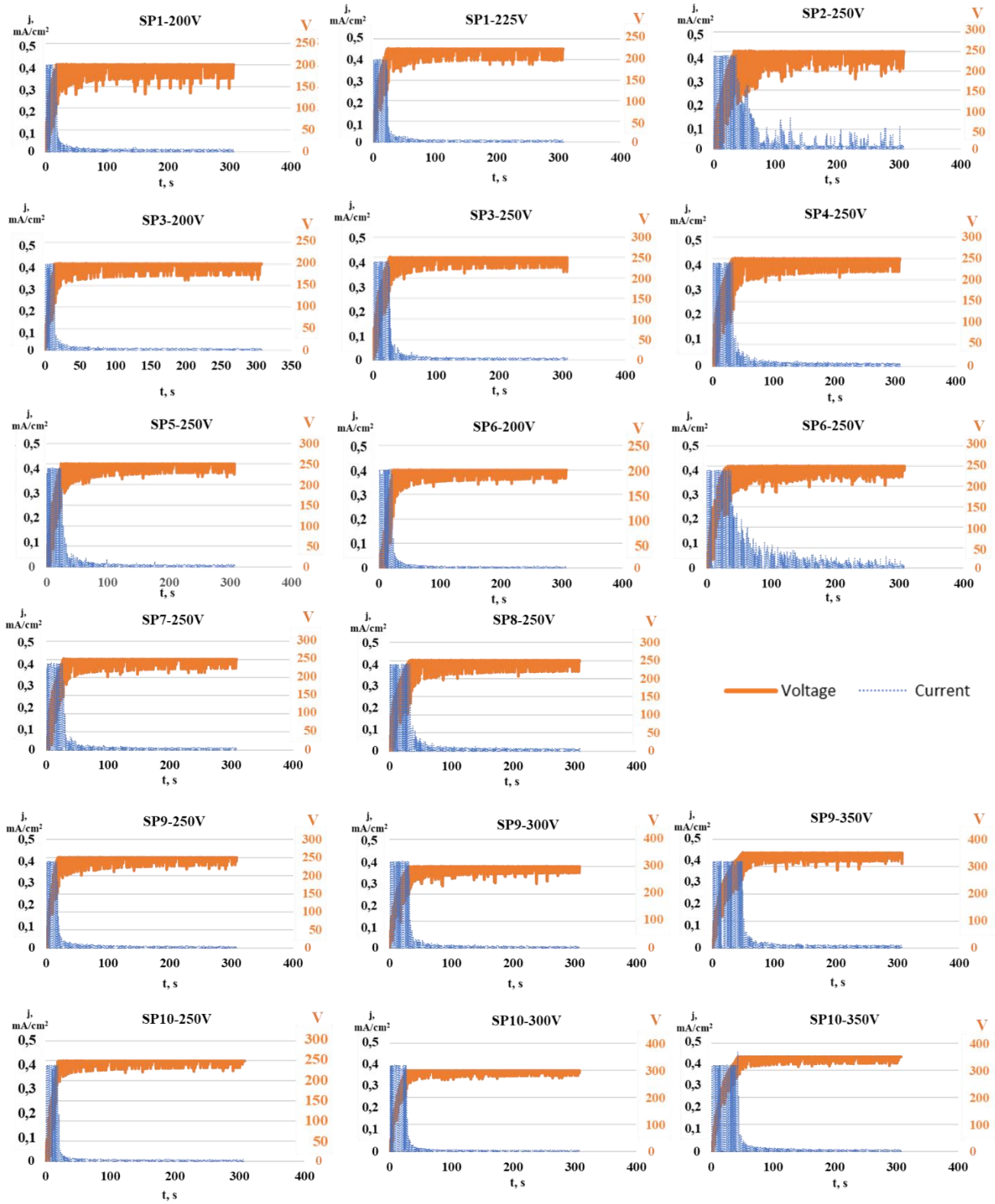

Figure 4.32 Voltage and current density evolution as a function of PEO processing time for P-Si-based electrolytes

Analysis of the curves indicates that the voltage reached and maintained the desired level over an extended period. The current decreased to a minimum value. A change attributed to the development of an oxide layer, which inherently possesses poor conductivity. It is important to note that the oxide layer continued to form until this minimum current level was reached.

According to the obtained graphs it was clearly visible the first stage anodization. The time of increasing in voltage is differ for different electrolytes. The slope of the curves steeper for graphs obtained at higher voltage. The rate of the initial voltage rise indicates a rapid passivation of the sample surface at the beginning of the oxidation process [158]. Table 4.13 showed the time of stabilization of the voltage rate for tasted samples. The time of stabilization increased with increasing voltage.

Table 4.13 The time of voltage increase up to critical value, s

V\Sample no	**SP1**	**SP2**	**SP3**	**SP4**	**SP5**
200	18.1±0.6	15.1±0.6	14.4±1.0		
225	22.6±0.1				
250			30.4±4.1	30.3±2.9	28.0±5.0
V\Sample no	**SP6**	**SP7**	**SP8**	**SP9**	**SP10**
200	24.5±1.6				
250	38.8±2.5	27.4±0.6	31.5±1.6	19.2±1.2	21.4±2.4
300				31.8±0.1	28.8±1.3
350				49.1±1.1	44.0±1.2

Due to the differences in the voltages of the electrolytic systems, the resulting morphologies of the produced samples were investigated. Defined applied voltages were investigated for each electrolyte. Value close to the breakdown voltage and the highest possible voltage were used to observe the surface morphology. The SEM images of the surfaces are shown in Fig. 4.33. The surface morphology of the PEO coatings has typical porous structures with a variable diameter of pores.

SEM investigation allows evaluation of the quality surface morphology of the coatings and defines appropriate regimes. There were no observations of the well-built morphology of the PEO layer for low applied voltages for some electrolyte solutions. The samples SP2-150, SP3-150, SP4-200, SP5-200, SP7-200, SP8-200, SP9-200 and SP10-200 were removed from further investigation (Fig. 4.34).

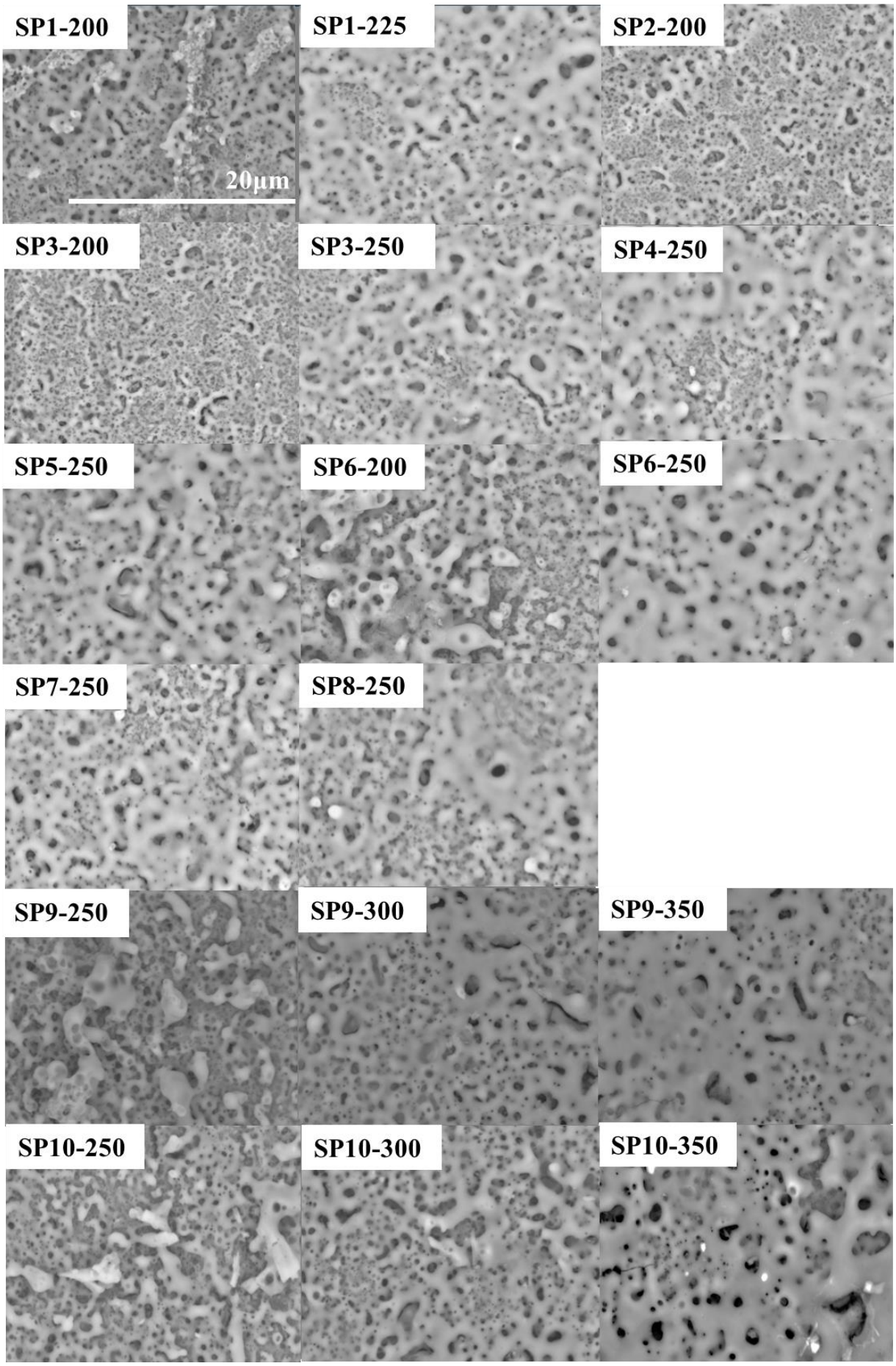

Figure 4.33 Surface morphology of the PEO coatings obtained in P-Si-based electrolytes.

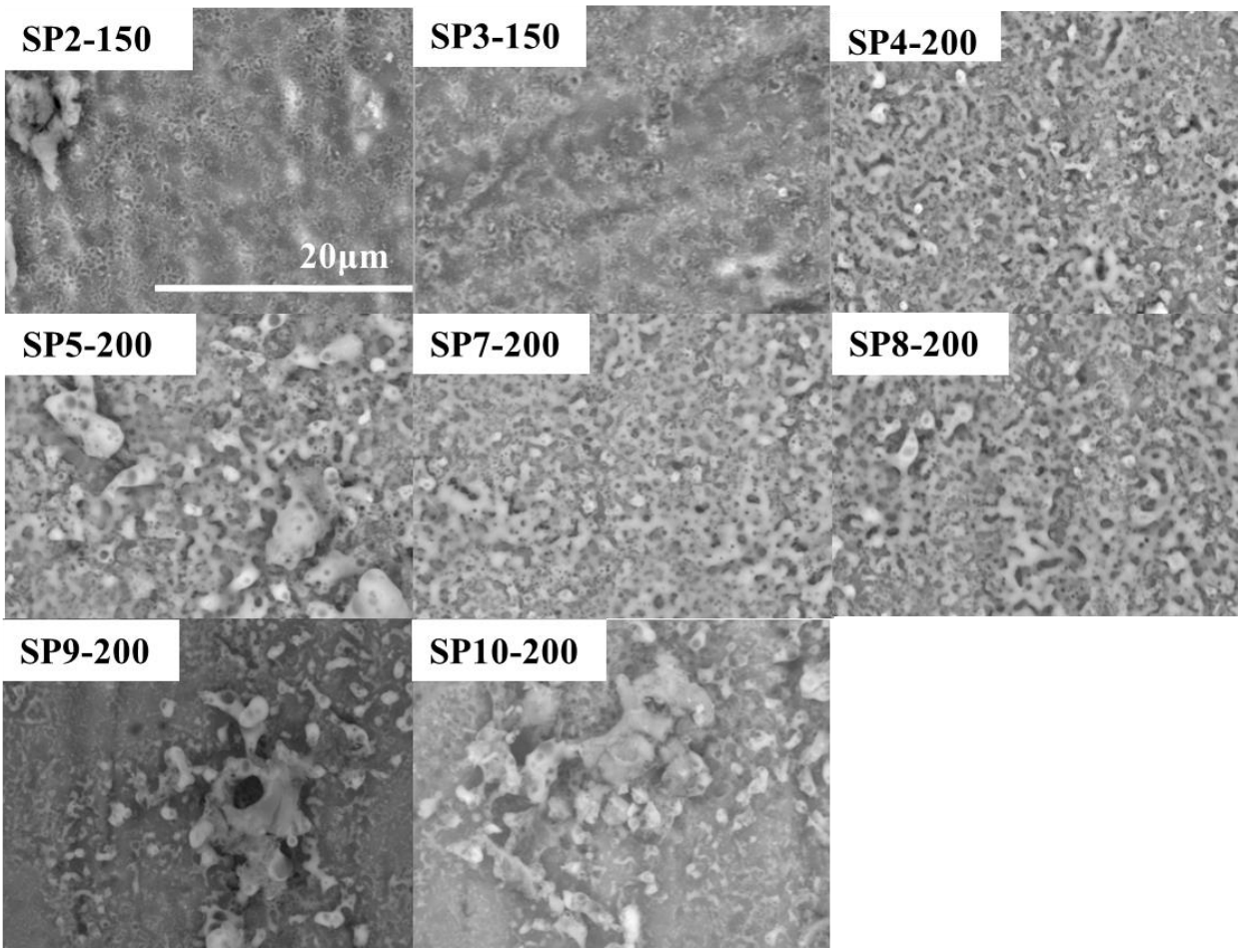

Figure 4.34 Surface morphology of the PEO coatings obtained in P-Si-based electrolytes and removed from experiment.

PEO coatings are characterized by the net-like (scaffold) surface morphology of the PEO coatings formed on the magnesium substrate. This morphology containing a network of micropores. Most of the pores were more spherical; however, some irregularly shaped and lenticular pores were also observed. Although, the coatings obtained at low voltage characterized by closed pores.

The coatings appeared well-formed, with visible interconnected oxide structures and varying degrees of porosity. Some samples, such as SP3-200 and SP5-250, show a more homogeneous distribution of pores, suggesting better uniformity. Low processing parameters (SP1-200, SP6-200) resulted in more pronounced structural inhomogeneity. The similar surface structure showed the coatings for SP9 and SP10 solutions at 250 voltages. However, voltage increasing had positive influence on the surface morphology.

Table 4.14 summarized key parameters, including pore size and the number of pores. Coatings at lower voltage exhibited similar pore size. SP1-225, SP9-300 and SP10-300 samples

showed the largest pore size. There was detected that voltage increasing decrease the number of pore size for samples SP1, SP3, SP6, SP9 and SP10.

Table 4.14 Data on pore analysis of the PEO coatings obtained in P-Si-based electrolytes P.s. – pore size, Np – number of the pores

Sample no	V	P.s., μm²	Np per μm²	Sample no	V	P.s., μm²	Np per μm²
SP1	**200**	0.09±0.12	0.7	**SP7**	**250**	0.1±0.2	0.9
	225	0.19±0.4*	0.5	**SP8**	**250**	0.13±0.3	0.7
SP2	**200**	0.1±0.12	0.9		**250**	0.13±0.3	1.1
SP3	**200**	0.05±0.18	2.1	**SP9**	**300**	0.2±0.5*	0.7
	250	0.08±0.16	0.6		**350**	0.16±0.4	0.6
SP4	**250**	0.08±0.15	0.3		**250**	0.08±0.2	1.3
SP5	**250**	0.1±0.2	0.4	**SP10**	**300**	0.2±0.4*	0.42
SP6	**200**	0.05±0.1	1.23		**350**	0.13±0.3	0.7
	250	0.2±0.4	0.31				

The Figure 4.35 presents a set of histograms showing the pore size distribution for PEO coatings obtained on SP1-SP10. Each histogram provides the frequency (in percentage) of pores corresponding to specific pore size ranges (in μm²). The highest bar corresponds the smallest pore size range 0-0.1 μm² for all samples. The amount of small pores decrease with increasing the voltage that characterized for SP1, SP6, SP9 and SP10 samples group. Larger pores are less frequent, with their occurrence reducing significantly as pore size increases.

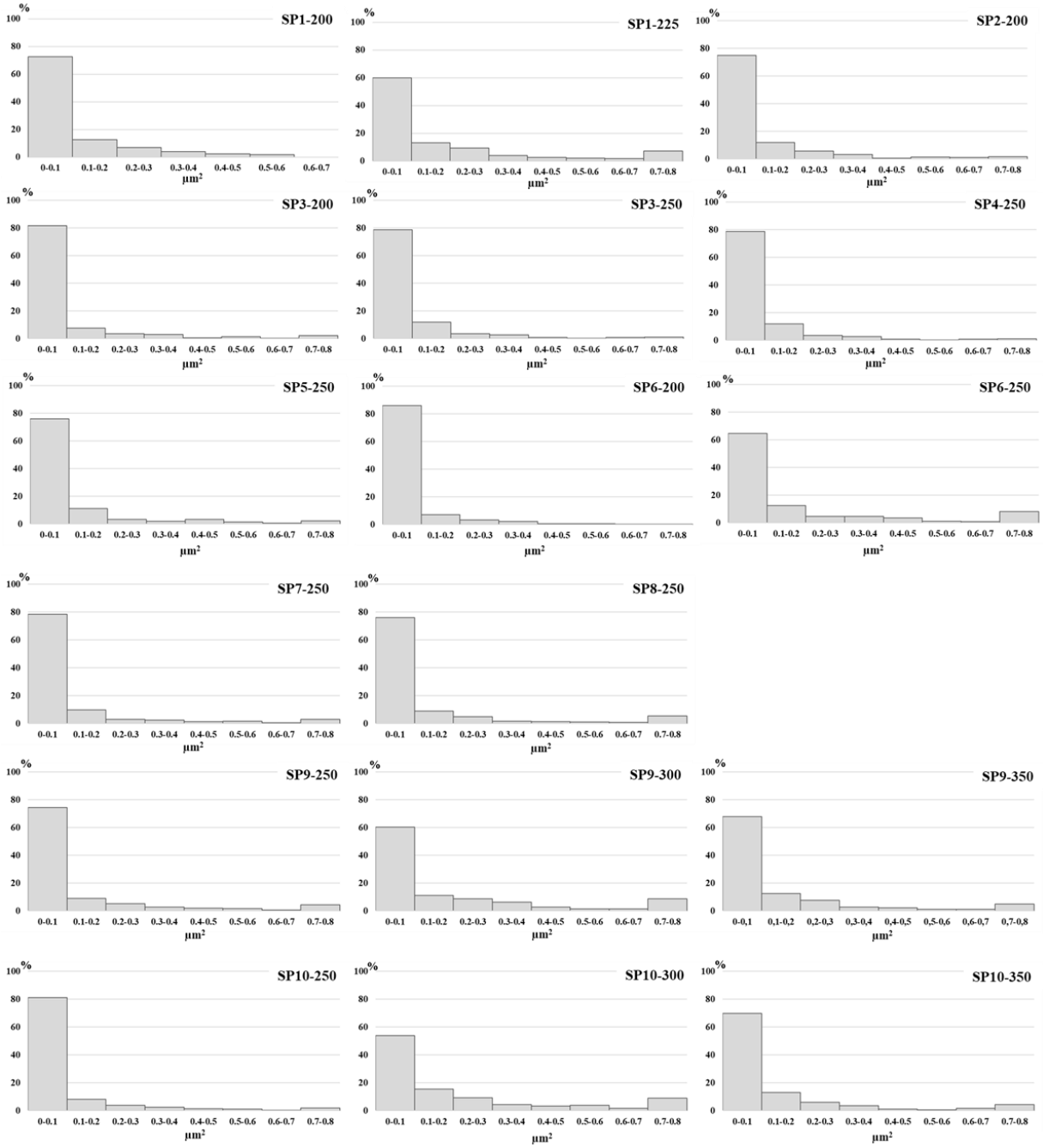

Figure 4.35 Pore size distribution on ceramic coatings formed after PEO in P-Si-based electrolytes.

The provided Figure 4.36 contains a series of cross-sectional SEM images that represent microstructural characteristics of the SP1-SP10 coatings. Cross-sectional images of the obtained coatings revealed a significant variation in morphology. At 200 V, the coatings were characterized by a predominantly compact structure with only a few pores. Increasing the voltage to 250 V led to a greater coating thickness, accompanied by larger inner pore sizes and a higher pore density.

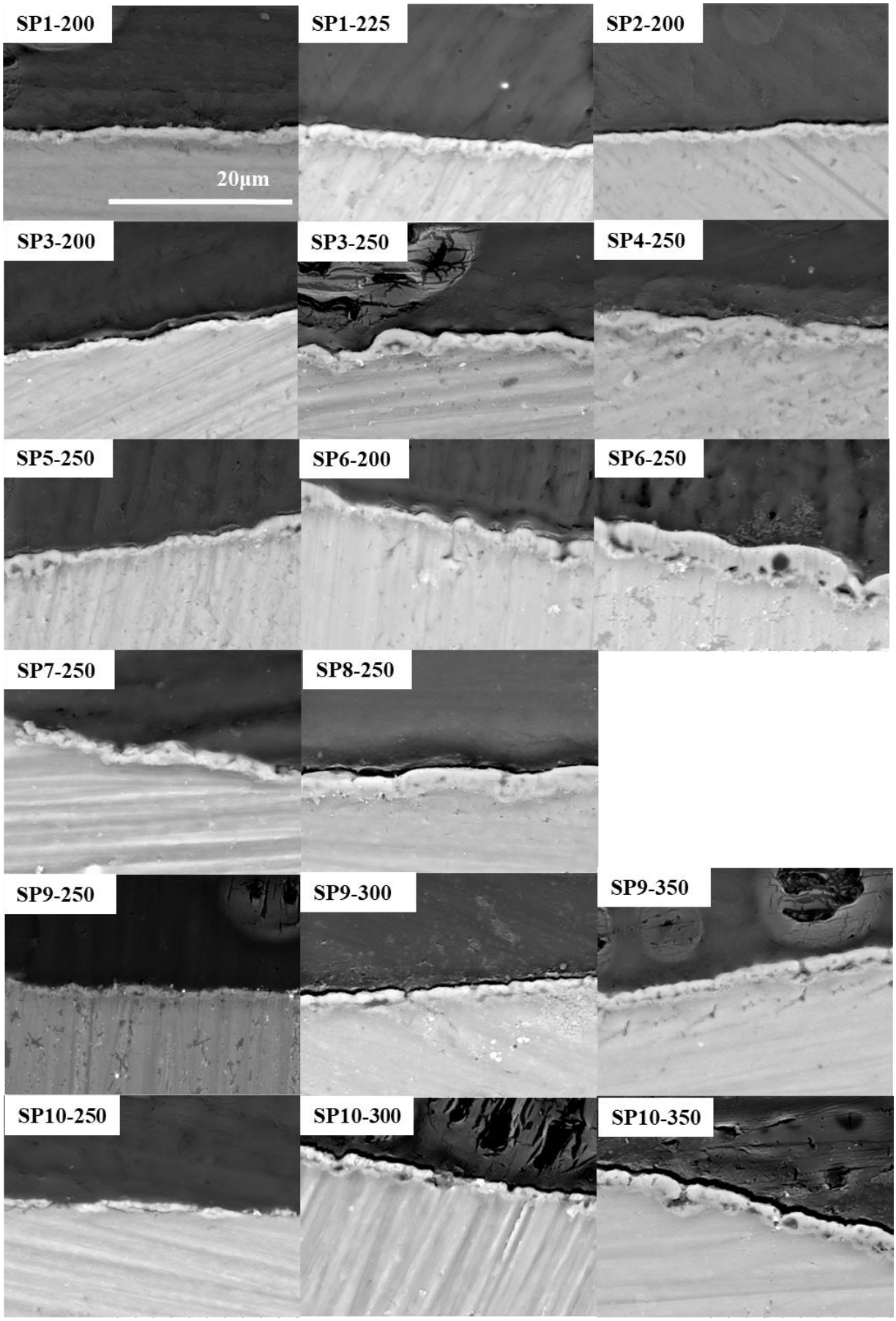

Figure 4.36 Scanning electron micrographs showing the cross-section of the PEO coatings obtained in P-Si-based electrolytes

Table 4.15 presents the results of thickness measurements for the coatings obtained from SP1–SP10 samples. The values are expressed as mean ± standard deviation, with * indicating statistically significant differences compared to the baseline group (200 V, $p < 0.05$). A clear influence of the applied voltage on coating thickness was observed in the SP3, SP6, SP9, and SP10 sample groups. In general, higher voltages resulted in thicker coatings, with thickness values ranging from 1.6 to 3.8 μm. However, for SP9 and SP10, the coating thickness at 250 V was lower compared to the other samples.

Table 4.15 Thickness of the PEO coatings formed in P-Si-based electrolytes (μm), *p<0.05

V\Sample no	**SP1**	**SP2**	**SP3**	**SP4**	**SP5**
200	1.2±0.3	0.8±0.3	0.8±0.3		
225	1.7±0.4				
250			2.0±0.4*	2.0±0.4	1.6±0.6
V\Sample no	SP6	SP7	SP8	SP9	SP10
200	1.9±0.7				
250	3.8±0.7*	1.8±0.4	2.5±0.3	0.9±0.2	0.9±0.2
300				1.2±0.4	1.2±0.2
350				2.3±0.6*	1.8±0.4*

3D reconstruction was applied for characterization the surface topography of the P-Si-based coatings (Fig. 4.37). The surfaces characterized high development morphology for coatings with higher applied voltages. It was clear visible for SP4-250, SP6-250, SP7-250 and SP8 samples. The series samples SP9 and SP10 showed dependence surface relief on applied voltages. Higher voltages leading to increased visual surface roughness.

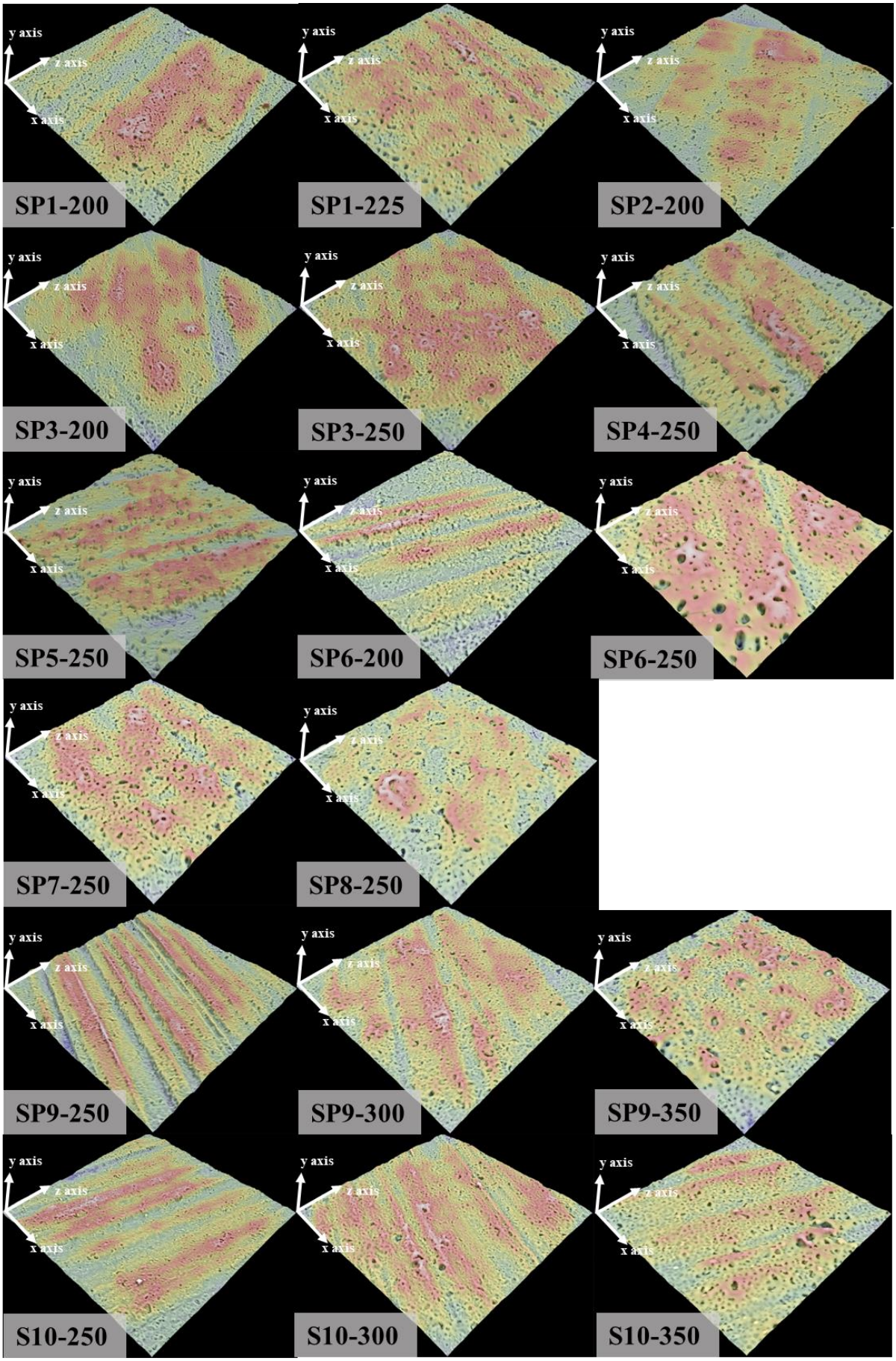

Figure 4.37 3D surface visualization of PEO coatings obtained in P-Si-based electrolytes

Table 4.16 showed the parameter of the roughness for PEO coatings formed in P-Si-based electrolytes, with p<0.05. Values are presented as mean ± standard deviation, and * denotes statistically significant differences compared to the baseline group (200 V). Table observation detected the surface roughness generally had similar value. However, the surface of SP4-250, SP6-250 and SP8-250 samples displayed the highest roughness compared to other coatings.

Table 4.16 Ra roughness parameter of the PEO coatings formed in P-Si-based electrolytes, p<0.05

V\Sample no	**SP1**	**SP2**	**SP3**	**SP4**	**SP5**
200	0.28±0.03	0.26±0.02	0.25±0.01		
225	0.28±0.02				
250			0.34±0.02	0.4±0.04*	0.35±0.03
V\Sample no	**SP6**	**SP7**	**SP8**	**SP9**	**SP10**
200	0.3±0.04				
250	0.62±0.07*	0.36±0.01	0.38±0.01*	0.33±0.02	0.24±0.04
300				0.36±0.03	0.24±0.02
350				0.34±0.01	0.28±0.01

Table 4.17 compiled the static water contact angle measurements for PEO coatings formed in P-Si-based electrolytes under different applied voltages.

Table 4.17 Static water contact angle for the PEO coatings formed coatings obtained in P-Si-based electrolytes, p<0.05

V\Sample no	**SP1**	**SP2**	**SP3**	**SP4**	**SP5**
200	33±5	31±4	30±5		
225	25±7				
250			21±3	31±4	23±2
V\Sample no	SP6	SP7	SP8	SP9	SP10
200	32±7				
250	38±7*	30±3	23±4	38±10*	34±6
300				37±6	29±3
350				30±6	20±3*

The values are presented as mean ± standard deviation, and p<0.05. The results indicated that all surfaces exhibited hydrophilic properties, with contact angles ranging from 20° to 38°. The

SP6-250 and SP9-250 surfaces demonstrated the highest contact angle values, while the SP10-350 surface exhibited the lowest.

Figure 4.38 illustrates the dynamic water contact angle behavior of PEO coatings formed in P-Si-based electrolytes at different applied voltages. The obtained graphs confirm the hydrophilic nature of the coatings, as the contact angle values gradually decreased over time for all samples. For most coatings, the water droplet spread across the surface within approximately 100 seconds. However, the SP8-250 sample exhibited notably high sorption properties, which accelerated the water spreading process.

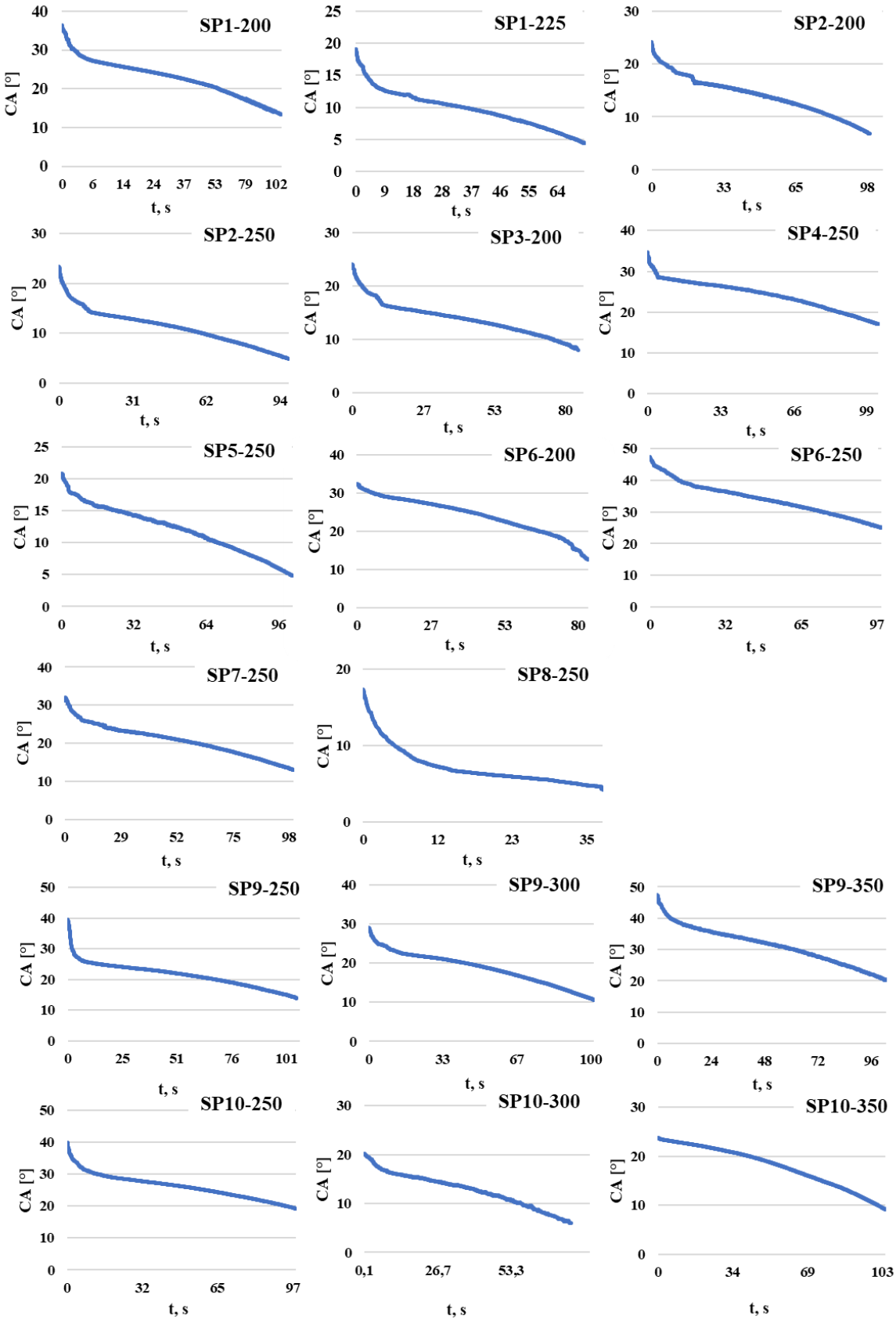

Figure 4.38 Dynamic water contact angle of the PEO coatings formed in P-Si-based electrolytes

The composition of the coatings was analyzed using EDX measurements, and the results are summarized in Table 4.18. This table provides data on magnesium (Mg), silicon (Si), sodium (Na), oxygen (O*), phosphorus (P), and calcium (Ca). Additionally, the Mg/Si ratio was calculated to emphasize the relative magnesium-to-silicon content in the coatings. Electrolytes for samples SP1–SP8 consisted of dissolved sodium silicate, while SP10 electrolytes included calcium-based particles. The results indicate that elements from the electrolyte are incorporated into the coating during processing. Was detected that magnesium content decreases significantly with increasing applied voltage, while silicon and phosphorus content increase correspondingly. This pattern of reduced Mg and increased Si is consistent across different solution groups. The increasing silicon concentration in the electrolytes leads to a higher volume of silicates in the coating, which is particularly evident in the SP4-250 sample. The highest phosphorus content was observed in the coatings for SP6-250, SP9-350, and SP10-350.

Table 4.18 Semi-quantitative EDX analysis of the PEO surface coatings on magnesium, at.%

Sample no	V	Mg	Si	Na	O*	P	Ca	Mg/Si
SP1	200	39	4	1	53	3	-	9,1
	225	33	5	1	57	4	-	6,2
SP2	200	43	4	0,2	51	1	-	9,7
SP3	200	42	4	0,3	52	2	-	10,5
	250	29	7	1	60	3	-	4,5
SP4	250	25	8	2	61	4	-	3,0
SP5	250	28	6	2	60	4	-	4,5
SP6	200	39	2	1	54	5	-	20,1
	250	23	3	3	64	7	-	7,2
SP7	250	27	6	2	61	4	-	4,3
SP8	250	27	6	2	61	4	-	4,3
SP9	250	45	-	-	51	3	-	-
	300	35	-	-	59	6	-	-
	350	30	-	-	62	7	-	-
SP10	250	45	0,3		52	3	0,1	180
	300	36	0,3	0,2	58	5	0,1	105
	350	30	1,1	0,5	61	7	0,4	27

EDX maps investigation identified the element distribution of the obtained PEO coatings (Fig. 4.39). P was detected in all coatings, indicating that elements are uniformly incorporated into the coating. However samples obtained at higher voltage had more poweful signal. Also, Si was identified in all coatings, that have silicates in electrolyte btheesides SP10-250 sample. The signal of the Si- elemets was stronger at higher applied voltage. The presence of Ca was characteristic of surfaces SP10 which coincides with the electrolyte composition.

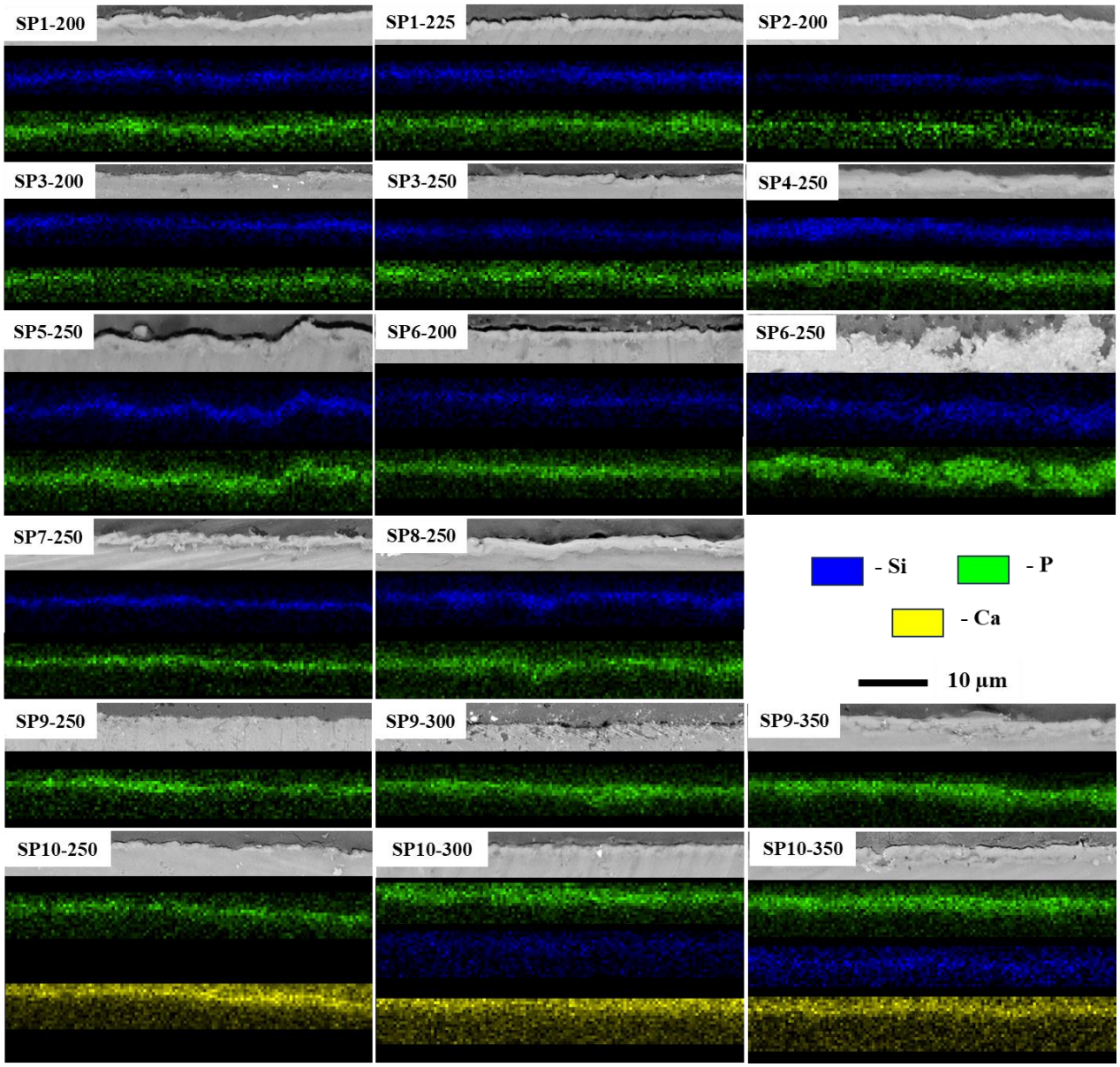

Figure 4.39 Cross section elemental distribution map of P-Si-based PEO coatings

Based on morphological and chemical properties of the coatings the samples presented in the Table 4.18 were chosen for ICP investigation. Figure 4.40 visualize the surface morphology of the P-Si-based samples after ICP investigations. Considering the detailed analysis from the SEM images, it can be concluded that corrosion occurred on the magnesium samples during 42 hours for all types of the surfaces. All surfaces retain a porous structure except for the SP9-300 sample. The structure of the coatings becomes smoother except for the SP2-250 coating. Fine-crystalline corrosion products are observed on SP8-250 coating and for SP9 and SP10 samples. Also, SP1-SP6 coatings characterized by cracks appearance.

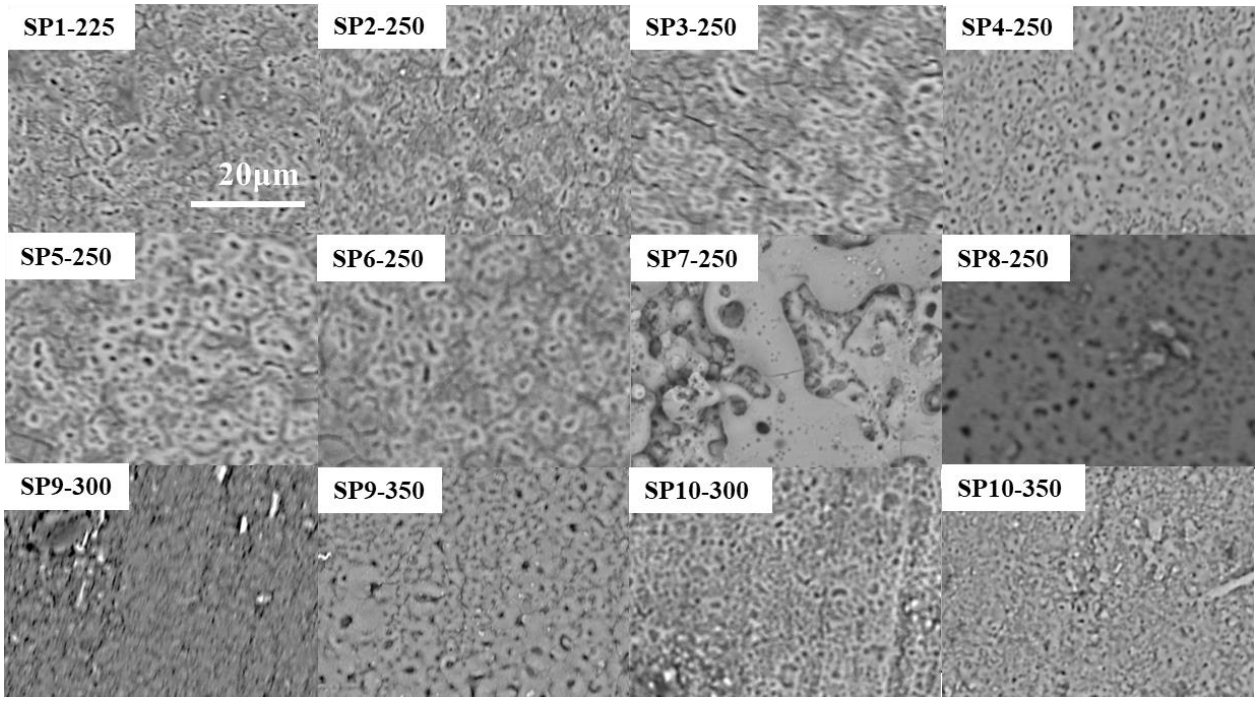

Figure 4.40 SEM images of the P-Si-based electrolytes after ICP measurements

Collected solutions after immersion test were evaluated by ICP analysis. The ion release characteristics of magnesium (Mg), silicon (Si), Phosphorous (P) and Calcium (Ca) from coatings were detected (Table 4.19). The data, expressed in milligrams per cubic decimeter ($mg \cdot dm^{-3}$), reflects the mean values and associated standard deviations (±SD) for each sample.

The Mg release did not vary among the samples. The concentration of released ions was higher upon the time. The same situation was observed by other elements as well. Their concentration also increased with immersion time. The amount of phosphorus and silicon in the tasted liquid was higher for samples where these elements were more abundant in the coating, such as SP4-250.

Table 4.19 The results of ICP analysis of the ion release characteristics ($mg \cdot dm^{-3}$)

Sample no	t, h	Mg	P	Si	Ca
SP1 250	1	2.6±0.13	0.5±0.03	0.04±0.01	-
	22	3.0±0.02	0.24±0.01	0.11±0.02	-
	42	6.4±0.2	0.42±0.02	0.1±0.02	-
SP3 250	1	2.8±0.3	0.4±0.02	0.03±0.02	-
	22	3.2±0.6	0.3±0.02	0.8±0.01	-
	42	7.0±0.4	0.5±0.03	1.2±0.3	-
SP4 250	1	4.1±0.3	0.6±0.02	0.7±0.02	-
	22	6.2±0.5	1.0±0.04	1.2±0.3	-
	42	8.1±0.3	1.2±0.03	2.3±0.5	-
SP5 2 50	1	2.7±0.12	0.2±0.02	0.05±0.01	-
	22	5.13±0.07	0.3±0.01	0.11±0.02	-
	42	7.01±0.13	0.5±0.03	0.1±0.02	-
SP6 250	1	6.75±0.4	1.08±0.04	<0.01	-
	22	8.01±0.3	0.9±0.02	0.03±0.02	-
	42	11.0±0.4	0.87±0.01	0.06±0.01	-
SP7 250	1	1.4±0.04	0.3±0.02	0.07±0.01	-
	22	3.9±0.02	0.34±0.01	0.06±0.01	-
	42	7.7±0.2	0.7±0.03	0.2±0.01	-
SP8 250	1	3.5±0.04	0.6±0.02	0.01±0.01	-
	22	4.2±0.07	0.3±0.01	0.12±0.01	-
	42	18.5±0.6	1.04±0.05	0.1±0.01	-
SP9 300	1	1.5±0.06	0.1±0.01	-	-
	22	4.4±0.04	0.3±0.02	-	-
	42	8.0±0.4	0.5±0.01	-	-
SP9 350	1	2.2±0.04	0.04±0.01	-	-
	22	15.3±0.04	0.05±0.04	-	-
	42	8.3±0.04	0.6±0.02	-	-
SP10 300	1	3.5±0.04	0.2±0.01	0.1±0.03	0.01±0.01
	22	4.1±0.1	0.2±0.01	0.1±0.01	0.06±0.13
	42	14.1±0.1	0.4±0.01	0.2±0.01	0.09±0.01

Sample no	t, h	Mg	P	Si	Ca
SP10 350	1	2.6±0.04	0.14±0.01	0.12±0.003	0.015±0.001
	22	6.6±0.08	0.2±0.01	0.16±0.01	0.06±0.01
	42	24.0±0.5	0.3±0.01	0.223±0.08	0.05±0.01

Cell culture experiment was conducted to evaluate cytotoxic properties of the SP6 250, SP7 250, SP8 250, SP9 (300,350), SP10 (300,350) samples compared with pure Mg. The experiment was conducted into 24 well cell culture plates. The Mg specimens were placed into this plate. Cells were seeded on the samples and control wells in concentration of 2×10^4 cells·cm^{-2}. The samples were cowered with full medium.

The Figure 4.41 showed the values of reassuring reduction for first day of incubation with U2OS cells. The results of the assay indicated the high level of reassuring reduction for all samples especially for control. The signal of the fluorescence decreased also for all samples on third day of incubation. It should be noted that level of reassuring reduction became lower 5% for SP7-250V, SP8-250V, SP9-300V, SP10-300V and SP10-350V on 3-d day of incubation and decrease up to 0 % for 6-th day of incubation (Fig.4.42). Control samples on third day also showed the highest level of reassuring reduction. However, at 6 day of incubation it reduces up to 10%. Sample SP9-350 exhibited a reassuring reduction of 29±1.27% initially. By the 6th day of immersion, this value decreased to 9±0.4%.

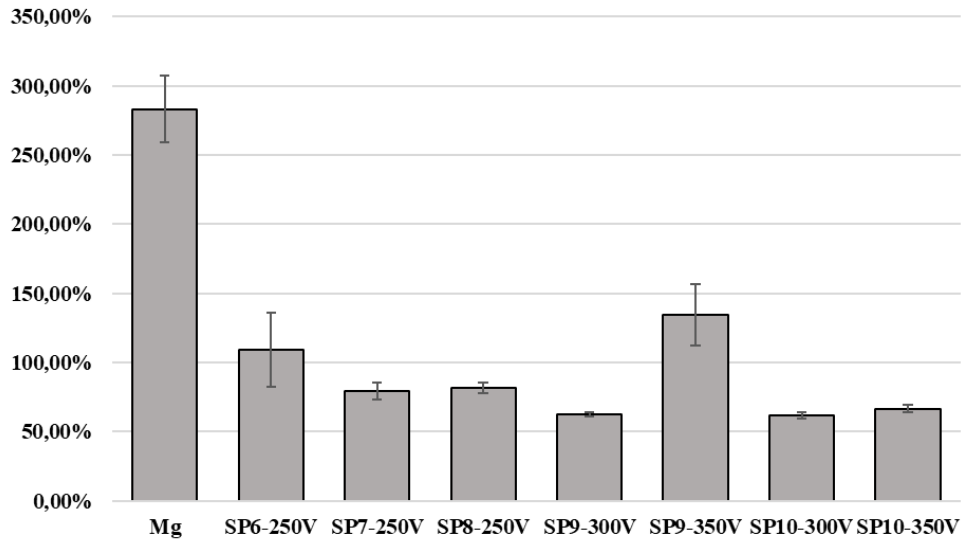

Figure 4.41 Cell viability of PEO coatings examined on 1 day by the resazurin reduction assay

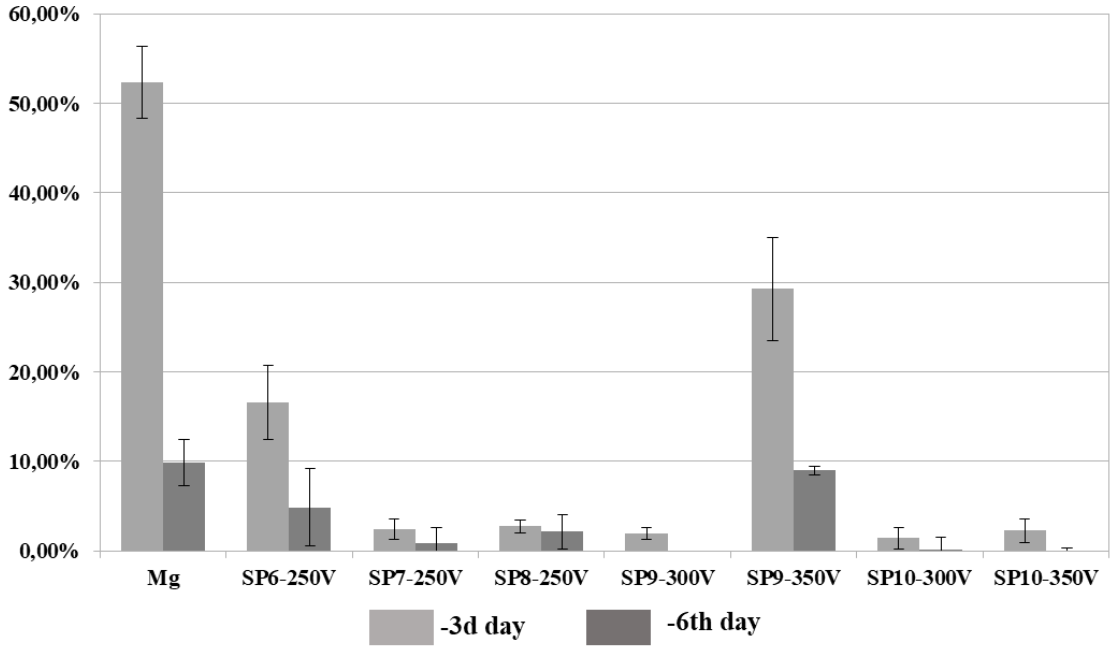

Figure 4.42 Cell viability of PEO coatings examined on 3d and 6th day by the resazurin reduction assay

Fluorescent staining (Fig. 4.43) was used to explain the results of cytotoxicity assays. Fluorescent staining was used to support the results of the cytotoxicity assays. This method was applied to the control samples and SP9-350 to confirm or refute the findings obtained from the resazurin assay. ActinRed and Hoechst fluorescent dyes were used to detect cells on the surface. This is a commonly used combination in cell imaging to visualize cytoskeletal architecture and nuclear morphology. Actin was stained red, typically using phalloidin conjugated with a red fluorophore. Nuclei were stained with Hoechst, a blue-fluorescent dye that binds to DNA. As seen in Figure 4.43, no live cells were observed; only cell nuclei were detected, which can confirm cell adhesion on the beginning of the experiment.

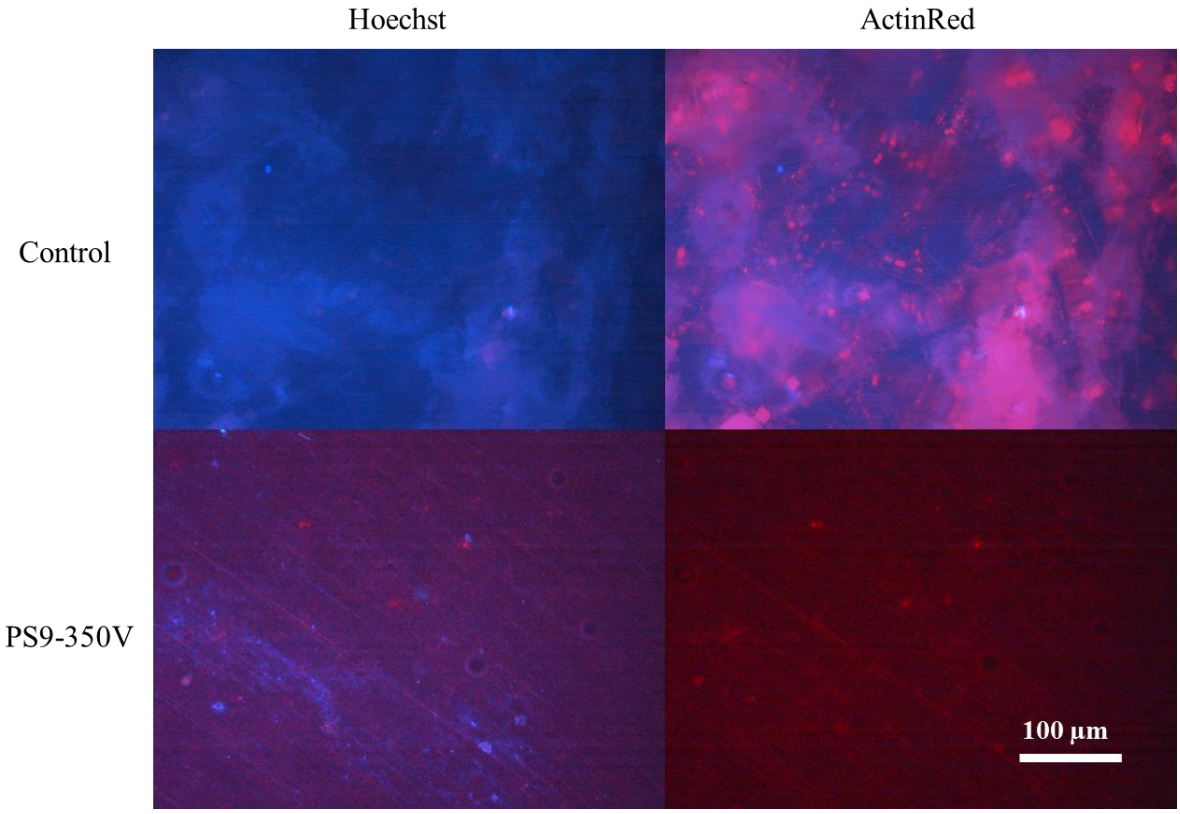

Figure 4.43 Fluorescence staining of the MG63 cells monolayer on the PEO coatings. Magnification: 100 times

The ActinRed is bound specifically to the cell's fibronectin (F-actin) to exhibit orange-red fluorescence; the nuclei showed blue fluorescence after counterstaining with Hoechst. Scale bar: 10 µm. The morphology of the cells was observed under an inverted microscope.

4.3.2. Discussion

The voltage-time plots (Fig 4.32) characterize the phenomena occurring at the electrode/electrolyte interface. These stages include normal anodizing, spark anodizing, micro-spark oxidation, and arc oxidation. According to the obtained data, the time required to reach the critical voltage primarily depends on the applied voltage. Higher voltages result in a prolonged duration before reaching the critical voltage. PEO coatings obtained at lower voltages were primarily characterized by finer discharge channels, whereas larger channels were observed at higher applied voltages. The average pore size in the PEO coating increases with the applied voltage for the coatings SP1, SP9, and SP10 [159].

Usually, the PEO process has been done in alkaline electrolytes with various additives. Alkaline were used as pH and solution conductivity adjuster. For example, Ko et al. showed that the coatings on AZ31 alloy that were developed in an electrolyte with high KOH concentrations

present high corrosion resistance. Among additives there are many compounds like phosphates, silicates and flourides. Quasemi et al. have reported that the presence of SiO_3^{2-} anion results in thickness increase and corrosion resistance of the coating in comparison with PO_4^{3-} and AlO^{2-} anions [160]. The prsence of calcium, phosphorus, and fluoride ions increase in bioactivity of the coating. Valerio et al. showed that a silicon-ion was containing coating results in increasing the multiplication and secretion of collagen and higher cell survival in comparison with the coating without silicon [78]. The phospate as additives showed is the most effective in strengthening the coating compactness and thickness [161]. Added to this, the presence of compounds containing Ca, Si, and P [79], results in an increase in corrosion resistance and hydroxyapatite formation of AZ31 alloy. Also, the presence of Na, Si, and Ca [162] results in an increase in corrosion resistance and hardness value, added to better formation of hydroxyapatite in SBF comparing with the titanium substrate.

Therefore, alkaline silicate electrolyte was used for PEO treatment. We scrutinized the general influence of phosphate additives in electrolytes during the PEO process on morphologies, compositions, and corrosion protection of oxide coatings.

PEO of Mg in P-Si-based electrolyte developed highly porous oxide coatings. The anodized surfaces exhibit a characteristic of dispersed pores, ranging mostly in areas up to 0.1 μm^2. The micropores in the range of 0.5–5 μm^2 are formed due to the continuous discharges and breakdown of the coating layers during the oxidation process and the egress of trapped gases from the discharge channels [52][163]. As shown in Fig. 4.33, micropores are unevenly distributed within the ceramic coating, forming micro-pore walls. While this compromises corrosion protection, it may be advantageous for orthopedic applications by enhancing cell adhesion and promoting osseointegration [52]. Coatings produced under higher voltage conditions display a more uniform distributed pore pattern. Moreover, it was observed that increasing the voltage up to 300 V led to an increase in the average pore size, while simultaneously reducing the number of pores per unit surface area (Fig. 4.44). While, by increasing the proportion of phosphate or changing the type of alkaline did not influence the size of pores and the surface roughness.

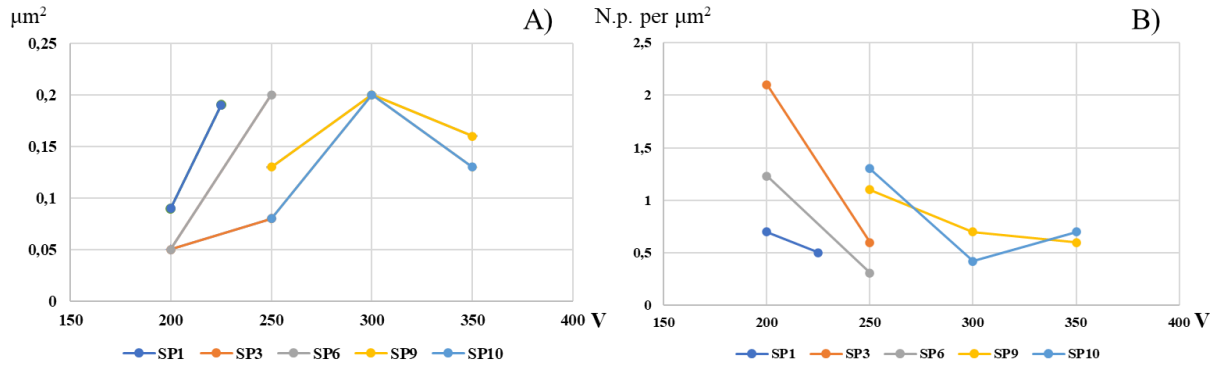

Figure. 4.44 Dependence of A) average pore size and B) number of pores on anodizing voltage

During the formation of the PEO coating, the Mg substrate undergoes a chemical transformation into its oxide. The coating grows simultaneously inward and outward from the bulk metal surface. With the exception of the SP9-250 sample, no discontinuities were observed between the coatings and the substrate, indicating good adhesion [164]. A key observation from the data is the significant variation in coating thickness [165]. Cross-sectional analysis reveals that coating thickness increases with higher voltage. Additionally, high voltage influenced the formation of a relatively compact porous inner region in the SP6-250 samples. Moreover, the surface thickness became thicker with increasing concentration of phosphates. The effect of influences phosphates on the thickness of the coatings were detected also by other researchers [60], [161].

Typically, surface roughness increases with the thickness due to the presence of large channels formed by single sparking [166]. However, this trend is evident only in the SP6-250 coating. The other coatings exhibit similar Ra values despite differences in thickness.

In the studies by Srinivasan et al., it was demonstrated that an increase in the final voltage in a silicate electrolyte led to an increase in the thickness and roughness of the coatings. This is explained by the formation of larger sparks at higher voltages and, accordingly, the hardening of a greater amount of coating compounds [167].

Several clear trends [168], [169] highlight the relationship between processing conditions, such as applied voltage, and the elemental composition of the PEO coatings. The obtained results of the EDX analysis detected that the chemical composition of the coatings depend on the concentration of electrolyte components. EDX-analysis results of coatings revealed the electrolyte components incorporate into coating. With the increasing concentration of silicates, the amount of silicon in the coating also increased. A similar trend is observed for phosphates. Some researchers have observed elemental relationships, noting that an increase in $Na_2SiO_3 \cdot 9H_2O$ corresponds to a

decrease in magnesium and phosphorus [170]. However, in our study, no such correlation between phosphorus and silicon was detected.

Wettability is a key physicochemical property of hard surfaces. The modification of magnesium samples in the proposed electrolytes enhanced surface hydrophilicity, facilitating the penetration of water droplets into the coating. The static contact angle measurements for PEO coatings indicated wettability within the range of 21° to 38°. These findings suggest that PEO-coated surfaces in sodium silicate- and phosphate-based electrolytes exhibit characteristics associated with biocompatibility [57].

The SP9 and SP10 solutions were used to examine the effect of insoluble silicates on coating parameters. Silicate particles did not influence the morphological characteristics of the obtained coatings. However, at 350 V applied voltage, crystals appeared on the surface, indicating a higher degree of silicate particle incorporation (Fig. 4.45). EDX analysis of the region confirmed these findings, showing that higher voltage leads to greater silicate incorporation into the coating (Table 4.18). Moreover, silicates did not interfere with phosphate inclusion. The figure confirms the calcium-silicate nature of the particles. However, the calcium content in the coating remained low under various conditions.

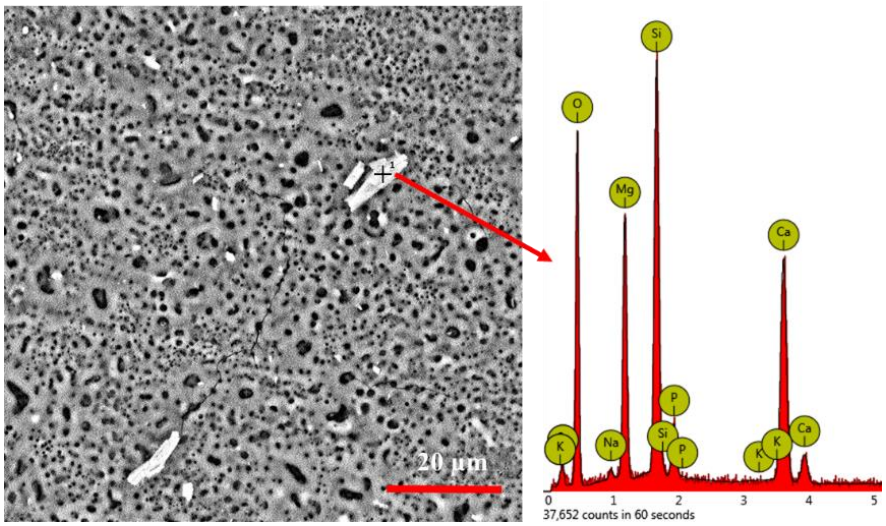

Figure 4.45 SEM images of SP10-350 surface samples and spot EDX analysis of the crystals

An increase in silicates within the SP10 coating leads to a decrease in the contact angle value compared to the SP9 coating, which, in turn, indicates an enhancement of hydrophilic properties. Figure 4.46 clearly showed these visible changes of wettability properties of the tasted samples.

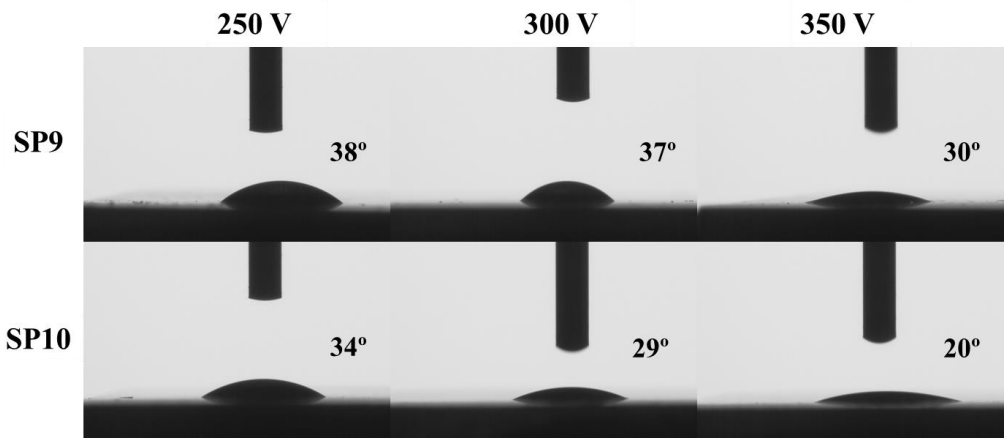

Figure 4.46 Visualisation of contacte angle measurement of the PEO coatings

Our previous results also confirmed the positive effect of silicates on wettability properties of the coatings [72].

ICP analysis is a valuable technique for assessing ion release and surface behavior of coatings on magnesium (Mg) substrates. It enables precise quantification of ions released during corrosion processes, providing insights into the degradation behavior and biocompatibility of Mg-based implants [73].

Coating SP6-250V shows a higher Mg ion release, starting at 6.75 ± 0.4 mg·dm^{-3} at 1 hour and reaching 11.0 ± 0.4 mg·dm^{-3} at 42 hours, suggesting a relatively rapid corrosion rate (Fig. 4.47). While SP7-250V exhibits a lower initial release of 1.4 ± 0.04 mg·dm^{-3} at 1 hour, increasing to 7.7 ± 0.2 mg·dm^{-3} at 42 hours, indicating a more controlled degradation.

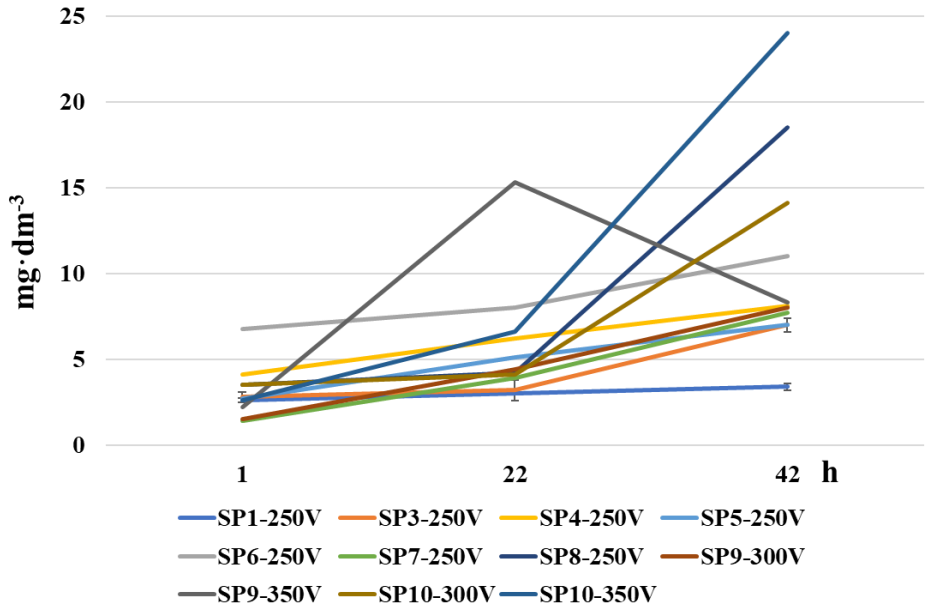

Figure 4.47 Release of Mg ion concentrations with time during immersion in dionized water

Most of coatings demonstrate more controlled release rates. These observations are consistent with existing studies that highlight the effectiveness of coatings in mitigating the corrosion of magnesium alloys [8], [73]. Results of the analyses of the surface morphology confirmed the obtained data of the ion relies. The release of phosphorus and silicon ions was lower compared to magnesium ions, likely due to the reduced incorporation rates of these elements into the PEO coatings.

Based on the chemical composition and surface morphology characterization following ICP analysis, the coatings SP6 250, SP7 250, SP8 250, SP9 (300, 350), and SP10 (300, 350) were selected for the evaluation of cytotoxic properties in comparison with pure Mg.

The initial interactions between cells and implant surfaces are crucial in determining the success of temporary implants, particularly concerning cell adhesion, which influences subsequent tissue integration and healing. Several studies have highlighted the significance of these early events [7].

In all cases, the relative cell viability was defined as the absorbance/fluorescence ratio from the sample to the absorbance/fluorescence measured for negative control and represented as a mean value ± standard deviation [171].

On the first day of incubation, the observed high levels of resazurin reduction align with the inductively coupled plasma analysis results. This suggests that the reduction was primarily due to the released magnesium ions rather than the metabolic activity of viable cells. By the third day, resazurin reduction more accurately reflected cellular viability. The data indicates that cells successfully adhered to the surface of SP9-350V, and the decreased release of magnesium ions allowed the cells to maintain their viability. The signals of the fluorescence at the third day decreased for pointed samples that indicated of increasing of toxicity effect. The 6^{th} day of investigation was characterized by the low signal that was indicated of absence of life cells on the tested surfaces besides sample SP9-350V.

In practice, this means that viable cells exhibit consistent reducing power. Resazurin is converted to resorufin within cells through electron transfer from NAD(P)H or by substituting molecular oxygen as an electron acceptor. This conversion reflects the metabolic activity of live cells. However, reduction can also occur through non-cellular electron donors, which may compromise the validity of the alamarBlue assay [172].

Cell-permeable fluorescent dye Hoechst 33342 is suitable for staining the nuclei of living or fixed cells and tissues. A cell-permeable dye that binds preferentially to adenine-thymine (A-T) rich regions in the minor groove of double-stranded DNA, emitting blue fluorescence upon binding. ActinRed 555 is a high-affinity probe conjugated to the red-orange, fluorescent dye

tetramethylrhodamine (TRITC), specifically targeting F-actin in fixed cells. This reagent provides bright and specific staining of actin filaments, facilitating detailed visualization of the cytoskeleton.

Fluorescent staining techniques was used to understanding the interaction cellular components with tasted material. The obtained results indicate the complete absence of viable cells on the surface of the control samples. There were no observed live cells on Mg sample according to the obtained results. The signal of the reassuring pointed caused by corrosion process.

4.4 Plasma electrolytic oxidation coatings on Mg in phosphate-based solutions with addition of Ca-based particles

4.4.1 Results

Based on literature, to achieve the objectives of this dissertation work, the corresponding electrolytes were prepared, as presented in Table 3.3. Phosphate-based solutions were combined with calcium-containing particles to enhance the anti-corrosion and biocompatibility properties of magnesium samples. Firstly, the prepared electrolyte compositions were tested. The obtained graphs of voltage versus time for a PEO process were used for choosing the appropriate electrolyte and voltage parameters (Fig. 4.48).

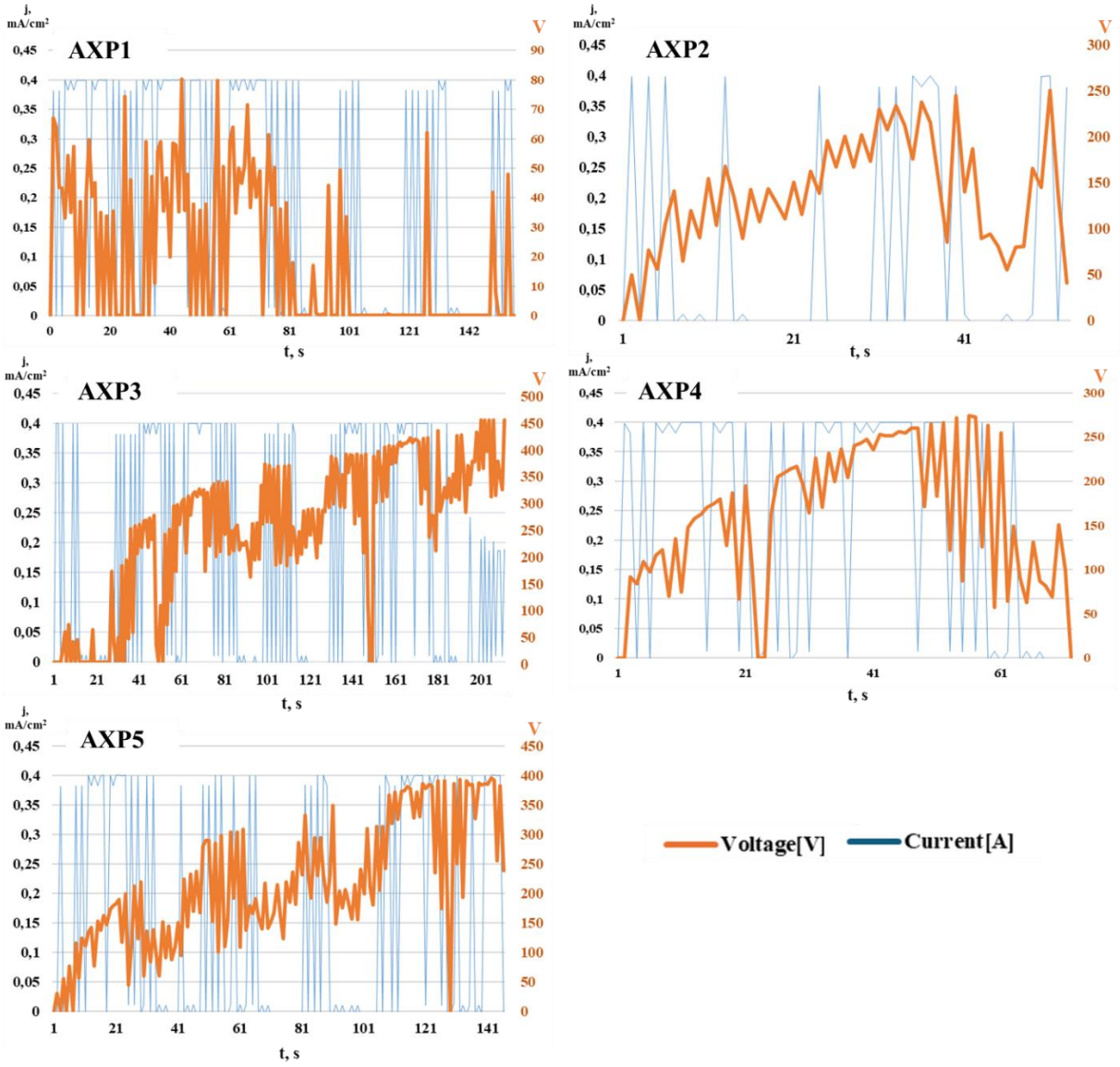

Figure 4.48 Graphs of voltage and current versus time for a PEO process pertaining to tasted electrolytes

The graphs showed the characteristic voltage and current flows of the plasma electrolytic oxidation process for each electrolytic system. Obtained graphs show resultant voltage value for each solution. The voltage could increase up to 450V and the current remained rather stable.

According to the obtained graphs, it is evident that the process proceeds well for next solutions: AXP2-AXP5. The electrolyte AXP1 was removed from the experiment. Additionally, based on the graph, it was concluded that a series of voltages can be applied to each solution. The resulting surfaces with the applied voltages are presented in the Figure 4.49. Evaluation of the surface features indicated that the best electrolyte composition was AXP5, whereas other coatings were characterized by unevenness and the presence of numerous cracks. Thus, the electrolyte composition AXP5 was selected as the basis for further experimentation. It was also decided to increase the voltage regimes up to 350V. According to the dissertation goal, calcium-based particles were chosen as the source of calcium, such as egg-shell, $CaSiO_3$, $CaCO_3$. All electrolyte compositions are presented in Table 3.3. The chosen voltages for P-Ca-based electrolytes were noted in Table 3.6.

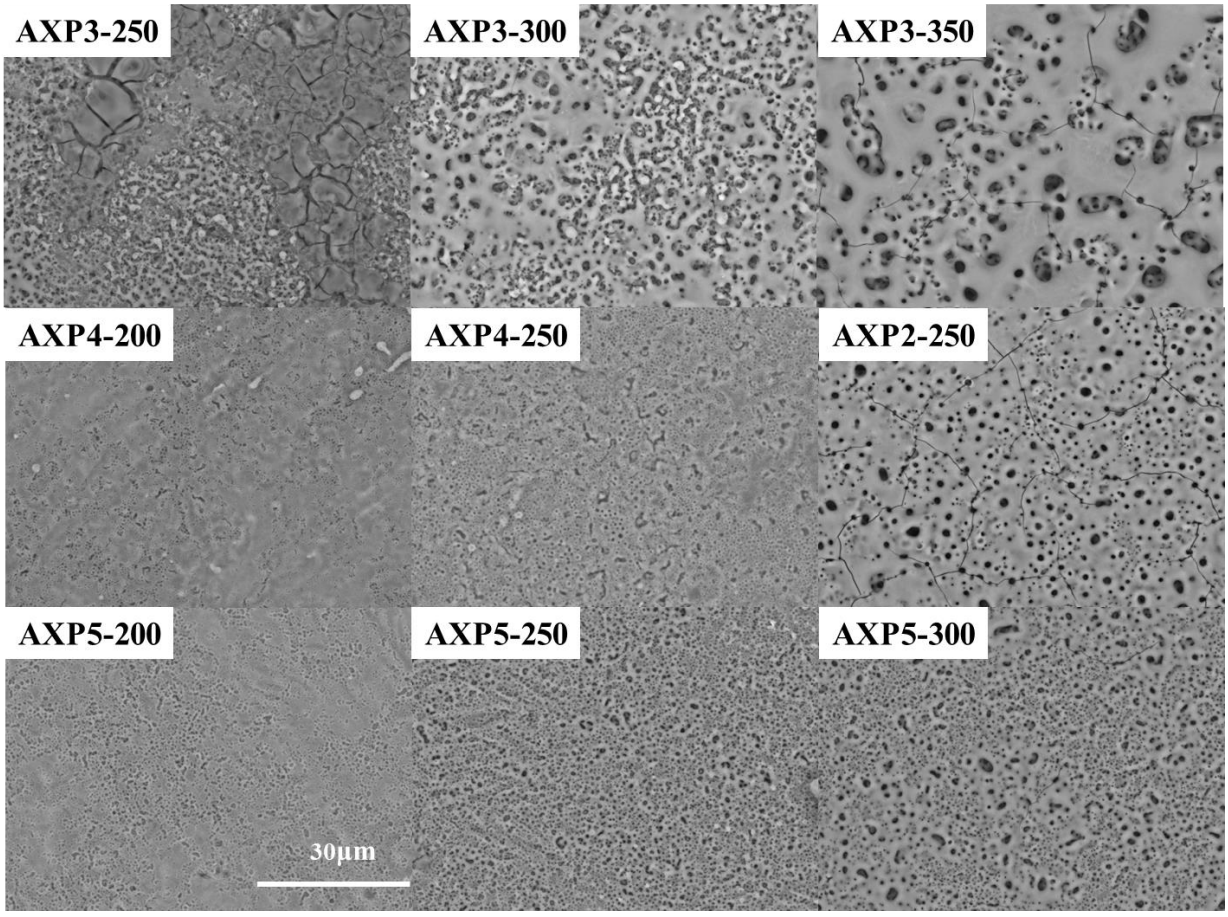

Figure 4.49 Surface morphology of the PEO coatings obtained in hexametaphosphate

Figure 4.50 illustrates the evolution of voltage and current density during the PEO process for P-Ca-based electrolytes. Analysis of the curves indicates that the voltage reached and maintained the desired level over an extended period. The current gradually decreased to a minimum value, a change attributed to the formation of an oxide layer with inherently poor conductivity. Notably, the oxide layer continued to develop until the current reached its minimum level.

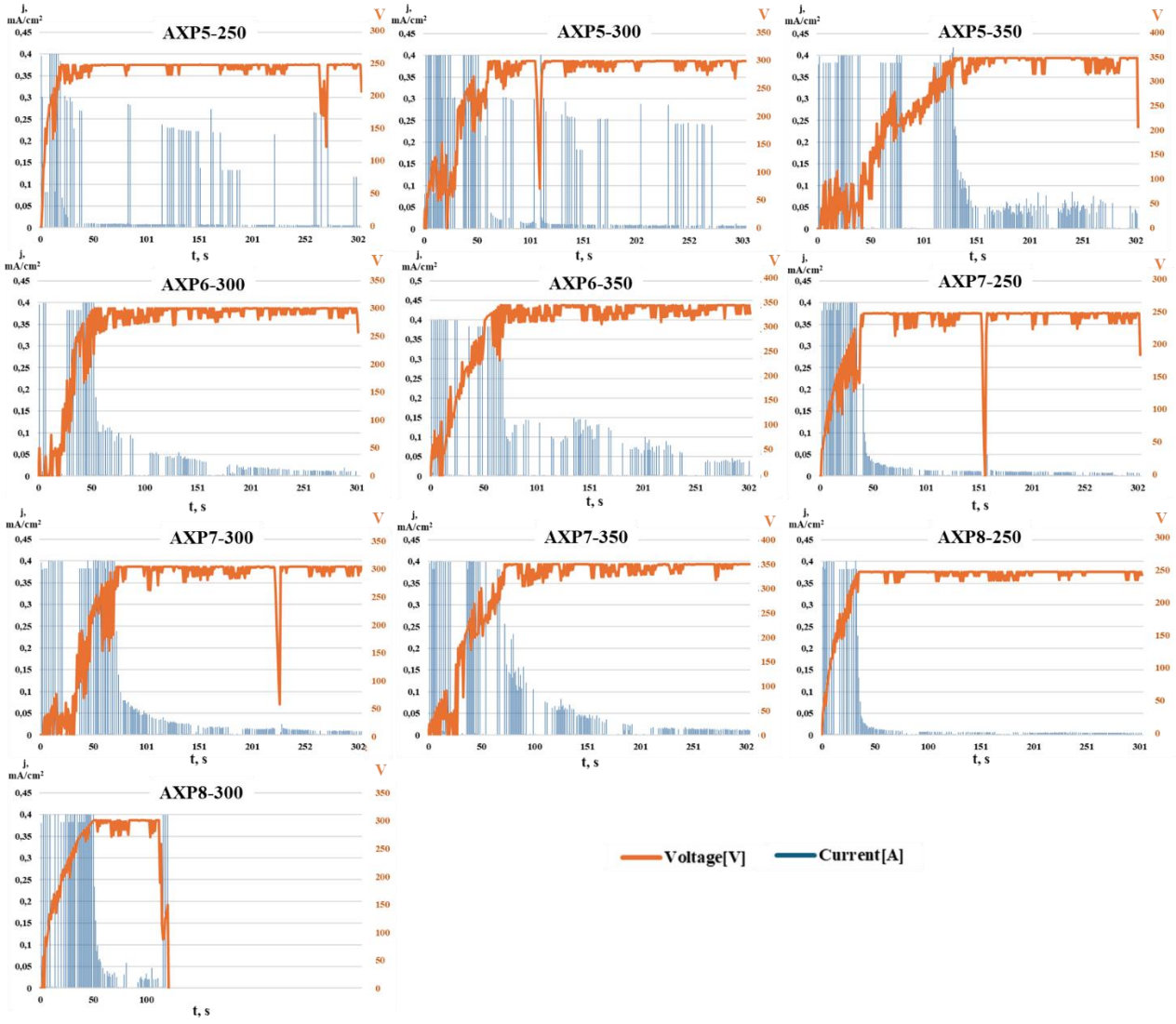

Figure 4.50 Voltage and current density evolution as a function of PEO processing time for P-Ca-based electrolytes

According to the obtained graphs it was clearly visible the first stage anodization. The time of increasing in voltage is differ for different electrolytes. The slope of the curves steeper for graphs obtained at higher voltage. The rate of the initial voltage rise indicates a rapid passivation of the sample surface at the beginning of the oxidation process [158]. According to the graph, there was

impossible to apply 300 v to AXP8 electrolyte. Therefore, only the AXP8-250 sample is considered further in the work. Table 4.20 showed the time of stabilization of the voltage rate for tasted samples. The time of stabilization increased with increasing voltage.

Table 4.20 The time of voltage increase up to critical value, s

V/sample	AXP5	AXP6	AXP7	AXP8
250	39±6	-	53±12	35±8
300	64±17	57±12	72±6	-
350	118±10	101±22	78±9	-

Due to variations in the voltages of the electrolytic systems, the resulting sample morphologies were analyzed. Specific applied voltages were examined for each electrolyte, including values near the breakdown voltage and the maximum achievable voltage, to assess their impact on surface morphology. The SEM images of these surfaces are presented in Figure 4.50. The PEO coatings exhibit characteristic porous structures with varying pore diameters.

The SEM analysis enabled the assessment of the surface morphology quality of the coatings and helped determine suitable processing conditions. For some electrolyte solutions, lower applied voltages did not result in a well-formed PEO layer. As a result, the AXP7-250V samples were excluded from further analysis (Fig. 4.51).

PEO coatings exhibit a net-like (scaffold) surface morphology formed on the magnesium substrate, featuring a network of micropores. Most pores appear spherical, though some irregular and lenticular shapes are also present. Cracks were observed in the PEO layers of investigated samples. The formation and progression of cracks showed a systematic relationship with the applied voltage. A voltage of 300V caused cracks to appear on the sample surfaces. Higher voltage led to an increase in both the number and spread of cracks.

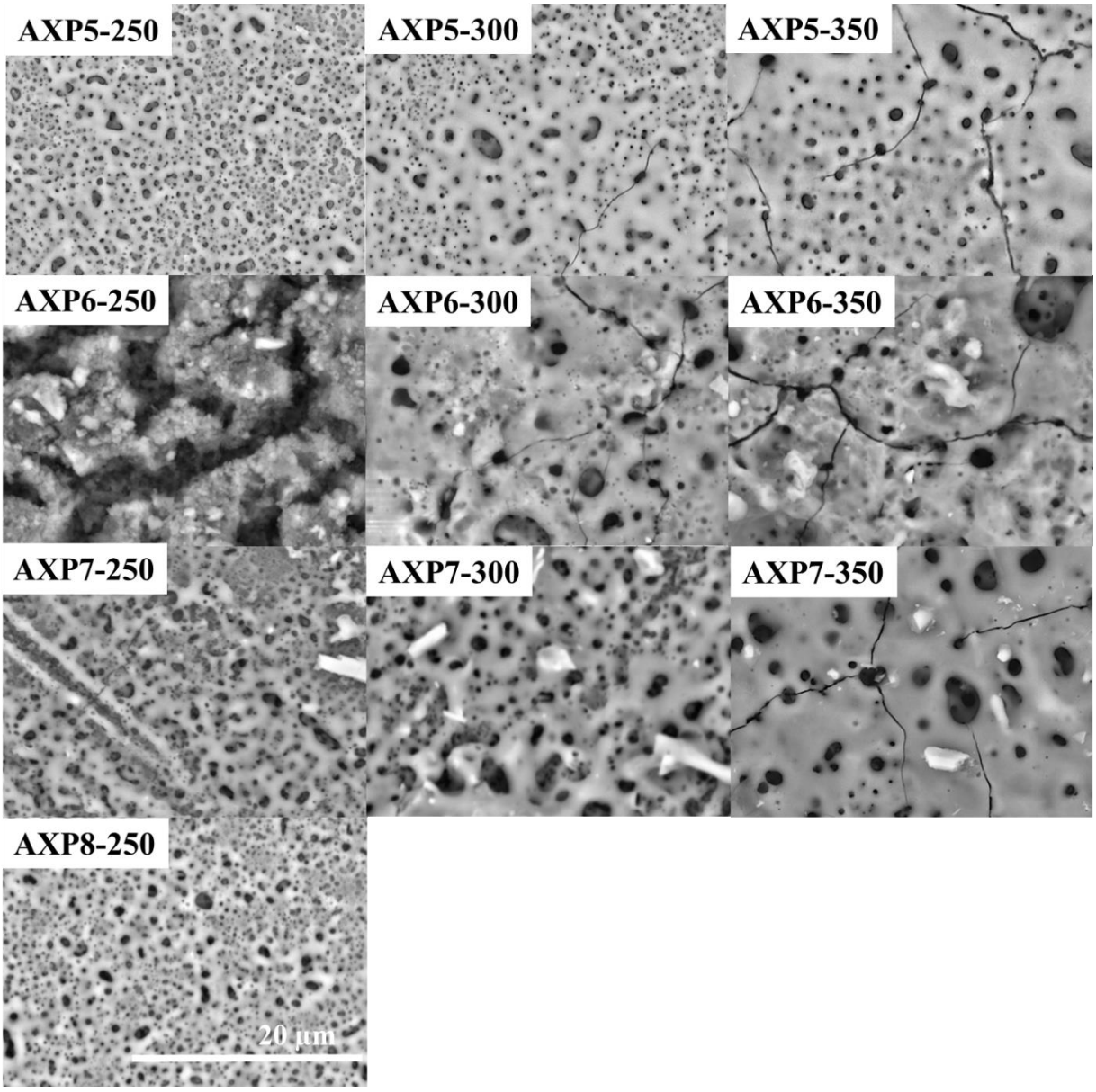

Figure 4.51 Surface morphology of the PEO coatings obtained in P-Ca-based electrolytes

The coatings appeared well-formed, with visible interconnected oxide structures and varying degrees of porosity. Some samples, such as AXP5-250, AXP5-300 and AXP5-350 showed a more homogeneous distribution of pores, suggesting better uniformity. The average pore size of AXP5 samples did not depends on applied voltage (Table 4.21). AXP6 samples characterized by inhomogeneity structural morphology. Egg-shell edition resulted in increasing average pore size. The high voltage cased increasing the average pore size from 0.4 up to 0.6 μm. AXP7 samples showed the similar surface structure. The voltage increasing had influence on the surface morphology increasing average pore size of the silicate-based coatings. The highest pore density was observed for the AXP5-250 surface. An increase in stress led to a decrease in the number of

pores per unit area. For the AXP5 group, this decrease was 4.6 times, for the AXP6 group - 2 times, and for the AXP7 sample group - 6 times.

Table 4.21 Surface morphological features **(**number of pores per square, average pore diameter for PEO treated Mg surfaces)

Coatings	**V**	**Pore diameter, µm**	**Number of pores, N·µm^{-2}**
AXP5	250	0.15±0.2	1.4
	300	0.14±0.3	0.7
	350	0.3±0.5	0.3
AXP6	300	0.4±0.8	0.2
	350	0.6±1.6*	0.1
AXP7	250	0.4±0.2	0.6
	300	0.4±0.7	0.3
	350	1.0±1.7*	00.1
AXP8	250	0.1±0.2	0.8

To characterize the distribution of pores on the surface, the obtained pore size data were divided into 12 groups (Fig. 4.52). For each of the studied surfaces, the largest percentage of pores had a size of up to 0.5 micrometers and amounted to 50%. Additionally, all surfaces exhibited a tendency for the pore size to shift to the right with increasing voltage. Comparison of coatings obtained at 300 voltages showed that the addition of silicate positively influenced the pore size distribution and reduced the proportion of small pores.

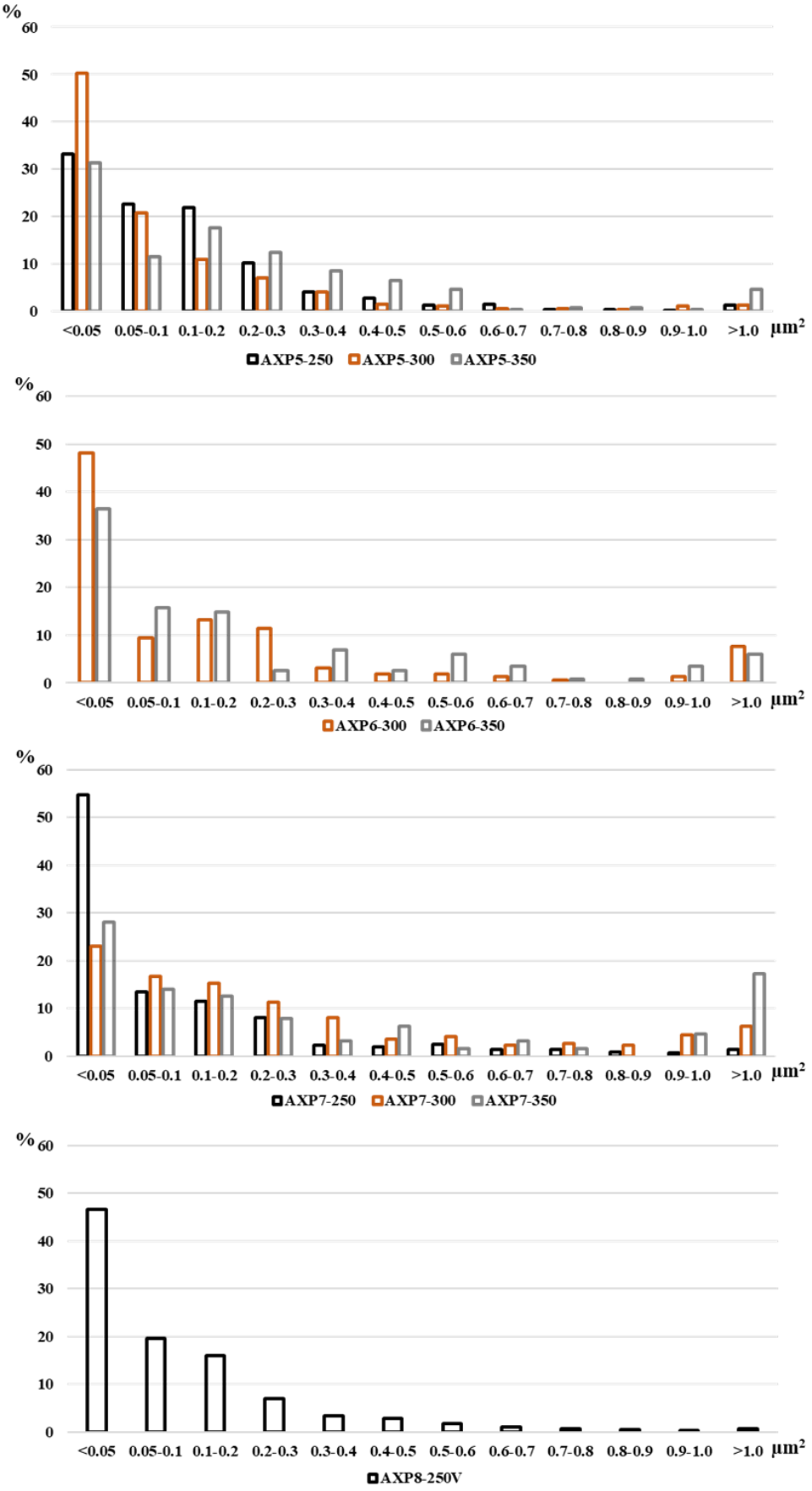

Figure 4.52 Distribution of pore sizes of the PEO coatings obtained in hexametaphosphate without and with Ca-based particles

The provided Figure 4.53 contains a series of cross-sectional SEM images that represent microstructural characteristics of the AXP5-AXP8 coatings. The AXP5 coating has uniformly distributed pores at applied voltages of 250 and 300 volts. Increasing the voltage leads to the formation of larger pores and causes heterogeneity in the coating cross-section. Analysis of PEO cross sections demonstrated notable structural heterogeneity in the layers of AXP6–AXP8 samples. Large pores often penetrated nearly to the substrate surface, resulting in cavity formation. Notably, layers produced at 250 V were systematically the most compact across all samples. The image illustrates a noticeable increase in coating thickness as the voltage rises from 250 to 300 V for AXP5 samples and from 300 to 350 V for AXP6 and AXP7 samples.

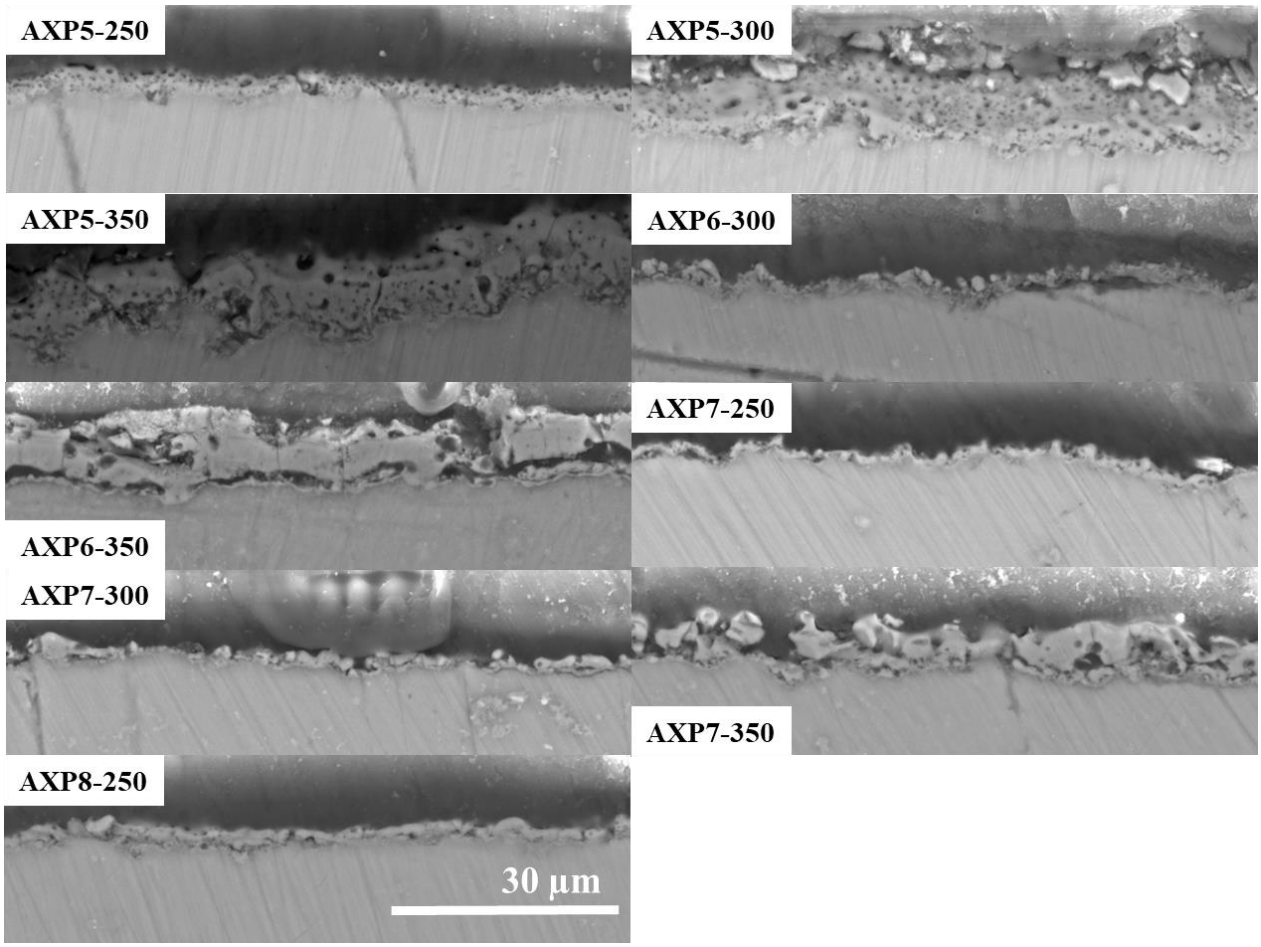

Figure 4.53 Scanning electron micrographs showing the cross-section of the PEO coatings obtained in P-Ca-based electrolytes

Table 4.22 presents the results of thickness thickness measurements for the coatings obtained from AXP5– AXP8 samples. The values are expressed as mean ± standard deviation, with * indicating statistically significant differences compared to the baseline group (250 V,

$p < 0.05$). A clear influence of the applied voltage on coating thickness was observed in the AXP5, AXP6, and AXP7 sample groups. In general, higher voltages resulted in thicker coatings, with thickness values ranging from 6.6 to 9.4 μm. The control sample showed the lower thickness of the coating at 250 V compared to the other samples.

Table 4.22 Thickness of the PEO coatings formed in P-Ca-based electrolytes (μm), *p<0.05

V/Sample no	AXP5,	AXP6	AXP7	AXP8
250	1.8±0.3	-	2.2±1.0	3.6±1.2
300	3.5±1.0	5.8±1.8	2.5±0.8	-
350	8.6±1.2*	9.4±2.8*	6.6±1.3*	-

Table 4.23 showed the parameter of the roughness for PEO coatings formed in P-Ca-based electrolytes, with p<0.05. Values are presented as mean ± standard deviation, and * denotes statistically significant differences compared to the baseline group (250 V). Table observation detected the surface roughness generally had similar value at lower applied voltage. However, the surface of AXP6-350 and AXP7-350 samples displayed the highest roughness compared to other coatings.

Table 4.23 Parameter Ra of roughness of the PEO coatings formed in P-Ca-based electrolytes (μm), *p<0.05

V/Sample no	AXP5	AXP6	AXP7	AXP8
250	0.75±0.15	-	0.8±0.12	0.36±0.09*
300	0.79±0.18	1.11±0.21	1.05±0.22	-
350	1.0±0.13	1.21±0.22*	1.22±0.24*	-

Using 3D reconstruction, the surface topography of the coatings was determined (Fig. 4.54). The development of the coatings was influenced by the applied voltage, with higher voltages leading to increased visual surface roughness. Additionally, the incorporation of particles enhanced the surface relief, resulting in more pronounced textural features.

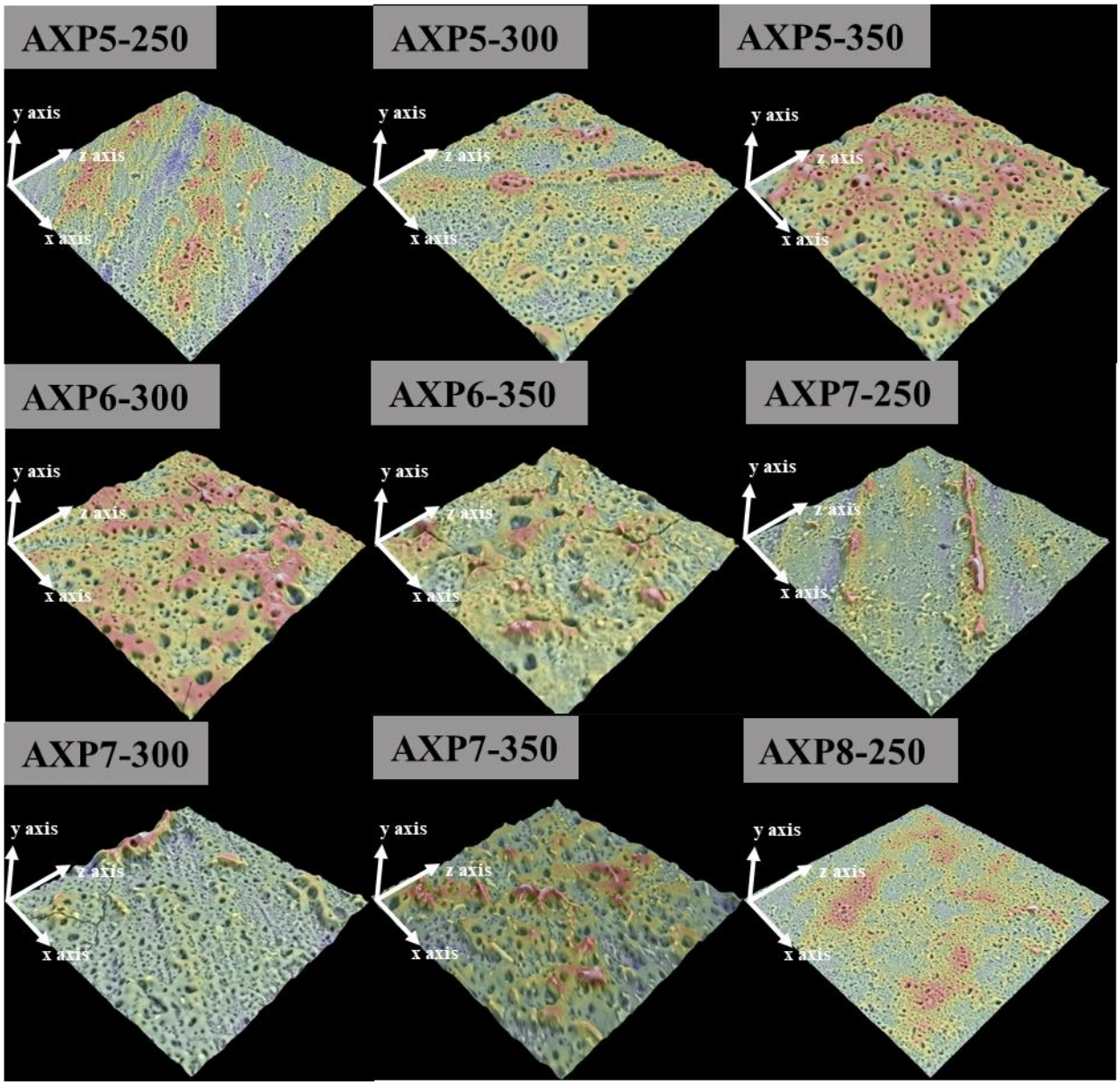

Figure 4.54 3D surface visualization of PEO coatings obtained in hexametaphosphate without and with Ca-based particles

Table 4.24 compiled the static water contact angle measurements for PEO coatings formed in P-Ca-based electrolytes under different applied voltages. The values are presented as mean ± standard deviation, and p<0.05. The results indicated that all surfaces exhibited hydrophilic

properties, with contact angles ranging from 32° to 80°. The APX6-300 surfaces demonstrated the lowest contact angle values, while the other surface exhibited the highest.

Table 4.24 Wettability (CA, °) of the obtained PEO coatings obtained in hexametaphosphate without and with Ca-based particles

V/Sample no	AXP5,	AXP6	AXP7	AXP8
250	80±17	-	60±17	55±15
300	83±2	32±17	83±13	-
350	65±6	74±20	61±2	-

Figure 4.55 illustrates the dynamic water contact angle behaviour of PEO coatings formed in hexametaphosphate without and with Ca-based particles at different applied voltage. The obtained graphs confirm the hydrophilic nature of the coatings, the contact angle values gradually decreased over time for all samples. For most coatings, the water droplet spread across the surface over than 150 seconds.

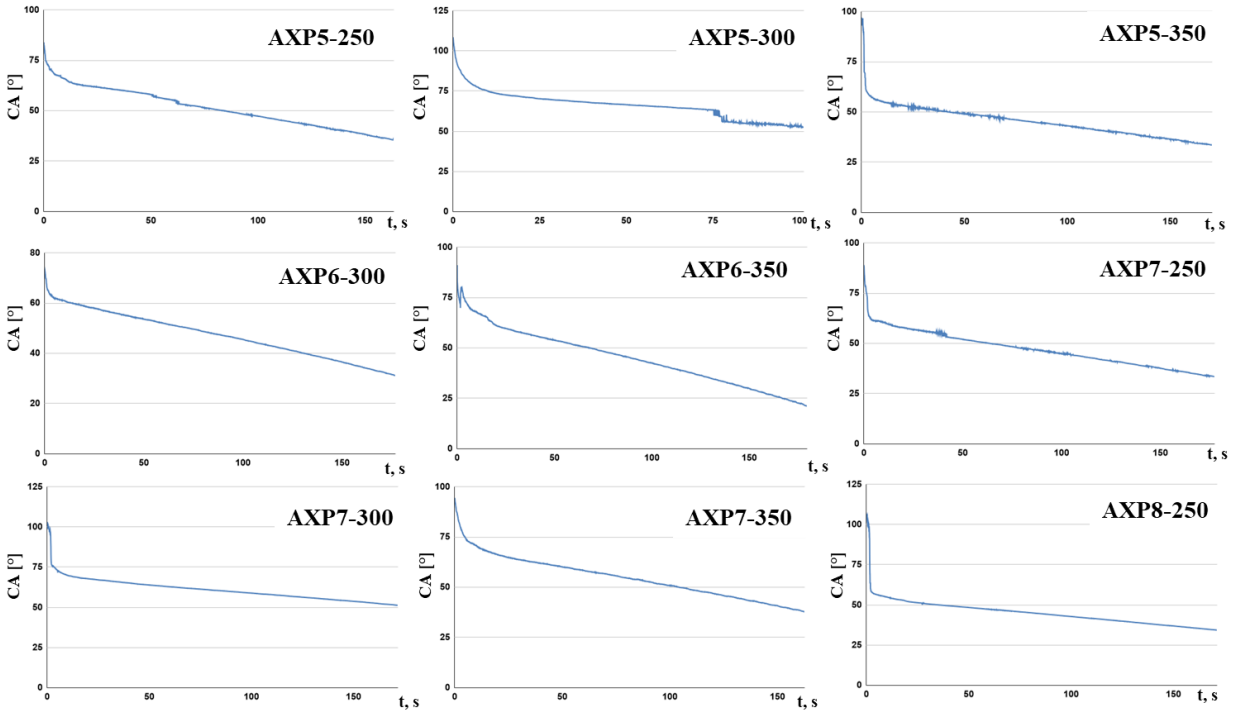

Figure 4.55 Dynamic water contact angle of the PEO coatings formed in hexametaphosphate without and with Ca-based particles

The elemental composition of the coatings was determined by energy-dispersive X-ray spectroscopy (EDX), and the results are summarized in Table 4.25. The analysis included

magnesium (Mg), silicon (Si), sodium (Na), oxygen (O), phosphorus (P), and calcium (Ca). The APX5 samples were prepared in a dissolved electrolyte, whereas the other coatings were obtained using electrolytes supplemented with Ca-based particles. The results confirmed the incorporation of electrolyte-derived elements into the coatings. A consistent decrease in Mg content was observed with increasing applied voltage across all sample groups. Phosphorus was present in a dissolved form in all cases. Notably, APX5 and APX7 coatings showed a higher P content at increased voltages, while the APX6 coatings maintained a relatively stable P level regardless of voltage. The applied voltage also influenced the incorporation of Ca and Si, with the highest Ca content detected in the APX6-350 coating.

Table 4.25 Semi-quantitative EDX analysis of the PEO surface coatings on magnesium, at.%

Coatings	**V**	**Mg**	**O**	**P**	**Na**	**Ca**	**Si**	**Ca/P**
APX5	250	49	44	7	0.1	-	-	-
	300	39	49	11	1.3	-	-	-
	350	36	49	12.5	2.4	-	-	-
APX6	300	32	48	12	1.4	6	-	0.5
	350	30	47	11	2	10	-	0.9
APX7	250	49	42	6	-	1	2	0.17
	300	33	49	10	1	3	4	0.3
	350	31	48	11	1	4	5	0.4
APX8	250	49	42	8	-	1	-	0.13

Figure 4.56 presents elemental distribution maps of the PEO coatings. The analysis focused on three key elements: P, Si, and Ca. Phosphorus was detected in all coatings, with its distribution corresponding to the cross-sectional scanograms. All elemental maps indicated a uniform incorporation of phosphorus. Coatings formed at higher voltages exhibited a stronger P signal. Silicon was detected exclusively in the AXP7 coatings. Calcium was present in the AXP6, AXP7, and AXP8 coatings, and its distribution maps also revealed a uniform signal across the coatings.

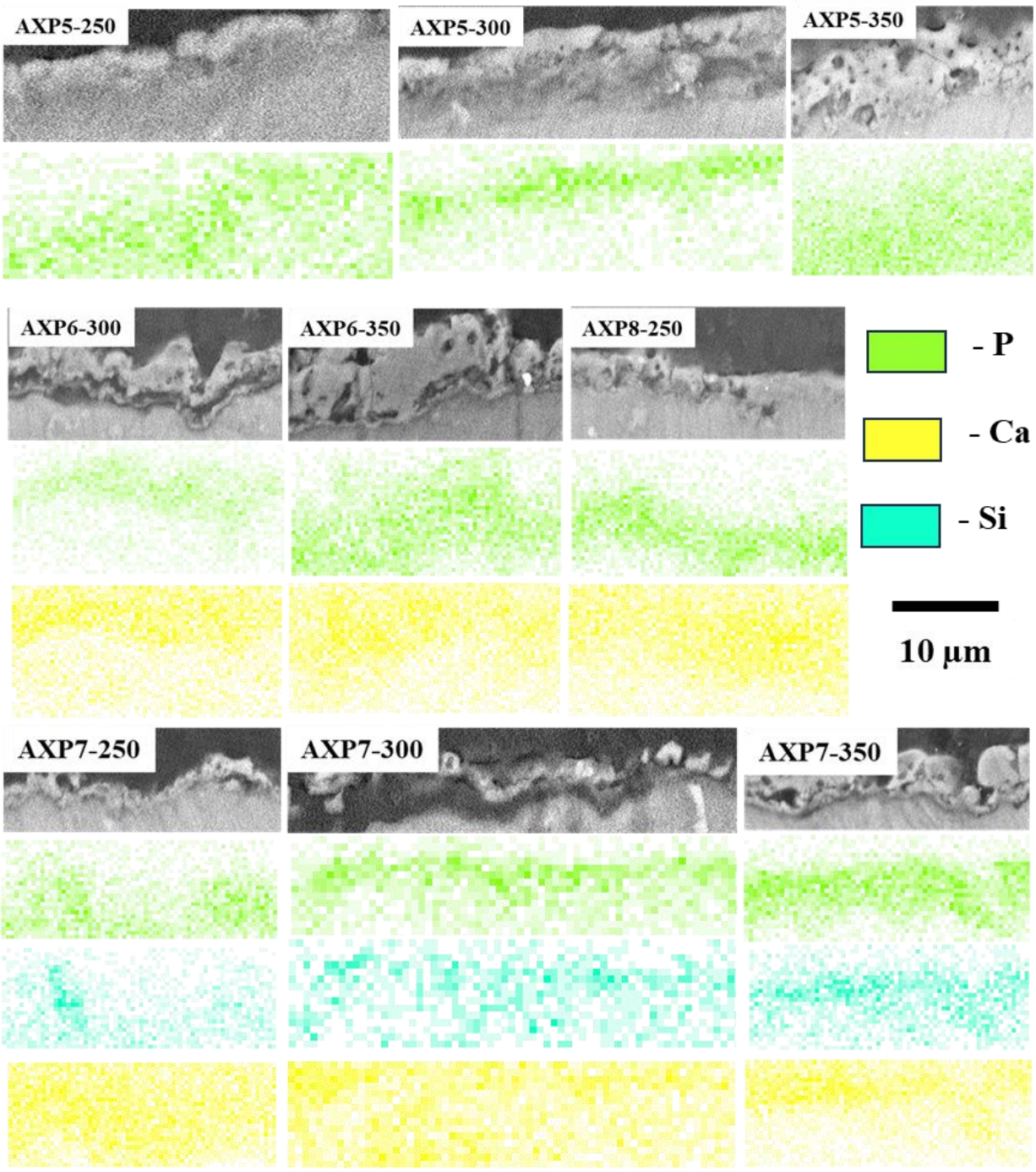

Figure 4.56 Cross section elemental distribution map of Ca-P-based PEO coatings

Figure 4.57 visualize the surface morphology of the formed in hexametaphosphate without and with Ca-based particles samples after ICP investigations. Considering the detailed analysis from the SEM images, it can be concluded that corrosion occurred on the magnesium samples during 42 hours for all types of the surfaces. All surfaces retain a porous structure except for the AXP7-250, AXP8-250 sample. The structure of the AXP5 type coatings becomes smoother.

Collected solutions after immersion test were evaluated by ICP analysis. The ion release characteristics of magnesium (Mg), silicon (Si), Phosphorous (P) and Calcium (Ca) from coatings

were detected (Table 4.26). The data, expressed in milligrams per cubic decimeter ($mg \cdot dm^{-3}$), reflects the mean values and associated standard deviations (±SD) for each sample.

The Mg release did not vary among the samples during the first hour of investigation. Samples 42AXP6-300, AXP6-350, and AXP8-250 exhibited a high level of Mg release after 42 hours of incubation. The concentration of other released ions increased over time for all samples. Their levels also rose with prolonged immersion. The amounts of calcium and silicon in the test solution were higher in samples where these elements were more abundant in the coating. The P release did not show significant variation among the samples.

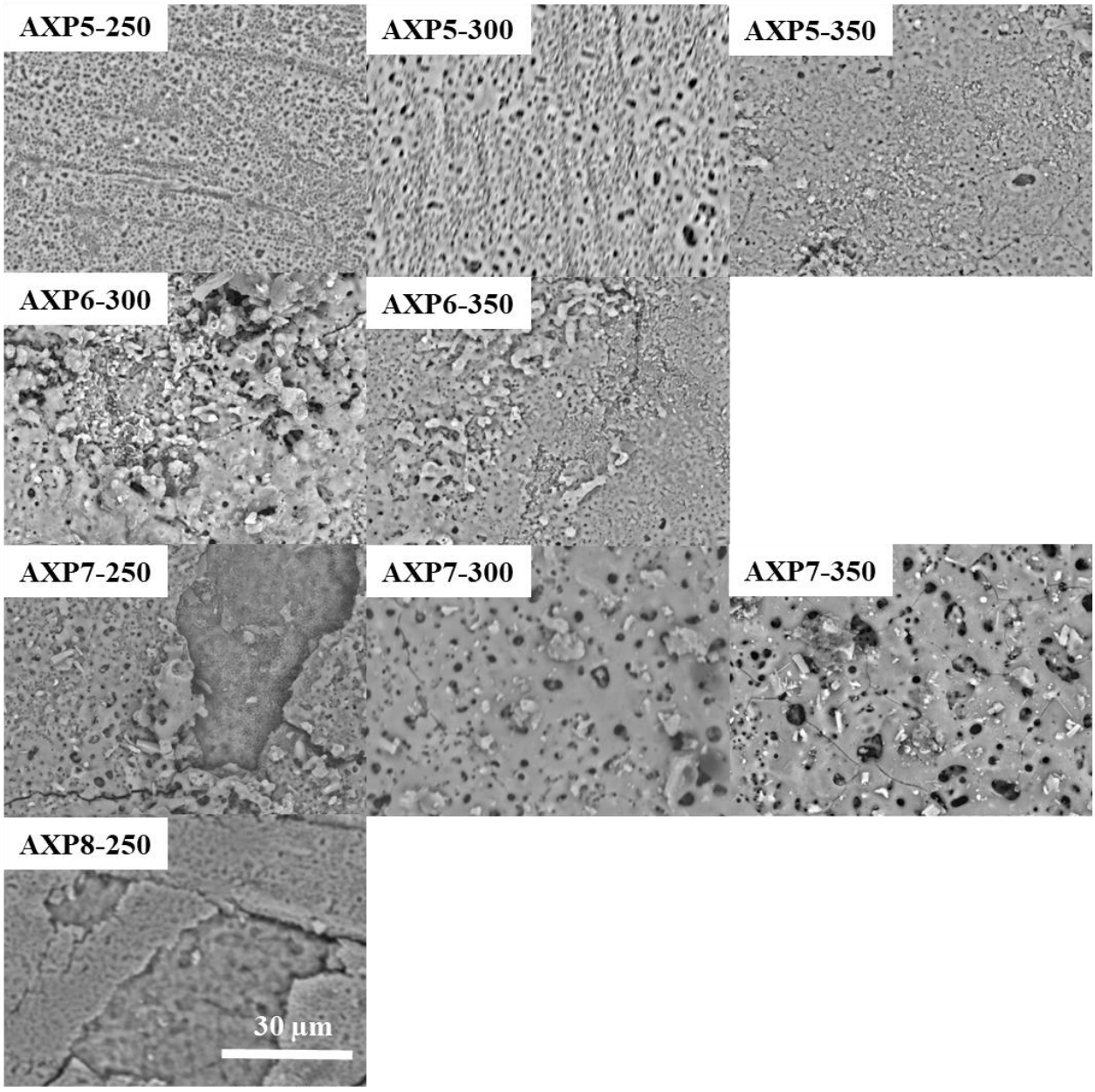

Figure 4.57 SEM images of PEO coatings obtained in hexametaphosphate without and with Ca-based particles after ICP measurements

Table 4.26 The results of ICP analysis of the ion release characteristics ($mg \cdot dm^{-3}$)

Sample no	t, h	Mg	P	Si	Ca
AXP5 250	1	2.2±0.04	0.1±0.01	-	-
	22	7.1±0.1	0.5±0.2	-	-
	42	6.2±0.1	0.3±0.01	-	-
AXP5 300	1	2.5±0.4	0.15±0.02	-	-
	22	3.7±0.1	0.32±0.01	-	-
	42	7.8±0.2	0.5±0.01	-	-
AXP5 350	1	4.4±0.04	1.02±0.02	-	-
	22	5.6±0.11	0.6±0.01	-	-
	42	9.0±0.4	0.7±0.01	-	-
AXP6 300	1	4.0±0.01	0.3±0.01	-	0.3±0.02
	22	12.0±0.7	0.42±0.02	-	0.44±0.1
	42	24.3±0.3	0.5±0.01	-	1.22±0.03
AXP6 350	1	5.2±0.1	0.7±0.04	-	0.5±0.03
	22	6.1±0.1	0.23±0.01	-	0.3±0.02
	42	12.0±0.5	0.4±0.01	-	0.54±0.03
AXP7 250	1	2.8±0.02	0.45±0.01	0.04±0.01	0.02±0.01
	22	3.5±0.2	0.08±0.01	0.12±0.02	0.14±0.01
	42	8.3±0.4	0.3±0.01	1.3±0.2	0.3±0.04
AXP7 300	1	2.8±0.1	0.4±0.01	0.06±0.01	0.1±0.01
	22	4.6±0.07	0.32±0.02	0.9±0.02	0.2±0.01
	42	9.3±0.07	0.5±0.01	1.4±0.03	0.3±0.01
AXP7 350	1	1.9±0.02	0.2±0.01	0.2±0.01	0.2±0.01
	22	5.8±0.1	0.3±0.01	1.1±0.02	0.4±0.01
	42	7.3±0.3	0.4±0.01	1.4±0.03	0.3±0.04
AXP8 250	1	3.0±0.04	0.5±0.03	-	0.14±0.02
	22	6.5±0.1	0.5±0.01	-	0.21±0.02
	42	17.5±1.1	0.84±0.03	-	0.4±0.02

Cell culture experiment was conducted to evaluate cytotoxic properties of the AXP5 (300, 350), AXP6 (300, 350) and AXP7 (300, 350) samples compared with pure Mg. The experiment

was conducted into 24 well cell culture plates. The Mg specimens were placed into this plate. Cells were seeded on the samples and control wells in concentration of 2×10^4 cells·cm^{-2}. The samples were cowered with full medium.

The graph (Fig. 4.58) shows the values of resazurin reduction after one day of incubation with U2OS cells. The results of the assay indicated a high level of resazurin reduction for all samples, especially for the control. The fluorescence signal significantly decreased for the AXP5 and AXP7 samples on the third day of incubation (Fig. 4.59). It should be noted that the level of resazurin reduction dropped below 5% for the AXP5 and AXP7 groups on the sixth day of incubation. The control samples also showed the highest level of resazurin reduction on the third day. However, by the sixth day of incubation, it decreased to 10%. The AXP6-300 sample exhibited a resazurin reduction of 9.14 ± 0.85% on the third day. By the sixth day of immersion, this value increased to 20.08 ± 1.32%. The AXP6-350 samples showed the highest levels of resazurin reduction on both the third and sixth days, corresponding to 61.13 ± 0.35% and 55.85 ± 0.37%, respectively.

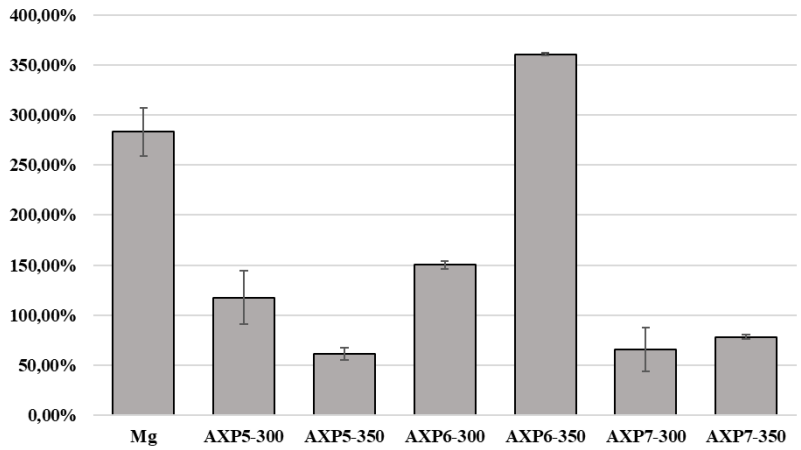

Figure 4.58 Cell viability of PEO coatings examined on 1 day by the resazurin reduction assay

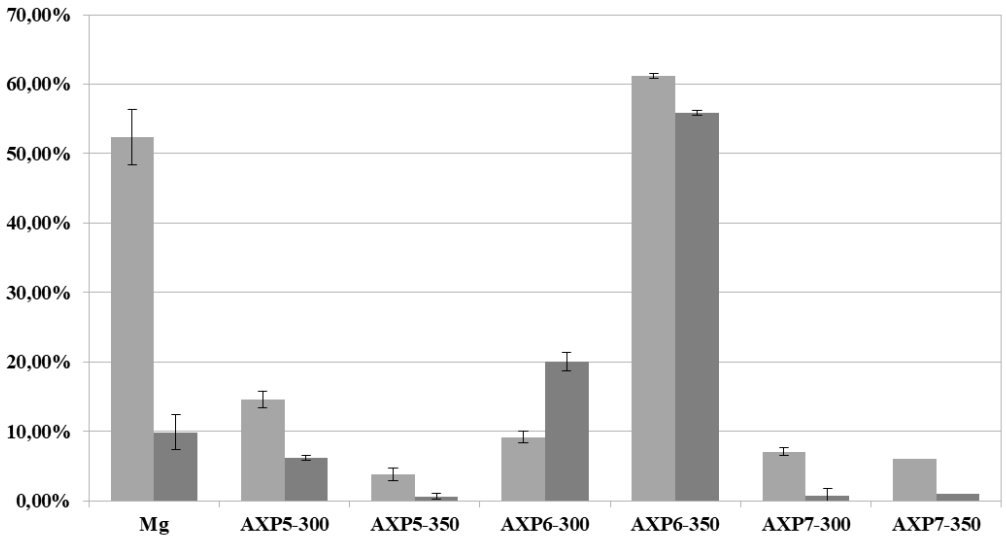

Figure 4.59 Cell viability of PEO coatings examined on 3d and 6th day by the resazurin reduction assay

Fluorescent staining was used to explain the results of cytotoxicity assays. Fluorescence microscopy analysis demonstrated the presence of cells on the AXP6-300 and AXP6-350 surfaces, with a higher number observed on the AXP6-350 samples (4.60). Cells seeded on AXP6-type surfaces exhibited viability, as confirmed by the resazurin reduction assay and fluorescence imaging. ActinRed bound specifically to the cell's fibronectin (F-actin) to exhibit orange-red fluorescence; the nuclei showed blue fluorescence after counterstaining with Hoechst. Scale bar: 10 μm. The morphology of the cells was observed under an inverted microscope.

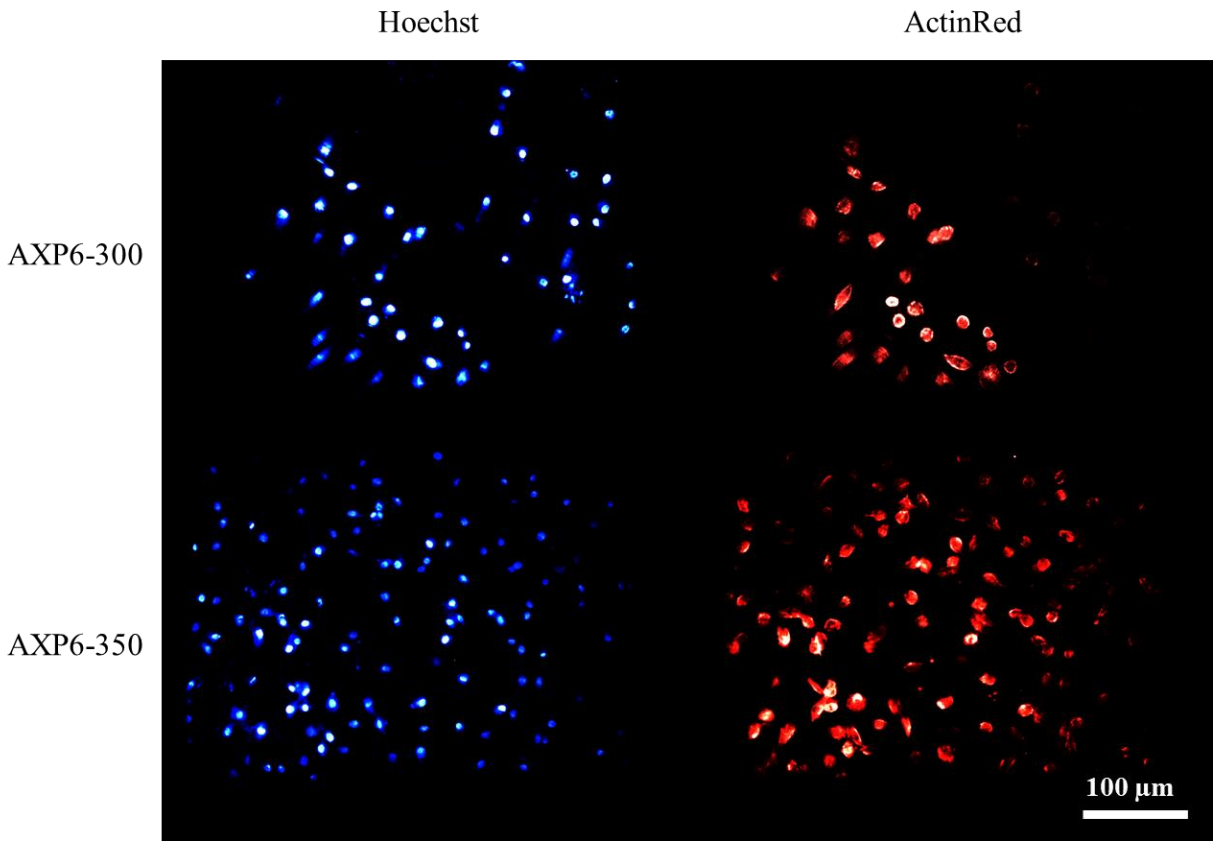

Figure 4.60 Fluorescence staining of the MG63 cells monolayer on the PEO coatings. Magnification: 100 times

4.4.2. Discussion

For ceramic coatings, the preparation of a bio-ceramic coating is of greater importance, as it typically contains Ca, P, and other essential elements that enhance biocompatibility and bioactivity. In their study, Zhongping Yao et al. worked on fabricating a bio-ceramic coating on a magnesium alloy containing Ca and P using the PEO method. The Ca/P ratio in the coating was controlled by adjusting the processing parameters. Regulating the concentration of Ca^{2+} in the electrolyte was an effective method for modifying the Ca/P ratio in the coating in both systems [173].

According to the literature, the presence of sodium hexametaphosphate ($(NaPO_3)_6$) in the electrolyte promoted coating growth, improved coating compactness and the bond strength between the coating and the substrate, thereby enhancing both corrosion and wear resistance [174], [174]. Most studies have focused on applying this electrolyte to aluminum; however, there is a lack of information regarding its use for magnesium.

Literature data and our previous results have shown that there are two possible pathways for calcium incorporation during the PEO process: calcium can be introduced into the electrolyte

in either dissolved form (e.g., calcium acetate, calcium glycerophosphate) or undissolved form (e.g., $CaCO_3$ particles, $CaSiO_3$) [139], [173], [175], [176].

The fourth part of the thesis focused on identifying the optimal parameters and electrolyte composition for utilizing Ca-based particles in the formation of Ca–P-based coatings. Figure 4.61 visualizes the scheme of coating formation in electrolyte with particle addition.

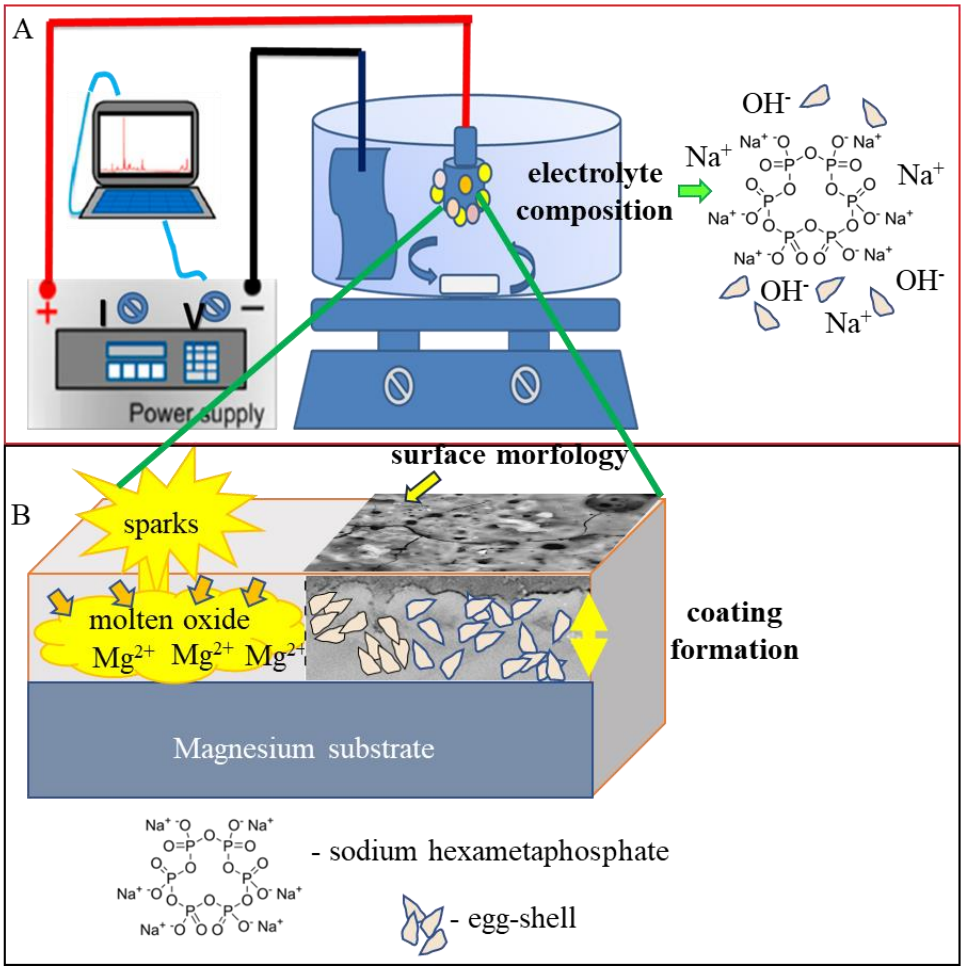

Figure 4.61 The process of formation of PEO coating A) scheme of the process of the plasmaelectrolytic oxidation technique; B) the process of formation of coating

It can be seen from Figure 4.49 that the voltage-time curve obtained with the PEO process parameters in the electrolytes can only be divided into two regions and no longer showed the aforementioned drop stage. The voltage initially increased to applied voltage at a higher rise rate, then a stable state was basically maintained until the PEO process of finished [174].

Zhuang Junjie and al. examined the effect of various additives on the performance of PEO coatings formed on AZ31 magnesium alloy in phosphate-based electrolytes. It was found that an electrolyte composition based on Na_3PO_4 resulted in a very rough and porous surface. The addition

of particles led to distinct surface morphologies, which was explained by the altered discharge characteristics during the PEO process [177].

The addition of sodium hexametaphosphate resulted in a less rough but well-developed surface morphology. The incorporation of particles, particularly egg-shell particles, combined with high applied voltage, led to increased surface roughness. Figure 4.62 illustrates the particle-induced increase in pore size and demonstrates that particle addition helped stabilize the number and distribution of pores as the voltage increased.

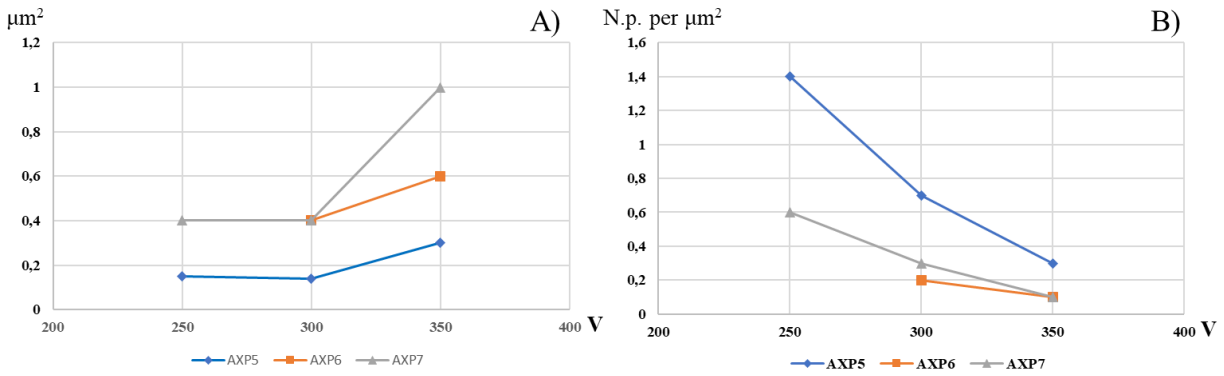

Figure 4.62 Dependence of A) average pore size and B) number of pores on anodizing voltage

Given the electrochemical nature of plasma electrolyte oxidation processes, the voltage and current characteristics of the applied electricity may significantly influence the properties of the coatings. Several parameters such as polarity of current and voltage, frequency, current density and duty cycle have been addressed in literature. The literature contains data on the increase in coating thickness due to the rise in pulse voltage. Srinivasan et al. obtained coatings with thickness of 30 μm in phosphate electrolyte under constant voltage. During investigation there was examine the effect of process parameters on coatings produced using a impulse applied current. The measured potential output during the treatment process is typically associated with the microstructural characteristics of the coating. This potential output manifested as a gradually rising curve with distinct regions, each representing different stages in the coating development process [178].

Pore size, porosity, and pore interconnectivity are among the most critical structural parameters for tissue engineering applications. Numerous studies have demonstrated that an optimal pore size ranging from 380 to 405 μm is favorable for the adhesion and proliferation of chondrocytes and osteoblasts, while a pore size of 290–310 μm is considered optimal for fibroblast growth and bone tissue formation, as it supports proper cellular function [179]. For classification purposes, pore sizes in engineered tissues are typically categorized as follows: small scale (less

than 100 µm), intermediate scale (100–500 µm), and large scale (greater than 500 µm) [179]. According to this classification, the addition of egg-shell particles resulted in the formation of a surface with pores predominantly in the intermediate size range, which is suitable for supporting various types of tissue regeneration.

Regarding the heterophosphate-based electrolyte composition, the thickness of all coatings was dependent on the applied voltage. Higher voltages resulted in increased coating thickness. Moreover, the addition of egg-shell particles further influenced the coating structure, contributing to the formation of thicker layers. Certain studies have demonstrated that adding particles to the electrolyte can lead to an increase in coating thickness. This is due to the particles' ability to alter the discharge characteristics during the PEO process, promoting more substantial oxide layer formation [180].

A Ca/P atomic ratio of approximately 1.67, which is close to that of stoichiometric hydroxyapatite, is considered favorable for promoting apatite precipitation [181]. During the PEO process, a Ca/P ratio of approximately 0.9 can be achieved in the coating at higher applied voltages (Fig. 4.63). The pore size generated under these conditions facilitates the incorporation of egg-shell particles. The resulting coating is characterized by a uniform distribution of these particles.

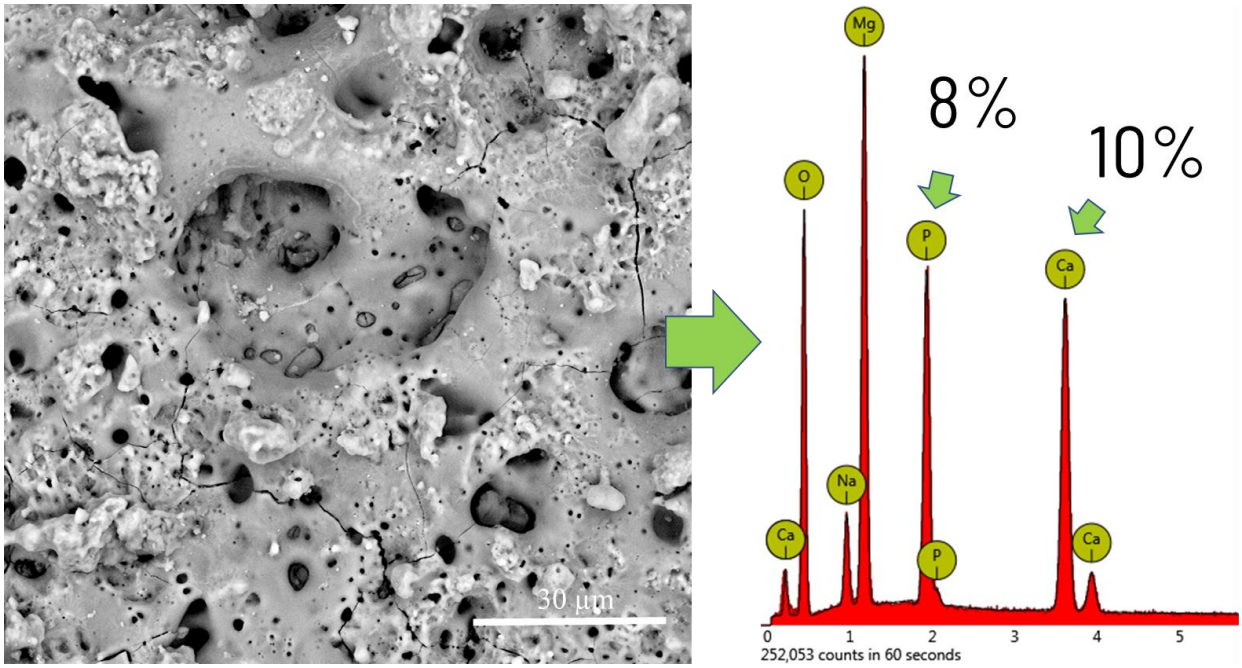

Figure 4.63 SEM images of APX6-350 surface samples with EDX region analysis of the coating

Our results clearly confirmed the relationship between contact angle measurements and surface morphology. The degree of hydrophobicity or hydrophilicity of a sample surface is determined by contact angle (CA) measurements. According to Young's equation, a surface is

considered hydrophobic when the contact angle exceeds 90°, and hydrophilic when it is less than 90° [182]. The Figure 4.64 illustrates the wettability characteristics of the obtained coatings. Rougher surfaces with increased surface area exhibited higher contact angles, indicating enhanced hydrophobicity [183].

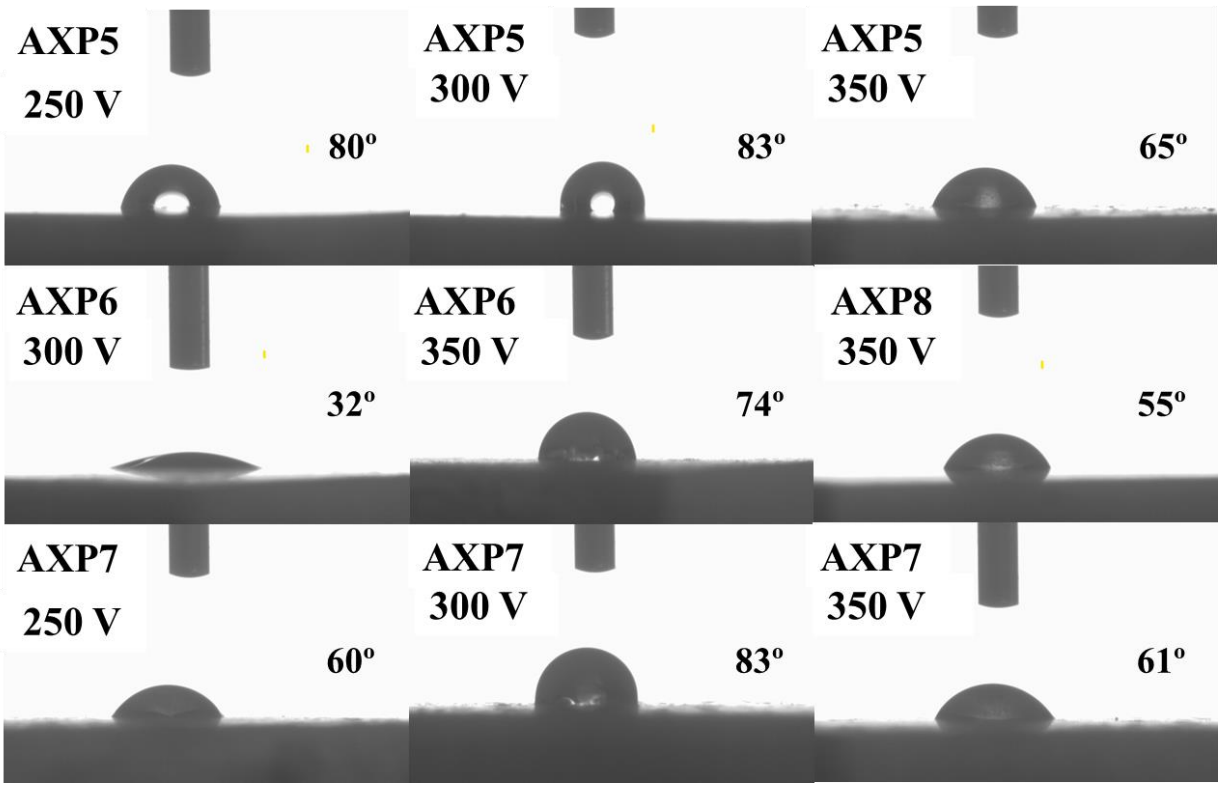

Figure 4.64 Visualization of contact angle measurement of the PEO coatings

According to a study by Zhao-Qi Zhang, hydrophobic coatings can enhance corrosion protection by serving as a barrier between the metal surface and corrosive agents [184]. In our investigation, the hydrophobic properties of the coating contributed to improved corrosion resistance, as confirmed by SEM analysis of the surface after immersion in distilled water.

Matthew Crago and all. [185] demonstrated that hydrophobic surface modifications can either promote or inhibit protein adsorption, depending on van der Waals interactions. The positive effects of hydrophobicity can be attributed to strong hydrophobic interactions between the surface and proteins, which may induce conformational changes in the proteins, facilitating more favorable interactions with the material. Moreover, reduced surface energy can minimize unfavorable interactions, thereby enhancing cell adhesion [186].

All previously presented results, conclusions, and assumptions help to explain the observed cell culture outcomes for the AXP6 samples. The AXP6-350 coatings were characterized by a thicker and denser layer, which enhanced their corrosion resistance, as confirmed by ICP analysis

and SEM observations. Moreover, the increased hydrophilicity contributed to improved corrosion protection. Additionally, the higher applied voltage during the PEO process facilitated greater incorporation of phosphorus and calcium into the coating, which positively influenced cellular metabolic activity. The appropriate pore size and well-developed surface morphology further supported cell adhesion and migration. These combined factors are consistent with the results of the resazurin reduction assay and fluorescence staining, both of which confirmed the biocompatibility of the AXP6-350 coating.

CHAPTER V - SUMMARY AND CONCLUSIONS

As part of this doctoral dissertation, plasma electrolytic oxidation (PEO) coatings on magnesium were developed and characterized to improve corrosion resistance, bioactivity, and antibacterial functionality. The research was divided into four main stages. In the first stage, the influence of silicate concentration and applied voltage on the uniformity and morphology of the coatings was examined. The second stage focused on the incorporation of silver nanoparticles (AgNPs) into the coatings obtained in the first stage, with the aim of imparting antibacterial properties. The third stage involved the investigation of combined phosphate- and silicate-based electrolytes to improve the anti-corrosion and biocompatibility properties of the coatings. The fourth stage addressed the use of phosphate-based solutions in combination with calcium-containing particles to further enhance the corrosion resistance and biocompatibility of magnesium.

Below are the main conclusions drawn from the conducted research:

Influence of silicate concentration and voltage on coating morphology.

- Increasing the applied voltage (up to 225 V) and silicate concentration led to the formation of highly porous, volcano-like ceramic coatings with a foam- or scaffold-like surface structure.
- Coatings developed at higher voltages exhibited increased thickness and pore size but reduced pore density. Some surfaces showed microcracks due to thermal stresses, potentially affecting corrosion behavior.
- Optimal coating morphology and uniformity were obtained in Si20-based electrolytes at intermediate voltages, balancing porosity and compactness.
- SEM and EDX analyses confirmed incorporation of Si and F into the oxide layers. The Mg/Si ratio of ~2.5 was identified as optimal for enhancing structural integrity and corrosion resistance.
- Wettability ranged from hydrophobic to weakly hydrophilic depending on pore structure and surface roughness. Contact angles varied between 90° and 118°.
- Ringer immersion tests demonstrated that coatings with greater thickness and compactness offered improved corrosion resistance, although crack formation during immersion led to localized degradation over time.
- Future research should focus on the controlled release of bioactive ions (Mg^{2+}, SiO_3^{2-}, Ag^{+}), improving coating-substrate adhesion, and validating in vivo performance of the most promising systems.

Incorporation of silver nanoparticles (agnps) for antibacterial functionality.

- Introduction of AgNPs into silicate-based electrolytes resulted in coatings with increased pore size and slightly reduced thickness, particularly at lower voltages.
- AgNP-modified surfaces showed significant time-dependent antibacterial activity, attributed to increased local pH and sustained Ag^{+} ion release, as confirmed by ICP and XPS analyses.
- EDX analysis did not detect Ag directly, suggesting low surface concentration or deep embedding of nanoparticles.
- Coatings with AgNPs retained corrosion resistance comparable to Ag-free coatings at high voltages, demonstrating good compactness.

Coatings from combined silicate-phosphate electrolytes.

- Integration of phosphate ions into silicate electrolytes led to the formation of porous yet more compact oxide layers with improved corrosion resistance and wettability.
- Increased phosphate content enhanced coating thickness, reduced magnesium ion release, and improved cell viability compared to pure silicate coatings.
- ICP data showed more stable Mg^{2+} release profiles.
- Static contact angles in the range of 21°–38° indicated increased surface hydrophilicity, which supported improved cell adhesion and integration.
- Selected coatings (e.g., SP9-350) demonstrated favorable corrosion resistance, surface topography, and biological compatibility.

Incorporation of calcium-containing particles into phosphate electrolytes.

- The incorporation of calcium-containing particles (such as $CaCO_3$ or egg-shell powder) into phosphate-based electrolytes enabled the formation of structurally advanced oxide coatings with bioactive potential.
- Coatings produced at elevated voltages (e.g., 350 V) exhibited increased thickness and more uniform distribution of pores in the intermediate size range (100–500 μm), suitable for tissue regeneration applications.
- SEM and EDX analysis confirmed successful incorporation of calcium and phosphorus into the oxide matrix, along with the presence of calcium-phosphate-rich regions and embedded particles.
- The applied process parameters promoted the formation of coatings with high structural integrity and adhesion, without delamination or surface discontinuities.
- These coatings showed enhanced corrosion resistance in immersion tests, and ICP analysis demonstrated a favorable ion release profile, with moderated magnesium ion release and detectable levels of Ca and P.

- Biological evaluation revealed improved metabolic activity and cell adhesion, particularly in AXP6-350 samples, which exhibited a dense morphology, adequate porosity, and a composition conducive to biocompatibility and osteoconductivity.

The obtained results directly contribute to the strategic goals of the PhD project. The conducted investigations support the feasibility of developing functionalized ceramic coatings on magnesium-based biomaterials by using natural additives, such as egg-shell particles, and tailoring electrochemical processing parameters:

1. Electrolyte composition and particle incorporation, especially with the addition of calcium- and phosphate-containing compounds (e.g., sodium hexametaphosphate and egg-shell particles), significantly influence the coating growth, morphology, and composition. The addition of egg-shell particles contributed to the formation of a thicker, denser surface layer and increased calcium incorporation, both of which are essential for enhancing osteoconductivity.

2. PEO process parameters, such as applied voltage and current regime, play a critical role in controlling the Ca/P ratio, coating thickness, and pore characteristics. The ability to reach a Ca/P ratio near 1.67 under optimized conditions (e.g., at 350 V) is promising for the formation of hydroxyapatite-like layers that support apatite precipitation and bone cell activity.

3. Surface porosity and pore size distribution, modified by particle addition, resulted in pore dimensions falling within the intermediate scale range (100–500 μm) - ideal for osteoblast and fibroblast attachment and proliferation. These structural features support bone tissue ingrowth and mechanical integration with host tissue.

4. The coatings exhibited favorable wettability and hydrophobic/hydrophilic balance, as assessed via contact angle measurements. Surfaces with higher roughness displayed increased contact angles, correlating with enhanced corrosion resistance, as confirmed by SEM and immersion testing. This dual function—protective and bioactive—is crucial for temporary implants undergoing controlled degradation.

5. The biofunctional performance of the AXP6-350 coatings was validated by cell culture studies, including resazurin assay and fluorescence microscopy. The coatings supported cell viability, adhesion, and metabolic activity, indicating strong biocompatibility of the developed surface layers.

REFERENCES

[1] F. Z. Akbarzadeh *et al.*, «A state-of-the-art review on recent advances in the fabrication and characteristics of magnesium-based alloys in biomedical applications», *J. Magnes. Alloy.*, vol 12, no 7, pp 2569–2594, 2024, doi: 10.1016/j.jma.2024.06.015.

[2] N. Sezer, Z. Evis, S. M. Kayhan, A. Tahmasebifar, i M. Koç, «Review of magnesium-based biomaterials and their applications», *J. Magnes. Alloy.*, vol 6, no 1, pp 23–43, 2018, doi: 10.1016/j.jma.2018.02.003.

[3] Y. Chen, Z. Xu, C. Smith, i J. Sankar, «Recent advances on the development of magnesium alloys for biodegradable implants», *Acta Biomater.*, vol 10, no 11, pp 4561–4573, 2014, doi: 10.1016/j.actbio.2014.07.005.

[4] F. Z. Akbarzadeh, E. R. Ghomi, i S. Ramakrishna, «Improving the corrosion behavior of magnesium alloys with a focus on AZ91 Mg alloy intended for biomedical application by microstructure modification and coating», *Proc. Inst. Mech. Eng. Part H J. Eng. Med.*, vol 236, no 8, pp 1188–1208, 2022, doi: 10.1177/09544119221105705.

[5] N. S. Grewal, G. K. Sharma, K. Kumar, i U. Batra, «Thermally and mechanically tuned interfaces of magnesium alloys for bioimplant applications», *Surfaces and Interfaces*, vol 41, 2023, doi: 10.1016/j.surfin.2023.103284.

[6] B. Istrate, C. Munteanu, I. V. Antoniac, i Ștefan C. Lupescu, «Current Research Studies of Mg–Ca–Zn Biodegradable Alloys Used as Orthopedic Implants—Review», *Crystals*, vol 12, no 10, 2022, doi: 10.3390/cryst12101468.

[7] D. Bairagi i S. Mandal, «A comprehensive review on biocompatible Mg-based alloys as temporary orthopaedic implants: Current status, challenges, and future prospects», *J. Magnes. Alloy.*, vol 10, no 3, pp 627–669, 2022, doi: 10.1016/j.jma.2021.09.005.

[8] S. Seetharaman, D. Sankaranarayanan, i M. Gupta, «Magnesium-Based Temporary Implants: Potential, Current Status, Applications, and Challenges», *J. Funct. Biomater.*, vol 14, no 6, 2023, doi: 10.3390/jfb14060324.

[9] X. Lin *et al.*, «Biodegradable Mg-based alloys: biological implications and restorative opportunities», *Int. Mater. Rev.*, vol 68, no 4, pp 365–403, 2023, doi: 10.1080/09506608.2022.2079367.

[10] K. Chen, J. Dai, i X. Zhang, «Improvement of corrosion resistance of magnesium alloys for biomedical applications», *Corros. Rev.*, vol 33, no 3–4, pp 101–117, 2015, doi: 10.1515/corrrev-2015-0007.

[11] Y. K. Kim *et al.*, «Gas formation and biological effects of biodegradable magnesium in a

preclinical and clinical observation», *Sci. Technol. Adv. Mater.*, vol 19, no 1, pp 324–335, 2018, doi: 10.1080/14686996.2018.1451717.

[12] L. Xu, X. Liu, K. Sun, R. Fu, i G. Wang, «Corrosion Behavior in Magnesium-Based Alloys for Biomedical Applications», *Materials (Basel).*, vol 15, no 7, 2022, doi: 10.3390/ma15072613.

[13] L. An, Y. Ma, L. Sun, Z. Wang, i S. Wang, «Investigation of mutual effects among additives in electrolyte for plasma electrolytic oxidation on magnesium alloys», *J. Magnes. Alloy.*, vol 8, no 2, pp 523–536, 2020, doi: 10.1016/j.jma.2019.09.003.

[14] M. Saini, «Implant biomaterials: A comprehensive review», *World J. Clin. Cases*, vol 3, no 1, p 52, 2015, doi: 10.12998/wjcc.v3.i1.52.

[15] T. Zehra i M. Kaseem, «Recent advances in surface modification of plasma electrolytic oxidation coatings treated by non-biodegradable polymers», *J. Mol. Liq.*, vol 365, 2022, doi: 10.1016/j.molliq.2022.120091.

[16] Z. Qiao, Z. Shi, N. Hort, N. I. Zainal Abidin, i A. Atrens, «Corrosion behaviour of a nominally high purity Mg ingot produced by permanent mould direct chill casting», *Corros. Sci.*, vol 61, pp 185–207, 2012, doi: 10.1016/j.corsci.2012.04.030.

[17] F. Cao *et al.*, «Corrosion of ultra-high-purity Mg in 3.5% NaCl solution saturated with Mg(OH)2», *Corros. Sci.*, vol 75, pp 78–99, 2013, doi: 10.1016/j.corsci.2013.05.018.

[18] K. Gusieva, C. H. J. Davies, J. R. Scully, i N. Birbilis, «Corrosion of magnesium alloys: The role of alloying», *Int. Mater. Rev.*, vol 60, no 3, pp 169–194, 2015, doi: 10.1179/1743280414Y.0000000046.

[19] A. D. Sudholz, K. Gusieva, X. B. Chen, B. C. Muddle, M. A. Gibson, i N. Birbilis, «Electrochemical behaviour and corrosion of Mg-Y alloys», *Corros. Sci.*, vol 53, no 6, pp 2277–2282, 2011, doi: 10.1016/j.corsci.2011.03.010.

[20] M. Salgueiro Azevedo, C. Allély, K. Ogle, i P. Volovitch, «Corrosion mechanisms of Zn(Mg,Al) coated steel: 2. The effect of Mg and Al alloying on the formation and properties of corrosion products in different electrolytes», *Corros. Sci.*, vol 90, pp 482–490, 2015, doi: 10.1016/j.corsci.2014.07.042.

[21] B. Xiao, G. L. Song, D. Zheng, i F. Cao, «A corrosion resistant die-cast Mg-9Al-1Zn anode with superior discharge performance for Mg-air battery», *Mater. Des.*, vol 194, 2020, doi: 10.1016/j.matdes.2020.108931.

[22] Y. Ali, D. Qiu, B. Jiang, F. Pan, i M. X. Zhang, «Current research progress in grain refinement of cast magnesium alloys: A review article», *J. Alloys Compd.*, vol 619, pp 639–651, 2015, doi: 10.1016/j.jallcom.2014.09.061.

[23] S. Q. Zhu i S. P. Ringer, «On the role of twinning and stacking faults on the crystal plasticity and grain refinement in magnesium alloys», *Acta Mater.*, vol 144, pp 365–375, 2018, doi: 10.1016/j.actamat.2017.11.004.

[24] M. Esmaily *et al.*, «Fundamentals and advances in magnesium alloy corrosion», *Prog. Mater. Sci.*, vol 89, pp 92–193, 2017, doi: 10.1016/j.pmatsci.2017.04.011.

[25] M. Liang *et al.*, «Enhanced corrosion resistance of Mg and Mg alloys with fs-laser printed hydrophobic and periodically microrippled surface for armor application», *Appl. Surf. Sci.*, vol 639, 2023, doi: 10.1016/j.apsusc.2023.158156.

[26] L. Huang *et al.*, «Effects of grain size and texture on stress corrosion cracking of friction stir processed AZ80 magnesium alloy», *Eng. Fail. Anal.*, vol 92, pp 392–404, 2018, doi: 10.1016/j.engfailanal.2018.06.012.

[27] B. Li i Y. Han, «Fast formation of a novel bilayer coating with enhanced corrosion resistance and cytocompatibility on magnesium», *RSC Adv.*, vol 5, no 57, pp 46109–46118, 2015, doi: 10.1039/c5ra04454e.

[28] C. Liu, Q. Li, J. Liang, J. Zhou, i L. Wang, «Microstructure and corrosion behaviour of laser surface melting treated WE43 magnesium alloy», *RSC Adv.*, vol 6, no 36, pp 30642–30651, 2016, doi: 10.1039/C5RA27010C.

[29] A. Fattah-alhosseini, R. Chaharmahali, i K. Babaei, «Impressive strides in amelioration of corrosion and wear behaviors of Mg alloys using applied polymer coatings on PEO porous coatings: A review», *J. Magnes. Alloy.*, vol 10, no 5, pp 1171–1190, 2022, doi: 10.1016/j.jma.2022.01.015.

[30] A. Fattah-alhosseini i R. Chaharmahali, «Impressive strides in amelioration of corrosion behavior of Mg-based alloys through the PEO process combined with surface laser process: A review», *J. Magnes. Alloy.*, vol 11, no 12, pp 4390–4406, 2023, doi: 10.1016/j.jma.2023.10.005.

[31] E. L. Colvin, «Aluminum Alloys: Corrosion», *Encycl. Mater. Sci. Technol.*, pp 107–110, 2001, doi: 10.1016/b0-08-043152-6/00022-x.

[32] G. Manivasagam i S. Suwas, «Biodegradable Mg and Mg based alloys for biomedical implants», *Mater. Sci. Technol. (United Kingdom)*, vol 30, no 5, pp 515–520, 2014, doi: 10.1179/1743284713Y.0000000500.

[33] X. Lu, C. Blawert, B. J. C. Luthringer, i M. L. Zheludkevich, «Controllable Degradable Plasma Electrolytic Oxidation Coated Mg Alloy for Biomedical Application», *Front. Chem. Eng.*, vol 4, 2022, doi: 10.3389/fceng.2022.748549.

[34] W. Yao *et al.*, «Recent advances in protective coatings and surface modifications for

corrosion protection of Mg alloys», *J. Mater. Res. Technol.*, vol 31, pp 3238–3254, 2024, doi: 10.1016/j.jmrt.2024.07.046.

[35] B. L. Jiang i Y. F. Ge, «Micro-arc oxidation (MAO) to improve the corrosion resistance of magnesium (Mg) alloys», *Corros. Prev. Magnes. Alloy. A Vol. Woodhead Publ. Ser. Met. Surf. Eng.*, pp 163–196, 2013, doi: 10.1533/9780857098962.2.163.

[36] X. Zhang, Z. Yao, Z. Jiang, Y. Zhang, i X. Liu, «Investigation of the plasma electrolytic oxidation of Ti6Al4V under single-pulse power supply», *Corros. Sci.*, vol 53, no 6, pp 2253–2262, 2011, doi: 10.1016/j.corsci.2011.03.005.

[37] B. L. Jiang i Y. M. Wang, «Plasma electrolytic oxidation treatment of aluminium and titanium alloys», *Surf. Eng. Light Alloy. Alum. Magnes. Titan. Alloy.*, pp 110–154, 2010, doi: 10.1533/9781845699451.2.110.

[38] M. Aliofkhazraei *et al.*, «Review of plasma electrolytic oxidation of titanium substrates: Mechanism, properties, applications and limitations», *Appl. Surf. Sci. Adv.*, vol 5, 2021, doi: 10.1016/j.apsadv.2021.100121.

[39] Y. Q. Almajidi *et al.*, «Unveiling the Effect of Particle Incorporation in PEO Coatings on the Corrosion and Wear Performance of Magnesium Implants», *Lubricants*, vol 11, no 12, 2023, doi: 10.3390/lubricants11120519.

[40] J. M. Albella, I. Montero, i J. M. Martinez-Duart, «A theory of avalanche breakdown during anodic oxidation», *Electrochim. Acta*, vol 32, no 2, pp 255–258, 1987, doi: 10.1016/0013-4686(87)85032-6.

[41] P. Samadi i I. A. Witonska, «Plasma electrolytic oxidation layers as alternative supports for metallic catalysts used in oxidation reaction for environmental application», *Catal. Commun.*, vol 181, 2023, doi: 10.1016/j.catcom.2023.106722.

[42] Z. Yao, Y. Jiang, F. Jia, Z. Jiang, i F. Wang, «Growth characteristics of plasma electrolytic oxidation ceramic coatings on Ti-6Al-4V alloy», *Appl. Surf. Sci.*, vol 254, no 13, pp 4084–4091, 2008, doi: 10.1016/j.apsusc.2007.12.062.

[43] L. O. Snizhko *et al.*, «Anodic processes in plasma electrolytic oxidation of aluminium in alkaline solutions», *Electrochim. Acta*, vol 49, no 13, pp 2085–2095, 2004, doi: 10.1016/j.electacta.2003.11.027.

[44] W. Xue, Z. Deng, R. Chen, i T. Zhang, «Growth regularity of ceramic coatings formed by microarc oxidation on Al-Cu-Mg alloy», *Thin Solid Films*, vol 372, no 1, pp 114–117, 2000, doi: 10.1016/S0040-6090(00)01026-9.

[45] L. Chang, «Growth regularity of ceramic coating on magnesium alloy by plasma electrolytic oxidation», *J. Alloys Compd.*, vol 468, no 1–2, pp 462–465, 2009, doi:

10.1016/j.jallcom.2008.01.069.

[46] A. Bordbar-Khiabani, B. Yarmand, i M. Mozafari, «Emerging magnesium-based biomaterials for orthopedic implantation», *Emerg. Mater. Res.*, vol 8, no 3, pp 305–319, 2020, doi: 10.1680/jemmr.18.00048.

[47] E. A. Olevsky i L. Froyen, «Impact of thermal diffusion on densification during SPS», *J. Am. Ceram. Soc.*, vol 92, no SUPPL. 1, 2009, doi: 10.1111/j.1551-2916.2008.02705.x.

[48] R. O. Hussein, X. Nie, i D. O. Northwood, «An investigation of ceramic coating growth mechanisms in plasma electrolytic oxidation (PEO) processing», *Electrochim. Acta*, vol 112, pp 111–119, 2013, doi: 10.1016/j.electacta.2013.08.137.

[49] G. Barati Darband, M. Aliofkhazraei, P. Hamghalam, i N. Valizade, «Plasma electrolytic oxidation of magnesium and its alloys: Mechanism, properties and applications», *J. Magnes. Alloy.*, vol 5, no 1, pp 74–132, 2017, doi: 10.1016/j.jma.2017.02.004.

[50] S. Durdu, A. Aytaç, i M. Usta, «Characterization and corrosion behavior of ceramic coating on magnesium by micro-arc oxidation», *J. Alloys Compd.*, vol 509, no 34, pp 8601–8606, 2011, doi: 10.1016/j.jallcom.2011.06.059.

[51] A. Fattah-alhosseini, M. Molaei, i K. Babaei, «The effects of nano- and micro-particles on properties of plasma electrolytic oxidation (PEO) coatings applied on titanium substrates: A review», *Surfaces and Interfaces*, vol 21, 2020, doi: 10.1016/j.surfin.2020.100659.

[52] A. Toulabifard, M. Rahmati, K. Raeissi, A. Hakimizad, i M. Santamaria, «The effect of electrolytic solution composition on the structure, corrosion, and wear resistance of peo coatings on az31 magnesium alloy», *Coatings*, vol 10, no 10, pp 1–19, 2020, doi: 10.3390/coatings10100937.

[53] F. Liu, D. Shan, Y. Song, i E. H. Han, «Effect of additives on the properties of plasma electrolytic oxidation coatings formed on AM50 magnesium alloy in electrolytes containing K2ZrF6», *Surf. Coatings Technol.*, vol 206, no 2–3, pp 455–463, 2011, doi: 10.1016/j.surfcoat.2011.07.054.

[54] G. Lv *et al.*, «Characteristic of ceramic coatings on aluminum by plasma electrolytic oxidation in silicate and phosphate electrolyte», *Appl. Surf. Sci.*, vol 253, no 5, pp 2947–2952, 2006, doi: 10.1016/j.apsusc.2006.06.036.

[55] G. Yeshmanova *et al.*, «Effect of electrolyte composition on the formation of PEO coatings on AA2024 aluminium alloy», *Surfaces and Interfaces*, vol 44, 2024, doi: 10.1016/j.surfin.2023.103797.

[56] G. H. Lv *et al.*, «Effects of current frequency on the structural characteristics and corrosion property of ceramic coatings formed on magnesium alloy by PEO technology», *J. Mater.*

Process. Technol., vol 208, no 1–3, pp 9–13, 2008, doi: 10.1016/j.jmatprotec.2007.12.125.

[57] S. Farshid i M. Kharaziha, «Micro and nano-enabled approaches to improve the performance of plasma electrolytic oxidation coated magnesium alloys», *J. Magnes. Alloy.*, vol 9, no 5, pp 1487–1504, 2021, doi: 10.1016/j.jma.2020.11.004.

[58] M. Esmaeili, M. Tadayonsaidi, i B. Ghorbanian, «The effect of PEO parameters on the properties of biodegradable Mg alloys: A review», *Surf. Innov.*, vol 9, no 4, pp 184–198, 2020, doi: 10.1680/jsuin.20.00057.

[59] A. Seyfoori, S. Mirdamadi, A. Khavandi, i Z. S. Raufi, «Biodegradation behavior of micro-arc oxidized AZ31 magnesium alloys formed in two different electrolytes», *Appl. Surf. Sci.*, vol 261, pp 92–100, 2012, doi: 10.1016/j.apsusc.2012.07.105.

[60] Y. Mori, A. Koshi, J. Liao, H. Asoh, i S. Ono, «Characteristics and corrosion resistance of plasma electrolytic oxidation coatings on AZ31B Mg alloy formed in phosphate - Silicate mixture electrolytes», *Corros. Sci.*, vol 88, pp 254–262, 2014, doi: 10.1016/j.corsci.2014.07.038.

[61] B. Hadzima *et al.*, «Peo of az31 mg alloy: Effect of electrolyte phosphate content and current density», *Metals (Basel).*, vol 10, no 11, pp 1–23, 2020, doi: 10.3390/met10111521.

[62] S. Hiromoto i T. Yamazaki, «Micromorphological effect of calcium phosphate coating on compatibility of magnesium alloy with osteoblast», *Sci. Technol. Adv. Mater.*, vol 18, no 1, pp 96–109, 2017, doi: 10.1080/14686996.2016.1266238.

[63] J. Dou, Y. Chen, Y. Chi, H. Li, G. Gu, i C. Chen, «Preparation and characterization of a calcium-phosphate-silicon coating on a Mg-Zn-Ca alloy via two-step micro-arc oxidation», *Phys. Chem. Chem. Phys.*, vol 19, no 23, pp 15110–15119, 2017, doi: 10.1039/c7cp02672b.

[64] R. F. Zhang, S. F. Zhang, J. H. Xiang, L. H. Zhang, Y. Q. Zhang, i S. B. Guo, «Influence of sodium silicate concentration on properties of micro arc oxidation coatings formed on AZ91HP magnesium alloys», *Surf. Coatings Technol.*, vol 206, no 24, pp 5072–5079, 2012, doi: 10.1016/j.surfcoat.2012.06.018.

[65] J. Liang, L. Hu, i J. Hao, «Characterization of microarc oxidation coatings formed on AM60B magnesium alloy in silicate and phosphate electrolytes», *Appl. Surf. Sci.*, vol 253, no 10, pp 4490–4496, 2007, doi: 10.1016/j.apsusc.2006.09.064.

[66] F. Muhaffel i H. Cimenoglu, «Development of corrosion and wear resistant micro-arc oxidation coating on a magnesium alloy», *Surf. Coatings Technol.*, vol 357, pp 822–832, 2019, doi: 10.1016/j.surfcoat.2018.10.089.

[67] V. Subbotina, V. Bilozerov, O. Subbotin, S. Kniaziev, O. Volkov, i O. Lazorko, «New features of surface modification of magnesium alloys by microarc oxidation (MAO)»,

Funct. Mater., vol 30, no 4, pp 590–596, 2023, doi: 10.15407/fm30.04.590.

[68] B. Rakhadilov, A. Zhassulan, D. Baizhan, A. Shynarbek, K. Ormanbekov, i T. Aldabergenova, «The effect of the electrolyte composition on the microstructure and properties of coatings formed on a titanium substrate by microarc oxidation», *AIMS Mater. Sci.*, vol 11, no 3, pp 547–564, 2024, doi: 10.3934/MATERSCI.2024027.

[69] B. Shi *et al.*, «Advances in amelioration of plasma electrolytic oxidation coatings on biodegradable magnesium and alloys», *Heliyon*, vol 10, no 4, 2024, doi: 10.1016/j.heliyon.2024.e24348.

[70] C. Zhao, X. Wang, B. Yu, M. Cai, Q. Yu, i F. Zhou, «Research Progress on the Wear and Corrosion Resistant Plasma Electrolytic Oxidation Composite Coatings on Magnesium and Its Alloys», *Coatings*, vol 13, no 7, 2023, doi: 10.3390/coatings13071189.

[71] N. G. Azzahra, J. Widakdo, T. Sudiro, W. S. Hung, i A. Anawati, «Characteristics of plasma electrolytic oxide coating on magnesium-hydroxyapatite composites», *Mater. Lett.*, vol 356, 2024, doi: 10.1016/j.matlet.2023.135601.

[72] Y. Husak *et al.*, «Bioactivity performance of pure mg after plasma electrolytic oxidation in silicate-based solutions», *Molecules*, vol 26, no 7, 2021, doi: 10.3390/molecules26072094.

[73] L. Qiu, C. Zhang, X. Yang, F. Peng, Y. Huang, i Y. He, «A SiO2 layer on PEO-treated Mg for enhanced corrosion resistance and bone regeneration», *Front. Bioeng. Biotechnol.*, vol 10, 2022, doi: 10.3389/fbioe.2022.1053944.

[74] F. Liu, J. Yu, Y. Song, D. Shan, i E. H. Han, «Effect of potassium fluoride on the in-situ sealing pores of plasma electrolytic oxidation film on AM50 Mg alloy», *Mater. Chem. Phys.*, vol 162, pp 452–460, 2015, doi: 10.1016/j.matchemphys.2015.06.014.

[75] H. Sampatirao, S. Radhakrishnapillai, S. Dondapati, E. Parfenov, i R. Nagumothu, «Developments in plasma electrolytic oxidation (PEO) coatings for biodegradable magnesium alloys», *Mater. Today Proc.*, vol 46, pp 1407–1415, 2021, doi: 10.1016/j.matpr.2021.02.650.

[76] X. N. Gu *et al.*, «Corrosion resistance and surface biocompatibility of a microarc oxidation coating on a Mg-Ca alloy», *Acta Biomater.*, vol 7, no 4, pp 1880–1889, 2011, doi: 10.1016/j.actbio.2010.11.034.

[77] A. B. Khiabani, A. Ghanbari, B. Yarmand, A. Zamanian, i M. Mozafari, «Improving corrosion behavior and in vitro bioactivity of plasma electrolytic oxidized AZ91 magnesium alloy using calcium fluoride containing electrolyte», *Mater. Lett.*, vol 212, pp 98–102, 2018, doi: 10.1016/j.matlet.2017.10.072.

[78] P. Valerio, M. M. Pereira, A. M. Goes, i M. F. Leite, «The effect of ionic products from

bioactive glass dissolution on osteoblast proliferation and collagen production», *Biomaterials*, vol 25, no 15, pp 2941–2948, 2004, doi: 10.1016/j.biomaterials.2003.09.086.

[79] Y. F. Wu *et al.*, «In vivo study of microarc oxidation coated biodegradable magnesium plate to heal bone fracture defect of 3 mm width», *Colloids Surfaces B Biointerfaces*, vol 158, pp 147–156, 2017, doi: 10.1016/j.colsurfb.2017.06.031.

[80] L. Xu *et al.*, «Effect of oxidation time on cytocompatibility of ultrafine-grained pure Ti in micro-arc oxidation treatment», *Surf. Coatings Technol.*, vol 342, pp 12–22, 2018, doi: 10.1016/j.surfcoat.2018.02.044.

[81] E. Santos *et al.*, «Effect of anodizing time on the mechanical properties of porous titania coatings formed by micro-arc oxidation», *Surf. Coatings Technol.*, vol 309, pp 203–211, 2017, doi: 10.1016/j.surfcoat.2016.11.063.

[82] K. R. Shin, Y. S. Kim, H. W. Yang, Y. G. Ko, i D. H. Shin, «In vitro biological response to the oxide layer in pure titanium formed at different current densities by plasma electrolytic oxidation», *Appl. Surf. Sci.*, vol 314, pp 221–227, 2014, doi: 10.1016/j.apsusc.2014.06.121.

[83] Y. Wang *et al.*, «Effect of frequency on the structure and cell response of Ca- and P-containing MAO films», *Appl. Surf. Sci.*, vol 256, no 7, pp 2018–2024, 2010, doi: 10.1016/j.apsusc.2009.09.041.

[84] S. Hariprasad, M. Ashfaq, T. Arunnellaiappan, M. Harilal, i N. Rameshbabu, «Role of electrolyte additives on in-vitro corrosion behavior of DC plasma electrolytic oxidization coatings formed on Cp-Ti», *Surf. Coatings Technol.*, vol 292, pp 20–29, 2016, doi: 10.1016/j.surfcoat.2016.03.016.

[85] M. Babaei, C. Dehghanian, P. Taheri, i M. Babaei, «Effect of duty cycle and electrolyte additive on photocatalytic performance of TiO2-ZrO2 composite layers prepared on CP Ti by micro arc oxidation method», *Surf. Coatings Technol.*, vol 307, pp 554–564, 2016, doi: 10.1016/j.surfcoat.2016.09.050.

[86] H. Cimenoglu, M. Gunyuz, G. T. Kose, M. Baydogan, F. Uğurlu, i C. Sener, «Micro-arc oxidation of Ti6Al4V and Ti6Al7Nb alloys for biomedical applications», *Mater. Charact.*, vol 62, no 3, pp 304–311, 2011, doi: 10.1016/j.matchar.2011.01.002.

[87] M. Roknian, A. Fattah-alhosseini, i S. O. Gashti, «Plasma Electrolytic Oxidation Coatings on Pure Ti Substrate: Effects of Na3PO4 Concentration on Morphology and Corrosion Behavior of Coatings in Ringer's Physiological Solution», *J. Mater. Eng. Perform.*, vol 27, no 3, pp 1343–1351, 2018, doi: 10.1007/s11665-018-3236-7.

[88] M. Vakili-Azghandi, A. Fattah-alhosseini, i M. K. Keshavarz, «Optimizing the electrolyte chemistry parameters of PEO coating on 6061 Al alloy by corrosion rate measurement:

Response surface methodology», *Meas. J. Int. Meas. Confed.*, vol 124, pp 252–259, 2018, doi: 10.1016/j.measurement.2018.04.038.

[89] A. Bordbar-Khiabani, S. Ebrahimi, i B. Yarmand, «Highly corrosion protection properties of plasma electrolytic oxidized titanium using rGO nanosheets», *Appl. Surf. Sci.*, vol 486, pp 153–165, 2019, doi: 10.1016/j.apsusc.2019.05.026.

[90] X. Lu *et al.*, «Plasma electrolytic oxidation coatings with particle additions – A review», *Surf. Coatings Technol.*, vol 307, pp 1165–1182, 2016, doi: 10.1016/j.surfcoat.2016.08.055.

[91] N. B. Mohammed *et al.*, «Effect of PMMA sealing treatment on the corrosion behavior of plasma electrolytic oxidized titanium dental implants in fluoride-containing saliva solution», *Mater. Res. Express*, vol 9, no 12, 2022, doi: 10.1088/2053-1591/aca7b5.

[92] I. Patrascu, M. C. Ducu, A. D. Negrea, S. G. Moga, i A. G. Plaiasu, «Overview on plasma electrolytic oxidation of magnesium alloys for medical and engineering applications», *IOP Conf. Ser. Mater. Sci. Eng.*, vol 1251, no 1, p 012001, 2022, doi: 10.1088/1757-899x/1251/1/012001.

[93] Z. Zhang, F. He, C. Huang, Z. Song, J. Yang, i X. Wang, «Effect of Fe3+ and F− on black micro-arc oxidation ceramic coating of magnesium alloy», *Int. J. Appl. Ceram. Technol.*, vol 19, no 4, pp 2203–2212, 2022, doi: 10.1111/ijac.14008.

[94] M. Rahmati, K. Raeissi, M. R. Toroghinejad, A. Hakimizad, i M. Santamaria, «Corrosion and wear resistance of coatings produced on AZ31 Mg alloy by plasma electrolytic oxidation in silicate-based K2TiF6 containing solution: Effect of waveform», *J. Magnes. Alloy.*, vol 10, no 9, pp 2574–2587, 2022, doi: 10.1016/j.jma.2021.07.026.

[95] X. Ma *et al.*, «Influence of combined B4C/C particles on the properties of microarc oxidation coatings on Mg-Li alloy», *Surf. Coatings Technol.*, vol 438, 2022, doi: 10.1016/j.surfcoat.2022.128399.

[96] L. Yu, J. Cao, i Y. Cheng, «An improvement of the wear and corrosion resistances of AZ31 magnesium alloy by plasma electrolytic oxidation in a silicate-hexametaphosphate electrolyte with the suspension of SiC nanoparticles», *Surf. Coatings Technol.*, vol 276, pp 266–278, 2015, doi: 10.1016/j.surfcoat.2015.07.014.

[97] X. Jin *et al.*, «β-TCP particles additive synergistically improves corrosion resistance and biocompatibility of micro-arc oxide coated magnesium alloy», *Mater. Today Commun.*, vol 36, 2023, doi: 10.1016/j.mtcomm.2023.106694.

[98] J. Lv i Y. Cheng, «Amorphous coatings on tantalum formed by plasma electrolytic oxidation in aluminate electrolyte and high temperature crystallization treatment», *Surf. Coatings Technol.*, vol 434, 2022, doi: 10.1016/j.surfcoat.2022.128171.

[99] Y. Wang, D. Wei, J. Yu, i S. Di, «Effects of Al2O3 nano-additive on performance of micro-arc oxidation coatings formed on AZ91D Mg alloy», *J. Mater. Sci. Technol.*, vol 30, no 10, pp 984–990, 2014, doi: 10.1016/j.jmst.2014.03.006.

[100] M. Gheytani, M. Aliofkhazraei, H. R. Bagheri, H. R. Masiha, i A. S. Rouhaghdam, «Wettability and corrosion of alumina embedded nanocomposite MAO coating on nanocrystalline AZ31B magnesium alloy», *J. Alloys Compd.*, vol 649, pp 666–673, 2015, doi: 10.1016/j.jallcom.2015.07.139.

[101] A. Keyvani, M. Zamani, M. Bahamirian, E. Nikoomanzari, A. Fattah-alhosseini, i H. Sina, «Role of incorporation of ZnO nanoparticles on corrosion behavior of ceramic coatings developed on AZ31 magnesium alloy by plasma electrolytic oxidation technique», *Surfaces and Interfaces*, vol 22, 2021, doi: 10.1016/j.surfin.2020.100728.

[102] S. Esmaili, T. Ahmadi, A. A. Nourbakhsh, H. R. Bakhsheshi-Rad, i F. Berto, «Corrosion Behavior and Biocompatibility of Graphene Oxide-Plasma Electrolytic Oxidation Coating on Magnesium Alloy», *Phys. Mesomech.*, vol 25, no 6, pp 583–599, 2022, doi: 10.1134/S1029959922060108.

[103] C. Yang, L. Sheng, C. C. Zhao, D. Wu, i Y. Zheng, «Regulating the ablation of nanoparticle-doped MAO coating on Mg alloy by MgF2 passivation layer construction», *Mater. Lett.*, vol 355, 2024, doi: 10.1016/j.matlet.2023.135559.

[104] C. Yang *et al.*, «NaF assisted preparation and the improved corrosion resistance of high content ZnO doped plasma electrolytic oxidation coating on AZ31B alloy», *J. Magnes. Alloy.*, 2023, doi: 10.1016/j.jma.2023.02.008.

[105] W. Liang *et al.*, «Prospective applications of bioactive materials in orthopedic therapies: A review», *Heliyon*, vol 10, no 16, 2024, doi: 10.1016/j.heliyon.2024.e36152.

[106] S. Askari, E. Yazdani, L. Arabuli, H. Goldadi, S. A. Shahidi Marnani, i M. Emami, «Invitro and invivo examination for bioceramic degradation», *J. Compos. Compd.*, vol 4, no 12, pp 169–175, 2022, doi: 10.52547/jcc.4.3.7.

[107] Q. Han *et al.*, «Fabrication of Ag containing antibacterial PEO coatings on pure Mg», *Mater. Lett.*, vol 293, 2021, doi: 10.1016/j.matlet.2021.129731.

[108] E. Zhang, X. Zhao, J. Hu, R. Wang, S. Fu, i G. Qin, «Antibacterial metals and alloys for potential biomedical implants», *Bioact. Mater.*, vol 6, no 8, pp 2569–2612, 2021, doi: 10.1016/j.bioactmat.2021.01.030.

[109] K. M. Lee, K. R. Shin, S. Namgung, B. Yoo, i D. H. Shin, «Electrochemical response of ZrO2-incorporated oxide layer on AZ91 Mg alloy processed by plasma electrolytic oxidation», *Surf. Coatings Technol.*, vol 205, no 13–14, pp 3779–3784, 2011, doi:

10.1016/j.surfcoat.2011.01.033.

[110] M. Mujtaba *et al.*, «Lignocellulosic biomass from agricultural waste to the circular economy: a review with focus on biofuels, biocomposites and bioplastics», *J. Clean. Prod.*, vol 402, 2023, doi: 10.1016/j.jclepro.2023.136815.

[111] A. Ridwan, M. N. Uddin, A. K. Neon, i M. A. Bappy, «Advances in Green Biomaterials for Biomedical Implants and Tissue Engineering», pp 479–502, 2025, doi: 10.1007/978-3-031-79110-9_17.

[112] B. Makurat-Kasprolewicz *et al.*, «Green engineered biomaterials for bone repair and regeneration: Printing technologies and fracture analysis», *Chem. Eng. J.*, vol 494, 2024, doi: 10.1016/j.cej.2024.152703.

[113] N. Jiang *et al.*, «Promoting osseointegration of Ti implants through micro/nanoscaled hierarchical Ti phosphate/Ti oxide hybrid coating», *ACS Nano*, vol 12, no 8, pp 7883–7891, 2018, doi: 10.1021/acsnano.8b02227.

[114] S. Lossdörfer *et al.*, «Microrough implant surface topographies increase osteogenesis by reducing osteoclast formation and activity», *J. Biomed. Mater. Res. - Part A*, vol 70, no 3, pp 361–369, 2004, doi: 10.1002/jbm.a.30025.

[115] Y. Su, I. Cockerill, Y. Zheng, L. Tang, Y. X. Qin, i D. Zhu, «Biofunctionalization of metallic implants by calcium phosphate coatings», *Bioact. Mater.*, vol 4, pp 196–206, 2019, doi: 10.1016/j.bioactmat.2019.05.001.

[116] J. K. Singh i H. S. Lee, «Enhanced corrosion resistance properties of 15Al-85Zn coating by post-treatment with sodium hexa-meta phosphate in saline solution», *Corros. Sci.*, vol 226, 2024, doi: 10.1016/j.corsci.2023.111684.

[117] F. M. C. Gonçalves *et al.*, «Remineralizing effect of a fluoridated gel containing sodium hexametaphosphate: An in vitro study», *Arch. Oral Biol.*, vol 90, pp 40–44, 2018, doi: 10.1016/j.archoralbio.2018.03.001.

[118] W. J. Bae, S. S. Jue, S. Y. Kim, J. H. Moon, i E. C. Kim, «Effects of sodium tri- and hexametaphosphate on proliferation, differentiation, and angiogenic potential of human dental pulp cells», *J. Endod.*, vol 41, no 6, pp 896–902, 2015, doi: 10.1016/j.joen.2015.01.038.

[119] J. Li, T. Zhang, Z. Liao, Y. Wei, R. Hang, i D. Huang, «Engineered functional doped hydroxyapatite coating on titanium implants for osseointegration», *J. Mater. Res. Technol.*, vol 27, pp 122–152, 2023, doi: 10.1016/j.jmrt.2023.09.239.

[120] S. Mondal *et al.*, «Hydroxyapatite: A journey from biomaterials to advanced functional materials», *Adv. Colloid Interface Sci.*, vol 321, 2023, doi: 10.1016/j.cis.2023.103013.

[121] M. Ramazanoglu i Y. Oshi, «Osseointegration and Bioscience of Implant Surfaces - Current Concepts at Bone-Implant Interface», *Implant Dent. - A Rapidly Evol. Pract.*, 2011, doi: 10.5772/16936.

[122] O. Suzuki, «Octacalcium phosphate (OCP)-based bone substitute materials», *Jpn. Dent. Sci. Rev.*, vol 49, no 2, pp 58–71, 2013, doi: 10.1016/j.jdsr.2013.01.001.

[123] I. O. Oladele, S. A. Adekola, N. I. Agbeboh, B. A. Isola-Makinde, i B. O. Adewuyi, «Synthesis and Application of Sustainable Tricalcium Phosphate Based Biomaterials From Agro-Based Materials: A Review», *Biomed. Eng. Comput. Biol.*, vol 15, 2024, doi: 10.1177/11795972241293525.

[124] M.-L. Fontaine, C. Combes, T. Sillam, G. Dechambre, i C. Rey, «New Calcium Carbonate-Based Cements for Bone Reconstruction», *Key Eng. Mater.*, vol 284–286, pp 105–108, 2005, doi: 10.4028/www.scientific.net/kem.284-286.105.

[125] D. Pham Minh, N. Lyczko, H. Sebei, A. Nzihou, i P. Sharrock, «Synthesis of calcium hydroxyapatite from calcium carbonate and different orthophosphate sources: A comparative study», *Mater. Sci. Eng. B*, vol 177, no 13, pp 1080–1089, 2012, doi: 10.1016/j.mseb.2012.05.007.

[126] X. Xia, J. Chen, J. Shen, D. Huang, P. Duan, i G. Zou, «Synthesis of hollow structural hydroxyapatite with different morphologies using calcium carbonate as hard template», *Adv. Powder Technol.*, vol 29, no 7, pp 1562–1570, 2018, doi: 10.1016/j.apt.2018.03.021.

[127] Z. S. Abdullah, M. S. Mahmood, F. M. A. Abdul-Ameer, i A. A. Fatalla, «Effect of commercially pure titanium implant coated with calcium carbonate and nanohydroxyapatite mixture on osseointegration», *J. Med. Life*, vol 2023, no 1, pp 52–61, 2023, doi: 10.25122/jml-2022-0049.

[128] O. Oleshko *et al.*, «In vitro biological characterization of silver-doped anodic oxide coating on titanium», *Materials (Basel).*, vol 13, no 19, pp 1–12, 2020, doi: 10.3390/ma13194359.

[129] M. Ezzahmouly *et al.*, «Micro-computed tomographic and SEM study of porous bioceramics using an adaptive method based on the mathematical morphological operations», *Heliyon*, vol 5, no 12, 2019, doi: 10.1016/j.heliyon.2019.e02557.

[130] M. Ignatova *et al.*, «Bio-Based Electrospun Fibers from Chitosan Schiff Base and Polylactide and Their Cu2+ and Fe3+ Complexes: Preparation and Antibacterial and Anticancer Activities», *Polymers (Basel).*, vol 14, no 22, 2022, doi: 10.3390/polym14225002.

[131] C. T. Rueden *et al.*, «ImageJ2: ImageJ for the next generation of scientific image data», *BMC Bioinformatics*, vol 18, no 1, 2017, doi: 10.1186/s12859-017-1934-z.

[132] P. Karlova *et al.*, «Comparison of 2D and 3D Plasma Electrolytic Oxidation (PEO)-Based Coating Porosity Data Obtained by X-ray Tomography Rendering and a Classical Metallographic Approach», *Materials (Basel).*, vol 15, no 18, 2022, doi: 10.3390/ma15186315.

[133] R. Pasricha i D. Sachdev, «Biological characterization of nanofiber composites», *Nanofiber Compos. Biomed. Appl.*, pp 157–196, 2017, doi: 10.1016/B978-0-08-100173-8.00007-7.

[134] K. Diedkova *et al.*, «Novel electrically conductive electrospun PCL-MXene scaffolds for cardiac tissue regeneration», *Graphene 2D Mater.*, vol 9, no 1–2, pp 59–76, 2024, doi: 10.1007/s41127-023-00071-5.

[135] S. S. Latthe, C. Terashima, K. Nakata, i A. Fujishima, «Superhydrophobic surfaces developed by mimicking hierarchical surface morphology of lotus leaf», *Molecules*, vol 19, no 4, pp 4256–4283, 2014, doi: 10.3390/molecules19044256.

[136] H. T. Jaafar i B. M. D. Aldabbagh, «Investigation of superhydrophobic/hydrophobic materials properties using electrospinning technique», *Baghdad Sci. J.*, vol 16, no 3, pp 632–638, 2019, doi: 10.21123/bsj.2019.16.3.0632.

[137] Y. Husak *et al.*, «Antibacterial coatings on magnesium formed via plasma electrolytic oxidation in CuO suspension», *Mater. Chem. Phys.*, vol 323, 2024, doi: 10.1016/j.matchemphys.2024.129627.

[138] S. Kyrylenko *et al.*, «MXene-Assisted Ablation of Cells with a Pulsed Near-Infrared Laser», *ACS Appl. Mater. Interfaces*, vol 14, no 25, pp 28683–28696, 2022, doi: 10.1021/acsami.2c08678.

[139] S. Kyrylenko *et al.*, «Effects of the sources of calcium and phosphorus on the structural and functional properties of ceramic coatings on titanium dental implants produced by plasma electrolytic oxidation», *Mater. Sci. Eng. C*, vol 119, 2021, doi: 10.1016/j.msec.2020.111607.

[140] V. Korniienko *et al.*, «Biological Behaviour of Chitosan Electrospun Nanofibrous Membranes After Different Neutralisation Methods», *Prog. Chem. Appl. Chitin its Deriv.*, vol 27, pp 135–153, 2022, doi: 10.15259/pcacd.27.010.

[141] J. Dou, J. Wang, H. Li, Y. Lu, H. Yu, i C. Chen, «Enhanced corrosion resistance of magnesium alloy by plasma electrolytic oxidation plus hydrothermal treatment», *Surf. Coatings Technol.*, vol 424, 2021, doi: 10.1016/j.surfcoat.2021.127662.

[142] S. Jalota, S. B. Bhaduri, i A. C. Tas, «Using a synthetic body fluid (SBF) solution of 27 mM HCO3- to make bone substitutes more osteointegrative», *Mater. Sci. Eng. C*, vol 28, no 1, pp 129–140, 2008, doi: 10.1016/j.msec.2007.10.058.

[143] C. Blawert i P. Bala Srinivasan, «Plasma electrolytic oxidation treatment of magnesium alloys», *Surf. Eng. Light Alloy. Alum. Magnes. Titan. Alloy.*, pp 155–183, 2010, doi: 10.1533/9781845699451.2.155.

[144] D. Y. Hwang, Y. M. Kim, i D. H. Shin, «Corrosion resistance of plasma-anodized AZ91 Mg alloy in the electrolyte with/without potassium fluoride», *Mater. Trans.*, vol 50, no 3, pp 671–678, 2009, doi: 10.2320/matertrans.MER2008345.

[145] Z. Wang, Y. Ma, i Y. Wang, «Effect of v2o5 additive on micro-arc oxidation coatings fabricated on magnesium alloys with different loading voltages», *Metals (Basel).*, vol 10, no 9, pp 1–14, 2020, doi: 10.3390/met10091146.

[146] M. Sarkar, M. Hasanuzzaman, F. Gulshan, i A. Rashid, «Surface, Mechanical and Shape Memory Properties of Biodegradable Polymers and Their Applications», *Encycl. Mater. Plast. Polym.*, vol 1–4, pp 1092–1099, 2022, doi: 10.1016/B978-0-12-820352-1.00050-X.

[147] D. E. Heath i S. L. Cooper, «Polymers: Basic Principles», *Biomater. Sci. An Introd. to Mater. Third Ed.*, pp 64–79, 2013, doi: 10.1016/B978-0-08-087780-8.00008-5.

[148] A. Saini, H. Messenger, i L. Kisley, «Fluorophores 'turned-On' by Corrosion Reactions Can Be Detected at the Single-Molecule Level», *ACS Appl. Mater. Interfaces*, vol 13, no 1, pp 2000–2006, 2021, doi: 10.1021/acsami.0c18994.

[149] A. Fattah-alhosseini, R. Chaharmahali, i K. Babaei, «Effect of particles addition to solution of plasma electrolytic oxidation (PEO) on the properties of PEO coatings formed on magnesium and its alloys: A review», *J. Magnes. Alloy.*, vol 8, no 3, pp 799–818, 2020, doi: 10.1016/j.jma.2020.05.001.

[150] A. Anawati, M. F. Fitriana, i M. D. Gumelar, «Improved corrosion resistance of magnesium alloy az31 in ringer lactate by bilayer anodic film/beeswax–colophony», *Coatings*, vol 11, no 5, 2021, doi: 10.3390/coatings11050564.

[151] S. Elmore, «Apoptosis: A Review of Programmed Cell Death», *Toxicol. Pathol.*, vol 35, no 4, pp 495–516, 2007, doi: 10.1080/01926230701320337.

[152] A. Fattah-alhosseini, M. Molaei, M. Nouri, i K. Babaei, «Antibacterial activity of bioceramic coatings on Mg and its alloys created by plasma electrolytic oxidation (PEO): A review», *J. Magnes. Alloy.*, vol 10, no 1, pp 81–96, 2022, doi: 10.1016/j.jma.2021.05.020.

[153] L. Ren, X. Lin, L. Tan, i K. Yang, «Effect of surface coating on antibacterial behavior of magnesium based metals», *Mater. Lett.*, vol 65, no 23–24, pp 3509–3511, 2011, doi: 10.1016/j.matlet.2011.07.109.

[154] M. L. Verma i H. D. Sahu, «Ionic conductivity and dielectric behavior of PEO-based silver ion conducting nanocomposite polymer electrolytes», *Ionics (Kiel).*, vol 21, no 12, pp 3223–

3231, 2015, doi: 10.1007/s11581-015-1517-9.

[155] Y. Husak *et al.*, «Influence of silver nanoparticles addition on antibacterial properties of PEO coatings formed on magnesium», *Appl. Surf. Sci.*, vol 654, 2024, doi: 10.1016/j.apsusc.2024.159387.

[156] R. Yahya i N. M. Alharbi, «Biosynthesized silver nanoparticles-capped chondroitin sulfate nanogel targeting microbial infections and biofilms for biomedical applications», *Int. J. Biol. Macromol.*, vol 253, 2023, doi: 10.1016/j.ijbiomac.2023.127080.

[157] I. X. Yin, J. Zhang, I. S. Zhao, M. L. Mei, Q. Li, i C. H. Chu, «The antibacterial mechanism of silver nanoparticles and its application in dentistry», *Int. J. Nanomedicine*, vol 15, pp 2555–2562, 2020, doi: 10.2147/IJN.S246764.

[158] J. Sovík *et al.*, «The Effect of Mechanical Pretreatment on the Electrochemical Characteristics of PEO Coatings Prepared on Magnesium Alloy AZ80», *Materials (Basel).*, vol 16, no 16, 2023, doi: 10.3390/ma16165650.

[159] Y. Zhang *et al.*, «Incorporation of magnesium phosphate into magnesium oxide on Mg[sbnd]Ag alloy through plasma electrolytic oxidation», *Surf. Coatings Technol.*, vol 447, 2022, doi: 10.1016/j.surfcoat.2022.128822.

[160] A. Ghasemi, V. S. Raja, C. Blawert, W. Dietzel, i K. U. Kainer, «The role of anions in the formation and corrosion resistance of the plasma electrolytic oxidation coatings», *Surf. Coatings Technol.*, vol 204, no 9–10, pp 1469–1478, 2010, doi: 10.1016/j.surfcoat.2009.09.069.

[161] Z. Li *et al.*, «Effect of phosphate additive on the morphology and anti-corrosion performance of plasma electrolytic oxidation coatings on magnesium—lithium alloy», *Corros. Sci.*, vol 157, pp 295–304, 2019, doi: 10.1016/j.corsci.2019.06.005.

[162] S. Cheng, D. Wei, Y. Zhou, i H. Guo, «Characterization and properties of microarc oxidized coatings containing Si, Ca and Na on titanium», *Ceram. Int.*, vol 37, no 6, pp 1761–1768, 2011, doi: 10.1016/j.ceramint.2011.03.006.

[163] A. Heydarian, M. Atapour, A. Hakimizad, i K. Raeissi, «The effects of anodic amplitude and waveform of applied voltage on characterization and corrosion performance of the coatings grown by plasma electrolytic oxidation on AZ91 Mg alloy from an aluminate bath», *Surf. Coatings Technol.*, vol 383, 2020, doi: 10.1016/j.surfcoat.2019.125235.

[164] N. Mehri Ghahfarokhi, B. Shayegh Broujeny, A. Hakimizad, i A. Doostmohammadi, «Plasma electrolytic oxidation (PEO) coating to enhance in vitro corrosion resistance of AZ91 magnesium alloy coated with polydimethylsiloxane (PDMS)», *Appl. Phys. A Mater. Sci. Process.*, vol 128, no 2, 2022, doi: 10.1007/s00339-021-05239-5.

[165] M. Štrbák *et al.*, «Effect of Plasma Electrolytic Oxidation on the Short-Term Corrosion Behaviour of AZ91 Magnesium Alloy in Aggressive Chloride Environment», *Coatings*, vol 12, no 5, 2022, doi: 10.3390/coatings12050566.

[166] Y. Yildiz, M. M. Sundaram, K. P. Rajurkar, i A. Altintas, «Correlation of surface roughness and recast layer thickness in electrical discharge machining», *Proc. Inst. Mech. Eng. Part E J. Process Mech. Eng.*, vol 231, no 3, pp 414–424, 2017, doi: 10.1177/0954408915600949.

[167] P. B. Srinivasan, C. Blawert, M. Störmer, i W. Dietzel, «Characterisation of tribological and corrosion behaviour of plasma electrolytic oxidation coated AM50 magnesium alloy», *Surf. Eng.*, vol 26, no 5, pp 340–346, 2010, doi: 10.1179/174329409X379246.

[168] M. Mohedano, C. Blawert, i M. L. Zheludkevich, «Silicate-based Plasma Electrolytic Oxidation (PEO) coatings with incorporated CeO2 particles on AM50 magnesium alloy», *Mater. Des.*, vol 86, pp 735–744, 2015, doi: 10.1016/j.matdes.2015.07.132.

[169] E. Cakmak, K. C. Tekin, U. Malayoglu, i S. Shrestha, «The effect of substrate composition on the electrochemical and mechanical properties of PEO coatings on Mg alloys», *Surf. Coatings Technol.*, vol 204, no 8, pp 1305–1313, 2010, doi: 10.1016/j.surfcoat.2009.10.012.

[170] D. M. Baghdadabad, A. R. M. Baghdadabad, i S. M. M. Khoei, «Characterization of bioactive ceramic coatings synthesized by plasma electrolyte oxidation on AZ31 magnesium alloy having different Na2SiO3·9H2O concentrations», *Mater. Today Commun.*, vol 25, 2020, doi: 10.1016/j.mtcomm.2020.101642.

[171] R. Podgórski, M. Wojasiński, i T. Ciach, «Nanofibrous materials affect the reaction of cytotoxicity assays», *Sci. Rep.*, vol 12, no 1, 2022, doi: 10.1038/s41598-022-13002-w.

[172] B. Vieira-da-Silva i M. A. R. B. Castanho, «Resazurin Reduction-Based Assays Revisited: Guidelines for Accurate Reporting of Relative Differences on Metabolic Status», *Molecules*, vol 28, no 5, 2023, doi: 10.3390/molecules28052283.

[173] Z. Yao, L. Li, i Z. Jiang, «Adjustment of the ratio of Ca/P in the ceramic coating on Mg alloy by plasma electrolytic oxidation», *Appl. Surf. Sci.*, vol 255, no 13–14, pp 6724–6728, 2009, doi: 10.1016/j.apsusc.2009.02.082.

[174] D. dong Wang *et al.*, «Evolution process of the plasma electrolytic oxidation (PEO) coating formed on aluminum in an alkaline sodium hexametaphosphate ((NaPO3)6) electrolyte», *J. Alloys Compd.*, vol 798, pp 129–143, 2019, doi: 10.1016/j.jallcom.2019.05.253.

[175] S. Luo, Q. Wang, R. Ye, i C. S. Ramachandran, «Effects of electrolyte concentration on the microstructure and properties of plasma electrolytic oxidation coatings on Ti-6Al-4V

alloy», *Surf. Coatings Technol.*, vol 375, pp 864–876, 2019, doi: 10.1016/j.surfcoat.2019.07.053.

[176] O. Banakh *et al.*, «The influence of the electrolyte nature and PEO process parameters on properties of anodized Ti-15Mo alloy intended for biomedical applications», *Metals (Basel).*, vol 8, no 5, 2018, doi: 10.3390/met8050370.

[177] J. Zhuang, R. Song, H. Li, i N. Xiang, «Effect of Various Additives on Performance of Plasma Electrolytic Oxidation Coatings Formed on AZ31 Magnesium Alloy in the Phosphate Electrolytes», *J. Wuhan Univ. Technol. Mater. Sci. Ed.*, vol 33, no 3, pp 703–709, 2018, doi: 10.1007/s11595-018-1881-1.

[178] P. H. Sobrinho, Y. Savguira, Q. Ni, i S. J. Thorpe, «Statistical analysis of the voltage-time response produced during PEO coating of AZ31B magnesium alloy», *Surf. Coatings Technol.*, vol 315, pp 530–545, 2017, doi: 10.1016/j.surfcoat.2017.02.029.

[179] A. Zaeri, K. Cao, F. Zhang, R. Zgeib, i R. C. Chang, «A review of the structural and physical properties that govern cell interactions with structured biomaterials enabled by additive manufacturing», *Bioprinting*, vol 26, 2022, doi: 10.1016/j.bprint.2022.e00201.

[180] M. Seyfi, A. Fattah-alhosseini, M. Pajohi-Alamoti, i E. Nikoomanzari, «Effect of ZnO nanoparticles addition to PEO coatings on AZ31B Mg alloy: antibacterial effect and corrosion behavior of coatings in Ringer's physiological solution», *J. Asian Ceram. Soc.*, 2021, doi: 10.1080/21870764.2021.1940728.

[181] M. Sowa *et al.*, «Bioactivity of coatings formed on Ti-13Nb-13Zr alloy using plasma electrolytic oxidation», *Mater. Sci. Eng. C*, vol 49, pp 159–173, 2015, doi: 10.1016/j.msec.2014.12.073.

[182] F. Rupp *et al.*, «A review on the wettability of dental implant surfaces I: Theoretical and experimental aspects», *Acta Biomater.*, vol 10, no 7, pp 2894–2906, 2014, doi: 10.1016/j.actbio.2014.02.040.

[183] J. Li, J. Wang, Y. Liu, D. Bian, i Y. Zhao, «Surface modification of ceramic coating for enhanced hydrophobicity and wear properties», *Int. J. Appl. Ceram. Technol.*, vol 19, no 5, pp 2648–2663, 2022, doi: 10.1111/ijac.14103.

[184] Z. Q. Zhang *et al.*, «Corrosion resistance and superhydrophobicity of one-step polypropylene coating on anodized AZ31 Mg alloy», *J. Magnes. Alloy.*, vol 9, no 4, pp 1443–1457, 2021, doi: 10.1016/j.jma.2020.06.011.

[185] M. Crago, A. Lee, T. P. Hoang, S. Talebian, i S. Naficy, «Protein adsorption on blood-contacting surfaces: A thermodynamic perspective to guide the design of antithrombogenic polymer coatings», *Acta Biomater.*, vol 180, pp 46–60, 2024, doi:

10.1016/j.actbio.2024.04.018.

[186] M. Ferrari, F. Cirisano, i M. Carmen Morán, «Mammalian cell behavior on hydrophobic substrates: Influence of surface properties», *Colloids and Interfaces*, vol 3, no 2, 2019, doi: 10.3390/colloids3020048.

RESEARCH OUTPUTS

Papers related to the doctoral thesis

1. **Husak Yevheniia**, Olszaniecki Jan, Pykacz Justyna, Ossowska Agnieszka, Blacha-Grzechnik Agata, Waloszczyk Natalia, Babilas Dorota, Varava Yuliia, Korniienko Viktoriia, Diedkova Kateryna, Kyrylenko Sergiy, Aden Hodzic, Manfred Krichbaum, Xiaopeng Lu, Dryhval Bohdan, Pogorielov Maksym, Simka Wojciech: Influence of silver nanoparticles addition on antibacterial properties of PEO coatings formed on magnesium, Applied Surface Science, Elsevier BV - North-Holland, vol. 654, 2024, Article number: 159387, pp. 1-17, DOI:10.1016/j.apsusc.2024.159387.
2. **Husak Yevheniia**, Pogorielov Maksym, and Simka Wojciech: Influence of silicates and phosphates anions on the formation of ceramic coatings on magnesium - Engineering of Biomaterials no. 172, 2024, p 04. doi:10.34821/eng.biomat.172.2024.04
3. Dryhval Bohdan, **Husak Yevheniia**, Sulaieva Oksana, Deineka Volodymyr, Pernakov Mykola, Lyndin Mykola, Romaniuk Anatoli, Simka Wojciech, and Pogorielov Maksym: In Vivo Safety of New Coating for Biodegradable Magnesium Implants - Materials 16, 2023, no. 17: 5807. https://doi.org/10.3390/ma16175807.

Papers not related to the doctoral thesis

1. **Husak Yevheniia**, Ma Jirui, Wala-Kapica Marta, Leśniak-Ziółkowska Katarzyna, Babilas Dorota, Blacha-Grzechnik Agata, Dulski Mateusz, Gawecki Robert, Pogorielov Maksym, Simka Wojciech: Antibacterial coatings on magnesium formed via plasma electrolytic oxidation in CuO suspension, Materials Chemistry and Physics, ELSEVIER SCIENCE SA, vol. 323, 2024, Article number: 129627, pp. 1-13, DOI:10.1016/j.matchemphys.2024.129627.
2. **Husak Yevheniia**, Grebnevs Vladlens, Altundal Sahin, Kazek-Kesik Alicja, Yanovska Anna, Maciej Artur, Gudakov Oleksii, Korniienko Victoriia, Viter Roman, Pogorielov Maksym, Simka Wojciech: Effect Of CaP-particles on Ceramic-like Coatings Formed on Magnesium via Anodisation,, 01–04, 2022 IEEE 12th International Conference "Nanomaterials: Applications & Properties" (IEEE NAP-2022) Krakow, Poland, Sep. 11-16, 2022 https://doi.org/10.1109/nap55339.2022.9934636.
3. Samokhin Yevhen, Varava Yuliia, Diedkova Kateryna, Yanko Ilya, Korniienko Valeriia, **Husak Yevheniia**, Iatsunskyi Igor, Grebnevs Vladlens, Bertiņs Maris, Banasiuk Rafal: Electrospun chitosan/polylactic acid nanofibers with silver nanoparticles: structure, antibacterial, and cytotoxic properties, ACS Applied Bio Materials, American Chemical Society, vol. 8, no. 2, 2025, pp. 1027-1037, DOI:10.1021/acsabm.4c01252.

4. Butsyk Anna, Varava Yulia, Moskalenko Roman, **Husak Yevheniia**, Piddubnyi Artem, Denysenko Anastasiia, Korniienko Valeriia, Ramanaviciute Agne, Banasiuk Rafal, Pogorielov Maksym: Copper nanoparticle loaded electrospun patches for infected wound treatment: from development to in-vivo application, Polymers, MDPI, vol. 16, no. 19, 2024, Article number: 2733, pp. 1-18, DOI:10.3390/polym16192733.

5. Holubnycha Viktoriia, **Husak Yevheniia**, Korniienko Viktoriia, Bolshanina Svetlana, Tveresovska Olesia, Myronov Petro, Holubnycha Marharyta, Butsyk Anna, Borén Thomas, Banasiuk Rafal: Antimicrobial activity of two different types of silver nanoparticles against wide range of pathogenic bacteria, Nanomaterials, MDPI, vol. 14, no. 2, 2024, Article number: 137, pp. 1-19, DOI:10.3390/nano14020137.

6. Diedkova Kateryna, Pogrebnjak Alexander D., Kyrylenko Sergiy, Smyrnova Kateryna, Buranich Vladimir V., Horodek Pawel, **Husak Yevheniia**, Simka Wojciech, Stolarczyk Agnieszka, Blacha-Grzechnik Agata: Polycaprolactone - MXene nanofibrous scaffolds for tissue engineering, ACS Applied Materials & Interfaces, American Chemical Society, vol. 15, no. 11, 2023, pp. 14033-14047, DOI:10.1021/acsami.2c22780.

7. Kyrylenko Sergiy, Sowa Maciej, Kazek-Kęsik Alicja, Stolarczyk Agnieszka, Pisarek Marcin, **Husak Yevheniia**, Korniienko Viktoriia, Michalska Joanna, Jakóbik-Kolon Agata, Simka Wojciech: Nitrilotriacetic acid improves plasma electrolytic oxidation of titanium for biomedical applications, ACS Applied Materials & Interfaces, American Chemical Society, vol. 15, no. 16, 2023, pp. 19863-19876, DOI:10.1021/acsami.3c00170.

8. Samokhin Yevhen, Varava Yuliia, Diedkova Kateryna, Yanko Ilya, **Husak Yevheniia**, Radwan-Pragłowska Julia, Pogorielova Oksana, Janus Łukasz, Pogorielov Maksym, Korniienko Viktoriia: Fabrication and characterization of electrospun chitosan/polylactic acid (CH/PLA) nanofiber scaffolds for biomedical application, Journal of Functional Biomaterials, MDPI, vol. 14, no. 8, 2023, Article number: 414, pp. 1-17, DOI:10.3390/jfb14080414.

9. Mishchenko Oleg, Yanovska Anna, Sulaieva Oksana, Moskalenko Roman, Pernakov Mykola, **Husak Yevheniia**, Korniienko Viktoriia, Deineka Volodymyr, Kosinov Oleksii, Varakuta Olga: From synthesis to clinical trial: novel bioinductive calcium deficient HA/β-TCP bone grafting nanomaterial, Nanomaterials, MDPI, vol. 13, no. 12, 2023, Article number: 1876, pp. 1-20, DOI:10.3390/nano13121876.

10. Diedkova Kateryna, **Husak Yevheniia**, Simka Wojciech, Korniienko Viktoriia, Petrovic Bojan, Roshchupkin Anton, Stolarczyk Agnieszka, Waloszczyk Natalia, Yanko Ilya, Jekabsons Kaspars: Novel electrically conductive electrospun PCL-MXene scaffolds for cardiac tissue

regeneration, Graphene and 2D Materials Technologies, Springer Nature, vol. 9, 2023, pp. 59-76, DOI:10.1007/s41127-023-00071-5.

11. Kyrylenko Sergiy, Gogotsi Oleksiy, Baginskiy Ivan, Balitskyi Vitalii, Zahorodna Veronika, **Husak Yevheniia**, Yanko Ilya, Pernakov Mykolay, Roshchupkin Anton, Lyndin Mykola: MXene-assisted ablation of cells with a pulsed near-infrared laser, ACS Applied Materials & Interfaces, American Chemical Society, vol. 14, no. 25, 2022, pp. 28683-28696, DOI:10.1021/acsami.2c08678.

12. Korniienko Viktoriia, **Husak Yevheniia**, Radwan-Pragłowska Julia, Holubnycha Viktoriia, Samokhin Yevhen, Yanovska Anna, Varava Julia, Diedkova Kateryna, Janus Łukasz, Pogorielov Maksym: Impact of electrospinning parameters and post-treatment method on antibacterial and antibiofilm activity of chitosan nanofibers, Molecules, MDPI, vol. 27, no. 10, 2022, Article number: 3343, pp. 1-14, DOI:10.3390/molecules27103343.

13. Korniienko Viktoriia, **Husak Yevheniia**, Yanovska Anna, Altundal Şahin, Diedkova Kateryna, Samokhin Yevhen, Varava Yuliia, Holubnycha Viktoriia, Viter Roman: Biological behaviour of chitosan electrospun nanofibrous membranes after different neutralisation methods, Progress on Chemistry and Application of Chitin and Its Derivatives, Polish Chitin Society, vol. 27, 2022, pp. 135-153, DOI:10.15259/pcacd.27.010.

14. Saqib Muhammad, Beshchasna Natalia, Pelaccia Riccardo, Roshchupkin Anton, Yanko Ilya, **Husak Yevheniia**, Kyrylenko Sergiy, Reggiani Barbara, Cuniberti Gianaurelio, Pogorielov Maksym: Tailoring surface properties, biocompatibility and corrosion behavior of stainless steel by laser induced periodic surface treatment towards developing biomimetic stents, Surfaces and Interfaces, Elsevier BV, vol. 34, 2022, Article number: 102365, pp. 1-12, DOI:10.1016/j.surfin.2022.102365.

Participation in conferencest related to the doctoral thesis:

1. **Yevheniia Husak,** Sergiy Kyrylenko, Kukurika Vyacheslav, Maksym Pogorielov, Wojciech Simka. Reduction of Resazurin by Metallic Magnesium in Cell Culture Medium. UK-Poland-Ukraine Bioinspired Materials Conference 2022, 29-30 November 2022, online.
2. **Yevheniia Husak**, Joanna Michalska, Maksym Pogorielov, Wojciech Simka. Anodization as a recycling technology for fabrication multifunctional biocoatings. The Regional Meeting of the International Society of Electrochemistry, Praha, August 15th to 19 th , 2022.
3. **Yevheniia Husak.** Surface Modification of Ti and Mg for Bone Tissue Implants. 80 th International Scientific Conference of the University of Latvia, 11 February 2022(online).

4. **Yevheniia Husak**, Agnieszka Ossowska, Viktoriia Korniienko, Anna Yanovska, Maksym Pogorielov, Wojciech Simka. Effects of anodization parameters on physicochemical properties of the oxide coatings on magnesium. Leipzig University, 22 April 2022: Chance for Science Conference 2022, a conference for academics affected by the war in Ukraine (online).

5. **Yevheniia Husak**, Anna Skoczylas, Natalia Waloszczyk, Maksym Pogorielov, Wojciech Simka. Impact of Silicates and Phosphates on The Properties of Anodized Magnesium Implants.2023 IEEE 13th International Conference Nanomaterials: Applications & Properties Bratislava, SLOVAKIA, Sep. 10-15, 2023.

6. **Yevheniia Husak**, Anna Yanovska, Natalia Waloszczyk, Maksym Pogorielov, Wojciech Simka. The Fusion of Nature and Technology: Bioceramic Coatings for Magnesium Alloy Implants. NAP 2024, 8-13 September,2024, Ryga, Latvia.

7. **Yevheniia Husak**, Anna Skoczylas, Natalia Waloszczyk, Viktoriia Korniienko, Wojciech Simka. Synergistic Effect of Silicates and Phosphates on Magnesium Anodizing, 82nd International Scientific Conference of the University of Latvia, 8 February, 2024,Ryga, Latvia

Participation in conferences not related to the doctoral thesis:

1. **Yevheniia Husak**, Sergiy Kyrylenko, Bojan Petrovic, Pal Terek, Sanja Kojic, Zoran Bobic, Yuliia Varava, Artem Shmatkov, Maksym Pogorielov, Wojciech Simka. Three-Dimensional Bioactive Surface Structure on Ti-based Implants. The 2022 IEEE 12th International Conference “Nanomaterials: Applications & Properties” (IEEE NAP-2022), Kraków, POLAND, Sep. 11-16, 2022.

2. **Yevheniia Husak**, Pal Terek, Sanja Kojić, Zoran Bobić, Bojan Petrović, Sergiy Kyrylenko, Maksym Pogorielov, Wojciech Simka .Bio-mimetic bone-like surface structure of Ti-based implants. YUCOMAT 2022 & XII WRTCS Conferences, Herceg Novi, Montenegro, August 29 - September 2, 2022.

3. Maksym Pogorielov, Sergiy Kyrylenko, Oleksiy Gogotsi, Ivan Baginskiy, Vitalii Balitskyi, Veronika Zahorodna, **Yevheniia Husak**, Ilya Yanko, Mykolay Pernakov, Anton Roshchupkin, Mykola Lyndin, Bernhard B. Singer, Volodymyr Buranych, Oksana Sulaieva, Oleksandr Solodovnyk, Alexander Pogrebnjak, Yury Gogotsi. Pulsed NIR laser for photo-thermal ablation of MXene-loaded cells. YUCOMAT 2022 & XII WRTCS Conferences, Herceg Novi, Montenegro, August 29 - September 2, 2022.

4. **Yevheniia Husak**, Sergiy Kyrylenko, Anton Roshchupkin, Ilya Yanko, Wojciech Simka, Maksym Pogorielov A new highly developed titanate surface layer on titanium can support

attachment and proliferation of human cells. YUCOMAT 2022 & XII WRTCS Conferences, Herceg Novi, Montenegro, August 29 - September 2, 2022.

5. **Yevheniia Husak**, Sergiy Kyrylenko, Olesia Tverezovska, Oksana Petricenko, Viktoriia Holubnycha, Rafal Babasiuk, Viktoriia Korniienko. AgNPs stability after different post treatment. Twenty Fourth Annual Conference – YUCOMAT 2023, September 4-8, 2023, Herceg Novi, Montenegro.

6. **Yevheniia Husak**, Yuliia Varava, Natalia Waloszczyk, Viktoriia Korniienko, Kateryna Diedkova, Volodymyr Deineka, Veronika Zahorodna, Oleksiy Gogotsi, Wojciech Simka, Maksym Pogorielov. New approach of thin MXene coatings for PCL membrane, YUCOMAT 2024 & XIII WRTCS, 1-6 September, 2024, Herceg Novi, Montenegro.

Project activities

15. 04/010/BKM22/1043 Biofunctionalization of magnesium surfaces using the anodization process in solutions containing organic calcium compounds (menager).

16. 04/010/BKM23 Antibacterial oxide coatings based on insoluble and organic additives for Mg-based biomaterials (menager).

17. 32/014/SDU/10-22-29 Modification of the surface layer of titanium and its alloys by plasma electrolytic oxidation in solutions containing compounds of natural origin.

18. BKM-532/RCH1/2024 New approach of thin MXene and AgNPs coating for PCL and PLA membranes (menager).

19. M-ERA.NET Joint Call 2020 Hybrid Biodegradable Coating for One-Wire Peripheral Nitinol Stent for Prevention of Restenosis and Plaque Formation. Reference Number: project8067 (contractor).

20. H2020 project 777926 Nanostructural surface development for dental implant (contractor).

21. Erasmus+, Jean Monnet Programme, «Circular solutions in biomedicine – CircuMed», 2022-2025, Sumy State University, Ukraine (contractor).

22. Erasmus+, Jean Monnet Programme, «Modern European trends in biomedical higher education: Bionanomaterials», 2020-2022, Sumy State University, Ukraine (contractor).

23. Erasmus+, Jean Monnet Programme, «Medical education in the European Union: Challenges for Ukraine – MedEUk», 2019-2020, Sumy State University, Ukraine (contractor).

24. Grant of Ministry of Education and Science of Ukraine «Condition of mineralized tissues using new composites with Ag^{+} and Cu^{2+} nanoparticles», 0121U100471 (contractor).

25. Grant of Ministry of Education and Science of Ukraine «Determination of the efficiency of plasma electrooxidation for the modification of biodegradable alloys for orthopedics», 0119U100770 (contractor).

26. Grant of Ministry of Education and Science of Ukraine “Development of new haemostatic sponges”, №0116U006817.

27. Grant of Ministry of Education and Science of Ukraine “New antibacterial metal-chitosan nanocomposites – development and evaluation”, 0118U003577 (contractor).

28. Grant of CRDF Global (USA) – «Biosafety Improvement in Bacteriological Lab at Sumy State University», 2016 (contractor).

29. HORIZON-MSCA-2021-SE “Towards MXenes’ biomedical applications by high-dimensional immune MAPping” (contractor).

30. HORIZON-MSCA-2021-SE Project “Towards development of new antibacterial strategy for dentistry” (contractor).

Fundings

1. A SCHOLARSHIP FOR INTERNSHIP UNDER THE Erasmus + PROGRAM, 2022 to Technische Universität Bergakademie Freiberg. Eureca-Pro, 16th Freiberg Colloquium of Young Researchers: Responsible Consumption and Production in the Raw Material Sector.

Report - *“Plasma electrolytic oxidation as a recycling technology for biocoatings fabrication”.*

2. A SCHOLARSHIP: FOR STUDENTS AND RESEARCHERS FROM UKRAINE WITHOUT A PH.D. DEGREE - a special scholarship programme addressed at students and researchers from Ukraine without a PhD degree who have taken or will take refuge in Poland after the Russian invasion of Ukraine. Sources of funding for the: NCN, UMO-2022/01/4/ST5/00048 nr of the project04/010/ZZB23/1062. The period of participation: 01/03/2023 - 29/02/2024.

3. SUMMER SCHOOL, University of Novi Sad (Serbia) 2022 - Microfluidic chips and sensors from foodstuff and bioinspired materials under the project “Twinning for reaching sustainable scientific and technological excellence in the field of Green Electronics”, GREENELIT, H2020-WIDESPREAD-05-2020

Report - *“Plasma electrolytic oxidation as a recycling technology for biocoatings fabrication”.*

4. NIH4DS – New International Horizon for Doctoral School project. NIH4DS/Dz1/1_N1/2025.

Activities related to science popularization

1. Lecture "Electrochemical methods for tissue implant fabrication. Plasma electrolytic oxidation as a promising surface treatment for biomedical applications" to PhD and MSc students of the University of Latvia, Institute of Atomic Physics and Spectroscopy, Latvia, 07.05.2024.
2. Lecture " Egg-shells as a natural source of calcium for biocoatings on bone implants"at Jean Monnet International school, Universidade Federal de Lavras - Lavras - Minas Gerais – Brazil, 15.04.2024.